

UNIVERSITAT POLITÈCNICA DE VALÈNCIA



PROGRAMA OFICIAL DE POSGRADO  
**INGENIERÍA Y PRODUCCIÓN INDUSTRIAL**

## **DOCTORAL THESIS**

Study of the degradation mechanisms  
of the CoCrMo biomedical alloy in  
physiological media by electrochemical  
techniques and surface analysis

**Carlos Valero Vidal**

**Directed by:**

Dra. D<sup>a</sup> Anna Igual Muñoz

July 2012



A mis padres y a mi hermano  
por estar siempre ahí



Agradecer esta Tesis a toda esa gente que durante estos años ha compartido grandes momentos conmigo...

En primer lugar agradecérsela a mi directora, amiga y muchas de las veces hasta madre ANNA IGUAL MUÑOZ. Gracias no sólo por enseñarme todo lo que sé si no por transmitirme en todos los momentos la motivación por lo que hacemos y seguir adelante. Por ese proyecto que empezamos juntos hace tanto tiempo y del que me siento tan orgulloso. Me llevo un gran recuerdo de todos esos momentos vividos juntos (que no son pocos). Gracias por enseñarme muchas de las veces a cómo afrontar las cosas.... te deseo lo mejor, ¡te lo mereces!

Al Ministerio de Educación y Ciencia por su ayuda a través del financiamiento en el proyecto PROFIT CIT 300100-2007-0049 y de la Beca Predoctoral de Formación de Personal Universitario AP2007-01243 y al Ministerio de Ciencia e Innovación por el proyecto MAT 2011-22481. Asimismo, agradecer al Ministerio por la financiación de las dos estancias en Suiza en el *Institut des Matériaux* de la EPFL (Lausanne) gracias a la cual la presente Tesis Doctoral opta a la mención internacional.

Agradecerle también esta Tesis a mi supervisor de la estancia en Suiza, STEFANO MISCHLER. Gracias por la acogida, por la manera de pensar, por todo lo aprendido pero, sobre todo, por afrontar todo siempre con gran alegría. ¡Eres admirable!

Gracias a todo el grupo IEC. Gracias a vuestra ayuda ha sido mucho más fácil llevar esto a cabo. En especial a mis compañeras con los que empecé esta aventura, VIR y LUPITA, hasta los que me habéis acompañado en el final, CÉSAR, JORDI, TEPE y RAMÓN. ¡Gracias por todos esos grandes momentos!

A ISAAC, mi *hermano*, compañero, confidente,... con el que hace mucho tiempo empezamos y aún después de tantos años seguimos juntos. Lo peor de terminar la Tesis será separarnos, pero te deseo lo mejor en esta nueva etapa que viene. ¡Vales muchísimo! ¡Gracias por todo y mucha suerte!

Al departamento de Ingeniería Química y Nuclear, en especial a mis *tías* ALICIA, ISABEL y MARIA de las que me llevo un gran recuerdo.

Al grupo *Tribology - Materials, Surfaces & Interfaces* por su gran acogida y hacerme uno más desde el primer momento. ANABEL, NIKITAS, NIKOLA, NURIA, PIERRE y toda la gente extraordinaria con la que he compartido mis estancias en Suiza. A mis amigos BRAD, EDGAR, EVELINE, JAVI y LUIZ. En especial a SANDRA, por cuidarme tanto... me llevo una amiga para toda la vida. ¡Gracias por todo!

Agradecer a toda mi familia, en especial a mi MADRE, PADRE y a mi hermano ALBERTO. Por todos esos momentos, por aguantarme en los mejores y en los peores momentos, por ser siempre un grandísimo apoyo, por aceptar siempre todas las decisiones que he tomado en mi vida. ¡Os admiro! Y a esa nueva incorporación, ESTEFANIA, que te tengo tanto cariño.

Y por último, que no menos importante, a todo mi grupo de amigos en especial a ALBERTO, DAVID, DIANA, ELENITA, ESTEBAN, GIUSEPPE, ISA, JOSÉ, JUAN y LAURA por todos esos grandes momentos, por estar siempre tan unidos, por ser siempre simplemente así. A JAVI, mi *hermano*, mi gran apoyo en todo, con el que me siento tan unido, ¡no sabría que hacer sin ti! Y a mis dos grandes amigas, ANDREA y EVA, que aunque os tenga lejos siempre os llevo muy presentes. ¡Os quiero mucho a todos!

... a todos. Gracias!!!



## PUBLICATIONS RELATED TO THE DOCTORAL THESIS

---

### ARTICLES IN INTERNATIONAL JOURNALS

- *Electrochemical characterization of biomedical alloys for surgical implants in simulated body fluids.* C. Valero Vidal, A. Igual Muñoz.  
**Corrosion Science** 50 (2008) 1954-1961.
- *Effect of thermal treatment and applied potential on the electrochemical behaviour of CoCrMo biomedical alloy.* C. Valero Vidal, A. Igual Muñoz.  
**Electrochimica Acta** 54 (2009) 1798-1809.
- *Adsorption of bovine serum albumin on CoCrMo surface: effect of temperature and protein concentration.* C. Valero Vidal, A. Olmo Juan, A. Igual Muñoz.  
**Colloids and Surfaces B: Biointerfaces** 80 (2010) 1-11.
- *Influence of surface conditions on the adsorption process of bovine serum albumin (BSA) on CoCrMo biomedical alloy.* C. Valero Vidal, A. Igual Muñoz.  
**ECS transactions** 25 (2010) 187-201.
- *Study of the adsorption process of Bovine Serum Albumin (BSA) on passivated surfaces of CoCrMo biomedical alloy.* C. Valero Vidal, A. Igual Muñoz.  
**Electrochimica Acta** 55 (2010) 8445-8452.
- *Influence of electrochemical conditions on CoCrMo behaviour in simulated body fluids by Step Polarization technique.* A. Igual Muñoz, C. Valero Vidal.  
**ECS transactions** 28 (2010) 25-35.
- *Effect of physic-chemical properties of simulated body fluids on the electrochemical behaviour of CoCrMo alloy.* C. Valero Vidal, A. Igual Muñoz.  
**Electrochimica Acta** 56 (2011) 8239-8248.
- *Passivation of a CoCrMo PVD alloy with biomedical composition under simulated physiological conditions studied by EQCM and XPS.* C. Valero Vidal, A. Igual Muñoz, C.-O. A. Olsson, S. Mischler.  
**Journal of the Electrochemical Society** 159 (2012) C233-C243.

## CONGRESS PRESENTATIONS

- *Electrochemical characterization of biomedical alloys for surgical implants in simulated body fluids (Poster)*. C. Valero Vidal, A. Igual Muñoz. **BIOSURF VII. Functional Interfaces for Directing Biological Response**, Zurich (Switzerland), August 2007.
- *The effect of heat treatments on the corrosion behaviour of CoCrMo alloy by means of Electrochemical Impedance Spectroscopy (Oral presentation)*. C. Valero Vidal, A. Igual Muñoz. **European Corrosion Congress (EUROCORR'08)**, Edinburgh (United Kingdom), September 2008.
- *Influence of potential on the passive behaviour of CoCrMo alloy in simulated body fluids (Poster)*. C. Valero Vidal, A. Igual Muñoz. **59<sup>th</sup> International Society of Electrochemistry (ISE)**, Sevilla (Spain), September 2008.
- *Study of the passive behaviour of CoCrMo biomedical alloys in simulated body fluids (Oral presentation)*. C. Valero Vidal, A. Igual Muñoz. **214<sup>th</sup> Meeting on The Electrochemical Society**, Honolulu (U.S.A.), October 2008.
- *Study of the adsorption behaviour of albumin on CoCrMo by means of Electrochemical Impedance Spectroscopy (Poster)*. C. Valero Vidal, A. Olmo Juan, A. Igual Muñoz. **214<sup>th</sup> Meeting on The Electrochemical Society**, Honolulu (U.S.A.), October 2008.
- *Influence of passive conditions of CoCrMo biomedical alloy on the adsorption of albumin (Poster)*. C. Valero Vidal, A. Igual Muñoz. **2<sup>nd</sup> Workshop on Biotribology – Bridging Engineering and Medicine (ESF-EMBO). COST 533 Action on Materials for Improved Wear Resistance of Total Artificial Joints final meeting**, Guimaraes (Portugal), May 2009.
- *Influence of temperature and albumin concentration on the adsorption of bovine serum albumin (BSA) on a CoCrMo biomedical alloy (Poster)*. C. Valero Vidal, A. Igual Muñoz. **European Corrosion Congress (EUROCORR'09)**, Niza (France), September 2009.



- *Thermodynamical analysis of the adsorption process of albumin on CoCrMo biomedical alloy. Influence of surface conditions (Poster).* C. Valero Vidal, A. Igual Muñoz. **216<sup>th</sup> Meeting on The Electrochemical Society, Vienna (Austria)**, October 2009.
- *Step polarization test of implant biomedical alloy in physiologic conditions (Poster)* C. Valero Vidal, A. Igual Muñoz. **217<sup>th</sup> Meeting on The Electrochemical Society, Vancouver (Canada)**, April 2010.
- *Effect of pH on general electrochemical behaviour of CoCrMo biomedical alloy in phosphate buffer solutions (Poster).* C. Valero Vidal, A. Igual Muñoz. **European Corrosion Congress (EUCOCORR'10), Moscow (Russia)**, September 2010.
- *Passive behaviour of a CoCrMo biomedical alloy studied by EQCM and XPS (Poster).* C. Valero Vidal, S. Mischler, C.-O.A. Olsson, A. Igual Muñoz. **51<sup>st</sup> Corrosion Science Symposium, Southampton (United Kingdom)**, September 2010.
- *Nano-electrochemical characterization of CoCrMo biomedical alloy by EQCM and XPS (Oral Presentation).* C. Valero Vidal, S. Mischler, C.-O.A. Olsson, A. Igual Muñoz. **3<sup>rd</sup> European Conference on Tribology (ECOTRIB 2011) / 4<sup>th</sup> Vienna International Conference on Nano-Technology**, Vienna (Austria), June 2011.
- *Characterization of the passivity on CoCrMo alloy by EQCM and XPS (Oral Presentation).* C. Valero Vidal, S. Mischler, C.-O.A. Olsson, A. Igual Muñoz. **European Corrosion Congress (EUROCORR'11), Stockholm (Sweden)**, September 2011.
- *Corrosion of biomedical CoCrMo alloys under physiological solutions (Poster).* C. Valero Vidal, A. Igual Muñoz, C.-O.A. Olsson, S. Mischler. **19<sup>th</sup> International LDD&R (Local Drug Delivery Meeting and Cardiovascular Course on Revascularization & Molecular Strategies)**, Geneva (Switzerland), February 2012 (poster presentation prize).

## BOOK CHAPTERS

---

- *Electrochemical aspects in biomedical alloy characterization: Electrochemical Impedance Spectroscopy.* C. Valero Vidal, A. Igual Muñoz.

**INTECH Biomedical Engineering, Trends in Materials Science**

- *Synovial Fluid (joint fluid) role of protein adsorption on corrosion.* C. Valero Vidal, A. Igual Muñoz.

**Woodhead Publishing: Bio-tribocorrosion in biomaterials and medical implants**

**Under Revision**

## PREDOCTORAL STAYS IN A FOREIGN INSTITUTION

---

Two stays at the Materials Institute of the École Polytechnique Fédérale de Lausanne (EPFL) from January 2010 to July 2010 and from October 2011 to February 2012 were carried out.

The main objectives of this research are summarized as follows:

- To set-up an Electrochemical Quartz Crystal Microbalance (EQCM) for CoCrMo alloy characterization. The EQCM is basically a mass sensing device with the ability to measure mass changes in the nano-range on a quartz crystal resonator in real time. The EQCM is capable of measuring mass changes as small as a fraction of a monolayer or single layer atoms. This technique allows to analyze the influence of the physico-chemical properties of the CoCrMo surface on the passive growth or protein adsorption kinetics.
- To develop an experimental protocol to determine the adsorption/desorption mechanisms of proteins on a PVD-CoCrMo alloy and to study the passive film formation and dissolution of biomedical surfaces. To achieve this objective electrochemical techniques (potentiodynamic and potentiostatic tests) and in-situ techniques (EQCM) were used. Furthermore, in order to obtain a complete characterization of the surface ex-situ surface analysis will be carried out (X-Photoelectron Spectroscopy).

This research has contributed to enlarge the knowledge and experience on the electrochemical techniques and corrosion mechanisms of CoCrMo biomedical alloys. Chapter 6 *Study of the passivation and adsorption kinetics by EQCM and XPS* has been developed with the obtained results.



## ■ INDEX

### CHAPTER 1. Introduction

<b>1.1</b>	<b><i>Introduction</i></b>	<b>1</b>
<b>1.2</b>	<b><i>Corrosion in the human body</i></b>	<b>6</b>
1.2.1	<i>Adsorption of proteins. Bovine Serum Albumin</i>	13
<b>1.3</b>	<b><i>Corrosion of CoCrMo biomedical alloy</i></b>	<b>20</b>
1.3.1	<i>Biomedical alloy characterization</i>	20
1.3.2	<i>Electrochemical behaviour of the CoCrMo biomedical alloy. State of the art</i>	24
1.3.3	<i>Clinical implication of the passive dissolution of the CoCrMo alloy</i>	34
<b>1.4</b>	<b><i>References</i></b>	<b>39</b>

### CHAPTER 2. Objectives

	<b><i>Objectives</i></b>	<b>45</b>
--	--------------------------	-----------

### CHAPTER 3. Experimental techniques

<b>3.1</b>	<b><i>Introduction</i></b>	<b>49</b>
<b>3.2</b>	<b><i>Electrochemical techniques</i></b>	<b>50</b>
3.2.1	<i>Measurement of Open-Circuit Potential (OCP)</i>	52
3.2.2	<i>Potentiodynamic curves</i>	54
3.2.3	<i>Potentiostatic tests</i>	64
3.2.4	<i>Electrochemical Impedance Spectroscopy (EIS)</i>	67
3.2.4.1	Electrode response to a sinusoidal perturbation of the potential	67
3.2.4.2	Instrumentation	71
3.2.4.3	Interpretation of the impedance results. Equivalent Electrical Circuits (EEC)	72
3.2.4.4	Experimental considerations for biomaterials	79
3.2.5	<i>Electrochemical Quartz Crystal Microbalance (EQCM)</i>	80
3.2.5.1	Sauerbrey Equation	81
3.2.5.2	Limitations of Sauerbrey theory	84

<b>3.3</b>	<b><i>Surface Analysis</i></b>	<b>86</b>
3.3.1	<i>Scanning Electron Microscope (SEM)</i>	86
3.3.1.1	Technique principles and capacities	86
3.3.1.2	Experimental device and applied conditions	88
3.3.2	<i>X-Ray Photoelectron Spectroscopy (XPS)</i>	89
<b>3.4</b>	<b><i>References</i></b>	<b>94</b>

## **CHAPTER 4. Electrochemical characterization of CoCrMo alloy in simulated body fluids**

<b>4.1</b>	<b><i>Introduction</i></b>	<b>97</b>
<b>4.2</b>	<b><i>CoCrMo biomaterial alloy</i></b>	<b>100</b>
<b>4.3</b>	<b><i>Experimental set-up</i></b>	<b>102</b>
<b>4.4</b>	<b><i>Results and discussion</i></b>	<b>104</b>
4.4.1	<i>Influence of chemical composition and applied potential</i>	104
4.4.1.1	OCP	107
4.4.1.2	Potentiodynamic curves	109
4.4.1.3	Potentiostatic tests	113
	A) Cathodic domain	114
	B) Cathodic-anodic transition	116
	C) Passive domain	118
	D) Transpassive domain	121
4.4.1.4	Electrochemical Impedance Spectroscopy	123
	A) Cathodic domain	123
	B) Cathodic-anodic transition	127
	C) Passive domain	132
	D) Transpassive domain	139
4.4.2	<i>Influence of pH and aeration conditions of the simulated body fluids</i>	146
4.4.2.1	Experimental sequence	146
4.4.2.2	Results	148
	A) Open Circuit Potential Measurements	150

## CONTENTS

B) Potentiodynamic polarization curves	151
C) Potentiostatic tests	157
D) Electrochemical Impedance Spectroscopy	161
4.4.2.3 Discussion	167
A) Influence of pH	167
B) Influence of BSA	171
C) Influence of aeration	172
<b>4.5 Conclusions</b>	<b>174</b>
<b>4.6 References</b>	<b>174</b>

## CHAPTER 5. Mechanisms of BSA adsorption

<b>5.1 Introduction</b>	<b>181</b>
<b>5.2 Thermodynamical characterization of the BSA adsorption on CoCrMo surface</b>	<b>184</b>
5.2.1 Simulated Body fluids	184
5.2.2 Electrochemical measurements	184
5.2.3 Experimental results	186
A) Open Circuit Potential	186
B) Potentiodynamic curves	188
C) Electrochemical Impedance Spectroscopy	196
5.2.4 Influence of temperature. Arrhenius equation	208
5.2.5 Influence of BSA concentration on the passive behaviour. Langmuir isotherm.	214
<b>5.4 Influence of the BSA on CoCrMo passivated surfaces</b>	<b>220</b>
5.4.1 Introduction	220
5.4.2 Electrochemical measurements	220
5.4.3 Potentiodynamic curves	222
5.4.4 OCP	225
5.4.5 Applied passive potential	234
<b>5.5 Conclusions</b>	<b>242</b>
<b>5.6 References</b>	<b>244</b>

## CHAPTER 6. Study of the passivation and adsorption kinetics by EQCM and XPS

<b>6.1</b>	<b><i>Introduction</i></b>	<b>249</b>
<b>6.2</b>	<b><i>Experimental</i></b>	<b>251</b>
6.2.1	<i>Quartz Crystals</i>	251
6.2.2	<i>PVD deposits of CoCrMo layers on quartz crystals</i>	252
6.2.3	<i>Experimental Set-up</i>	254
6.2.4	<i>Correction constant for viscous loading</i>	263
6.2.5	<i>Calibration of the Sauerbrey constant</i>	265
6.2.6	<i>Electrochemical tests</i>	268
6.2.7	<i>X-Ray Photoelectron Spectroscopy</i>	269
<b>6.3</b>	<b><i>EQCM experiments</i></b>	<b>271</b>
6.3.1	<i>Potentiodynamic curves</i>	271
6.3.2	<i>Potential Step Measurements</i>	277
	A) <i>Passive domain</i>	283
	B) <i>Transpassive domain</i>	287
6.3.3	<i>XPS analysis</i>	287
<b>6.4</b>	<b><i>Discussion</i></b>	<b>300</b>
6.4.1	<i>Film growth in the passive domain</i>	300
6.4.2	<i>Film growth in the transpassive domain</i>	306
6.4.3	<i>Transpassive oxidation and dissolution of the CoCrMo alloy</i>	307
6.4.4	<i>Influence of temperature on mass and thickness change</i>	308
6.4.5	<i>Adsorption kinetics</i>	310
6.4.6	<i>Model of BSA-phosphates adsorption layer on the CoCrMo interface</i>	312
<b>6.5</b>	<b><i>Conclusions</i></b>	<b>316</b>
<b>6.6</b>	<b><i>References</i></b>	<b>318</b>



**CHAPTER 7. Conclusions**

<b>Conclusions</b>	<b>321</b>
1 <i>Electrochemical techniques</i>	322
2 <i>Passive dissolution</i>	323
3 <i>Transpassive dissolution</i>	324
4 <i>Adsorption</i>	325

**APPENDIX. List of symbols and abbreviations**

<i>List of symbols</i>	329
<i>Abbreviations</i>	335
<b>RESUMEN</b>	335
<b>RESUM</b>	337
<b>ABSTRACT</b>	339



# CHAPTER 1: INTRODUCTION

---

## 1.1. Introduction

**Biomaterial** can be defined as any substance (other than a drug), synthetic or natural, that can be used as a system or part of a system that treats, augments, or replaces any tissue, organ, or function of the body; especially, material suitable for use in prostheses that will be in contact with living tissue [1,2]. Such devices include artificial hips, knees, elbows, pacemakers, heart valves, intraocular lenses, etc. **Figure 1.1** summarizes the major applications of biomaterials in the human body [3-5].

**Biocompatibility** refers to the ability of a material to perform its desired function with respect to a medical therapy, without eliciting any undesirable local or systemic effects in the recipient or beneficiary of that therapy, but generating the most appropriate beneficial cellular or tissue response in that specific situation, and optimizing the clinically relevant performance of that therapy [6].

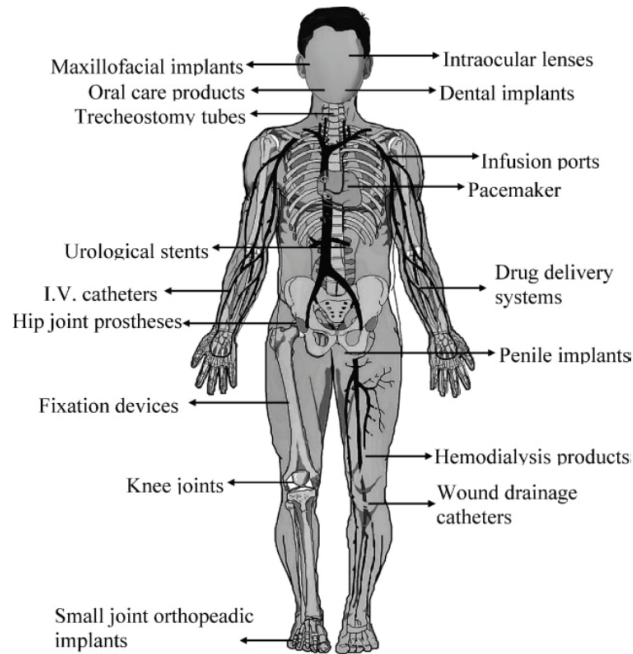


**Figure 1.1.** Major applications of biomaterials in the human body. Extracted from [3].

The field of biomaterials has evolved in such manner that more than 50 different materials are used in more than 40 types of complex prosthetic devices. One of the most important developments in clinical medicine has been the replacement of diseased joints with artificial implants. Since the early cemented hip replacements of the 1960s there has been a constant flow of new materials and designs for implantable devices and the number is steady increasing as technological process and medical practice allow for increased functionality and safety.

Total hip joint arthroplasty is increasing and surgeries affect 0.16-0.2 % of population per year [7]. Over 500.000 total hip replacements (THRs) are performed in the United States each year. These devices are implanted at all ages, from 20 to 80 years. The average life span of an implant is around 15 year although 10 % of the implanted prosthesis requires revision within 10 years [3,8]. This short life creates a problem for the growing number of people receiving implants that are younger than 40 years since not more than two replacements are possible. In addition, young people are generally more active which can induce multiple revision surgeries in their lifetimes that are

costly and increasingly harmful. Because of the increasing number of hip and knee replacements, degradation mechanisms must be studied in order to improve their durability and therefore try to decrease the need for revision surgery.

The properties that should exhibit a biomaterial for successful application in total joint replacement are:

- Biocompatible chemical composition to avoid adverse tissue reaction.
- Corrosion resistance to the body fluid which is considered one of the most aggressive environments (complex chemical composition).
- Acceptable strength to tolerate cyclic loading endured by the joint.
- Low modulus in order to minimize bone resorption.
- High wear resistance to minimize wear debris generation.

Metals and alloys are widely used as biomedical materials and are essential for orthopaedic implants, bone fixations, artificial joints, external fixations... since they can substitute for the function of hard tissues in orthopaedic. In particular, toughness, elasticity, rigidity, and electrical conductivity are important properties for metallic materials used in medical devices. Because the most important property of biomaterials is safety and biocompatibility, corrosion-resistant materials such as stainless steel, cobalt-chromium-molybdenum alloys and titanium alloys are commonly employed. However, there is still a significant concern associated with biomedical alloys related to the production of metal particles and ions [9,10] which can lead to cellular toxicity [11-13], metal hypersensitivity [14,15], and chromosomal changes [16]. Furthermore, the material release can lead to loss of biomaterial fixation and the consequently revision surgeries could be needed.

An innovate alternative to the use of stainless steel are the Co-Cr and Co-Cr-Mo alloys (ASTM F75, F90 and F562) which also present high biocorrosion resistance and lower rigidity. Furthermore, the absence of nickel in these alloys allows them to be employed in patients with sensibility and allergy to this element [10]. Titanium alloys are the most corrosion-resistance alloys within the metallic group of biomaterials but its low

wear resistance impedes them to be used where wear can occur [17]. CoCrMo alloys contain generally 26-30% of Cr, 5-7% of Mo and the balance composition of Co. Contemporary Co-Cr alloys are superior to stainless steel, both in fatigue and wear resistance, and are therefore preferred in total joints replacements, in both supportive and articulating locations. However, fatigue fracture still remains a possible complication [18], and corrosion issues after porosity initiation may occur [17].

Co-Cr and Co-Cr-Mo alloys are mainly used in hip (component that replace the spherical head of the femur and the component that assembles into the femur in order to give stability) and knee (femoral component) implants [8,19] represented in **Figure 1.2(a)** and **1.2(b)** respectively.

It is worth to note that the surrounding media of the metallic implants (body fluids) plays an important role on its durability. This fluid is one of the most aggressive environments due to the high concentration of chloride ions and organic compounds. The main components present in the body fluids are salts (NaCl, KCl, CaCl<sub>2</sub>), organic molecules (proteins) and inorganic species (phosphates). The general composition of the human biological fluids (plasma or serum and synovial fluid) is shown in **Table 1.1**. Fluid properties and composition can readily change as a result of disease, aging and drug ingestion [20].

**Table 1.1.** General chemical composition of the human biological fluids [20].

CHEMICAL COMPOSITION		
COMPOUND	PLASMA (SERUM)	SYNOVIAL FLUID
Bicarbonate	25-30 mM	-
Calcium	2.12-2.72 mM	1.2-2.4 mM
Chloride	100-108 mM	87-138 mM
Phosphorous (total)	2.87-4.81 mM	-
Potassium	3.5-4.7 mM	3.5-4.5 mM
Sodium	134-143 mM	133-139 mM
Amino acids	20-51 mg mL <sup>-1</sup>	-
Glucose	650-966 mg mL <sup>-1</sup>	-
Uric acid	30.5-70.7 mg mL <sup>-1</sup>	39 mg mL <sup>-1</sup>
Water	930-955 mg mL <sup>-1</sup>	960-988 mg mL <sup>-1</sup>
Albumin	37.6-54.9 mg mL <sup>-1</sup>	6-10 mg mL <sup>-1</sup>
IgG	6.4-13.5 mg mL <sup>-1</sup>	1.47-4.62 mg mL <sup>-1</sup>
Fibrinogen	2-4 mg mL <sup>-1</sup>	-

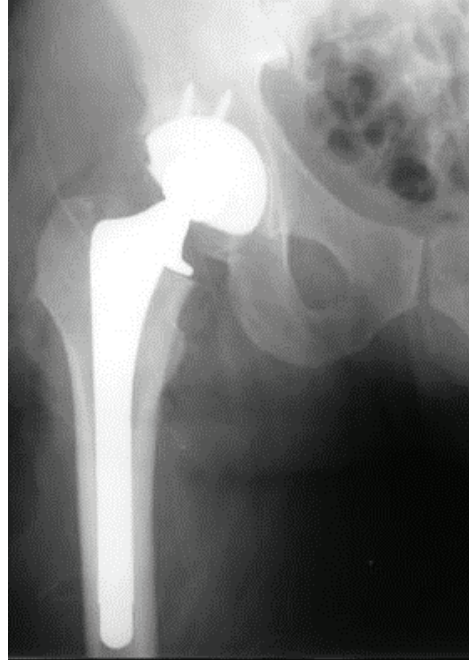
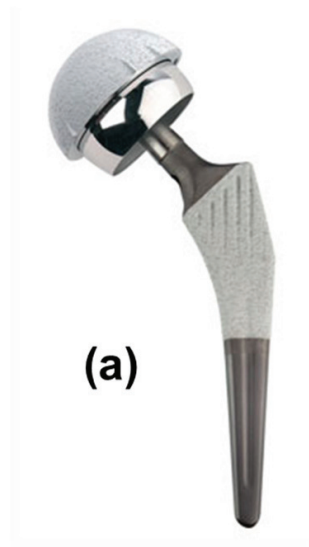
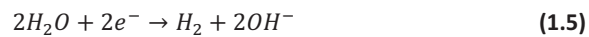
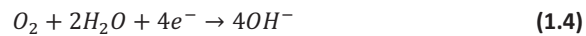


Figure 1.2. (a) Typical hip implant with femoral component and (b) knee implant.

## 1.2. Corrosion in the human body

The **corrosion process** is an irreversible chemical or electrochemical reaction occurring at the interface of the material representing the spontaneous dissolution of the metal ( $M$ ) by its reaction with the environment resulting in the loss of the material or in the dissolving of one of the constituents of the environment into the material [21]. The oxidation of the metal, **equation (1.1)**, is coupled to the reduction of the oxidizing agent (environment) which takes the electrons from the oxidation reaction. The **equations (1.2)** and **(1.3)** show the reduction reactions favoured in acidic media, while the **equations (1.4)** and **(1.5)** take place in neutral or alkaline media.



In order to understand the basis of these electrochemical reactions taking place on the biomaterial surface and their kinetics it is important to know the situation at the biomaterial/body fluid interface. This knowledge allows one to predict the corrosion behaviour of the biomaterial into the body related to its duration and the amount of metal ion release. **Figure 1.3** shows a scheme of the reaction steps (anodic and cathodic) occurring at the biomaterial surface during the corrosion process in liquid environments.

A charged surface is present in the metal in contact with the electrolyte. In order to maintain the electroneutrality of the interface, this surface leads to the formation of an **electric double layer** in the electrolyte. The charge distribution at the metal/electrolyte interface depends on: electronic properties of the solid, adsorption of water molecules and of hydrated cations and of chemisorption of anions. Therefore, the structure of the double layer varies with the chemical composition of the environment and with certain external conditions (i.e. applied potential). Thus, the



sum of the positive charges in the double layer equals the number of the negative ones. Different models have been proposed in order to explain the charge distribution at the metal/electrolyte interface. Helmholtz model is the simplest one which assumes the compensation of the surface excess charge by a monolayer of opposite charge (two planes different charged) where the potential linearly drops over the double layer. More advanced model (Stern model) describes the charge distribution in terms of an inner rigid layer and an outer diffusion layer (**Figure 1.4**). In biosystems, the electrical double layer formed onto metallic interfaces presents huge complexity due to the high variety of compounds that constitute the body fluids (ionic, inorganic, proteins, cells and biomolecules).

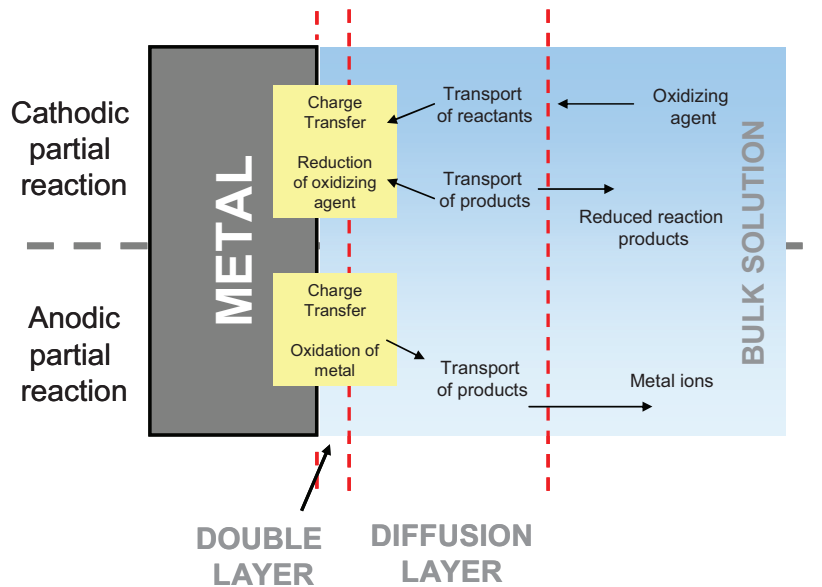


**Figure 1.3.** Reaction steps during the corrosion process of a metal in liquid environments [21].

The oxidizing agents present in the electrolyte diffuse towards the electrode surface where it reacts by accepting the electrons. Mass transport phenomena, taking place before or after the charge transfer reactions that could occur in the interface biomaterial/electrolyte, determine the concentration of the reactants and products at the electrode surface. The electrolyte layer contiguous to the metal surface in which the concentration of the reactants or products differs from that in the bulk electrolyte

is called the *diffusion layer*. The thickness of the diffusion layer mainly depends on the convection conditions where values between 1 and 100  $\mu\text{m}$  are typically reached. The diffusion layer is thicker than the electric double layer which has between 0.2 and 10 nm.

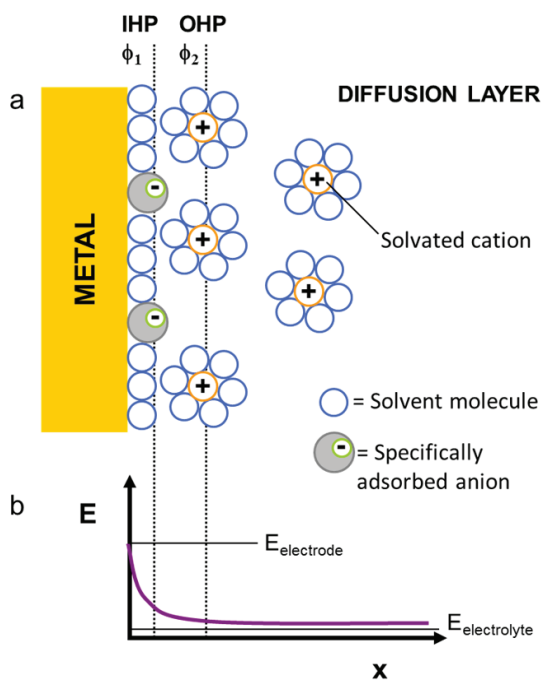


**Figure 1.4. (a)** Electrical double layer at metal-electrolyte interface in presence of chemisorbed anions [21]. Inner (IHP) and outer Helmholtz (OHP) layer forming the electric double layer is shown. The difference between the potentials  $\phi_1$  and  $\phi_2$  across the electrode/electrolyte interface highly influences the charge distribution of the electrical double layer. **(b)** Potential distribution on the electrode proximity.

In a bio-system involving metallic biomaterials several corrosion phenomena can take place: active dissolution, passivation, passive dissolution, transpassive dissolution, localized corrosion and adsorption.

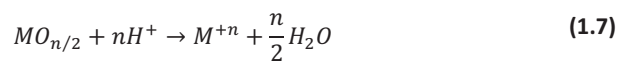
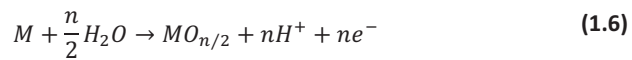
The *passivity* of metals consists in the formation of a thin oxide layer on their surface which protects the metal from its environment. Thus, the biomaterials are self-protected by the spontaneous formation of this thin oxide film being the kinetic factor that controls the corrosion rate in biological aqueous solutions. Therefore, the biocompatibility of these biomaterials is closely related to the stability of this oxide layer. The passive film plays two roles in limiting both the anodic and cathodic reactions, serving as a physical barrier for cations (ions positive charged) and anions (ions negative charged) transported to the metal surface as well as an electronic barrier for electrons.

The protectiveness of the passive film is determined by the rate of ion transfer through the film as well as the stability of the film against dissolution. A variety of factors can influence ion transport through the film, such as its chemical composition, structure, thickness and presence of defects. The nature and stability of a passive film on a particular metal or alloy depends on the environment conditions such as the chemical composition of the electrolyte, the redox conditions, the exposure time and temperature [17].

Typically, hydroxyl groups are found at the outer surface of the film. Their presence is due to the fact that the oxide surface is hydrated or it may result from the precipitation of a thin hydroxide layer from the solution. The chemical composition of the passive film formed on alloys is even more complicated because two or more metal cations are present in different concentrations. Indeed, the concentration ratio of cations in passive film on alloys often differs substantially from that expected from the alloy composition. Two phenomena, selective oxidation of alloy elements and selective dissolution of films constituents can contribute to this fact [21].

On the other hand, the metals free of oxide film are in their active state. The dissolution of these metallic materials is denominated *active dissolution* and involves a charge transfer at the metal-electrolyte interface. The generated ions are dissolved into the solution in form of hydrated or complexed species according to **equation (1.1)**. The concentration generated by dissolution often excess that of the bulk electrolyte which allows the continuous dissolution of these species; however,

when the solubility of the specie is overcome solid reaction products begin to precipitate forming a porous film (corrosion products). Nevertheless, **passive dissolution** takes place when passive metals are dissolved. In this case, cations are also generated in the interface metal/oxide film by a charge transfer reaction and the ions migrate across the passive film/electrolyte interface. **Equation (1.6)** shows the formation of the oxide film as a consequence of the cation ( $M^{+n}$ ) migration towards the outer surface and the anion ( $O^{2-}$ ) migration in the opposite direction while the **equation (1.7)** represents the passive dissolution where the cations are dissolved from the passive film into the solution. The overall reaction (**equations (1.6) and (1.7)**) is equivalent to **equation (1.1)**.



A scheme with the general reactions occurring during the oxide film formation and the passive dissolution are represented In **Figure 1.5**.

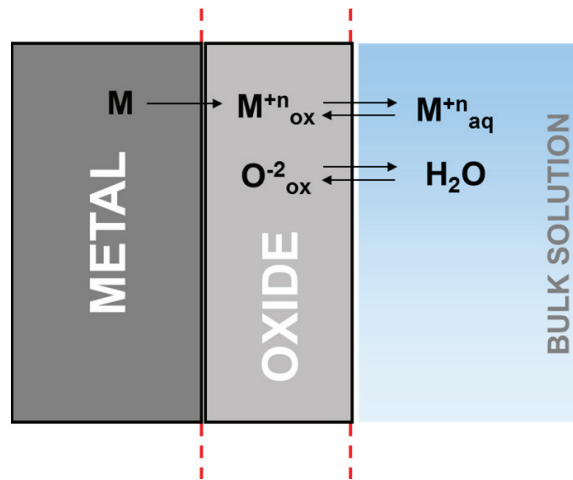


**Figure 1.5.** Scheme of the reactions taking place on the passive metal surface. Strong electric field is presented in the film which favours the cation/ion migration through the oxide passive film [21].

According to the described mechanisms, the phenomena which take place on the metal will determine the kinetic rate of the electrochemical reactions occurring on the metallic biomaterial. Taking into account the kinetics of the electrochemical reaction evolutions it is possible to differentiate three mechanisms depending on the rate-limiting step:

- Corrosion controlled by the kinetics of a **charge-transfer** reaction, either anodic or cathodic, at the metal-electrolyte interface. The kinetic/s reaction/s is determined by its activation energy.
- Corrosion controlled by the rate of **mass transport** of the oxidizing agent or of anodic reaction products. This mechanism is related to the overpotential generated as consequence of the different concentration of reactant and products between the bulk electrolyte and the metal interface.
- Corrosion controlled by the properties of the **passive film**. The reaction is then under anodic control and the average corrosion rate is often quite small.

**Transpassive dissolution** occurs when the protecting passive film is oxidized to species with higher oxidation valence which are characterized by high solubility (i.e.  $\text{Cr}^{+6}$ ,  $\text{Co}^{+6}$ ) [22]. It can occur below the potential for oxygen formation (uniform transpassive dissolution by film oxidation) or when oxygen evolution take places (high-rate transpassive dissolution). The first one, in the case of stainless steel and CoCrMo alloys, the oxidation is not sufficient to trigger high-rate of transpassive dissolution which is observed when the oxygen evolution is produced [23,24]. Dissolution at transpassive potentials is relevant to corrosion in strongly oxidizing media and in presence of highly oxidant species such as OH radicals and  $\text{H}_2\text{O}_2$  (intermediary compound produced in the metabolic reactions). The main problem of this this kind of oxidation is the generation of  $\text{Cr}^{+6}$  which presents high level of toxicity [13].

An important type of corrosion is the **localized corrosion** in which an intensive attack takes place in small local sites at a much higher rate than the rest of the surface (which is corroding at a much lower rate). The localized corrosion is associated with other

mechanical process (such as stress, fatigue and erosion) and other forms of chemical attack. The main form of localized corrosion in passive alloys (i.e. stainless steel) is the **pitting corrosion**; the metal is removed preferentially from vulnerable areas on the surface. The pitting corrosion is a local dissolution leading to the formation of cavities in passive metals or alloys that are exposed to environments with aggressive ions (i.e. chlorides) [25-27]. Pitting corrosion in CoCrMo is rarely observed, since this material fails by generalized transpassive corrosion. In surgical stainless steel, the pitting corrosion is more common since it is produced at lower potentials than the oxidation of the  $\text{Cr}^{+3}$  to  $\text{Cr}^{+6}$ . Other type of localized corrosion is the **crevice corrosion** which occurs when difference availability of oxygen takes place in regions of the biomaterial and therefore mass transfer is limited (occluded areas within the implant structure). In these areas, the presence of certain aggressive ions such as chloride ions diminishes the pH values and depletion of oxygen can contribute to the surface activation. The high amount of Cr in the oxide passive film formed onto CoCrMo alloys provides high corrosion resistance to this type of corrosion.

Other common phenomenon in biological systems is **adsorption** of certain species present in the body fluid (i.e. proteins, biomolecules and cells) onto the surface of metallic materials. The adsorption is established between the adsorbed species and the surface due to weak forces or Van der Waals and it can modify the passive dissolution rate of biomaterials among others.

### 1.2.1. ADSORPTION OF PROTEINS. BOVINE SERUM ALBUMIN.

Proteins are complex, high molecular weight organic compounds that consist of amino acids joined by peptide bonds. They have three dimensional structures. Each type of proteins has its own unique structure and function. The basic structure of an amino acid consists of four parts: an amino group (-NH<sub>2</sub>), a carboxyl group (-COOH), a central carbon (C) and side chain. The formation of hydrogen bonds between amino acids in the chains causes bonds and curves in the structure. There are four different aspects of a protein structure: primary, secondary, tertiary and quaternary structure [28]. Protein native state is known as a protein naturally folds, which means the secondary structure remains its functional shape. A protein in its native state is often described as *folded*. A protein that is not in its native state is said to be denatured (*unfolded*). Denatured proteins generally have no well-defined secondary structure [29].

The unsaturated bonds exhibited by atoms at a metal surface are available for fixing reactive species, atoms or molecules, present in the gas or liquid surrounding the surface. Such reaction, when limited to one monolayer or a fraction of a monolayer, is known as adsorption phenomenon or chemisorption. The presence of adsorbed species at the metal-liquid interface may greatly influence electrochemical processes involved in corrosion, such as anodic dissolution, cathodic reaction or passive film formation [30]. Thus, adsorption is the process through which a substance originally present in one phase is removed from this and it is accumulated at the interface between that phase and a separated (solid) phase. The adsorption of proteins is the initial stage involved in the adhesion of cells and the formation of biofilms on solid surfaces [31]. This protein adsorption is the intermediate in the adhesion of cells with the biomaterial surface [32].

The main aspects of the protein adsorption studies onto metallic biomaterials surfaces are focused in the adsorption kinetics [33,34], dynamic and thermodynamic properties [35-37], conformational structure [38] and function in the adsorbed state. All these properties of the adsorption phenomena allow one to determine the implication of these organic compounds on the corrosion behaviour of metallic biomaterials.

Different factors affect the adsorption of the protein on the material surface. The sequence of amino acids (primary structure) affects the protein-surface interaction since the bonds established between the amino acids determine the active zones of the protein available to interact with the surface [39].

The material properties play an important role on the adsorption process, above all properties of the material surface such as wettability, polar or ionic interaction, chemical structure and topography of the surface among others affect the nature and the amount of the adsorbed protein. Generally, hydrophobic surfaces are considered to be more protein-adsorbed than hydrophilic surfaces because of the strong hydrophobic interactions occurring at these surfaces, contrary to the repulsive solvation forces arising from strongly bound water at the hydrophilic surfaces [40,41].

The solution pH has also an important role in the protein adsorption since the overall charge of the protein changes depending on the acidity or alkalinity of the electrolyte. In acidic media the protein has positive charge as consequence of the amino group ( $-NH_2$ ) which becomes  $-NH_3^+$ . However, in alkaline solutions the carboxyl group ( $-COOH$ ) loses H and becomes  $-COO^-$  which contributes to the negative charge of the protein. Thus, the proteins can interact with the surface by electrostatic forces, although this force is rather weak and other interactions (e.g. wettability) becomes more significant [42]. Furthermore, the proteins can interact with other compounds present in the body fluid or even enter in competition with them for the metal sites which can modify the adsorption process [43].

Neville and Yan summarized how biological molecules influence material corrosion behaviour [28]:

- The adsorption of protein onto metallic surface modifies the availability of the **oxygen** present in the interface biomaterial/body fluid which can alter the electrochemical reaction occurring over the metallic surface. On the one hand, the adsorbed layer can hindered the oxygen evolution reaction (decrease of the cathodic reaction rate) and the charge transfer responsible for the passive film dissolution (anodic reaction) increasing the polarization resistance of the biomaterial and diminishing the corrosion rate [44]. In some cases, the lack of



oxygen can limit the diffusion of oxygen providing the breakdown of the passive layer and preferential corrosion on the oxygen deficient regions. On the other hand, thin layer of adsorbed protein can increase the oxygen concentration which increases the corrosion rate of the biomaterial because of the increase of the thermodynamic driving force for the electrochemical reactions.

- The protein adsorption can generate **compact layer** which can act like a barrier preventing the diffusion of metal ions or oxide from the metal surface to the electrolyte. Due to the decrease of the anodic reaction rate an increase of the corrosion resistance is expected.
- The protein can bind to metal ions (**organometallic complexes formation**) and transport them away from the solution/biomaterial interface, thus enhancing further dissolution [45-47]. To retain the equilibrium the dissolution rate of a base material increases and, consequently, suppresses the formation of the passive layer (in passive metallic biomaterials) [17,48,49].
- Certain biological molecules (cells and bacteria) can consume **hydrogen** in the bioenvironment as consequence of their metabolic process. Hydrogen is involved with cathodic reaction in the redox equilibrium of the corrosion process. Therefore, the consumption of hydrogen can increase the cathodic reaction rate, thus encouraging the anodic dissolution. In some cases, the hydrogen evolution reaction can be inhibited by the adsorption of proteins generating a diffusion layer that causes the anodic dissolution of the alloy to be under diffusion control [50].

The role of the proteins in a corrosive environment is governed by many factors such as the surface chemistry of the metal, protein adsorption characteristics, interaction of protein molecules with other ions present in the environment to produce organic complexes, and the transport of anionic or cationic charges around and away from the local environment. Thus, the protein can act as a boundary lubricant with a beneficial role on the wear behaviour [51]. Nevertheless, the effect of lubrication or adsorption can probably induce the metal ion dissolution from the metal [52].

Figure 1.6 shows an example in atomic and molecular level events that can happen when a metallic implant enter in contact with a biological environment. The chemical and electrochemical reactions that take place in a biological system are a complex phenomenon where becomes difficult to determine the implication of each compound.

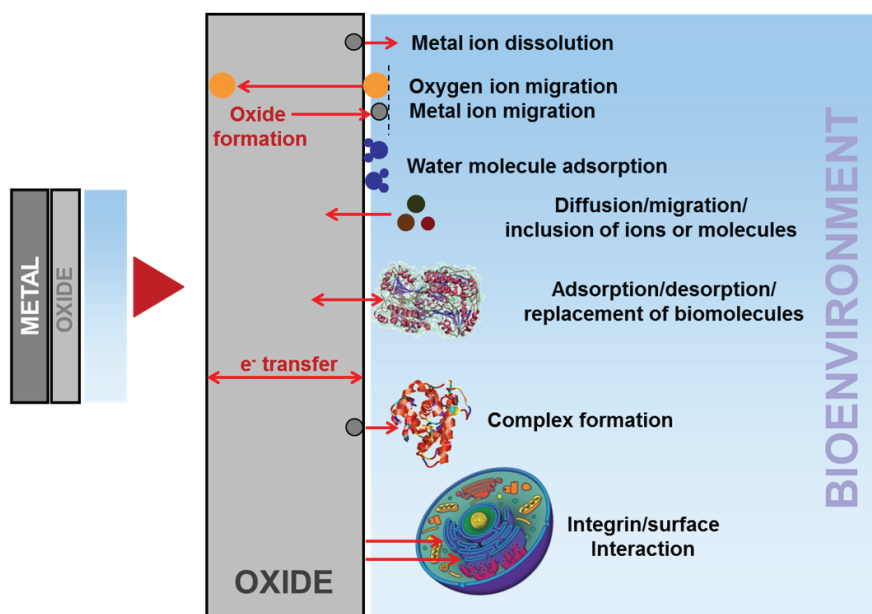


Figure 1.6. Processes and interactions at the oxide/environment interface [28,53].

According to Scharnweber [53] the interaction between the metallic biomaterial and the biological environment is a processes that can be divided in two groups:

- Processes from the implant towards the tissue: release of metal ions because of corrosion process and emission of particles caused by mechanical effects, modification of the local biological environment near the surface as a consequence of the alteration of the partial redox reactions of the corrosion process (increase of the pH, lowering of the O<sub>2</sub> partial pressure by a dominating cathodic partial reaction), influence over the adsorbed molecules by corrosion products generated and influence of surrounding cells by electric fields and current caused by corrosion.

- Processes from the biological environment towards the implant: diffusion, migration and inclusion into the metal of ions or molecules, decrease of the pH by local inflammation of the damaged tissue, dissolution process as consequence of ion-complexes formation and surface interaction with the cells.

It is important to point out that the mechanisms of interaction between the surrounding tissues and the surface of the metallic implant are not completely understood yet and remain a topic of fundamental research.

In this Thesis, **Bovine Serum Albumin** (BSA) has been selected as a model protein in order to analyse the implication of protein adsorption on the corrosion behaviour of CoCrMo alloy. BSA ( $M_r$  of 66300 Da with dimensions of  $15 \times 3.8 \times 3.8 \text{ nm}^3$ ) is the most abundant protein in the body fluids mainly in the circulatory system, **Figure 1.7**. The typical concentration of Serum Albumin is  $37.6\text{-}54.9 \text{ mg mL}^{-1}$  and  $6\text{-}10$  in the plasma (serum) and in the synovial fluid respectively [20]. The protein contributes 80 % to colloid osmotic blood pressure and is chiefly responsible for the maintenance of blood pH. The protein's (heart shaped) globular structure is achieved by the folding of its polypeptide chain (containing 585 amino acid residues) into three  $\alpha$ -helical domains [54,55]. Because of its high concentration, serum albumin arrives first at the implant's surface according to the laws of mass transport, and therefore plays an important role in the initial adsorption of proteins onto biomedical surfaces. The protein has high ability to reversibly bind to a large amount of ligands. Co, Cr, Fe and Ni can incorporate with albumin at carboxylate and tyrosine positions or bind with the  $-\text{SH}$  group of a single cysteine residue [56]. Albumin adsorption behaviour is different for different metal surfaces [57] and external conditions which makes difficult to extrapolate its actuation in different biological systems.

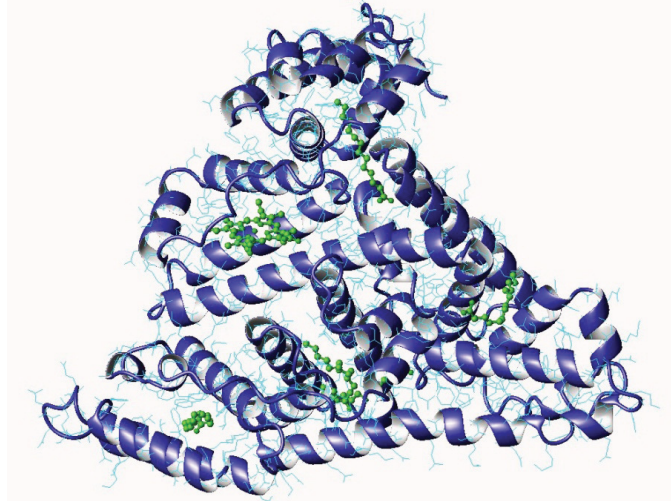


**Figure 1.7.** Three-structure of Bovine Serum Albumin.

In the study of the adsorption process, mathematical models for protein adsorption have been developed in order to understand the behaviour of the proteins in close proximity to or deposited onto the surface. Most models are focused in the kinetic study by means of rate equations. It is difficult to formulate a model which includes all the involved parameters in the adsorption process (structural rearrangements, lateral interactions, cooperative effects or overshootings) [58]. The simplest model is the **Langmuir** adsorption model which assumes that there are a fixed number of sites on the surface:

$$\frac{\partial \theta}{\partial t} = k_{ads} \cdot c_s \cdot \left(1 - \frac{\theta}{\theta_{max}}\right) - k_{des} \cdot \theta \quad (1.8)$$

Where  $\theta$  is the protein coverage,  $\theta_{max}$  is the maximum level of coverage without more available sites to adsorption,  $k_{ads}$  and  $k_{des}$  are the rate constants for adsorption and desorption respectively and  $c_s$  is the protein concentration directly above the surface. This model considers that each site is capable of adsorbing a single atom or molecule (equivalent sites) forming a monolayer with constant adsorption energy (no interactions between adsorbed species occurs). At equilibrium,  $\partial \theta / \partial t$  must be 0 and

both parts of the equation should be equal. Thus, Langmuir postulates that the exact shapes of  $k_{ads}$  and  $k_{des}$  are equal to  $c_s \cdot (1 - \theta)$  and  $(\theta)$  respectively which leads to the simplification of the general form of Langmuir isotherm [59,60]:

$$\theta = \frac{K \cdot c_s}{(1 + K \cdot c_s)} \quad (1.9)$$

Where  $K$  is the adsorption coefficient which is defined as follows:

$$K = \frac{k_{ads}}{k_{des}} \quad (1.10)$$

The adsorption of proteins from bulk solutions cause a depletion of the surface concentration which in turns leads to a transport from the bulk solution to the region above the surface. As a consequence, the surface concentration varies during the adsorption process which is often taken into consideration in the model.

Taking into account that the coverage can be defined as the relation between the amount of adsorbed protein  $\Gamma$  ( $\text{mol cm}^{-2}$ ) and the maximum value of  $\Gamma$  ( $\Gamma_{max}$ ), the **Langmuir isotherm** can be reformulated as:

$$\Gamma = \frac{B_{ADS} \cdot \Gamma_{max} \cdot c_s}{1 + B_{ADS} \cdot c_s} \quad (1.11)$$

in which  $B_{ADS}$  ( $\text{cm}^3 \text{mol}^{-1}$ ) is a parameter which reflects the affinity of the adsorbate molecules toward adsorption sites.

### 1.3. Corrosion of CoCrMo biomedical alloy

#### 1.3.1. BIOMEDICAL ALLOY CHARACTERIZATION

There are at least four compositions for cobalt-base alloys that are designated by ASTM (*American Section of the International Association for Testing Materials*). CoCrMo is a cast alloy commonly used in many applications and CoCrWNi is a wrought alloy that is more suitable for hot rolling. CoNiCrMo and CoNiCrMoWFe are less frequently used. The chemical composition and the mechanical properties required for this sort of alloys are regulated by the following specifications and they are summarized in **Table 1.II** and **1.III** respectively:

- **CoCrMo F75-87.** Standard specification for Cast Cobalt-Chromium-Molybdenum Alloy for Surgical Implant Application.
- **CoCrWNi F90-87.** Standard specification for Wrought Cobalt-Chromium-Tungsten-Nickel Alloy for Surgical Implant Application.
- **CoNiCrMo F562-84.** Standard specification for Wrought Cobalt-Nickel-Chromium-Molybdenum Alloy for Surgical Implant Application.
- **CoNiCrMoWFe F562-84.** Standard specification for Wrought Cobalt-Nickel-Chromium-Molybdenum-Tungsten-Iron Alloy for Surgical Implant Application.

**Table 1.II.** Chemical composition of cobalt-base alloys (ASTM,1992) [61].

CHEMICAL COMPOSITION				
ELEMENT	F75	F90	F562	F563
Cr	27-30	19-21	19-21	18-22
Mo	5-7	-	9-10.5	3-4
Ni	2.5 max	9-11	33-37	15-25
Fe	0.75 max	3 max	1 max	4-6
C	0.35 max	0.05-0.15	0.025 max	0.05 max
Si	1 max	0.4 max	0.15 max	0.5 max
Mn	1 max	1-2	0.15 max	1 max
W	-	14-16	-	3-4
P	-	-	0.015 max	-
S	-	0.03 max	0.01 max	0.01 max
Ti	-	-	1 max	0.5-3.5
Co	BALANCE			

**Table 1.III.** Mechanical properties of the cobalt-chromium alloys (ASTM,1992) [61].

<b>MECHANICAL PROPERTIES</b>			
<b>ELEMENT</b>	<b>F75</b>	<b>F90</b>	<b>F562</b>
<b>Traction resistance</b>	655 MPa	860 MPa	1793 MPa
<b>Fluence limit</b>	450 MPa	310 MPa	1585 MPa
<b>Lengthening</b>	8 %	10 %	8 %
<b>Area reduction</b>	8 %	-	35 %
<b>Fatigue resistance</b>	310 MPa	-	-

Cobalt-base alloys have an austenitic phase which is partially converted to a martensitic phase [62].

Cast alloys can be processed in a number of ways depending on the desired mechanical properties of the final product. The metallic implants with difficult geometry present problems to be mechanized and casting is the optimal method to be used. These as-cast alloys have to be treated in order to improve their mechanical and chemical properties since this process contributed to the generation of heterogeneities on the material. Porosity, chemical inhomogeneity and inter-dendritic structure are many of these heterogeneities which provide fragility and low fatigue resistance to the material.

The most common thermal treatments applied on the CoCr alloys are:

- *Solution Annealing* (SA) which allows the rupture of the dendritic structure improving the chemical homogenization of the material by applying a thermal cycle in argon atmosphere.
- *Hot Isostatic Pressing* (HIP) consists in a thermal process applying high temperature at the isostatic pressure of a gas. This treatment decreases the porosity and improves the fatigue properties of the alloy.
- The Porous Coating (PC) procedure is a thermal treatment employed in the manufacturing of surface prosthesis. Spherical beads are bonded to each other and the solid substrate by sintering at higher temperatures (around 1300°C) to achieve a strong particle-substrate bond [63]. This treatment increases the grain size and decreases the mechanical properties. Therefore, more thermal

treatments are required after the PC process in order to improve their properties. It is important to note that the incorporation of these spheres on the surface alloy improves the osteointegration of the implanted material.

These treatments produce a very important modification of the microstructure of the alloy, provide high amount of defects, such as porosity or lack of homogeneity and therefore they may change the biocompatibility of the alloys through the modification of the electrochemical properties. Main metallurgical changes produced by the high temperature sintered cycle consist of dissolution of interdendritic carbides, massive precipitation of lamellar carbide eutectic phases at grain boundaries, localized porosity from incipient melting that is not completely eliminated by following hot isostatic pressing, and grain boundary in fine-grained materials.

It is well known that these microstructure changes affect the mechanical properties and wear properties [63-65], but it is not clear if they affect the electrochemical behaviour of the material. According to Georgette and Davidson [66] the corrosion behaviour of CoCr alloys depends on the microstructure. A more stable, uniform oxide layer would be expected with a more homogenous matrix (annealed alloy) than with a highly dendritic (as cast) structure. On the contrary, Dobbs et al. [67] showed that heat treatment improved the mechanical properties of the alloy without loss of corrosion resistance. Similarly, Cawley et al. [64] analysed mechanical properties and hardness of a CoCrMo alloy thermally treated and they found a correlation between carbide volume fraction and wear-rate but they do not observed any influence on the mechanical properties. Jacobs et al. [63] stated that changes in the microstructure resulting from incipient melting of carbides during the porous coating sintering process may cause an increase in corrosion potential for porous-coated alloys as compared to conventional alloys. In addition, this carbide melting may predispose these alloys to accelerate intergranular corrosion. Preferential or localized corrosion of the porous coating can lead to crack and increase the susceptibility for failure. Placko et al. [68] also studied the effects of microstructure on the corrosion behaviour of CoCr porous coatings and they observed a progressive dissolution of the matrix with preferential attack of the grain boundaries and regions adjacent to carbides due to sensitization.



Clemow and Daniell [69] examined the influence of time and temperature upon the solution treatment on the metallurgical behaviour of CoCrMo alloy and they proposed that a reduction in the carbon content of this alloy would improve its solution treatment behaviour.

Finally there is not a common consensus on the influence of the corrosion and wear behaviour of CoCrMo alloys. A recent review on the effect of the environment and wear ranking and corrosion of biomedical CoCrMo alloys [70] has been carried out. The authors concluded that the reactions between contacting materials and environment played a crucial role emphasizing the importance of considering surface chemical dependent phenomena in the evaluation of biomedical alloys.

### 1.3.2. ELECTROCHEMICAL BEHAVIOUR OF THE CoCrMo BIOMEDICAL ALLOY. STATE OF THE ART

Literature search has been carried out using the topics “corrosion” and “CoCrMo” in the databases: ISI web of knowledge, Electrochemical Society, Medline and Science Direct. The development of the present Thesis has contributed to the elaboration of several papers which have been included in the **Table 1.IV**. Electrochemical techniques in combination with instrumental analysis were used to investigate the corrosion mechanisms of CoCrMo (passivity, transpassivity and adsorption of organic molecules).

**Figure 1.8** shows the evolution of the publications related to corrosion of CoCrMo biomedical alloys since 1996. It is observed a continuous increase of the cumulative number of papers. This increase coincides with the continuous increase of the implanted CoCrMo alloys in the biomedical field (artificial joints).

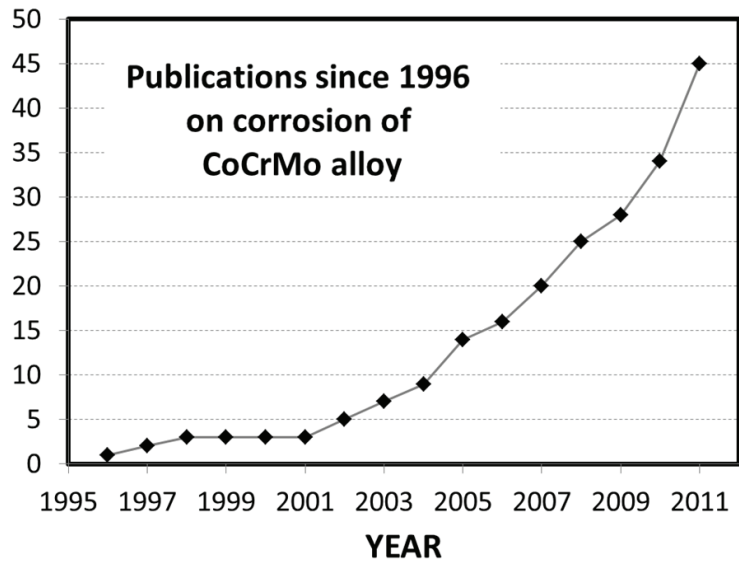


**Figure 1.8.** Number of publications since 1996 on corrosion of CoCrMo alloy.

Figure 1.IV. Summary of the published papers on corrosion of CoCrMo alloys from 1996 to 2012.

Reference	Year	CoCrMo	Environment <sup>a</sup>	Electrochemical technique <sup>b</sup>	Surface analysis <sup>c</sup>	Investigated parameters	Corrosion mechanisms
[71]	1996	HS-21 Precicast SA	Artificial saliva 37°C, pH 5	I, II, IV	A	Galvanic current Galvanic potential OCP vs time $i_{corr}$ , $E_{corr}$	Galvanic Crevice
[72]	1997	ASTM F75	PBS PBS+10% FBS PBS+10% BSA pH 7 and pH 2 room temperature	III		$i$ vs $t$ $i$ peak current	Depassivation Repassivation
[73]	1998	Remanium GM800 Dentarium ZrO <sub>2</sub> coating	Artificial saliva	III, IV	A, B, D AAS	$i_{corr}$ , $E_{corr}$ metal release	Active, passive and transpassive dissolution
[74]	1999	Co 63%, Cr 30%, Mo 5%	NaCl 0.15M (pH 7.8) Artificial saliva	III, IV	Raman	Surface composition	Passive dissolution
[75]	2001	ASTM F799-95 Co28Cr6Mo (Co 64.8%, Cr 29.0%, Mo 5.9%)	Deionized water Autoclaving Hanks' solution MEM+FBS L929 (mouse fibroblast)		C	Surface composition	Passive dissolution
[44]	2002	Cast Sulzer (Co 65.47%, Cr 27.70%, Mo 5.74%)	FBS Na <sub>2</sub> SO <sub>4</sub> (0.1M) pH 7, 25°C	I, V		OCP vs $t$ C and R vs $t$	Adsorption Passive dissolution

[76]	2003	Cast Sulzer (Co 65.47%, Cr 27.70%, Mo 5.74%) Sandblasted samples	FBS+antibiotic Na <sub>2</sub> SO <sub>4</sub> (0.1M) pH 7, 25°C	I, V	OCP vs t C and R vs t	Adsorption Passive dissolution
[77]	2003	Cast Sulzer (Co 65.47%, Cr 27.70%, Mo 5.74%)	Buffer citrate pH 3-6 PBS pH 7 Buffer borate pH 8-10 24°C	I, IV	OCP	Anodic Dissolution
[78]	2003	ASTM F75 (Co 67.77%, Cr 25.12%, Mo 5.62%)	Hank's solution SPS+glucose+tri- sodium citrate dehydrate (complexing agent) pH 7.5, RT	III, IV	C	Surface composition Thickness oxide film Passive and transpassive dissolution
[79]	2004	Co28Cr6Mo (cast Protasul-2 ASTM F75)	NaCl	IV	<b>A</b> <b>Raman</b>	Anodic dissolution Localized
[80]	2004	Co28Cr6Mo (Protasul-20) ASTM F75	NaCl SBF pH7.4, 37°C	III, IV, V	<b>C, K</b>  OCP <i>i</i> vs <i>t</i> C and R vs t Surface composition Thickness oxide film Dissolution of alloying elements	Passive and transpassive dissolution

CHAPTER 1. Introduction

[81]	2004	CoCrMo F75 (Co 66.4%, Cr 27.9%, Mo 3.4%) CoNiCrMo F562 (Co 33.4%, Cr 23%, Mo 6.1%, Ni 36%)	Hank's solution SPS EDTA-citrate (complexing agent) pH 7.8, 37°C	III, IV, V	$i_{corr}$ , $E_{corr}$ $R_p$ EEC vs solution chemistry OCP	Active, passive and transpassive dissolution
[82]	2004	Protasul-1 CoCrMo ASTM F75-87 Protasul-10 CoNiCrMo ASTM F562-84 Pure metals	Hank's solution (SPS) with and without addition of EDTA (pH 7.8)	III, IV	C Surface composition Thickness oxide film	Passive dissolution
[50]	2005	Cast Sulzer (Co 65.47%, Cr 27.70%, Mo 5.74%)	Buffer citrate (pH 4) PBS (pH 7) NaOH (pH 14) FBS 25°C	I, IV	OCP $i_{corr}$	Anodic dissolution
[65]	2005	Co29Cr6Mo Forging ratios Co29Cr6Mo1Ni ASTM F75-92	NaCl Hank's solution E-MEM+FBS (pH 5.5, 7.3, 8.3) 37°C	B, C	Crystalline structure Surface composition OCP vs $t$ $i_p$	Anodic and transpassive dissolution
[83]	2005	HC and LC ASTM F1537-94 ISO 5832-12	Deionised water pH 7.7; PBS pH 7.4 Synovial fluid pH 7.8-37°C	C, D, E Et-AAS		Passive dissolution
[84]	2005	Co28Cr6Mo ASTM F75	Art. Bone fluid (Burks and Peck) 37°C	I, III, IV	ICP-MS OCP, $R_p$ , $i_{corr}$ , $E_{br}$ $i$ vs $t$	Active, passive and transpassive dissolution

[85]	2006	Co30Cr6Mo (Good Fellow) Pure metals	Hank's+glucose pH 6.8, pH 2 25°C	IV, V	HR ICP-MS	$E_{corr}$ $R_p$ , $C_{dl}$	Passive and active dissolution Pitting
[86]	2006	Co26Cr6Mo ISO 5832-12 nitrogen ion implanted	SBF 37°C, pH 7.4		A, B, F ETAAS ICP-OES	Metal release	Passive dissolution
[87]	2007	Endocast SL (ISO 5832-12) Implanted Na- ions	SBF 37°C, pH 7	IV, V	C, G, H	$R_p$ , $E_b$ Morphology studies	Pitting
[43]	2007	CoCrMo Protasul-20	NaCl NaCl+BSA PBS PBS+BSA 37°C, pH 7.4	I, III, IV, V	C, D	OCP, $i_{corr}$ , $E_{corr}$ $R_p$ , $C_{dl}$ Surface composition	Passive dissolution Adsorption
[88]	2007	Pure Co Co30Cr6Mo (Goodfellow)	Hank's + glucose	IV, V		Cathodic peaks Equivalent electrical circuit	Active and passive dissolution Pitting
[89]	2007	HC CoCrMo LC CoCrMo	DMEM NaCl	I, III, IV	C	$E_{corr}$ , $i$ vs $t$	Active and passive dissolution
[90]	2008	HC CoCrMoNiFe LC CoCrMoNiFe	a-medium, PBS, Calf serum, artificial saliva, Ringer's, NaCl, Lactic acid, L- cysteine, HCl	IV	ICP-MS	Metal ion concentration Passive current density and potential	Anodic dissolution

CHAPTER 1. Introduction

			IV, V	C UV-Vis	OCP evolution $E_{corr}$ , $i_{corr}$ EEC	Passive dissolution Adsorption
[91]	2008	CoCrMo (Co 65.21%, Cr 27.29%, Mo 5.54%, Mn 0.65%, Si 0.69%, Ni 0.13%, Fe 0.22%, N 0.18%, C 0.089%)		Calf serum PBS $K_2CrO_4$ pH 7.4		
[92]	2008	AISI 316L Co28Cr6Mo ISO 5832-12	I, III, IV, V	NaCl NaCl+BSA PBS PBS+BSA 37°C, pH 7.4	$E_{corr}$ , $i_{corr}$ , $i_p$ , $E_{br}$ , $i_{pp}$ EEC	Active and passive dissolution Pitting
[93]	2009	Co30Cr6Mo (Goodfellow) Pure metals	IV, V	Hank's solution pH 6.8	Equivalent Electrical Circuits (EEC)	Passivity
[94]	2009	CoCrMo ASTM F75	IV, VI	NaCl PBS 25% BS 50% BS pH7.4	E, F, J	Passive dissolution
[95]	2009	CoCrMo (Co balance, Cr 28.4%, Mo 5.39%, Mn 0.38%, Si 0.8%, Ni 0.22%, Fe 0.22%, N 74 ppm, C 0.250%)	I, III, IV, V	BS (Sigma)	$OCP$ , $E_{corr}$ , $i_{corr}$ , $i_p$ , $E_{br}$ , $i_{pp}$ $i$ vs $t$ EEC	Passive and transpassive dissolution

			III, IV, V	A	
[96]	2010	MP35N CoCrMo alloy (Co 34.21%, Cr 20.48%, Mo 9.59%, Ni 34.82%)	PBS 37°C pH 7.4		Passive and transpassive dissolution
					$OCP$ $i$ vs $t$ EEC $R_p$ , $C_{dl}$ Thickness oxide film
[97]	2010	CoCrMo (Co balance, Cr 28.4%, Mo 5.39%, Mn 0.38%, Si 0.8%, Ni 0.22%, Fe 0.22%, N 74 ppm, C 0.250%)	NaCl NaCl+BSA 37°C pH 7.4	I, III, IV, V	Passive dissolution Adsorption
					$OCP$ , $E_{corr}$ , $i_{corr}$ , $i_p$ , $E_{br}$ $i_{pp}$ $i$ vs $t$ EEC $R_p$ , $C_{dl}$
[98]	2010	CoCrMo (Co balance, Cr 28.4%, Mo 5.39%, Mn 0.38%, Si 0.8%, Ni 0.22%, Fe 0.22%, N 74 ppm, C 0.250%)	PBS PBS+BSA 37°C pH 7.4	I, III, IV, V	Passive dissolution Adsorption
					$OCP$ , $E_{corr}$ , $i_{corr}$ , $i_p$ , $E_{br}$ $i_{pp}$ $OCP$ , $j$ vs $t$ EEC $R_p$ , $C_{dl}$
[99]	2011	CoCrMo (Co balance, Cr 28.4%, Mo 5.39%, Mn 0.38%, Si 0.8%, Ni 0.22%, Fe 0.22%, N 74 ppm, C 0.250%)	PBS PBS+BSA pH 3, 7, 4, 10 37°C O <sub>2</sub> /deaerated	III, IV, V	Passive dissolution Adsorption



CHAPTER 1. Introduction

[100]	2012	AISI 316L Co28Cr6Mo Ti6Al4V	PBS (ASTM-F2129) Adittion BSA	I, IV, V	C	Microstructure OCP vs t $E_{corr}$ , $E_{br}$ Surface composition EEC $R_p$ , $C_{dl}$ Corrosion rate	Passive dissolution
[101]	2012	Stellite 21	PBS 37°C and room temperature pH 7.4	III, IV, VII	C	$E_{corr}$ , $i_{corr}$ , $i_p$ , $E_{br}$ , $i_{pp}$ mass vs time Surface composition Thickness oxide film	Passive and transpassive dissolution

<sup>a</sup>**Environment:** PBS, phospahte buffered solution; FBS, fetal bovine serum; BSA, bovine serum albumin; SPS, simulated physiological solution; BS, bovine serum; SBF, simulated body fluid; E-MEM, Eagle's Minimum Essential Medium; HBSS, Hank's balanced salt solution; HA, hyaluronic acid; CS, calf serum; DMEM, Dubelco's Modified Eagle's Medium.

<sup>b</sup>**Electrochemical techniques:** I, Corrosion Potential; II, Galvanic cells (Zero resistance, Ammetry), III, Potentiostatic; IV, Potentiodynamic; V, Electrochemical Impedance Spectroscopy; VI, Electrochemical Noise; VII, Electrochemical Quartz Crystal Microbalance (EQCM).

<sup>c</sup>**Surface Analysis:** A, SEM (scanning electron microscopy); B, XRD (X-Ray diffraction); C, XPS (X-Ray Photoelectron Spectroscopy); D, AES (Auger Electron Spectroscopy); E, FIB (focused ion beam); F, AFM (atomic force microscopy); G, TEM (transmission electron microscopy); H, SIMS (secondary ion mass spectroscopy); I, OM (optical microscopy); J, FEG-SEM (field emission gun scanning electron microscopy); K, ICP-MS (inductive coupled plasma mass spectroscopy).

According to the presented research works, an approach of the electrochemical behaviour of the CoCrMo alloy in biological environments can be attained.

The high biocompatibility of the CoCrMo is related to the spontaneous formation of an oxide film that protects the metal from the surrounding environment (body fluid). It is well known that the properties of this oxide film control the chemical and mechanical properties of the biomaterial and therefore, its durability into the human body. The physico-chemical properties of the passive film also control the corrosion behaviour of the materials, the interaction with tissues and the electrolyte and thus the degree of the material biocompatibility. The properties of the film may change depending on the external conditions (i.e. temperature, potential...) but usually present similar composition due to the stability of that passive film.

The composition of the passive film of CoCrMo alloys presents high content in Cr (mainly Cr(III) and smaller amount of Cr(OH)<sub>3</sub>) with a minor contribution of Co and Mo oxides [43,78,80].

A direct relation between the thickness of the passive film and the applied potential (increasing around 1 nm V<sup>-1</sup> in the passive domain) was observed by Milosev and Strehblow [78]. Hanawa et al. [75] studied by X-ray photoelectron spectroscopy (XPS) the surface oxide film formed on CoCrMo in quasi-biological environments and determined that Cr and Mo were distributed at the inner layer of the film while the Co was dissolved from the film, reaching a thickness of 2.5-2.9 nm.

The alloying elements play an important role in the electrochemical behaviour of the alloy. Metikos et al. [85] demonstrated that the corrosion behaviour of the passive alloy is determined by the presence of Cr although its corrosion resistance is higher due to the beneficial effect of the Mo on the passivity. According to Li et al. [74], Mo in the alloy does not react with the electrolyte since the passive film (composed by Cr and Co species) protects the underlying Mo from further oxidation. They also observed that at lower potentials the Cr species play major role in the passivation of the alloy while at higher potentials Co species take on these roles. Cr also contributes to increase the corrosion resistance of the alloy [88].

The major dissolving specie from the alloy is Co which strongly depends on the electrochemical conditions [80]. Contu et al. [44] proved that the variations of the polarization resistance of the alloy immersed in serum was due to Co dissolution from the oxide film.

The exact chemistry of the passive layer is highly dependent on the chemical composition of the electrolyte [43]. Therefore, special care has to be taken when formulating the simulated body fluids in order to obtain electrochemical results for clinical application.

Test solution ranges from pure water to complex electrolytes containing more than 40 species including absorbable organic molecules and antibiotics [50]. The choice of complex body fluids which approaches the fluid to more realistic body conditions limits the mechanistic interpretation of the components on the corrosion behaviour of the alloy. Temperature is an important parameter since some electrochemical reactions can be accelerated at body temperature (37°C) changing the corrosion mechanism from that occurring at room temperature [17]. The pH of the electrolytes is also an important parameter controlling the conformation of organic molecules and thus their surface reactivity. In general, the selected electrolytes are buffered solutions which maintain constant the neutral pH of the media approaching in-vivo conditions.

At this moment, there is not a general consensus in the scientific community about the best "simulated body fluid" to be used for characterizing metallic biomedical alloys. Further research on the influence of the solution chemistry on the corrosion mechanisms is required to solve this problem (to avoid this uncertainty).

Different biomedical grades of CoCrMo alloys are used. With respect to the carbon content in the alloy, low carbon (carbon content less than 0.15 wt.%) and high carbon (carbon content between 0.15 % and 0.3 wt.%) were studied. The main differences between the selected alloys is their microstructure [64]. In addition, further differences are observed depending on the fabrication process: cast alloys are mainly used for knee joints while wrought alloys are used for component of simpler geometry (hip joints). Thermal treatments improve the mechanical properties of the alloy

providing commonly more homogeneous microstructures [64,67]. All those processes affect the overall electrochemical behaviour of the alloy [66,102].

Different electrochemical measurements can be carried out in order to analyse the corrosion behaviour of the CoCrMo alloy in biosystems. Open Circuit Potential (OCP) measurement describes the equilibrium condition and is the technique which better represents practical situations (potential is established by the kinetic equilibrium between oxidation and reduction reaction). However, this potential can vary with time [80] and is dependent on small variations in sample preparation procedure and solution composition among others [43,91,103]. External imposed potential (potentiostatic tests) are carried out in order to control the oxide film on the CoCrMo alloy [43,78,80,81]. Electrochemical Impedance Spectroscopy allows one to characterize the interface biomaterial/electrolyte under OCP or by imposed potential which commonly complement the results obtained by the previous measurements [43,80,85,91,93]. Electrochemical quartz crystal microbalance permits to measure the mass variation on the interface biomaterial/electrolyte together with the electrochemical measurements. Thus, the electrochemical behaviour of the alloy can be analyzed by the combination of all these techniques together Surface Analysis (composition of the oxide film) [43,65,74,75,78,80,82].

### **1.3.3. CLINICAL IMPLICATION OF THE PASSIVE DISSOLUTION OF THE CoCrMo ALLOY**

The main corrosion mechanism of CoCrMo alloys in the body fluids is passive dissolution. In vitro [10,11,104] and in vivo [16,105] tests confirm that metal ion release from the CoCrMo alloys takes place through that corrosion mechanism. Different phenomena as a consequence of metal ion release occur into the human body such as transportation, metabolism, accumulation in organs, allergy and carcinoma [10,11,16,46,52,105]. These effects can be generally harmful for human health, mainly in the case of the CoCrMo where the alloying elements Cr and Co generate high risk of carcinogenicity. Although the definitive effects of these metal ions have not been determined, toxicity and metal allergy are the most significant

concerns. For example, it has been demonstrated that  $\text{Cr}^{3+}$  and  $\text{Co}^{2+}$  have a toxicity effect on osteoblast and induced cell mortality [9]. Chromium ions exist in two oxidation states:  $\text{Cr}^{+3}$  and  $\text{Cr}^{+6}$  where the latter is more harmful since it is carcinogenic.

Chromium predominates in the blood (51%) because it is taken up by red blood cells while cobalt has the largest relative abundance (76 %) because it is transported from tissues to the blood and it is eliminated in the urine [7]. The affinity of both ions to bind with organic compounds is very similar [106].

Catelas et al. [12,107,108] quantitatively analysed the macrophage apoptosis and necrosis induced by cobalt and chromium ions in vitro, **Figure 1.8**. The first consists in a mode of cell death that occurs under normal physiological conditions and the cell is an active participant in its own demise while necrosis occurs when cells are exposed to extreme variance from physiological conditions which may result in damage to the plasma membrane. The results demonstrated that macrophage mortality induced by metal ions depends on ion type, concentration and incubation time. Apoptosis was predominant after 24 h with both ions while high concentrations induced mainly necrosis after 48 h. Therefore, the results show that  $\text{Co}^{2+}$  and  $\text{Cr}^{3+}$  ions induce tissue damage (cell mortality) specially at large concentration of the ions in vivo.

The extrapolation of these results to the human body is an evidence that a real implication of the Cr and Co ions into the body exists. Although, the behaviour of these ions into the body is unknown, the design of new biomaterials which decreases the release of them into the body is required. Furthermore, this decrease will improve the durability of the implant into the body reducing the number of surgical revisions.

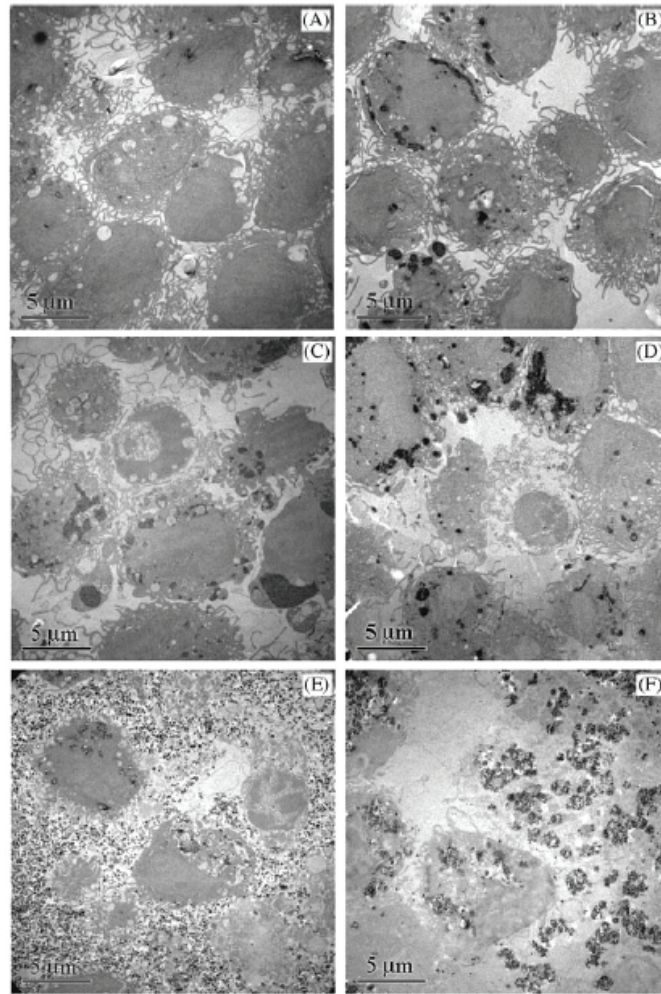


**Figure 1.8.** Effects of Co<sup>2+</sup> and Cr<sup>+3</sup> ions on macrophage morphology. (A) and (B) are representative of macrophages alone (controls) after 24 and 48 h incubation, respectively. (C) Representative of macrophages incubated with Co<sup>2+</sup> for 24 h and (D) for 48 h. (E) Representative of macrophages incubated with Cr<sup>+3</sup> for 24 h and (F) for 48 h. Extracted from [107].

According to Hanawa [52] metal ion release into the body do not always damages the body. The partner for combination with metal ion is critical. Every molecule has a chance to combine with the ion. An ion is active and immediately reacts with water molecule or inorganic anion by considering the number and size (weight) of the molecule (**Figure 1.9(left)**). On the other hand, inactive ions do not immediately combine with water molecules and inorganic anions and survive as an ionic state for long time (**Figure 1.9(right)**). Therefore, these ions have more chance to combine with biomolecules and reveal toxicity.

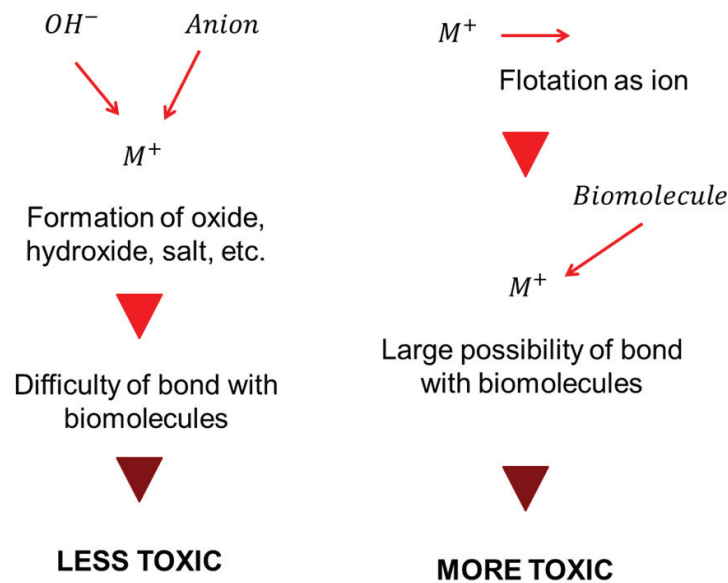


**Figure 1.9.** Toxicity of metal ions classified with the possibility of bond with water molecules and anions [52].

Simultaneously to the effect of the biomaterials implanted in the human body there is also an influence of the body fluids on the biomaterials.

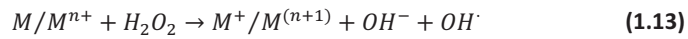
Lin and Bumgardner [109] demonstrated that macrophage cells and their released reactive chemical species change the surface composition of CoCrMo alloy. They

proposed several mechanisms in which the reactive chemical species ( $H_2O_2$ ,  $O_2^-$  and NO) released by activate cells further oxidized the alloys surfaces:

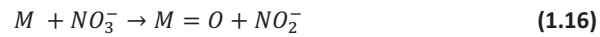
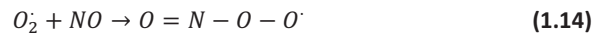
- Reduction of  $H_2O_2$  (**equation (1.12)**) and the released oxygen may further react with the metal.



- $H_2O_2$  also participates in the formation of hydroxyl radicals ( $OH^\cdot$ ) in the presence of metal ( $M$ ) or metal ions according to the **reaction (1.13)** and thus further oxidizes metal oxides on the surface (especially transition metals such as Cr) [110,111].



- Superoxide rapidly reacts with nitric oxide to form peroxynitrite (**1.14**) or nitrate (**1.15**) which may initiate additional oxidation and nitration reactions (**1.16**) [112].



Changes in the composition of the surface oxide of the alloy over time by cells are important for the understanding of host-material interactions and the release of corrosion products from the alloy.



#### 1.4. References

- [1] J. W. Boretos and N. J. Eden, Contemporary Biomaterial, park Ridge, NJ., 1984.
- [2] F. Burny, M. Donkerwolcke, D. Muster, Materials Science and Engineering: A 199 (1995) 53-59.
- [3] A. Balamurugan, S. Rajeswari, G. Balossier, A. H. S. Rebelo, J. M. F. Ferreira, Materials and Corrosion 59 (2008) 855-869.
- [4] D. Hill, Design Engineering of Biomaterials for Medical Devices, John Wiley and Sons, Chichester, 1988.
- [5] G. Manivasagam, D. Dhinasekaran, A. Rajamanickan, Recent Patents on Corrosion Science 2 (2010) 40-54.
- [6] D. F. Williams, Biomaterials 29 (2008) 2941-2953.
- [7] A. Sargeant, T. Goswami, Materials & Design 28 (2007) 155-171.
- [8] K. S. Katti, Colloids and Surfaces B: Biointerfaces 39 (2004) 133-142.
- [9] C. Fleury, A. Petit, F. Mwale, J. Antoniou, D. J. Zukor, M. Tabrizian, O. L. Huk, Biomaterials 27 (2006) 3351-3360.
- [10] Y. Okazaki, E. Gotoh, Biomaterials 26 (2005) 11-21.
- [11] M. A. Germain, A. Hatton, S. Williams, J. B. Matthews, M. H. Stone, J. Fisher, E. Ingham, Biomaterials 24 (2003) 469-479.
- [12] I. Catelas, A. Petit, D. J. Zukor, O. L. Huk, Journal of Materials Science: Materials in Medicine 12 (2001) 949-953.
- [13] S. M. Horowitz, W. T. Luchetti, J. B. Gonzales, C. K. Ritchie, Journal of biomedical materials research 41 (1998) 468-473.
- [14] Granchi D., Cenni E., G. Trisolino, Giunti A., Baldini N., Journal of Biomedical Materials Research. Part B: Applied Biomaterials 77 (2006) 257-264.
- [15] N. J. Hallab, K. Mikecz, J. J. Jacobs, Journal of biomedical materials research 53 (2000) 480-489.
- [16] A. Masse, M. Bosetti, C. Buratti, O. Visentin, D. Bergadano, M. Cannas, Journal of Biomedical Materials Research Part B-Applied Biomaterials 67B (2003) 750-757.
- [17] S. Virtanen, I. Milosev, E. Gomez-Barrena, R. Trebse, J. Salo, Y. T. Konttinen, Acta Biomaterialia 4 (2008) 468-476.

- [18] A. G. Della Valle, B. Becksac, J. Anderson, T. Wright, B. Nestor, P. M. Pellicci, E. A. Salvati, *The Journal of Arthroplasty* 20 (2005) 1084-1088.
- [19] P. S. Walker, B. L. Gold, *Wear* 17 (1971) 285-299.
- [20] J. Black and G. Hastings, *Handbook of biomaterial properties (Blood and related fluids)*, London (United Kingdom), 1998.
- [21] D. Landolt, *Corrosion and surface chemistry of metals*, 2007.
- [22] P. Marcus and J. Oudar, *Corrosion mechanisms in theory and practice*, New York (United States of America), 1995.
- [23] P. Schmutz, D. Landolt, *Electrochimica Acta* 45 (1999) 899-911.
- [24] P. Schmutz, D. Landolt, *Corrosion Science* 41 (1999) 2143-2163.
- [25] Q. Bi, W. Liu, J. Ma, J. Yang, Y. Pu, Q. Xue, *Tribology International* 42 (2009) 1081-1087.
- [26] Z. Szklarska-Smialowska, *Pitting corrosion of metals*, Houston, Texas (United States of America), 1986.
- [27] J. Shu, H. Bi, X. Li, Z. Xu, *Corrosion Science* 57 (2012) 89-98.
- [28] D. Landolt and S. Mischler, *Tribocorrosion of passive metals and coatings*, Woodhead Publishing, 2011.
- [29] C. J. V. Oss, R. J. Good, *Journal of Protein Chemistry* 7 (1988) 179-183.
- [30] M. Alkan, Ö. Demirbas, M. Dogan, O. Arslan, *Microporous and Mesoporous Materials* 96 (2006) 331-340.
- [31] T. A. Horbett and J. L. Brash, *Proteins at Interfaces II. Fundamentals and applications*, American Chemical Society, Washington, DC, 1995.
- [32] Y. Arima, H. Iwata, *Biomaterials* 28 (2007) 3074-3082.
- [33] I. Frateur, J. Lecoer, S. Zanna, C. O. A. Olsson, D. Landolt, P. Marcus, *Electrochimica Acta* 52 (2007) 7660-7669.
- [34] A. Ithurbide, I. Frateur, A. Galtayries, P. Marcus, *Electrochimica Acta* 53 (2007) 1336-1345.
- [35] S. Omanovic, S. G. Roscoe, *Langmuir* 15 (1999) 8315-8321.
- [36] D. R. Jackson, S. Omanovic, S. G. Roscoe, *Langmuir* 16 (2000) 5449-5457.
- [37] S. Omanovic, S. G. Roscoe, *Journal of Colloid and Interface Science* 227 (2000) 452-460.

- [38] J.F.Foster, V.M.Rosenoer, M.Oratz, M.A.Rothschild, Albumin Structure, Function and Uses, in: 1997, 53.
- [39] J. Zhu, N. Xu, C. Zhang, *Advances in Contraception* 15 (1999) 179-190.
- [40] L. C. Xu, C. A. Siedlecki, *Biomaterials* 28 (2007) 3273-3283.
- [41] H. Noh, E. A. Vogler, *Biomaterials* 27 (2006) 5801-5812.
- [42] Y. Yu, G. Jin, *Journal of Colloid and Interface Science* 283 (2005) 477-481.
- [43] A. Igual Muñoz, S. Mischler, *Journal of the Electrochemical Society* 154 (2007) C562-C570.
- [44] F. Contu, B. Elsener, H. Bohni, *Journal of biomedical materials research* 62 (2002) 412-421.
- [45] A. C. Lewis, M. R. Kilburn, P. J. Heard, T. B. Scott, K. R. Hallam, G. C. Allen, I. D. Learmonth, *Journal of Orthopaedic Research* 24 (2006) 1587-1596.
- [46] J. J. Jacobs, J. L. Gilbert, R. M. Urban, *Journal of Bone and Joint Surgery-American Volume* 80A (1998) 268-282.
- [47] S. G. Steinemann, *Injury-International Journal of the Care of the Injured* 27 (1996) 16-22.
- [48] A. Minovic, I. Milosev, B. Pihlar, *Jornal of Materials Science: Materials in Medicine* 14 (2003) 69-77.
- [49] I. Milosev, *Journal of Applied Electrochemistry* 32 (2002) 311-320.
- [50] F. Contu, B. Elsener, H. Böhni, *Corrosion Science* 47 (2005) 1863-1875.
- [51] C. Myant, R. Underwood, J. Fan, P. M. Cann, *Journal of the Mechanical Behavior of Biomedical Materials* 6 (2012) 30-40.
- [52] T. Hanawa, *Materials Science and Engineering: C* 24 (2004) 745-752.
- [53] D. Scharnweber, *Biodegradation of Metals*, in: K. H. J. Editors-in-Chief: Buschow, W. C. Robert, C. F. Merton, Bernard Ilshner, J. K. Edward, M. Subhash, Patrick Veyssièrè (eds.), *Encyclopedia of Materials: Science and Technology* (Second Edition), Oxford, 2001, 555-560.
- [54] S. Sugio, A. Kashima, S. Mochizuki, M. Noda, K. Kobayashi, *Protein Engineering* 12 (1999) 439-446.
- [55] N. Ahmed, P. J. Thornalley, *Maillard Reaction: Chemistry at the Interface of Nutrition, Aging, and Disease* 1043 (2005) 260-266.
- [56] G. C. F. Clark, D. F. Williams, *Journal of biomedical materials research* 16 (1982) 125-134.

- [57] R. L. Williams, D. F. Williams, *Biomaterials* 9 (1988) 206-212.
- [58] M. Rabe, D. Verdes, S. Seeger, *Advances in Colloid and Interface Science* 162 (2011) 87-106.
- [59] S. Sohn, D. Kim, *Chemosphere* 58 (2005) 115-123.
- [60] Y. Liu, *Colloids and Surfaces A: Physicochemical and Engineering Aspects* 274 (2006) 34-36.
- [61] M. Comín, R. Dejoz, C. Atienza, J. Prat, J. L. Peris, P. Vera, A. Gil, and C. Reig, *Biomecánica articular y sustituciones protésicas*, 1998.
- [62] J. A. Disegi, R. L. Kennedy, and R. Pilliar, *Cobalt-base alloys for biomedical applications*, 1999.
- [63] J. J. Jacobs, R. M. Latanision, R. M. Rose, S. J. Veeck, *Journal of Orthopaedic Research* 8 (1990) 874-882.
- [64] J. Cawley, J. E. P. Metcalf, A. H. Jones, T. J. Band, D. S. Skupien, *Wear* 255 (2008) 999-1006.
- [65] S. Hiromoto, E. Onodera, A. Chiba, K. Asami, T. Hanawa, *Biomaterials* 26 (2005) 4912-4923.
- [66] F. S. Georgette, J. A. Davidson, *Journal of biomedical materials research* 20 (1986) 1229-1248.
- [67] H. S. Dobbs, J. L. M. Robertson, *Journal of Materials Science* 18 (1983) 391-404.
- [68] H. E. Placko, S. A. Brown, J. H. Payer, *Journal of biomedical materials research* 39 (1998) 292-299.
- [69] A. J. T. Clemow, B. L. Daniell, *Journal of biomedical materials research* 13 (1979) 265-279.
- [70] A. Igual Muñoz, S. Mischler, *Journal of Materials Science: Materials in Medicine* 22 (2011) 437-450.
- [71] H. Luthy, C. P. Marinello, L. Reclaru, P. Scharer, *Journal of Prosthetic Dentistry* 75 (1996) 515-524.
- [72] J. R. Goldberg, J. L. Gilbert, *Journal of biomedical materials research* 37 (1997) 421-431.
- [73] H. C. Hsu, S. K. Yen, *Dental Materials* 14 (1998) 339-346.
- [74] Y.-S. Li, K. Wang, P. He, B. X. Huang, P. Kovacs, *Journal of raman spectroscopy* 30 (1999) 97-103.

- [75] T. Hanawa, S. Hiromoto, K. Asami, *Applied Surface Science* 183 (2001) 68-75.
- [76] F. Contu, B. Elsener, H. Bohni, *Journal of Biomedical Materials Research Part A* 67A (2003) 246-254.
- [77] F. Contu, B. Elsener, H. Bohni, *Journal of the Electrochemical Society* 150 (2003) B419-B424.
- [78] I. Milosev, H.-H. Strehblow, *Electrochimica Acta* 48 (2003) 2767-2774.
- [79] A. Dorner-Reisel, C. Schürer, G. Irmer, E. Müller, *Surface and Coatings Technology* 177-178 (2004) 830-837.
- [80] A. W. E. Hodgson, S. Kurz, S. Virtanen, V. Fervel, C.-O. A. Olsson, S. Mischler, *Electrochimica Acta* 49 (2004) 2167-2178.
- [81] A. Kocijan, I. Milosev, D. K. Merl, B. Pihlar, *Journal of Applied Electrochemistry* 34 (2004) 517-524.
- [82] A. Kocijan, I. Milosev, B. Pihlar, *Journal of Materials Science-Materials in Medicine* 15 (2004) 643-650.
- [83] A. C. Lewis, M. R. Kilburn, I. Papageorgiou, G. C. Allen, C. P. Case, *Journal of Biomedical Materials Research Part A* 73A (2005) 456-467.
- [84] L. Reclaru, P. Y. Eschler, R. Lerf, A. Blatter, *Biomaterials* 26 (2005) 4747-4756.
- [85] M. Metikos-Hukovic, Z. Pilic, R. Babic, D. Omanovic, *Acta Biomaterialia* 2 (2006) 693-700.
- [86] O. Öztürk, U. Türkan, A. E. Eroglu, *Surface and Coatings Technology* 200 (2006) 5687-5697.
- [87] J. Baszkiewicz, D. Krupa, B. Rajchel, J. A. Kozubowski, A. Barcz, J. W. Sobczak, A. Kosinski, *Vacuum* 81 (2007) 1306-1309.
- [88] M. Metikos-Hukovic, R. Babic, *Corrosion Science* 49 (2007) 3570-3579.
- [89] Y. Yan, A. Neville, D. Dowson, *Wear* 263 (2007) 1105-1111.
- [90] Y. Okazaki, E. Gotoh, *Corrosion Science* 50 (2008) 3429-3438.
- [91] A. Ouerd, C. Alemany-Dumont, B. Normand, S. Szunerits, *Electrochimica Acta* 53 (2008) 4461-4469.
- [92] C. Valero Vidal, A. Igual Muñoz, *Corrosion Science* 50 (2008) 1954-1961.
- [93] M. Metikos-Hukovic, R. Babic, *Corrosion Science* 51 (2009) 70-75.
- [94] D. Sun, J. A. Wharton, R. J. K. Wood, L. Ma, W. M. Rainforth, *Tribology International* 42 (2009) 99-110.

- [95] C. Valero Vidal, A. Igual Muñoz, *Electrochimica Acta* 54 (2009) 1798-1809.
- [96] Bruce G.Pound, *Journal of biomedical materials research* 94A (2010) 93-102.
- [97] C. Valero Vidal, A. Olmo Juan, A. Igual Muñoz, *Colloids and Surfaces B: Biointerfaces* 80 (2010) 1-11.
- [98] C. Valero Vidal, A. Igual Muñoz, *Electrochimica Acta* 55 (2010) 8445-8452.
- [99] C. Valero Vidal, A. Igual Muñoz, *Electrochimica Acta* 56 (2011) 8239-8248.
- [100] S. Karimi, T. Nickchi, A. Alfantazi, *Corrosion Science* 53 (2011) 3262-3272.
- [101] C. Valero Vidal, A. Igual Muñoz, C.-O. A. Olsson, S. Mischler, *Journal of the Electrochemical Society* 159 (2012) C233-C243.
- [102] L. Casabán Julián, A. Igual Muñoz, *Tribology International* 44 (2011) 318-329.
- [103] S. Karimi, T. Nickchi, A. Alfantazi, *Corrosion Science* 53 (2011) 3262-3272.
- [104] K. Merritt, S. A. Brown, *Journal of biomedical materials research* 29 (1995) 627-633.
- [105] J. H. Dumbleton, M. T. Manley, *Journal of Arthroplasty* 20 (2005) 174-188.
- [106] J. Yang, J. Black, *Biomaterials* 15 (1994) 262-268.
- [107] I. Catelas, A. Petit, H. Vali, C. Fragiskatos, R. Meilleur, D. J. Zukor, J. Antoniou, O. L. Huk, *Biomaterials* 26 (2005) 2441-2453.
- [108] O. L. Huk, I. Catelas, F. Mwale, J. Antoniou, D. J. Zukor, A. Petit, *The Journal of Arthroplasty* 19 (2004) 84-87.
- [109] H. Y. Lin, J. D. Bumgardner, *Biomaterials* 25 (2004) 1233-1238.
- [110] P. Tengvall, H. Elwing, L. Sjöqvist, I. Lundström, L. M. Bjursten, *Biomaterials* 10 (1989) 118-120.
- [111] P. Tengvall, I. Lundström, L. Sjöqvist, H. Elwing, L. M. Bjursten, *Biomaterials* 10 (1989) 166-175.
- [112] W. H. Koppenol, *Free Radical Biology and Medicine* 25 (1998) 385-391.

## CHAPTER 2: OBJECTIVES

---

The main goal of the Doctoral Thesis is the study of the corrosion behaviour of CoCrMo biomedical alloy used for total or partial joint replacements under physiological conditions by electrochemical techniques and surface analysis. The fundamental understanding of the degradation mechanisms occurring on this biomedical alloy (i.e. electrochemical dissolution and protein adsorption) and their interaction is needed for improving the material design and predicting long-term durability of implants.

The electrochemical behaviour of the alloy is related to the stability of the oxide film formed on the CoCrMo alloy surface. Thus, an electrochemical characterisation of the alloy was carried out initially in order to understand the implication of the different physico-chemical properties of the body fluids on the stability of this oxide film. Subsequently, the effect of the organic compounds (proteins) present in the body fluids on the passivation properties was analysed. Finally, the study of the passive film kinetics together with the protein adsorption kinetics was required in order to know the response of the passive film formation in physiological environments.

The Thesis is divided into seven chapters: introduction, objectives, experimental techniques, electrochemical characterization of CoCrMo alloy in simulated body fluids, mechanisms of Bovine Serum Albumin (BSA) adsorption, study of the passivation and adsorption kinetics by Electrochemical Quartz Crystal Microbalance (EQCM) and X-Ray Photoelectron Spectroscopy (XPS) and conclusions. **Figure 2.1** schematically shows the structure of the Doctoral Thesis indicating the main objectives of each chapter. These objectives can be summarized as follows:

1. Study of the influence of several physico-chemical properties of simulated body fluids (chemical composition, pH, oxygen content) and applied potential on the general electrochemical behaviour of a high-carbon CoCrMo biomedical alloy. The effect of the protein adsorption in acidic, neutral and alkaline media was also analysed. In order to reach this objective, conventional electrochemical techniques such as Open-Circuit Potential (OCP) measurements, potentiodynamic polarization curves, potentiostatic tests and Electrochemical Impedance Spectroscopy (EIS) were used.
2. Study of the adsorption mechanisms of the Bovine Serum Albumin on the CoCrMo surface and thermodynamical analysis of the adsorption process by extracting characteristic parameters (activation energy, Gibbs free energy, entropy and enthalpy of the adsorption process) through electrochemical techniques. The effect of applied potential and passivation time on the BSA adsorption was also analysed. To achieve this objective, electrochemical measurements at OCP and at an applied passive potential, together with EIS analysis, were carried out.
3. Evaluation of the anodic behaviour (passivation) and adsorption kinetics of a CoCrMo alloy under physiological conditions. In order to determine the kinetics of these processes, EQCM and XPS in simulated body fluids at room temperature and 37°C were used. For this purpose, the mass change during potential sweeps from a low to a higher passive potential or transpassive potential were evaluated and correlated to passive film growth. Furthermore,



## CHAPTER 2. Objectives

BSA was added into the electrolyte in order to analyse its implication on the rate of the passive film growth. The study was completed with XPS analysis to determine the chemical composition and the thickness of the oxide film. A quantitative comparison between EQCM and XPS to evaluate the anodic behaviour of the CoCrMo biomedical alloys was also done. The experimental part of this chapter was carried out at the École Polytechnique Fédérale de Lausanne (EPFL) in Switzerland during 11 months.

Long-term durability of biomaterials implanted in the human body depends on a huge variety of factors which determine two main degradation mechanisms: corrosion and wear behaviour. This Thesis describes the corrosion mechanisms of CoCrMo alloys which are needed to better understand the biomaterial behaviour under more realistic situations (i.e. under tribocorrosion conditions).

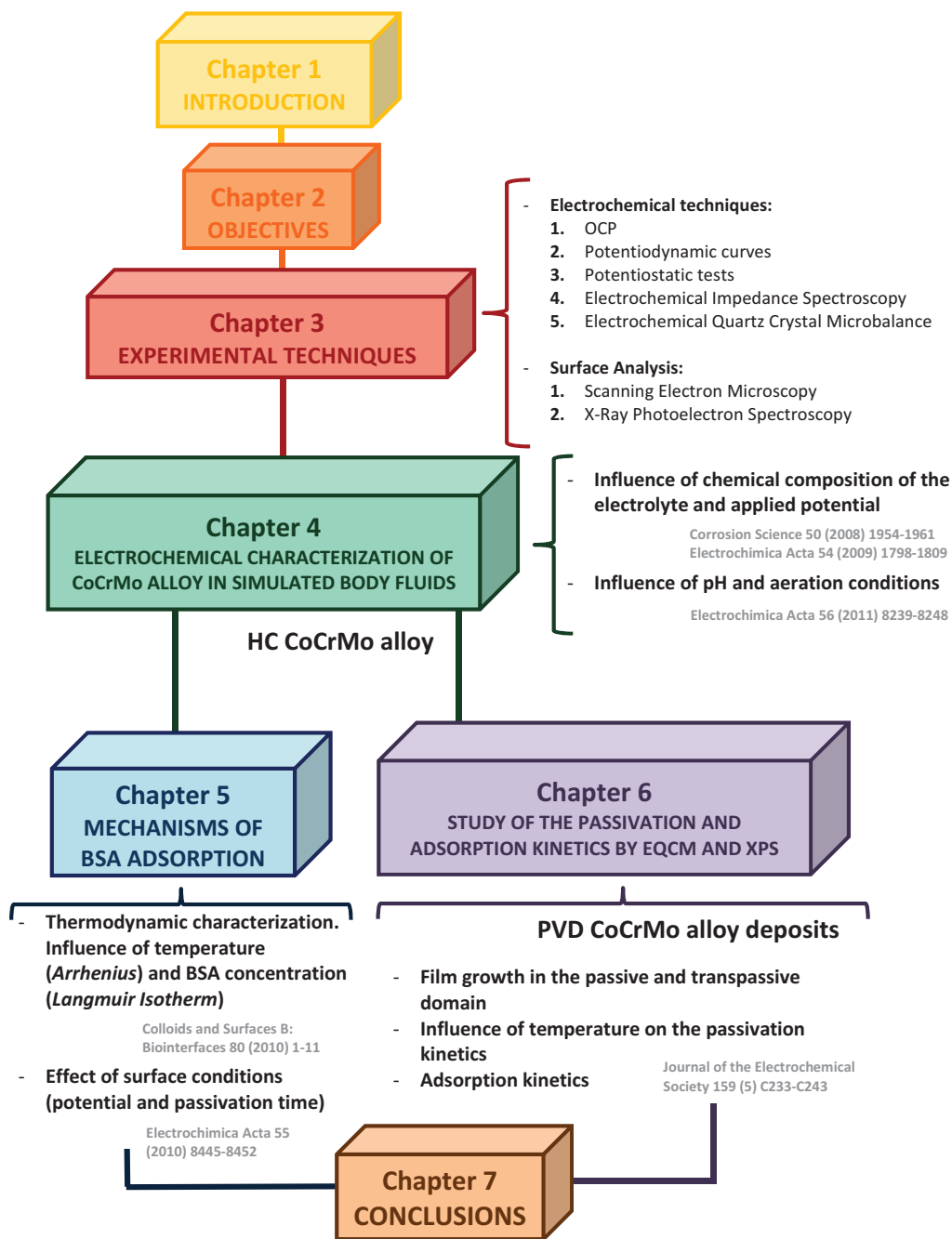


**Figure 2.1.** Scheme of the Doctoral Thesis structure and the publications related to the content of the different chapters.

## CHAPTER 3: EXPERIMENTAL TECHNIQUES

---

### 3.1. Introduction

In this chapter a description of the experimental techniques employed for approaching the objectives of the present Thesis are exposed. The basic principles and the experimental set-up concerning each technique are defined in order to show their applicability on the electrochemical characterization of the CoCrMo biomedical alloy under different physiological conditions.

The Chapter is divided in two sections according to the type of the experimental techniques: electrochemical and surface analysis techniques. The first section includes a group of techniques related to the response of the biomaterial under physiological conditions applying different electrical signals. With them, the electrochemical behaviour of the alloy in biological systems can be analysed in-situ. On the other hand, surface analysis techniques allow one to characterize the surface chemistry of the CoCrMo surface ex-situ. Microstructure, composition and thickness of the oxide film can be evaluated using these techniques.

### 3.2. Electrochemical techniques

The basic configuration of three-electrode is used for carrying out the electrochemical measurements (**Figure 3.1(a)**). The electrode system is formed by: the working (the investigated biomaterial), the reference and the counter (auxiliary) electrodes.

The **reference electrode** is needed to measure the potential of an electrode and it has a stable and well-defined electrode potential. The stability of the electrode potential is reached by employing a redox system with constant (buffer or saturated) concentration of each participant of the redox reaction. Thus, the properties that should satisfy a reference electrode are: reproducible potential value, thermodynamically well-defined reaction, non-polarizable (not sensible to current flow) and easy use [1]. The **silver/silver chloride electrode** (Ag/AgCl) is used in the present Thesis (**Figure 3.1(b)**); therefore, all potentials are given with respect to this electrode, the standard of which is 0.205 V with respect to the standard hydrogen electrode.

The **counter electrode** is made from inert materials such as gold, platinum or graphite and its function is to ensemble the electrical circuit by control the current either applied or measured. The potential of the auxiliary electrode is usually not measured and is adjusted to balance the reaction occurring at the working electrode. This configuration allows the potential of the working electrode to be measured against a known reference electrode without compromising the stability of that reference electrode by passing current over it. The counter electrodes employed in this experimental work are platinum and gold electrodes (**Figure 3.1(b)** shows the platinum electrode).

The three electrodes are connected to the potentiostat which is essentially an electronic amplifier that regulates the current between the working and the counter electrode and the potential between the working and the reference electrode. Generally, depending on the electrochemical measurement, either the current or the potential is fixed and the other signal will be measured. The **Figure 3.1(a)** schematically shows the electrodes and their connection to the potentiostat. In the present Thesis, all electrochemical measurements were carried out using a potentiostat Solartron 1286.

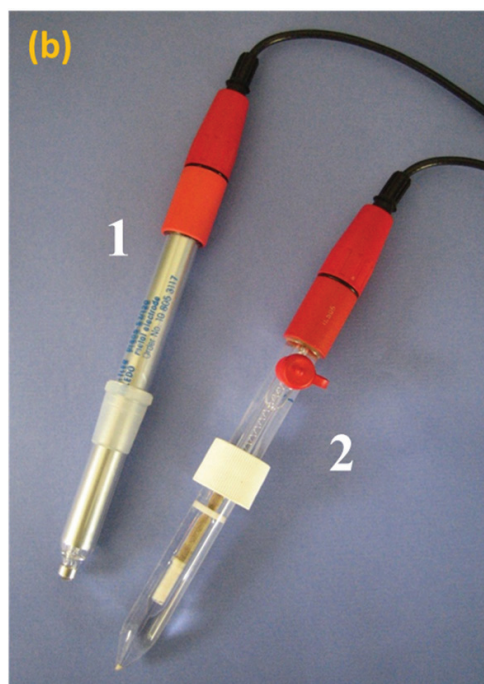
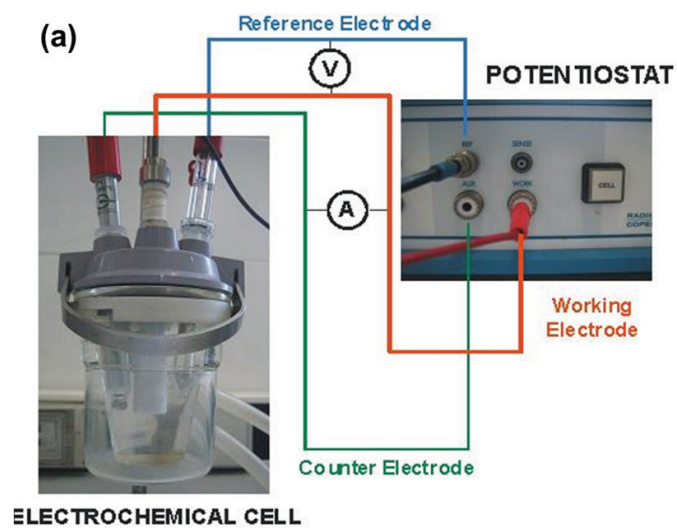


**Figure 3.1.** (a) Typical electrochemical cell with electrodes in connection with the potentiostat. (b) Counter electrode<sup>1</sup> of platinum and silver chloride (Ag/AgCl) as Reference electrode<sup>2</sup>.

### 3.2.1. MEASUREMENT OF OPEN-CIRCUIT POTENTIAL (OCP)

The open circuit potential (OCP) is the potential set up spontaneously by an electrode in absence of external current. Thus, at open-circuit potential (i.e. under free corrosion conditions), the anodic and cathodic reactions occurs simultaneously and at the same rate. Therefore, the total current flow is zero and cannot be directly measured. For a **single electrode**, whenever only one electrode reaction takes place on a metal surface, the open circuit potential corresponds with the equilibrium potential ( $E_{rev}$ ) (Figure 3.2(a)) according to the equation (3.1).



When an electric current flows through the electrode/electrolyte interface the potential of the electrode differs from the open circuit potential. Potential higher than the OCP indicates that an anodic current is crossing the interface while lower values means that the current is cathodic.

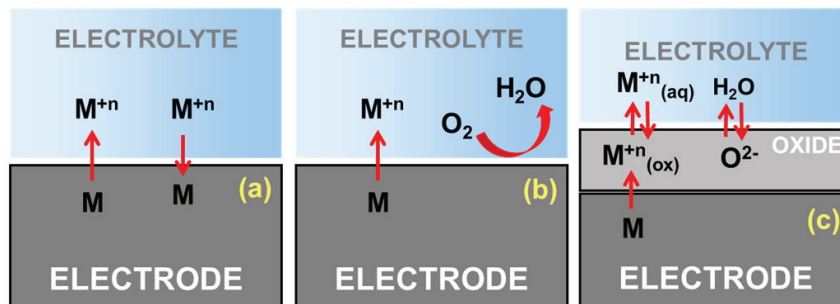


Figure 3.2(a) Metal electrode in contact with its own ions (single electrode), (b) with aerated conditions (mixed electrode) and (c) passivation of the metal.

Commonly several electrode reactions take place simultaneously at a metal/electrolyte interface. Such systems are referred to as **mixed electrodes**. In a biosystem, where the metallic biomaterials remain in contact with the body fluids, some electrode reactions can take place simultaneously such as the reduction of oxygen presents in the body fluid (Figure 3.2(b)) and the oxidation of the metal (Figure 3.2(c)). Thus, the metal is corroded without any external current.

In electrochemical systems the OCP is measured during certain time, i.e. before the polarization measurements, in order to stabilize the electrochemical conditions of the samples into the electrolyte. This measurement is useful because can give us an initial information about the surface state (nobility) of the biomaterial in the studied media. In addition, information about the progress of possible chemical reactions taking place on the electrode surface can be studied if the OCP evolution is analysed with time, i.e. formation of the oxide film. In this case, when the biomaterial is spontaneously passivated (without applying any external current) the OCP shifts towards more anodic potentials (more noble) with time until reaching a steady-state value of potential (**Figure 3.2(c)**).

The OCP measurements can draw a relative comparison of the nobility of the alloys in the test situations but this electrochemical variable is not specific to reversible phenomena and therefore Nernst's equilibrium equation is no longer valid [2]. The nature of the metal/solution interface varies with time and consequently, the OCP is no longer characteristic of the metal. It also depends on the experimental conditions, particularly on the electrolyte composition, the temperature and the oxygen content of the electrolyte and on the surface state of the metal.

OCP varies depending on the solution and the change is attributed to both the anodic dissolution of the implant materials and the reduction reaction (mainly the oxygen reduction reaction) [3] which can be useful as an indicator of the influence of the solution chemistry on the cathodic reaction [4-6]. Nevertheless, additional experimental techniques as below mentioned are needed to corroborate and complete the conclusions extracted from the OCP analysis. Furthermore, no clear corrosion mechanisms can be obtained from the simple measurement of the OCP and it is also worth noting that this technique does not give information on the kinetics of the corrosion reactions. Therefore, this technique will be employed for an initial characterization of the CoCrMo biomaterial in the simulated body fluids.

### 3.2.2. POTENTIODYNAMIC CURVES

This technique consists in measuring the current density as a function of the applied potential when the latter is swept at a constant rate using a function generator to drive the potentiostat. Thus, a registration of the current density versus potential is obtained. The potentiodynamic curves constitutes the first approach in a corrosion study since it permits to observe the effect of variables such as chemical composition of the electrolyte, temperature, and immersion time among others on the different electrochemical reactions taking place on the electrode surface.

ASTM G5-94(2004) [7] establishes a standard protocol for measuring potentiodynamic curves where experimental conditions such as scan rate and range of applied potentials are indicated. Nevertheless, these experimental conditions vary depending on the type of research.

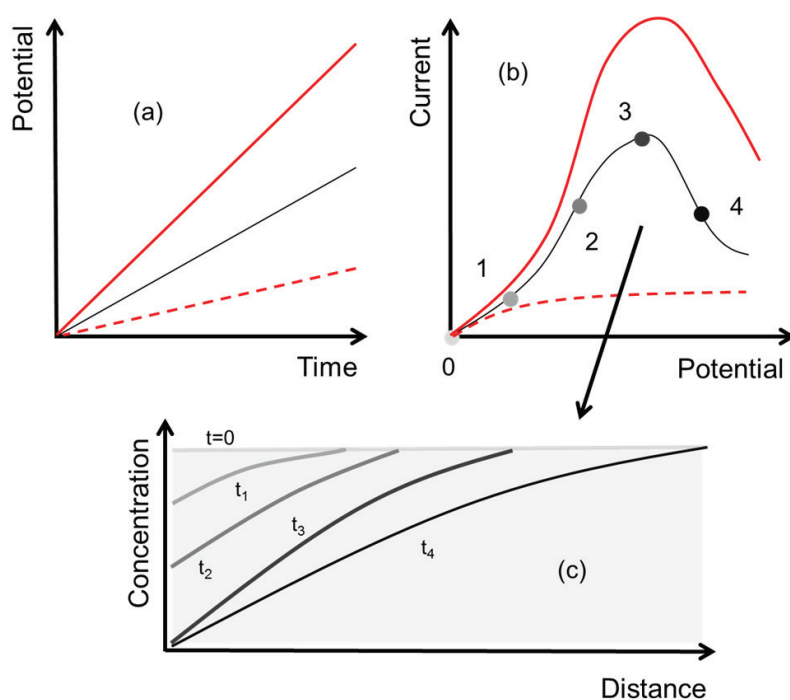


**Figure 3.3.** (a-b) Current measured during linear potential sweeps at different sweep rates and (c) concentration profiles near the electrode in one of them.



One of these variables is the scan rate of potential which has to be sufficiently slow to permit steady state mass transport conditions at the electrode surface without limiting current plateau.

**Figure 3.3(a-b)** schematically shows the effect of the scan rate on current density. In this reaction the reactant is consumed at the electrode with the variation of potential which is only due to the concentration overpotential. The red-dotted curve represents a linear sweep with a very slow rate capable of reaching the steady-state mass transport conditions at the electrode surface and limiting current plateau. If the scan rate increases, the concentration profiles can no longer attain the steady state and as consequence one maximum current is obtained. This maximum is more pronounced whether the scan rate further increases (red-line curve).

At first, the concentration gradient at the surface increases with time while the surface concentration of the reactants decreases. Under these conditions the concentration gradient at the surface, and hence the current, exceeds the value corresponding to steady state mass transport. Once the surface concentration of the reactant reaches zero, the concentration gradient at the surface progressively decreases and approaches the steady-state value.

**Equation (3.2)** provides a criterion for the selection of the maximum scan rate while still working under steady state conditions with respect to mass transport. The  $\tau_v^*$  dimensionless time allows one to characterize the transition from non-steady-state to steady-state conditions [1].

$$\tau_v^* = \frac{D R T}{\delta^2 n F \lambda} \quad (3.2)$$

where  $D$  is the diffusion coefficient ( $\text{m}^2 \text{s}^{-1}$ ),  $R$  is the gas constant ( $\text{J mol}^{-1} \text{K}^{-1}$ ),  $T$  is the temperature (K),  $\delta$  is the thickness of the diffusion layer (m),  $n$  is the change number,  $F$  is the Faraday constant ( $\text{C mol}^{-1}$ ) and  $\lambda$  is the potential sweep rate ( $\text{V s}^{-1}$ ).

Thus, it is possible to identify two limiting cases depending on the value of the  $\tau_v^*$  dimensionless time. If  $\tau_v^* \gg 1$  the steady-state mass is reached which means the concentration profile in the diffusion layer corresponds to that of the steady state and

the limiting current density depends exclusively on convection conditions. On the other hand, if  $\tau_v^* \ll 1$  non-steady-state mass transport regime is attained and therefore the concentration profile inside the diffusion layer changes with time and the effect of convection is considered negligible.

As a rule of thumb, for a value of  $\tau_v^* > 20$  the error in the measured steady-state limiting current is less than 1 %. The **equation (3.2)** shows that to attain a steady state, the scan rate must be the slower the larger the diffusion layer thickness, i.e. the weaker the convection.

With respect to the range of applied potentials (initial and final potential value in the polarization scan), this is varied from cathodic to anodic value. This potential range presents great variability and it is determined by the objectives to be achieved.

In all polarization curves the total current density  $i$  is given by the sum of the partial anodic current density ( $i_a$ ) and the partial cathodic current density ( $i_c$ ) as described by the **equation (3.3)**. By convention, the anodic current density is positive ( $i_a > 0$ ) and the cathodic current is negative ( $i_c < 0$ ). The potential at which the total current shifts from cathodic to anodic current is called corrosion potential ( $E_{corr}$ ) and is characterized because the current density of both semi-reactions are equal. Thus, the value of the current density of these semi-reactions is the corrosion current density ( $i_{corr}$ ) which is directly related to the corrosion rate of the material in the studied media.

$$i = i_a + i_c \quad (3.3)$$

The value of the total current density can vary depending on the mechanisms that control the evolution of the anodic and cathodic partial reactions. When the electrode is moved from its equilibrium situation, by the potential difference applied across the electrode/electrolyte interface, the transfer of charged species (ions and electrons) through this interface is influenced. For the oxidation and reduction reactions an activation energy barrier (different for the two partial reactions) must be overcome which is changed upon the applied polarization. If the interfacial reaction is slower than the other reaction steps (mass transfer of reactions partners to or from the surface) the reaction rate is controlled by the **activation** energy for the **charge**

*transfer*. As the activation energy depends on the applied potential, the current-potential relationship follows the so-called **Butler-Volmer equation** which exponentially relates the current and the potential. The **Figure 3.4** shows the partial current densities and the total current density of a mixed electrode controlled by activation.

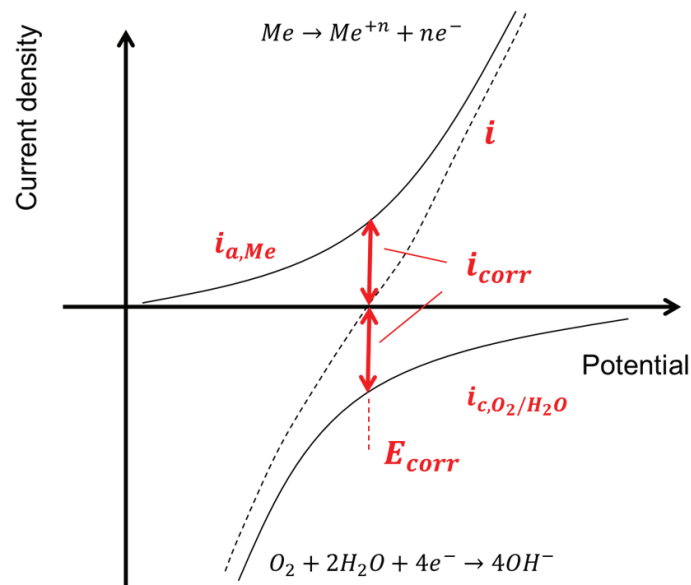


**Figure 3.4.** Partial current densities ( $i_{a,Me}$ ,  $i_{c,O_2/H_2O}$  in solid lines) and total current density ( $i$ , in dotted lines) of mixed electrode near the corrosion potential.

The Butler-Volmer equations for the anodic and the cathodic partial reaction are expressed by the **equations (3.4)** and **(3.5)** respectively:

$$i_a = i_{corr} \cdot \exp\left(\frac{\alpha \cdot n \cdot F}{R \cdot T} \eta\right) \quad (3.4)$$

$$i_c = -i_{corr} \cdot \exp\left(\frac{-(1 - \alpha) \cdot n \cdot F}{R \cdot T} \eta\right) \quad (3.5)$$

In these expressions the proportionality constant  $\alpha$  is the charge transfer coefficient and its value is situated between 0 and 1. This parameter indicates the fraction of the interfacial potential at an electrode/electrolyte interface that helps in lowering the

free energy barrier for the electrochemical reaction. On the other hand,  $\eta$  is the polarization (overpotential) which expresses the difference between the potential of a mixed electrode subjected to anodic or cathodic polarization and its corrosion potential ( $E_{corr}$ ).

Including the **equations (3.4)** and **(3.5)** into the equation **(3.3)** the most common form of Butler-Volmer equation for a mixed potential is obtained (**equation (3.6)**).

$$i = i_{corr} \cdot \left[ \exp\left(\frac{\alpha \cdot n \cdot F}{R \cdot T} \eta\right) - \exp\left(\frac{-(1 - \alpha) \cdot n \cdot F}{R \cdot T} \eta\right) \right] \quad (3.6)$$

The anodic and cathodic Tafel coefficients ( $\beta_a, \beta_c$ ) are defined in the **equations (3.7)** and **(3.8)** respectively:

$$\beta_a = \frac{R \cdot T}{\alpha \cdot n \cdot F} \quad (3.7)$$

$$\beta_c = \frac{R \cdot T}{(1 - \alpha) \cdot n \cdot F} \quad (3.8)$$

Thus, including the Tafel coefficients into the **equation (3.6)**, the Butler-Volmer equation becomes:

$$i = i_{corr} \cdot \left[ \exp\left(\frac{\eta}{\beta_a}\right) - \exp\left(-\frac{\eta}{\beta_c}\right) \right] \quad (3.9)$$

For relative high polarizations and depending on the  $\eta$  sign one of both exponentials terms are negligible and therefore the **equation (3.6)** can be rewritten. The **anodic Tafel region** is the domain of potential corresponding to  $\eta/\beta_a \gg 1$ .

$$i \approx i_a = i_{corr} \cdot \exp\left(\frac{\eta}{\beta_a}\right) \quad (3.10)$$

And taking the logarithms yields:

$$\eta = -\beta_a \ln i_{corr} + \beta_a \ln i \quad (3.11)$$

The **anodic Tafel line** is obtained converting the latter expression to base-10 logarithm, defining  $a_a$  and  $b_a$  as anodic Tafel constants:

$$\eta = \underbrace{-2.303 \beta_a \log i_{corr}}_{a_a} + \underbrace{2.303 \beta_a \log i}_{b_a} \quad (3.12)$$

On the other hand, the **cathodic Tafel region** corresponds to the potential domain where  $\eta/\beta_c \ll -1$  is established.

$$i_T \approx i_c = -i_{corr} \cdot \exp\left(\frac{\eta}{\beta_c}\right) \quad (3.13)$$

Applying the logarithm in the expression:

$$\eta = \beta_c \ln i_{corr} - \beta_c \ln|i| \quad (3.14)$$

Thus, it is possible to define the Tafel equation of a cathodic reaction (**cathodic Tafel line**) using the cathodic Tafel constants  $a_c$  and  $b_c$ :

$$\eta = \underbrace{2.303 \beta_c \log i_{corr}}_{a_c} - \underbrace{2.303 \beta_c \log|i|}_{b_c} \quad (3.15)$$

Therefore, if the overpotential is represented against the current density  $i$  on logarithmic scale (**Figure 3.5**), a linear relationship between both is obtained whenever the overpotential is large in absolute value, which permits to determine experimentally the kinetic parameters  $i_{corr}$ ,  $\beta_a$  and  $\beta_c$ .

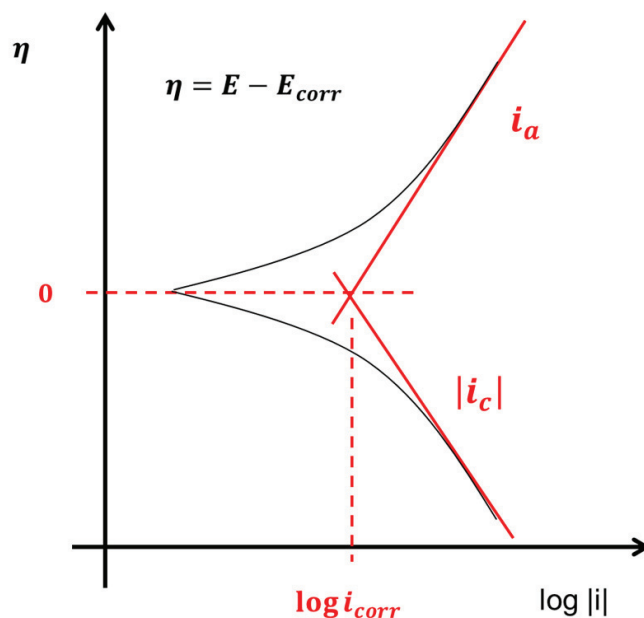


**Figure 3.5.** Evans diagram showing anodic and cathodic partial current densities and total current density of an electrode reaction on a logarithmic scale. Determination of  $i_{corr}$  from a  $\eta$  vs  $\log|i|$  curve.

The **Tafel equations (3.12) and (3.15)** describe the anodic and cathodic limits of the Butler-Volmer equation. The extrapolation of an experimental polarization curve, measured from the Tafel region to the reversible potential ( $E_{corr}$ ), reveals the corrosion current density ( $i_{corr}$ ). Thus, the Tafel coefficients  $\beta_a$  and  $\beta_c$  can be extracted from the slopes of the straight lines  $\eta$  vs  $\log|i|$  in the Tafel region.

Therefore, it can be concluded that for a sufficient large values of polarization from the corrosion potential (usually selected overpotential above 50 mV) Butler-Volmer equation simplifies the Tafel equation. Thus, the corrosion current density and the corrosion potential is obtained experimentally from the crossing point of the anodic and cathodic Tafel slopes as represented in **Figure 3.5** (straight-line portions of the  $\eta - \log|i|$  plots at more than 50 mV from the corrosion potential). The value of  $E_{corr}$  obtained from the Tafel slopes was verified with the value of  $E_{corr}$  obtained as the potential at which the net current density (sum of the anodic partial current density and the cathodic partial current density) was equal to zero. Frequently, in some

polarization curves the anodic process is represented by the dissolution of the metal constituents through the passive film. When this process takes place at relative low potential (near the  $E_{corr}$ ), the anodic reaction cannot have a valid Tafel slope, and only the cathodic slope was used in these cases [8,9]. Corrosion current densities are determined by extrapolating the linear part of the cathodic curve (first plateau) to the corrosion vertical axis. For accurate interpretation of the results, the same procedure has been employed to extract the corrosion parameters in all curves.

Sometimes, the reaction is limited by **diffusion** which occurs when the **mass transport** is the determining reaction. In this case the charge transfer is faster compared with the diffusion of the reacting species in the surface or the dissolving cations away from the surface. Thus, the concentration of reactants and products in the bulk electrolyte differs from that found at the electrode surface. This leads to an overpotential that varies with the rate of transport of the reactants and products to and from the electrode. When the semi-reaction is controlled by diffusion mechanism, the current density is potential independent and is represented by the following equation:

$$i_{lim} = \frac{n \cdot F \cdot D_i \cdot C_i}{\delta} \quad (3.16)$$

where  $i_{lim}$  is the limiting current density,  $n$  is the charge number,  $F$  is the Faraday constant ( $95485 \text{ C mol}^{-1}$ ),  $D_i$  is the diffusion coefficient of the specie  $i$  (in  $\text{m}^2 \text{ s}^{-1}$ ),  $C_i$  is the concentration of the specie  $i$  and  $\delta$  is the thickness of the diffusion layer (in m).

The **Figure 3.6** represents the typical potentiodynamic curve of a passive metal. Four potential domains can be clearly distinguished: cathodic, anodic, passive and transpassive region. The cathodic domain includes potentials below the  $E_{corr}$  and the current is determined by the reduction of water and dissolved oxygen (if the experiment is carried out under aerated conditions). In acidic media, if the initial potential starts below the reversible potential of the hydrogen, the current will be also determined by the reduction reaction of the protons. As previously commented,  $E_{corr}$  corresponds to the potential where the current changes from cathodic (negative) to anodic (positive). The active region is observed for potentials above the  $E_{corr}$  which is characterized by the dissolution of the metal in form of soluble ions (hydrated or

complexed) and dissolved into the solutions. An increase of the anodic current density with the potential is observed in this region due to the reaction kinetics of active metal dissolution which obeys the Butler-Volmer equation.

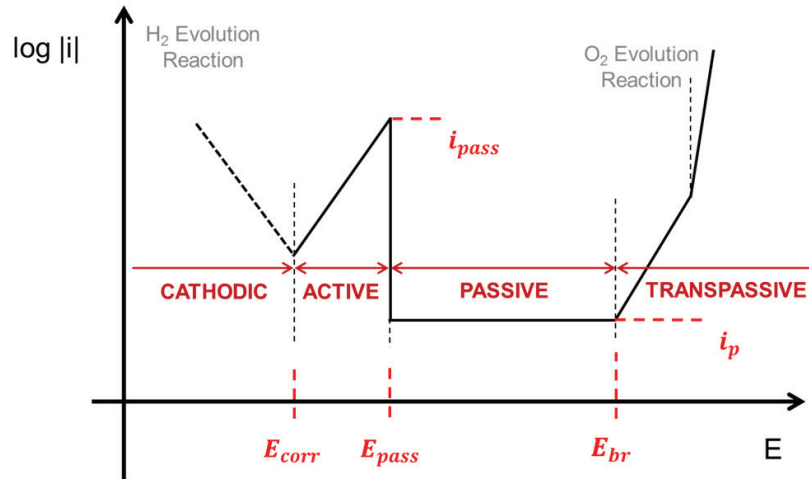


**Figure 3.6.** Schematic potentiodynamic polarization curve. In this case the water dissociation potential is more anodic than the transpassive potential of the working electrode.

The passive domain describes the state where the surface of the metal is covered by a thin protective layer which can slow down metal dissolution and therefore the current density considerably decreases. This layer is formed by reacting the metallic cations with the anions coming from the solution ( $O^{2-}$  and  $OH^-$ ) and depending on the system material/electrolyte can be rapidly formed. In some cases, the formation of the oxide layer occurs few millivolts above the  $E_{corr}$  (even at lower potentials) and the active pure domain disappears. In this case, the potential domain is usually called anodic-cathodic transition and usually is characterized by the generation of some fluctuations of the anodic current (until reaching the well stabilization of the oxide film).

Important parameters to describe the passive behaviour are defined: the passivation potential ( $E_{pass}$ ) separates the active from the passive potential region, the maximum current density corresponding to the  $E_{pass}$  is the passivation current density ( $i_{pass}$ ) and the passive current density ( $i_p$ ) corresponds to the current density that flows through



the metal electrode when the oxide film is formed onto the surface. Therefore, the  $i_p$  characterizes the dissolution behaviour of the metal in the passive potential region which is an important parameter in order to evaluate the protective quality of the passive film. Typically,  $i_p$  is one order of magnitude lower than  $i_{corr}$  for active dissolution [10].

Finally, the transpassive domain is characterized by the increase in current due to the uniform transpassive dissolution resulting from oxidation of the passive film as well as oxygen evolution due to water oxidation (whenever the potential was above the reversible potential of water oxidation). The transpassive dissolution can occur in some passive materials by pitting resulting from local film breakdown where the potential  $E_{br}$  is called pitting potential or critical pitting potential. The transpassivation potential or breakdown potential ( $E_{br}$ ) marks the end of the passive potential region and the transition from passive to transpassive behaviour.

In general, this method constitutes the first approach in a corrosion study and most analysis have been performed on the results obtained from the potentiodynamic polarization curves. Comparison between biomaterials and/or microstructure, surface treatments and coatings can be carried out according to the electrochemical parameters extracted from the potentiodynamic polarization curves. The potentiodynamic polarization curves are used to identify the electrochemical domains of a biomaterial in the body fluids solutions (i.e. cathodic, active-passive transition, passive and transpassive domain) [11,12].

### 3.2.3. POTENTIOSTATIC TESTS

Potentiostatic tests consist of measuring the transient of current when a selected potential  $E$  is imposed on the system. In this case, the potentiostat regulates the appropriate current between the working electrode (biomaterial) and the counter electrode in such a way as to keep the potential between the working electrode and the reference electrode constant. By means of this technique is possible to measure the evolution of the current density with time at an applied potential which allows one to follow the evolution of the electrochemical kinetics of the involved reactions.

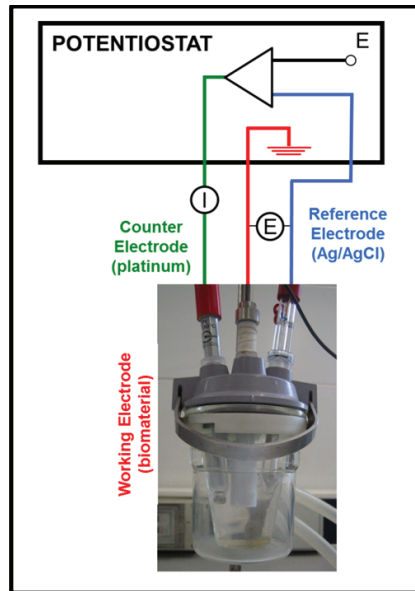


**Figure 3.7.** Experimental set up for potentiostatic measurements. Double-wall three electrode cell used for carrying out the electrochemical measurements.

The current measured during a potentiostatic test corresponds to the sum of the anodic ( $i_a$ ) and cathodic ( $i_c$ ) currents involving all the electrochemical reactions taking place on the electrode surface as described by the **equation 3.17** [3].

$$i_{measured} = \sum i_{a,i} + \sum i_{c,i} \quad (3.17)$$

Depending on the selected potential, anodic or cathodic reactions will be favoured. As previously commented, the measured current at the corrosion potential is zero

because of the anodic and cathodic reactions are equilibrated, i.e. both reactions occur at the same rate. Thus, when a cathodic potential is applied (potential below the corrosion potential) the dissolution rate of the metal is negligible and the measured current is determined by the kinetics of the cathodic reactions. On the contrary, for anodic potentials (above the corrosion potential) the rate of the cathodic reactions is negligible instead of metal oxidation which is favoured.

Faraday's law (**equation (3.18)**) establishes a relationship between the mass loss of metal and the current in the exposed anodic area.

$$m = \frac{I \cdot M_r \cdot t}{n \cdot F} \quad (3.18)$$

where  $m$  is the metal oxidized during time  $t$ ,  $I$  is the anodic current,  $F$  is the Faraday's constant ( $95485 \text{ C mol}^{-1}$ ),  $n$  is the oxidation valence and  $M_r$  is atomic mass of the metal. Therefore, the conversion of current into mass of oxidized metal can be determined by knowing the oxidation valence and if the metal oxidation is the prevailing contribution to the measured current.

Different interpretation can be driven from the potentiostatic tests. Milosev and Strehblow [13] studied the effect of applied potential on the composition, thickness and structure of the oxide layer formed on a CoCrMo in simulated physiological solutions (SPS). They demonstrated that the composition and thickness of the passive film was potential dependent. This technique can be also used in order to analyse the effect of solution chemistry on the passive behaviour of the CoCrMo alloy (influence of inorganic ions and organic compounds such as proteins) [11]. Furthermore, the potentiostatic tests allows one to identify the most soluble species of the metallic biomaterial in the simulated body fluid by applying high anodic potentials to the system used as accelerated tests. All these studies are completed with other electrochemical techniques (i.e. Electrochemical Impedance Spectroscopy) and surface analysis (i.e. X-Ray Photoelectron Spectroscopy) in order to get more reliable conclusions.

The electrochemical behaviour of the biomaterial in the different potential domains can be analysed by applying selected potentials within the cathodic, active, passive or

transpassive regions. In the studies of the electrochemical behaviour of biomedical alloys, the passive film characterization is a key factor since the control of the corrosion behaviour and durability of the biomaterial is related to the stability of this passive layer. The relevance of this technique, when an applied passive potential is selected, is the characterization of the passivation process and the kinetics of the passive film formation. In this case, when applying a passive potential, the current density abruptly increases until a maximum value and then diminishes until reaching a constant value due to the oxide film formation which generation reduces the transient of current density. Once the material is passivated, the value of the current density remains constant and stable. The final current density value, which is denoted as  $i_{pp}$ , gives information about the resistance of the oxide film formed on the biomaterial surface under passive potentiostatic conditions.

### 3.2.4. ELECTROCHEMICAL IMPEDANCE SPECTROSCOPY (EIS)

The Electrochemical Impedance Spectroscopy (EIS) is a relatively modern technique widely extended in several scientific fields. The EIS consists in a non-destructive technique when working under equilibrium conditions (free corrosion potential or open circuit potential), particularly sensible to small changes in the system that allows one to characterize material properties and electrochemical systems even in low conductive media.

The impedance method consists in measuring the response of an electrode to a sinusoidal potential modulation of small amplitude (typically 5-10 mV) at different frequencies. The alternative current (AC) modulation is superimposed either onto an applied anodic potential or cathodic potential or onto the corrosion potential [14].

EIS allows one to determine the influence of the environment (chemical composition of the electrolyte, oxygen content, pH) and external factors (applied potential) on the electrochemical properties of oxide film formed by means of the characterization of the interface electrolyte/biomaterial.

#### 3.2.4.1. Electrode response to a sinusoidal perturbation of the potential

An excitation sinusoidal signal  $E(t)$  is superimposed onto the steady-state potential of an electrode, expressed as a function of time ( $t$ ):

$$E(t) = E_0 \cdot \cos(\omega t) \quad (3.19)$$

where  $E_0$  is the amplitude (in volts),  $\omega$  is the radial frequency (in radians per second) defined also as  $\omega = 2\pi f$  and  $f$  is the frequency expressed in Hertz (Hz). In order to maintain a linear response of the electrode the modulation amplitude must not exceed 10 mV.

The sinusoidal introduction of the perturbation of potential on the system induces a sinusoidal current  $I(t)$ . The response signal  $I(t)$  is shifted in phase and has different amplitude.

$$I(t) = I_0 \cdot \cos(\omega f - \varphi) \quad (3.20)$$

where  $I_0$  is the amplitude (in amperes) and  $\varphi$  is the phase (in degrees).

The **Electrochemical Impedance** ( $Z$ ) is defined as the relation between the applied potential and the resulting intensity. The impedance expression is a function of the magnitude ( $Z_0$ ) and the phase shift ( $\varphi$ ). The ratio of the amplitudes of the applied signal and the response signal on the one hand and the phase shift between both signals on the other hand determines the impedance.

$$Z = \frac{E(t)}{I(t)} = \frac{E_0 \cdot \cos(\omega f)}{I_0 \cdot \cos(\omega f - \varphi)} = Z_0 \frac{\cos(\omega f)}{\cos(\omega f - \varphi)} \quad (3.21)$$

Using Euler's relationship (**equation (3.22)**) it is possible to represent these functions in the complex plane.

$$\exp(j\theta) = \cos\theta + j\sin\theta \quad (3.22)$$

where  $j^2 = -1$  is the imaginary number and  $\theta$  is the angle.

The sinusoidal perturbation of the potential and the current response are represented therefore by two vectors in the complex plane. Thus, the impedance  $Z$  is represented by a vector sum of the real and the imaginary part (**equation (3.23)**) characterized by the modulus  $Z_0$  and the phase shift  $\varphi$ .

$$Z = \frac{E_0 \cdot \exp(j\omega t)}{I_0 \cdot \exp(j\omega t - j\varphi)} = Z_0 \exp(j\varphi) = Z_0(\cos\varphi + j\sin\varphi) \quad (3.23)$$

$$Z = Z_{Re} + jZ_{Im} \quad (3.24)$$

The modulus (**equation (3.25)**) and the phase shift (**equation (3.26)**) can be calculated using Pythagoras' theorem and the adequate trigonometric relations:

$$|Z| = \sqrt{Z_{Re}^2 + Z_{Im}^2} \quad (3.25)$$

$$\varphi = \arctan\left(\frac{Z_{Im}}{Z_{Re}}\right) \quad (3.26)$$

Two graphical representations of the impedance spectra are possible. If the impedance  $Z$  is represented in the complex plane, where the real part is plotted on the  $x$ -axis and the imaginary part on the  $y$ -axis of a chart for different frequencies, the graphic is called **Nyquist diagram (Figure 3.8(a))**.

The impedance can also be represented displaying the modulus  $|Z|$  (in logarithmic scale) and the phase shift  $\varphi$  (both on the  $y$ -axis) as a function of the logarithmic of the frequency  $f$ . This presentation method is the **Bode plot (Figure 3.8(b))**.

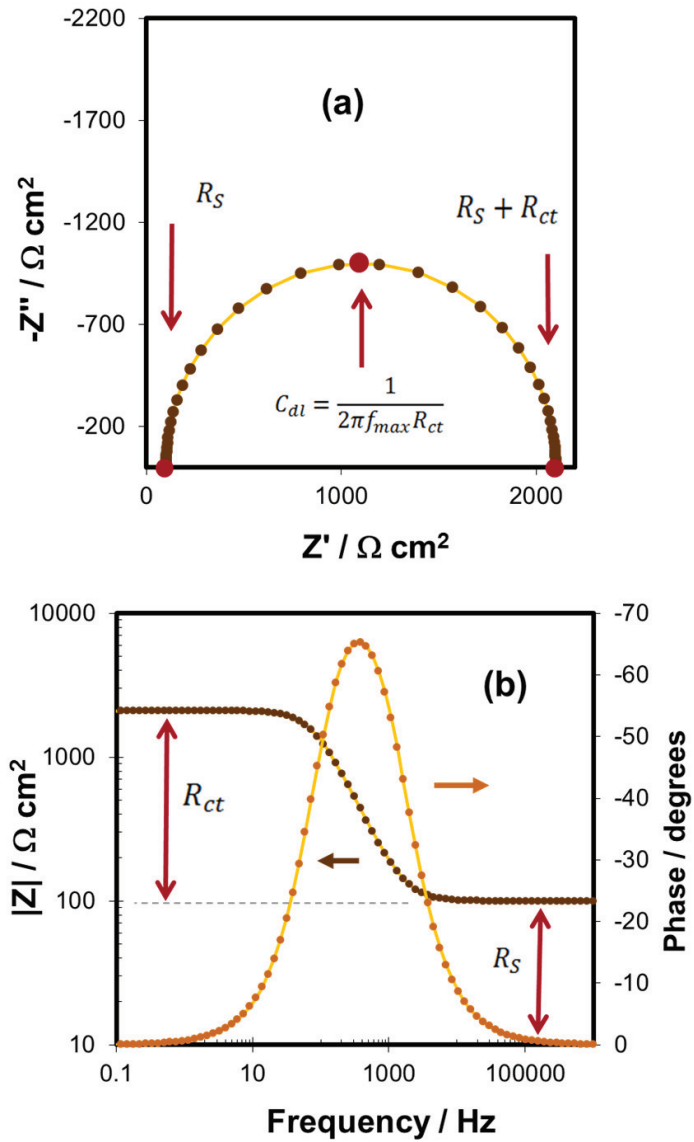


**Figure 3.8.** (a) Nyquist diagram and (b) Bode plot of impedance data for a simple equivalent circuit (Randless circuit with solution resistance ( $R_S$ ) of  $100 \Omega \text{ cm}^2$ , double layer capacitance ( $C_{dl}$ ) of  $1 \cdot 10^{-6} \text{ F cm}^{-2}$  and charge transfer resistance ( $R_{ct}$ ) of  $2000 \Omega \text{ cm}^2$ ).



## 3.2.4.2. Instrumentation

The conventional three-electrode cell configuration is employed for carrying out the EIS experiments. A potential ( $V$ ) is applied between the working electrode (WE, i.e. biomaterial) and the reference electrode (RE, Ag/AgCl electrode) and the current ( $I$ ) flowing through the working electrode and the counter electrode (CE, platinum) is measured.

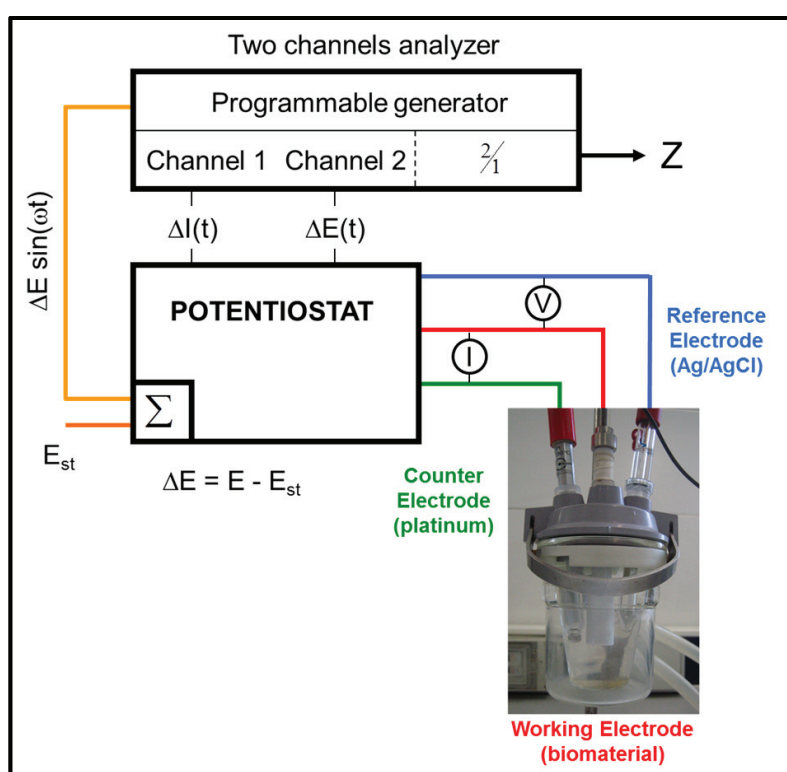


**Figure 3.9.** Experimental set up for impedance measurements using a transfer function analyser under potentiostatic control (a sinusoidal of weak amplitude  $\Delta E = E - E_{st}$  is superimposed onto the steady state potential  $E_{st}$  of an electrode).

The basic electronic instrumentation that allows one to obtain the impedance spectra in electrochemical systems consists on a generator-analyser of functions denominated Frequency Response Analyzer (FRA) or “lock-in amplifier”. FRA Solartron 1250 was used in the present Thesis. The FRA can analyse and apply sinusoidal signals in a widespread frequencies range to the potentiostat with fast response and sensibility.

A potentiostat applies a sinusoidal signal (**equation (3.19)**) to the working electrode in the electrochemical cell. The latter is often built into a two-channel transfer function analyser, thus permitting simultaneously measurement of the potential and the current. The system responds with a signal (**equation (3.20)**) that differs from the **equation (3.19)** by its phase and amplitude. The response of the electrode, measured by the analyser, determines the impedance  $Z$  response of the electrochemical system and the phase shift corresponding to each frequency.

#### **3.2.4.3. Interpretation of the impedance results. Equivalent Electrical Circuits.**

The interpretation of the EIS spectra can be realized by different ways. Some authors qualitatively analyse the EIS results comparing the spectra obtained under different experimental conditions. However, EIS data are commonly interpreted in terms of equivalent circuits. In this sense, the investigated parameters from the impedance experiments are common electrical elements (method used in the present Thesis).

This last interpretation of the impedance spectra requires the selection of an electric model that suitably fits the experimental data to a combination of electrical elements, **Table 3.I**. Thus, according to the selected model and its properties it is possible to obtain information about the electrochemical mechanisms and properties of the system. Common electrical elements and their corresponding meaning are described as follows:

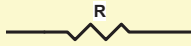
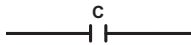
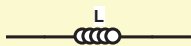
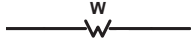
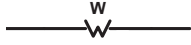
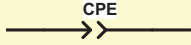
- **Resistance ( $R$ )**: describes some charge transfer across certain interface (i.e. metal/electrolyte). This resistance can be related to the resistivity present for one compound or dissolution to the charge transfer across them (solution resistance) or incorporated into one sub-circuit  $RC$  (electrical circuit formed by one resistance in parallel combination with one capacitance element) which corresponds to the transfer resistance or faradic resistance of the interface.
- **Capacitance ( $C$ )**: is characteristic to charge structures (double layers) considering these layers as parallel plate condenser. It is an element of easy

interpretation since describes properly the charge distribution at the electrode/electrolyte interface which in the simplest case (Helmholtz model) describes the compensation of the surface excess charge by a monolayer of the opposite charge. When this element is included into one sub-circuit  $RC$ , the adsorption of an intermediary specie product of one process of faradic relaxation can be presented. Nevertheless, the main advantage of this element is the capability of evaluating the thickness of the physical layer that is considered into the selected circuit. Generally, in real systems this element is corrected in order to take into account different aspects that can influence in its non-ideality.

- **Inductance ( $L$ ):** is associated with adsorption-desorption process occurring in the formation of layers (passive film). This element is physically worthless because of it is difficult to assimilate the inductance element in the electrode/electrolyte interface. However, at lower frequencies the inductive semicircle generated can be attributed to the relaxation of intermediate species of the surface concentration. Typically, the inductance is associated with  $RL$  sub-circuit where  $R$  corresponds to the charge transfer resistance associated with desorption inductive process.
- **Warburg ( $W$ ):** it represents linear diffusion under semi-infinite conditions. This also assumes the diffusion layer to possess an infinite thickness. The Warburg impedance is defined through an admittance  $Y_0$  (fitting parameter that contains the diffusion coefficients and other parameters that depend on electrochemical properties of the system) and a diffusion parameter  $B$ . This electrical element corresponds to the solution of the second Fick's equation with one-dimension and infinite conditions of resolution.

**Table 3.1** summarized the real and imaginary part of the impedance expression of the commonly used electrical elements.

**Table 3.1.** Impedance values of the electrical elements.

ELEMENT	SYMBOL	IMPEDANCE
Resistance		$R$
Capacitance		$-\frac{j}{\omega C}$
Inductor		$j\omega L$
Warburg (infinite)		$-\frac{1}{Y_0\sqrt{j\omega}}$
Warburg (finite)		$-\frac{\tanh(B\sqrt{j\omega})}{Y_0\sqrt{j\omega}}$
Constant Phase Element		$\frac{1}{Q(j\omega)^\theta}$

A combination of the defined electrical elements (resistance, capacitances and inductances) is selected in order to build an Equivalent Electrical Circuit (EEC) which simultaneously describes the physical properties of the system and better fits the experimental data.

In general, the usual guidelines for the selection of the best-fit *EEC* are (i) a minimum number of circuit elements employed to describe the electrochemical system, (ii) the Chi-squared value ( $\chi^2$ ) should be suitable low ( $\chi^2 \leq 10^{-4}$ ) and (iii) the errors associated with each element must be up to 5 % [15].

The impedance data has been analysed with the Zview 2.70 software package. Thus, the best fitting and the corresponding values of each element can be obtained. In addition, Chi-squared value and the error associated with each element is also acquired which allows to confirm the reliability of all them.

The simplest equivalent circuit used for fitting the experimental results is represented in the **Figure 3.10(a)**. In this case, the theoretical transference function is represented by means of parallel combination of the resistance  $R_{ct}$  (charge transfer resistance) and the capacitance  $C_{dl}$  (double layer capacitance related to the interactions in the electrode/electrolyte interface) both in series with the resistance  $R_S$  (electrolyte resistance).

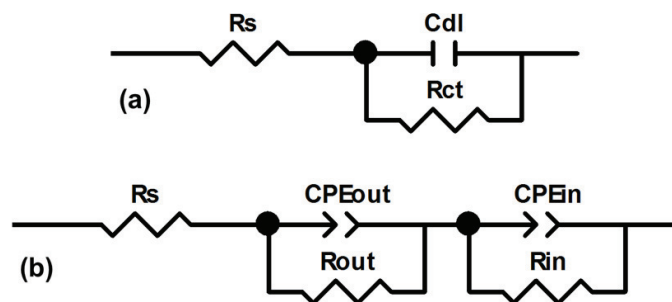


**Figure 3.10.** (a) Equivalent Electric Circuit (Randless) of the electrode-electrolyte interface and (b) Equivalent Circuit for the analysis of the impedance spectra of a CoCrMo passive alloy.

The impedance value of the system represented in **Figure 3.10(a)** is shown in **equation (3.27)**:

$$Z(\omega) = R_S + \left[ \frac{1}{\frac{1}{R_{ct}} + j\omega C_{dl}} \right] \quad (3.27)$$

The impedance spectrum obtained for the Randless Circuit is represented in **Figure 3.8**. This spectrum shows, in the higher frequency region, that  $\log|Z|$  tends to a constant value with a phase shift close to  $0^\circ$  when the frequency increases. This is a resistive behaviour and the values of the impedance correspond to  $R_S$ . This ohmic resistance is added in series to take into account the ohmic drop in the electrolyte between the reference electrode and working electrode. In the medium-lower frequencies range a linear relationship between  $\log|Z|$  and  $\log f$  is observed. For this ideal capacitive behaviour the slope is approximately -1. In this electrical circuit, the  $R_{ct}$  is expressed by

the **equation (3.28)** and corresponds to the diameter of the semicircle represented in Nyquist diagram (**Figure 3.8(a)**).

$$R_{ct} = \lim_{f \rightarrow 0} [(Z_f)_{real}] \quad (3.28)$$

In general, metallic biomaterials spontaneously passivate resulting in the formation of an oxide film in contact with the biological environment (biofilm) according to the scheme represented in **Figure 3.11**. In these passivated materials, EIS results under equilibrium conditions reach high values of impedance (around  $100 \text{ K}\Omega \text{ cm}^2$ ) which can be due to two superposed semicircles (time constants). When the oxide layer is chemically and physically stable and quite homogeneous, the impedance results are good fitted with the EEC proposed in **Figure 3.10(b)**, consisting on two *R-C* groups disposed in series. In the present Thesis, this EEC will be employed in order to characterize the passive film/electrolyte interface on CoCrMo alloy under different experimental conditions. The physical meaning of the selected EEC is attributed to the oxide resistance ( $R_{in}$ )/capacitance ( $C_{in}$ ) in parallel combination across the oxide and to the charge transfer resistance ( $R_{out}$ )/double layer capacitance ( $C_{out}$ ) parallel combination. In this case,  $R_p$  (polarization resistance of the system) can be calculated as the sum of  $R_{out}$  and  $R_{in}$  after fitting the experimental results to the EEC. Thus, two overlapped time constants can be considered in the impedance spectra, the first one related to the outer layer (attributed to the presence of inhomogeneous passive film and to the passive dissolution of the passive layer) and the second one related to the oxide film formed on the passivated metallic biomaterial.

Different authors used the same *EEC* on passive systems when two time constants were shown in the spectra assuming that the low-frequency time constants corresponded to the passive oxide film [11,16].

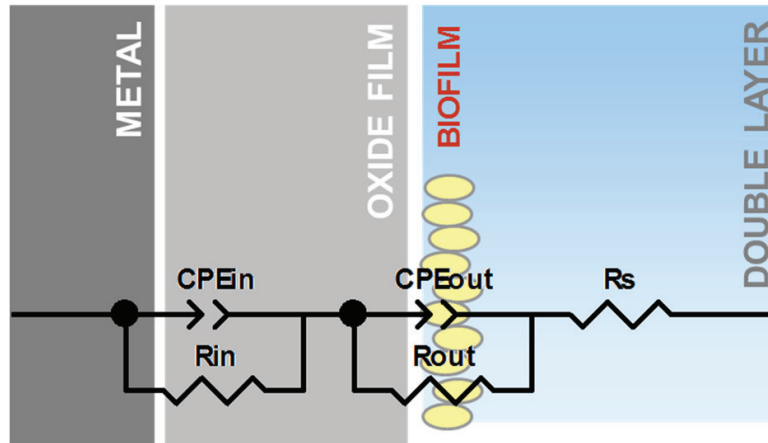


**Figure 3.11.** Scheme of the interface of a CoCrMo surface in contact with biological environments where the metal is covered by an oxide layer, and by an adsorbed organic film ("biofilm") and its description using an electrical circuit which permits the characterization of the system by means of electrical elements.

Generally, the real systems present non-ideal capacitive behaviour in contrast with the ideal shown by the Randless Circuit. These real systems show certain modification from an ideal capacitance behaviour which remark mainly lower value of the slope and lower phase angles. A **constant phase angle element (CPE)** is introduced to replace the capacitance and to describe the non-ideal behaviour which can be due to different physical phenomenon such as surface heterogeneity resulting from surface roughness, impurities, dislocations or grain boundaries [17]. These inhomogeneities are present on a microscopic level under the oxide phase and at the oxide electrolyte interface. Thus, *CPE* is defined in impedance representation as:

$$Z(\omega) = Z_0(j\omega)^{-n} \quad (3.29)$$

where  $Z_0$  is the *CPE* constant and  $n$  is the *CPE* exponent. Depending on  $n$ , *CPE* can represent resistance ( $n=0$ ,  $Z_0=R$ ), a capacitance ( $n=1$ ,  $Z_0=C$ ) or a Warburg impedance ( $n=0.5$ ,  $Z_0=W$ ). For  $0.5 < n < 1$  the *CPE* describes a distribution of dielectric relaxation times in the frequency space. The mathematical expression of the impedance of the electrode system is:

$$Z(\omega) = R_S + \left[ \frac{1}{\frac{1}{R_{out}} + j\omega C_{out}} \right] + \left[ \frac{1}{\frac{1}{R_{in}} + j\omega C_{in}} \right] \quad (3.30)$$

The value of the capacitance is a useful parameter since it could be related to the film thickness according to the **expression (3.31)** [18] which allows one to approximate, for anodic film growth, the dielectric behaviour of the oxide film with a plate capacitor [19,20].

$$C = \frac{\varepsilon \varepsilon_0 A}{d} \quad (3.31)$$

where  $\varepsilon$  denotes the relative dielectric constant of the layer,  $\varepsilon_0$  is the permittivity of the vacuum ( $8.85 \cdot 10^{-14}$  F cm<sup>-1</sup>),  $A$  the active area (in cm<sup>2</sup>) and  $d$  the film thickness (in cm).

In order to use the previous expression and relate the capacitance with the thickness of the capacitor, the CPE of each subcircuit (outer and inner) can be converted into a pure capacitance ( $C$ ) by means of the following equation [21]:

$$CPE = R^{n-1} \cdot C^n \quad (3.32)$$

where  $R$  correspond to  $R_{in}$  when calculating capacitance values of the inner layer of the passive film ( $C_{in}$ ) and  $R$  is calculated according to the **equation (3.33)** [22], from the solution resistance ( $R_S$ ) and the resistance of the outer layer passive film ( $R_{out}$ ) for determining  $C_{out}$ :

$$\frac{1}{R} = \frac{1}{R_S} + \frac{1}{R_{out}} \quad (3.33)$$

It is important to point out that external conditions, such as applied potential and hydrodynamic effects, may generate ambiguous values of the capacitance since dielectric properties of the system ( $\varepsilon$ ) can be altered [23-25]. Therefore, care has to be taken in order to obtain realistic values of layer thicknesses from capacitance values (**equation (3.31)**) under certain conditions.



#### 3.2.4.4. Experimental considerations for biomaterials

Biological systems are specific corrosion media which requires several experimental considerations in order to obtain significant data from EIS measurements:

1. The properties of the biomaterials and the biological environments may strongly change depending on the electrochemical conditions. Selection of very low frequencies in the impedance sweep requires longer experimental times and might conduct changes in the electrode surface, altering the steady-state conditions needed for the adequate impedance measurements. Thus, it is important to adapt the final frequency of the sweep to the system since it can introduce error in the impedance measurements obtained at the lowest frequencies [26].
2. The adsorption of organic compounds on the electrode surfaces may affect the impedance response; i.e. the adsorption of proteins in the reference electrode may cause errors in the potential measurements.
3. The biological solutions are highly susceptible to be contaminated by external agents (such as acids and metallic ions). For this reason, it is important the cleaning of the instrumentation to carry out the experimental tests. Furthermore, the use of sterilized materials is advisable when accurate results are desirables.

### 3.2.5. ELECTROCHEMICAL QUARTZ CRYSTAL MICROBALANCE

The Electrochemical Quartz Crystal Microbalance (EQCM) is known to be a powerful technique for studying the electrochemical process such as film modifications, mass transport phenomena and adsorption kinetics taking place at the interface of thin films [27]. This technique is based on the piezoelectric effect: the application of an applied electrical potential across the crystal induces a corresponding mechanical shear stress proportional to the applied potential [28]. Therefore, variations of the total mass occurring at the material surface can be measured quantitatively by a shift in the resonance frequency of the EQCM. The device is capable of measuring mass changes in the nanogram range [29].

Combined to an electrochemical set-up, one of the two electrodes, i.e. the one in contact with the solution, is used simultaneously to drive the crystal by means of an electric field and acts as a working electrode in the electrochemical cell. This arrangement permits to study different electrochemical phenomena in situ.

For using EQCM, the quartz oscillation should be limited to one particular mode, the high frequency thickness-shear mode because this mode is the most sensitive to mass change (**Figure 3.12**). The thickness-shear mode can be obtained by cutting the single crystal at a specific orientation with respect to the crystal axis and by choosing the proper resonator shape. The 10 MHz AT-cut used in this work, have an angle of  $35^{\circ}15'$  between the disk plane and its symmetry axis. The AT-cut quartzes are ideal candidate for EQCM applications because they show negligible temperature dependence, which permits to limit uncertainties in the frequency shift measurement [30].

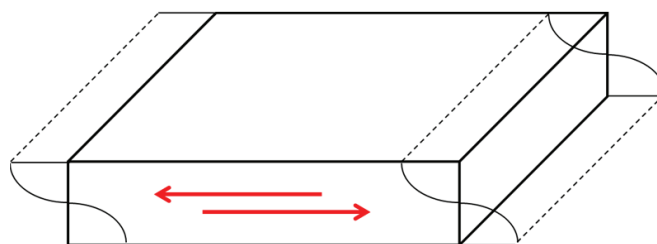


**Figure 3.12.** Thickness shear vibration in the fundamental mode.

3.2.5.1. Sauerbrey equation

In this section a theoretical procedure is developed in order to determine the Sauerbrey equation which relates the variation of the frequency with the variation of mass on one quartz crystal surface. This modelling neglects the presence of electrodes on the both faces of the quartz (superior and inferior) and admit that the material deposited on the surface has the same properties of the quartz.

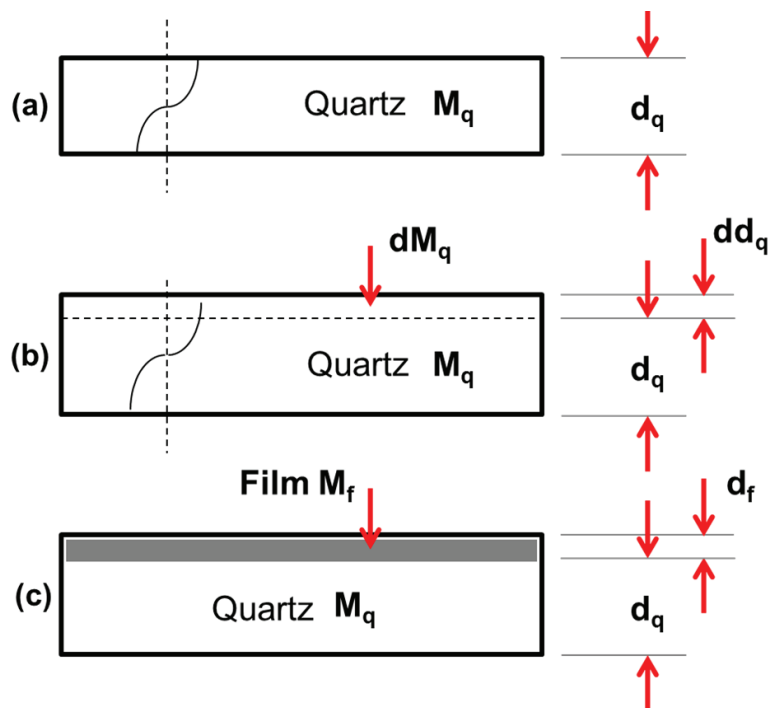


**Figure 3.13.** Principles and postulates related to modelling of the quartz microbalance. (a) In resonance, the thickness of the quartz corresponds to semi-wave length, (b) an increase of the quartz thickness decreases the frequency resonance of the crystal (increase of the wave length) and (c) the mass gain or loss in form of a film is treated as quartz (same physic and mechanical properties).

The deformation wave of one quartz crystal in shear mode resonator is function of its thickness (Figure 3.13(a)):

$$d_q = \frac{\lambda_q}{2} \tag{3.34}$$

where  $d_q$  is the quartz thickness (in  $\mu\text{m}$ ) and  $\lambda_q$  the length wave in shear mode (in  $\mu\text{m}$ ).

According to the relation between the wave propagation speed, frequency and wave length (**equation (3.35)**), the **equation (3.34)** can be rewritten as a function of the frequency and the wave propagation speed (**equation (3.36)**).

$$\lambda_q \cdot f_q = v_q \quad (3.35)$$

$$f_q \cdot d_q = \frac{v_q}{2} \quad (3.36)$$

where  $f_q$  is the resonance frequency of the unloaded crystal (in Hz),  $v_q$  is the transverse wave propagation speed (in  $\text{m s}^{-1}$ ).

The derivation of the **equation (3.36)** allows relating the variation of frequency with the variations of the crystal thickness (**Figure 3.13(b)**).

$$\frac{df_q}{f_q} = -\frac{dd_q}{d_q} \quad (3.37)$$

The **equation (3.37)** can be written as function of the mass of the quartz crystal:

$$\frac{df_q}{f_q} = -\frac{dM_q}{M_q} \quad (3.38)$$

where  $M_q$  is the mass (in ng) of the quartz crystal.

Sauerbrey hypothesis consider that for low mass changes, the mass addition on the crystal can be treated as a mass change of the quartz crystal mass. This relation is valid for the mass added or removed from the surface which is not involved in the quartz mass.

$$\frac{df_q}{f_q} = -\frac{dM}{M_q} \quad (3.39)$$

Where  $M$  is the mass (in ng) unrelated to the quartz crystal mass.

If a uniform distribution of material is added on the quartz crystal surface (**Figure 3.13(c)**), i.e. oxide passive film, the previous equation can be rewritten not considering the infinitesimal variation of material:

$$\frac{f - f_q}{f_q} = -\frac{M_f}{M_q} \quad (3.40)$$

where  $M_f$  is the mass (in ng) of the film and  $f$  (in Hz) is the frequency of the quartz with the film.

Taking into account the variation of mass per surface unit:

$$\frac{f - f_q}{f_q} = -\frac{m_f}{m_q} \quad (3.41)$$

where  $m_f$  and  $m_q$  are the mass of the film and the mass of the quartz per surface unit respectively, expressed both in  $\text{ng cm}^{-2}$ .

In the case of homogeneous materials, the mass per surface unit is related to the density and the thickness by means of the **equation (3.42)**:

$$m = d \cdot \rho \quad (3.42)$$

where  $d$  is the thickness and  $\rho$  is the density in  $\text{ng cm}^{-3}$ .

Thus, according to the exposed procedure, the Sauerbrey equation is obtained substituting the **equations (3.36) and (3.42) in the equation (3.41)**. For small changes in mass, the frequency shift  $\Delta f$  is linearly dependent on this mass variation, according to the following expression:

$$\Delta f_m = f - f_q = -\frac{2f_0^2}{\rho_q v_q} \cdot \Delta m \quad (3.43)$$

It is important to highlight that this expression is only due to mass variation (mass loading) related to changes in the total mass of the quartz due to mass added or removed from the surface material. For this statement, the variation of frequency ( $f-f_q$ ) is denoted by  $\Delta f_m$  and  $m_f$  as  $\Delta m$ . This relationship between the changes in the quartz electrode mass ( $\Delta m$ ) and the frequency shift ( $\Delta f_m$ ) due to mass loading was developed by Sauerbrey [29] and can be simplify as follow:

$$\Delta f_m = -C_f \cdot \Delta m \quad (3.44)$$

where  $C_f$  is the sensitivity factor (in Hz cm<sup>2</sup> ng<sup>-1</sup>) which can be rewritten taking into account the elastic shear modulus of the quartz ( $\mu_q$ , in N cm<sup>-2</sup>):

$$C_f = \frac{2f_0^2}{\rho_q v_q} = \frac{2f_0^2}{\sqrt{\rho_q \mu_q}} \cdot \Delta m \quad (3.45)$$

where  $\rho_q$  is the quartz density (in g cm<sup>-3</sup>).

### 3.2.5.2. Limitations of Sauerbrey theory

The variation of the frequency on the quartz also depends on the density, the viscosity of the liquid as well as on the roughness of the quartz, the temperature, the pressure and the internal stress [30]. In this section, the implication of these variables in the variation of the quartz frequency is briefly commented.

When the quartz is in contact with a viscous medium, the coupling will induce a large damped shear wave into the medium. The frequency shift due to viscosity and density of the oscillating quartz, when one face of a quartz crystal resonator is in contact with one liquid was first calculated by Kanazawa and Gordon [31]:

$$\Delta f_m = -f_0^{3/2} \left( \frac{\rho_l \eta_l}{\pi \rho_q \mu_q} \right)^{1/2} \quad (3.46)$$

where  $\rho_l$  and  $\eta_l$  are the density and the absolute viscosity of the liquid respectively.

It was also confirmed that changes in the double layer thickness affect the frequency shift. Kern and Landolt [32] showed that the viscosity of the electrolyte within the double layer differs from its bulk value. According to their model calculations at low electrolyte concentrations confirmed that the behaviour of the EQCM is sensitive to the effective thickness of the double layer but is rather insensitive to the assumed density and viscosity.

The difference of static pressure ( $\Delta p$ ) between the side of the quartz in contact with the solution and the one isolated from the liquid generates a frequency shift in a parabolic form according to the equation [33]:

$$\Delta f = K_1 \cdot \Delta p^2 \quad (3.47)$$

where  $K_1$  is a constant in  $\text{m}^4 \text{s}^{-1} \text{g}^{-1}$  and  $\Delta p$  is the difference of pressure between the quartz sides (in  $\text{g m}^{-2}$ ).

Eernisse [34] theoretically and experimentally showed that stresses in a thin film on a quartz resonator surface can set up sufficient static mechanical bias in the resonator to cause measurable shifts in the resonant frequency through finite strain effects. Thus, the **equation (3.48)** was proposed in order to explain the frequency shift due to stress taking into account the effect of the stress in deposits by considering only lateral deformations.

$$\Delta f = K_2 \cdot f_0 \cdot \frac{\Delta \gamma}{d} \quad (3.48)$$

where  $K_2$  is  $2.75 \cdot 10^{-11} \text{m}^2 \text{N}^{-1}$ ,  $f_0$  is the quartz frequency (in Hz),  $d$  is the deposit thickness (in m) and  $\Delta \gamma$  is the change in surface tension (in  $\text{N m}^{-1}$ ).

Although the variations of frequency in an electrochemical system varies with the viscosity of the liquid, pressure, internal stresses and roughness, Hamm [35] exposed that all of them are included within the same Gaussian distribution of sensibility [36,37] and therefore, the Sauerbrey theory is valid in order to model numerous practical test even under hydrodynamic and rotation conditions [38,39].

In the present Thesis, EQCM has been used to measure in situ mass variation on the interface biomaterial/electrolyte together with the electrical signal under different electrochemical conditions. This mass evolution allows one to determine the passivation kinetics under different applied potentials and temperature. Furthermore, adsorption kinetics of organic compounds present in the body fluids and its influence on the passivation kinetics of the CoCrMo alloy are also evaluated.

### **3.3. Surface Analysis**

Surface analysis methods refer those experimental techniques that give chemical information on surfaces to a depth of 2-3 nm or less. These methods are able to measure concentration variations over a depth of tens or even hundred of nanometres [1]. Two surface analysis methods have been employed in the development of the present Thesis: Scanning Electron Microscope (SEM) and X-Ray Surface Analysis (XPS).

#### **3.3.1. SCANNING ELECTRON MICROSCOPE (SEM)**

The scanning electron microscope (SEM) is an instrument used for characterizing surface structure and topography of organic and inorganic materials in non-destructive mode. This technique is well suited for the study of micrometre scale or even millimetre scale surface topography. The signal generated by SEM provides predominantly information about the morphology of the analysed material: superficial texture, grain morphology, approximation of the grain orientation in some materials, roughness and porosity on material surfaces. Furthermore, many SEMs are equipped with X-Ray dispersive analysis (EDAX) that permits chemical analysis of samples with high spatial resolution [1].

##### **3.3.1.1. Technique principles and capacities**

A tightly focused electron beam sweeps the sample surface at high speed generated by means of a wolfram filament subjected at high voltage and temperature. The charged anode is located in front of the filament which extracts the electrons from the cathode (wolfram) increasing their speed. The local electron flux depends on the angle created between the incident beam and the surface which is fixed by different lens and magnetic coils.

The energy exchange between the electron beam and the sample results in the reflection of high-energy electrons by elastic scattering, emission of secondary electrons by inelastic scattering and the emission of electromagnetic radiation, each of



which can be detected by specialized detectors. Thus, the electrons that interact with the sample are collected in different sensors depending on the analysis. One of the detectors monitors the secondary electron flux emitted by the irradiated sample. Therefore, the signals result from interactions of the electron beam with atoms at or near the surface of the sample generating an image that reflects the surface topography.

Other important aspect is the vacuum required by SEM for imaging the studied samples because a gas atmosphere rapidly spreads and attenuates electron beams. Consequently, more stability to the electrons beam is attained under vacuum conditions which also avoids the gas ionization.

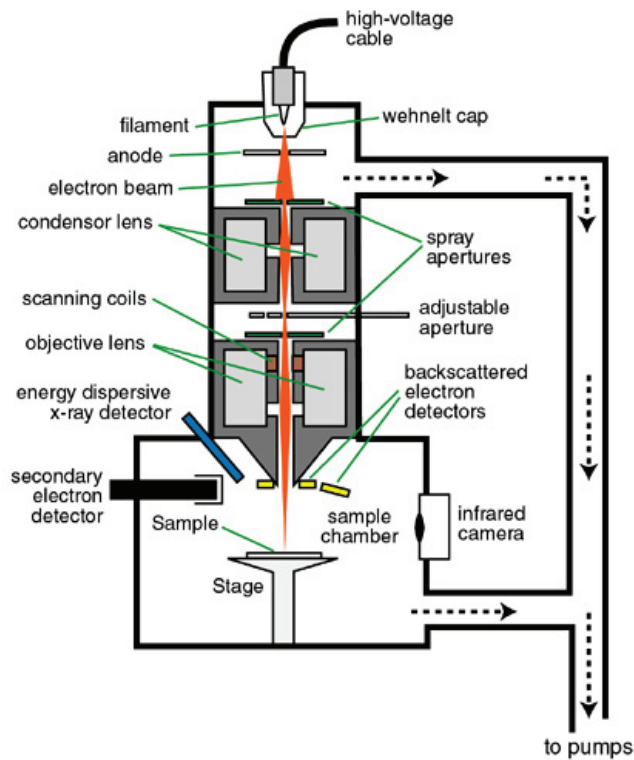


Figure 3.14. Scanning Electron Microscope (SEM) overview.

### **3.3.1.2. Experimental device and applied conditions**

The Scanning Electron Microscope (SEM) Scanning JEOL JSM-3600 has been used to characterize the microstructure of the CoCrMo PVD-deposits. A heat wolfram filament folded in form of "V" is used in this high resolution electronic microscope in order to improve the electrons emission. The power of 20 kV was applied in the analysis of the samples.

### 3.3.2. X-RAY PHOTOELECTRON SPECTROSCOPY (XPS)

**XPS** is based on the photoelectric effect, i.e. the energy ( $h\nu$ ) received by an atom when this adsorbs a photon is dissipated by the emission of an electron (photoelectron). In XPS, incident photons typically have an energy of 1 to 2 keV. The energy of the incident radiation results in the emission of electrons not only from the outer shells but also from core levels of all elements of the periodic table.

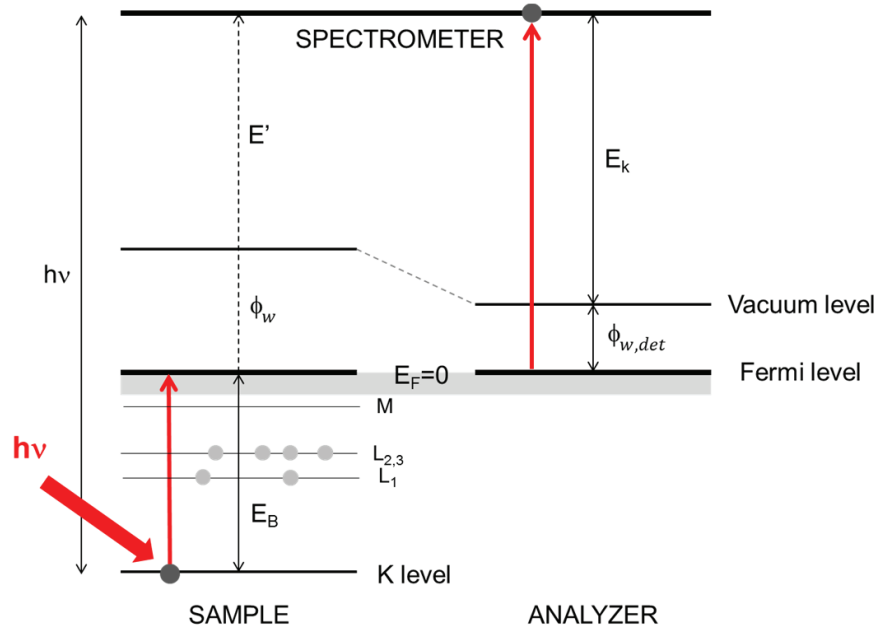


Figure 3.15. Energetics of the photoionization.

In XPS the kinetic energy of the photoelectrons emitted by the sample ( $E_k$ ) is measured. The electrical contact between the sample and the analyser equalizes their electrical potential and their Fermi levels. For this, it is convenient to take the Fermi level as a reference point of the measurement. Therefore, the expression for the energy balance (by arbitrarily setting  $E_f = 0$ ) can be written as follow:

$$E_k = h\nu - E_b - \phi_{w, det} \quad (3.49)$$

$E_b$  is the **binding energy of the electron** which corresponds to the energy difference between the Fermi level and the energy level from the photoelectron is extracted. The binding energy of an electron in a given shell is characteristic of the chemical element that emits the photoelectron. For this reason, XPS spectra are generally presented in terms of  $E_b$  rather than of  $E_k$ . The **work function** of the detector  $\phi_{w, det}$  characterizes the difference in energy between the Fermi level of the analyser and vacuum.

The **equation (3.49)** assumes that the photo-emission process is elastic; nevertheless if the photo-electrons suffer an energy change (energy loss) between photo-emission from an atom in the solid and its detection in the spectrometer the process will be inelastic. The X-Ray provides a series of characteristic peaks which reflects the binding energy of the electrons presents in the solid. The background registered to low kinetic energy (opposite direction of the binding energy) of the photo-electron peaks is due to inelastic-emission. Secondary electrons resulting from inelastic photo-emission increasingly dominate the background a lower kinetic energy.

When the photoelectron undergoes inelastic collisions (losing part of its energy) is no longer possible to determine its quantum state of origin from the energy balance. The average distance that an electron with a given energy travels in a solid without collisions is the **mean free path** ( $\lambda$ ). Thus, the inelastic mean free path (IMFP) can be also defined as the average distance covered by a moving particle between successive impacts (collisions) which modify its direction or energy or other particle properties [40]. In XPS, the mean free path is on the order of one nanometre. The mean free path and the escape angle  $\phi$  (angle of the detected electrons with respect to the normal to the sample surface) determine the **escape depth**  $\Lambda$  of the photoelectron which is perpendicular to the surface (**Figure 3.16**):

$$\Lambda = \lambda \cdot \cos \phi \quad (3.50)$$

The escape depth is therefore the distance normal to the surface at which the probability of an electron escaping without significant energy loss due to inelastic scattering process dropped to  $1/e$  (36.8 %) of its original value.

Photoelectrons that escape from depths less than the escape depth ( $\lambda$ ) escape from the lattice without collision and thus contribute to XPS peaks. The other photoelectrons become part of the background noise.

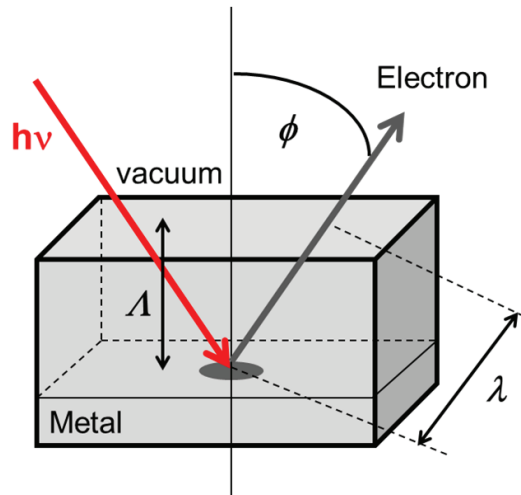


Figure 3.16. Electron escape depth and means free path of electrons.

The **Figure 3.17** shows an example of the XPS survey spectrum of CoCrMo alloy immersed in a Phosphate Buffer Saline solution. In this, the different peaks corresponding to the elements present in the alloy can be observed. There are number of peaks of each element because photoelectrons are emitted from several energy levels, nevertheless the highest intensities corresponds to the main state in which the element is found in the metal. The basic peaks are grouped in three groups: peaks from *core levels* (direct reflection of the electron structure of the element atoms) and *valence levels* (occupied by electrons of low binding energy) and peaks due to X-Ray excited Auger emission. The latter corresponds to the emission of an electron as consequence of the energy liberated when an electron (coming from outer core level) fill the level vacancy created by an electron (ejected from the inner shell of the target atom) after the irradiation of the solid with X-Ray or with an electron beam of suitable energy.

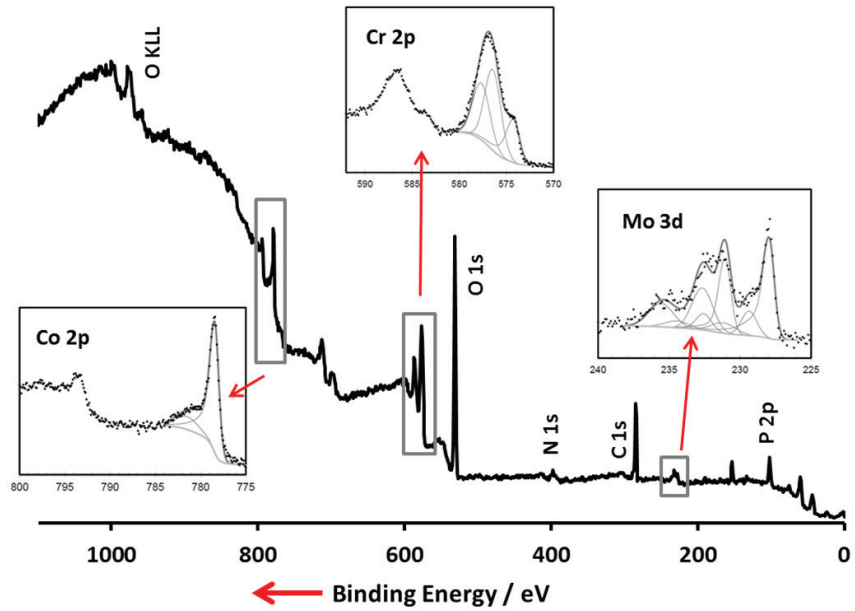


Figure 3.17. XPS survey spectrum of CoCrMo alloy (primary source is Mg  $K_{\alpha}$ ).

### Quantitative analysis

The equation that allows one to determine the intensity  $I_i$  of a given XPS peak for the element  $i$  is [1,40,41]:

$$I_i = \alpha \int_0^{\infty} c_i(z) \exp\left(-\frac{z}{\lambda}\right) dz \quad (3.51)$$

where  $c_i(z)$  is the concentration of the element  $i$  in the solid and  $z$  is the depth.

The proportional factor  $\alpha$  is obtained from the formula:

$$\alpha = \alpha_{sp} \cdot I_{RX} \cdot \sigma_e \quad (3.52)$$

where  $\alpha_{sp}$  is parameter dependent on the spectrometer used and its mode of operation,  $I_{RX}$  is the intensity of the incident radiation and  $\sigma_e$  is ionization cross section

or, expressed otherwise, the probability that an irradiated atom losses a photoelectron.

To integrate properly the **equation (3.51)** one needs first to decide which function best represents the concentration profile  $c_i(z)$  near the surface.

In the case of a homogeneous sample, integrating the **equation (3.51)** by  $z$  from 0 to infinite, the total intensity can be determined as:

$$I_{\infty} = \alpha \cdot c \cdot \lambda \cdot \cos \phi \quad (3.53)$$

If the sample is covered with an overlayer with a thickness  $d$ , the **equation (3.51)** must to be integrated from 0 to  $d$  and from  $d$  to infinity obtaining the intensity from the surface layer **(3.54)** and the bulk **(3.55)**:

$$I_{sf} = \alpha \cdot c_{sf} \cdot \lambda_{sf} \cdot \cos \phi \cdot \left[ 1 - \exp\left(-\frac{d}{\lambda_{sf} \cdot \cos \phi}\right) \right] \quad (3.54)$$

$$I_{bulk} = \alpha \cdot c_{bulk} \cdot \lambda_{bulk} \cdot \cos \phi \cdot \exp\left(-\frac{d}{\lambda_{sf} \cdot \cos \phi}\right) \quad (3.55)$$

Applying the mentioned **equation (3.51)** and provided the concentration of the substrate underneath the film is known, one can determine the concentration in the oxide film and its thickness. Therefore, XPS is a useful technique for the study of thin passive oxide film on metals.

### 3.4. References

- [1] D. Landolt, Corrosion and surface chemistry of metals, 2007.
- [2] L. Reclaru, P. Y. Eschler, R. Lerf, A. Blatter, *Biomaterials* 26 (2005) 4747-4756.
- [3] A. Igual Muñoz and S. Mischler, Inter-laboratory study on electrochemical methods for the characterisation of CoCrMo biomedical alloys in simulated body fluids, European Federation of Corrosion by Maney Publishing on behalf of The Institute of Materials, Minerals & Mining, 2011.
- [4] F. Contu, B. Elsener, H. Bohni, *Journal of biomedical materials research* 62 (2002) 412-421.
- [5] F. Contu, B. Elsener, H. Bohni, *Journal of the Electrochemical Society* 150 (2003) B419-B424.
- [6] F. Contu, B. Elsener, H. Böhni, *Corrosion Science* 47 (2005) 1863-1875.
- [7] ASTM G5-94 (2004) : "Standard Reference Test Method for Making Potentiostatic and Potentiodynamic Anodic Polarisation Measurements". 2004.
- [8] M. A. Ameer, A. M. Fekry, F. E.-T. Heakal, *Electrochimica Acta* 50 (2004) 43-49.
- [9] A. B. Silva, S. M. L. Agostinho, O. E. Barcia, G. G. O. Cordeiro, E. D'Elia, *Corrosion Science* 48 (2006) 3668-3674.
- [10] D. Landolt and S. Mischler, *Tribocorrosion of passive metals and coatings*, Woodhead Publishing, 2011.
- [11] A. Igual Muñoz, S. Mischler, *Journal of the Electrochemical Society* 154 (2007) C562-C570.
- [12] I. Milosev, H.-H. Strehblow, *Electrochimica Acta* 48 (2003) 2767-2774.
- [13] A. Kocijan, I. Milosev, B. Pihlar, *Journal of Materials Science-Materials in Medicine* 15 (2004) 643-650.
- [14] J. R. Scully, D. C. Silverman, and M. W. Kending, *Electrochemical impedance. Analysis and interpretation*, Philadelphia (United States of America), 1993.
- [15] M. Metikos-Hukovic, Z. Pilic, R. Babic, D. Omanovic, *Acta Biomaterialia* 2 (2006) 693-700.
- [16] A. Kocijan, I. Milosev, D. K. Merl, B. Pihlar, *Journal of Applied Electrochemistry* 34 (2004) 517-524.



### CHAPTER 3. Experimental techniques

- [17] F. B. Growcock, R. J. Jasinski, *Journal of the Electrochemical Society* 136 (1989) 2310-2314.
- [18] J. A. Helsen and H. J. Breme, *Metals as biomaterials*, United Kingdom, 1998.
- [19] P. Bommersbach, C. Alemany-Dumont, J. P. Millet, B. Normand, *Electrochimica Acta* 51 (2005) 1076-1084.
- [20] C.-O. A. Olsson, D. Landolt, *Electrochimica Acta* 48 (2003) 3999-4011.
- [21] N. P. Cosman, K. Fatih, S. G. Roscoe, *Journal of Electroanalytical Chemistry* 574 (2005) 261-271.
- [22] G. J. Brug, A. L. G. van den Eeden, M. Sluyters-Rehbach, J. H. Sluyters, *Journal of Electroanalytical Chemistry* 176 (1984) 275-295.
- [23] J. J. Gray, C. A. Orme, *Electrochimica Acta* 52 (2007) 2370-2375.
- [24] K.M.Ismail, S.S.El-Egamy, M.Abdelfatah, *Journal of Applied Electrochemistry* 31 (2001) 663-670.
- [25] T. P. Cheng, J. T. Lee, W. T. Tsai, *Electrochimica Acta* 36 (1991) 2069-2076.
- [26] A. W. E. Hodgson, S. Kurz, S. Virtanen, V. Fervel, C.-O. A. Olsson, S. Mischler, *Electrochimica Acta* 49 (2004) 2167-2178.
- [27] D.A.Buttry, M.D.Ward, *Chemical Reviews* 92 (1992) 1355-1379.
- [28] V. Daujotis, D. Jasaitis, R. Raudonis, *Electrochimica Acta* 42 (1997) 1337-1344.
- [29] G.Sauerbrey, *Zeitschrift für Physik* 155 (1959) 206-222.
- [30] M. G. Verge, "In-situ electrochemical quartz crystal microbalance studies on anodic film growth on valve metals," Ph.D. Thesis, 2003.
- [31] K.K.Kanazawa, J.G.Gordon, *Analytica Chimica Acta* 175 (1985) 99-105.
- [32] P. Kern, D. Landolt, *Journal of Electroanalytical Chemistry* 500 (2001) 170-177.
- [33] A. Grzegorzewski, K. E. Heusler, *Journal of Electroanalytical Chemistry and Interfacial Electrochemistry* 228 (1987) 455-470.
- [34] E. P. Eernisse, *Journal of Applied Physics* 43 (1972) 1330-1337.
- [35] D. Hamm, "Étude en temps réel de la croissance des films passifs sur le chrome et les alliages fer-chrome," Ph.D. Thesis, 2000.
- [36] D. M. Ullevig, J. F. Evans, *Analytical Chemistry* 52 (1980) 1467-1473.
- [37] D. M. Ullevig, J. F. Evans, M. G. Albrecht, *Analytical Chemistry* 54 (1984) 2341-2343.

- [38] C. Arkam, V. Bouet, C. Gabrielli, G. Maurin, H. Perrot, *Journal of the Electrochemical Society* 141 (1994) L103-L105.
- [39] P. Kern, D. Landolt, *Journal of the Electrochemical Society* 147 (2000) 318-325.
- [40] Miklós Mohai, "Development and applications of quantitative X-Ray Photoelectron Spectroscopy," Ph.D. Thesis, 2005.
- [41] D. Briggs and M. P. Seah, *Practical Surface Analysis by Auger and X-ray Photoelectron Spectroscopy*, J. Wiley, Chichester, 1983.

## CHAPTER 4: ELECTROCHEMICAL CHARACTERIZATION OF CoCrMo ALLOY IN SIMULATED BODY FLUIDS

---

### 4.1. Introduction

Cobalt-based alloys have been widely employed in orthopaedic implants and biocorrosion has been considered one of the most important problem for the long durability of implants into human bodies due to the release of metal ions that cause adverse physiological effects, toxicity, carcinogenicity and metal allergy [1-8]. Therefore, the study of the electrochemical behaviour of Co-based alloys is one of the key-factors for improving the biocompatibility of implants. The corrosion mechanisms and the resistance of CoCrMo alloys is explained by the spontaneous formation of a protective film with dielectric properties [9-13]. The composition of this layer is predominantly  $\text{Cr}_2\text{O}_3$  oxide with some minor contribution of other oxides (Co- and Mo-oxides, especially if the film is air formed) [10-12,14].

Different authors have stated that there is a high influence of the composition of the electrolytic media in the passivation behaviour of Co-based alloys. Milosev and Strehblow [15] demonstrated that proteins may have an important effect on the passivation behaviour of stainless steel; the protein can act as complexing agents for dissolved metal ions suppressing the formation on the protective oxide layer. Nevertheless, the effect of particular protein differs on different metals and alloys. Iglual and Mischler [14] studied the effect of the interactions between phosphate ions and Bovine Serum Albumin (BSA) in model-simulated body fluids on the passive behaviour of CoCrMo. In their work, phosphate ions and albumin molecules competitively adsorbed on CoCrMo implant alloy. Other investigations are centred in analysing the effect of the human serum on the corrosion behaviour of the alloys [16,17]. Thus, the presence of proteins can alter the stability of the passive layer due to their adsorption onto the biomaterial surface [15-20].

These organic molecules could limit the diffusion of oxygen to certain regions of the metallic surface, causing preferential corrosion of the oxygen-deficient regions and leading to the breakdown of the passive layer. The charge and the conformational structure [21] depends on the pH which can affect in different ways the electrochemical behaviour of the metallic biomedical alloys. Iturbide et al. [20] studied the influence of pH in passivated chromium surfaces. They demonstrated that the pH had not strong effect on the total amount of BSA adsorbed on the Cr surfaces. Furthermore, this study showed that electrostatic forces did not govern the interactions protein-passivated surface of Cr. However, the influence of pH on the BSA adsorption on CoCrMo alloy has not been carried out and it is one of the objectives of this chapter.

The pH in biological systems is modulated mainly by phosphate buffering and it is kept around 7.4 under normal conditions. Nevertheless, pH may be modified by several factors such as wound-healing process after surgery (reaching values from 5.5 to 9 with infection) or haematomas and corrosion in some local sites where the pH may drop to approximately pH 1 or even lower [22,23]. Furthermore, pH also plays a role in the formation and modification of different metal-complexes generated into the body.

#### CHAPTER 4. Electrochemical characterization of CoCrMo alloy in simulated body fluids

Moulton et al. [24] observed different behaviour on the protein adsorption depending on the solution pH.

The content of dissolved gases in the body fluids may also change the electrochemical behaviour of an implant [25-27]. The oxygen and carbon dioxide content in the surroundings of a biomaterial can vary depending on the body fluid and physiological conditions. These differences may have effects on the corrosion behaviour of biomaterials in vivo [22].

Another factor that can modify the interface solution/alloy is the presence of external agents. The presence of oxidant species in the electrolyte or electrochemical conditions (i.e. potential) may modify the properties of the passive film. Thus, it is important to study the effect of the applied potential on the electrochemical behaviour of CoCrMo alloys. Depending on the potential, cobalt forms two different passive layers in slightly alkaline solutions [28]. Milosev and Strehblow [10] also studied the composition, thickness and structure of the oxide layer formed on a CoCrMo alloy by electrochemical oxidation in simulated physiological solution, pH 7.5 at several applied potentials; they observed significant changes on thickness and chemical composition of the passive layer depending on the applied potential. In the lower potential range the passive film consisted predominantly of  $\text{Cr}_2\text{O}_3$  and  $\text{Cr}(\text{OH})_3$  and was up to 3 nm thicker while at higher potentials Co and Mo oxides (mainly in the form of  $\text{CoO}$  and  $\text{MoO}_3$ ) enter the passive layer which is accompanied by a significant increase in layer thickness.

The main objective of this chapter is to elucidate the effect of several physico-chemical properties of the simulated body fluids (chemical composition, pH, oxygen content and applied potential) on the electrochemical behaviour of a High-Carbon CoCrMo biomedical alloy. Electrochemical techniques such as Open-Circuit measurements, potentiodynamic polarization curves, potentiostatic tests and Electrochemical Impedance Spectroscopy (EIS) were employed in order to attain this objective.

## 4.2. CoCrMo biomaterial alloy

The selected CoCrMo alloy was provided by LAFITT (Valencia, Spain) with a nominal composition of the wrought alloy corresponding to the **ISO 5832-12**: Co (Balance), Cr (28.45 wt.%), Mo (5.39 wt.%), Mn (0.38 wt.%), Si (0.8 wt.%), Ni (0.22 wt.%) Fe (0.22 wt.%), N (74.9 ppm) and C (0.259 %wt.). Samples were machined in form of cylinders of 9 mm in diameter which were embedded in epoxy mount so that a surface of 0.65 cm<sup>2</sup> was exposed to the test solution. The CoCrMo alloy selected in order to carry out the general electrochemical characterization was the high-carbon alloy thermally treated by solution annealing (SA1), subjected to a porous coating (PC), a hot isostatic pressing (HIP) and a final solution annealing (SA2).

Microstructures of the CoCrMo alloys were revealed by etching with *Beraha III reagent* (base composition: 50g de NH<sub>4</sub>HF<sub>2</sub>, 600 ml of distilled water and 400 ml of concentrated HCl; with reagent composition of 1g of K<sub>2</sub>S<sub>2</sub>O<sub>5</sub> for each 100 ml of base solution). The samples were immersed in the *Beraha III reagent* for 30 seconds, cleaned and rinsed with distilled water, immersed in ethanol and finally dried with compressed air. After the etching, all samples were analysed by optical microscopy.

Microstructures of the as-cast material and the alloy after applying the thermal treatment are represented in **Figure 4.1(a)** and **(b)** respectively. In all cases carbides are mainly distributed within the grains boundaries and at the grain boundaries. The same microstructures were obtained by several authors [29-33] who determine that the composition of the carbides were mainly rich in chromium and molybdenum. Thermal treatments alter the chemistry and structure of carbides; generally, the carbide volume fraction decreased with time and with temperature of the heat treatments. Dobbs and Robertson [31] demonstrated that heat treatments caused carbide dissolution and elimination of both grain boundary precipitates and coring.

Microstructure of as-cast alloy reveals a dendrite structure. **Figure 4.1(a)** shows great amount of carbides both in the matrix and in the grain edge. The average content of carbides in the material has been calculated by image analysis and it lied around 6.5% of the area, **Figure 4.1(a')**.

CHAPTER 4. Electrochemical characterization of CoCrMo alloy in simulated body fluids

After applying the different thermal treatments the material is characterized by an enhanced growth of the grain size and a diminution of the amount of carbides in the grain boundaries. Thus, the microstructure exhibited finely dispersed intergranular carbides (Figure 4.1(b)). According to this microstructure, the carbides are mainly distributed at the grain boundaries and intergranular finely dispersed. The microstructure is characterized by a grain size of around  $0.06 \text{ mm}^2$  and a diminution of the amount of carbides in the grain boundaries compared to the as-cast alloy, Figure 4.1(b').

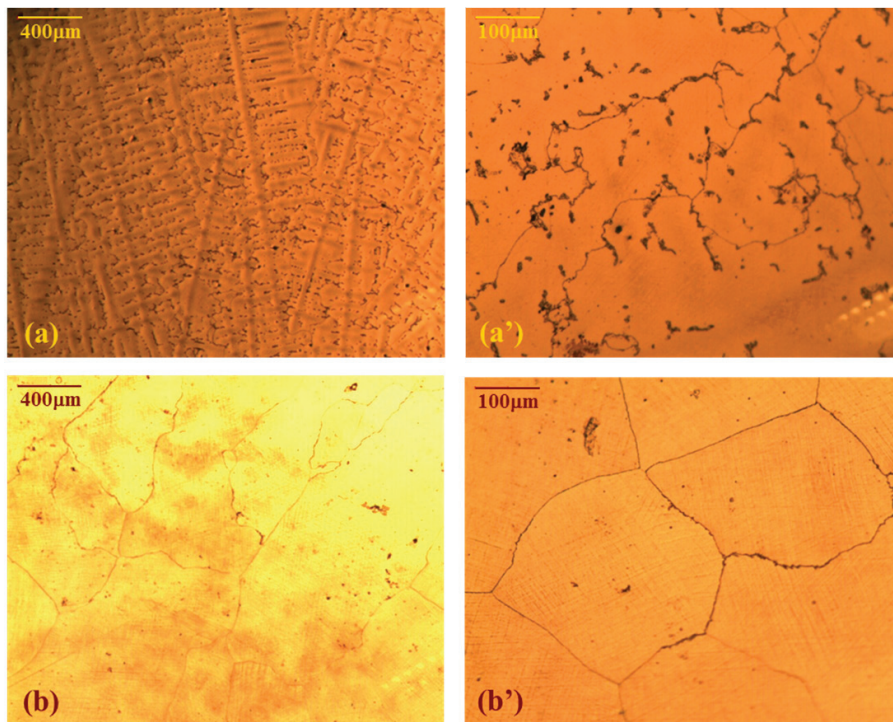
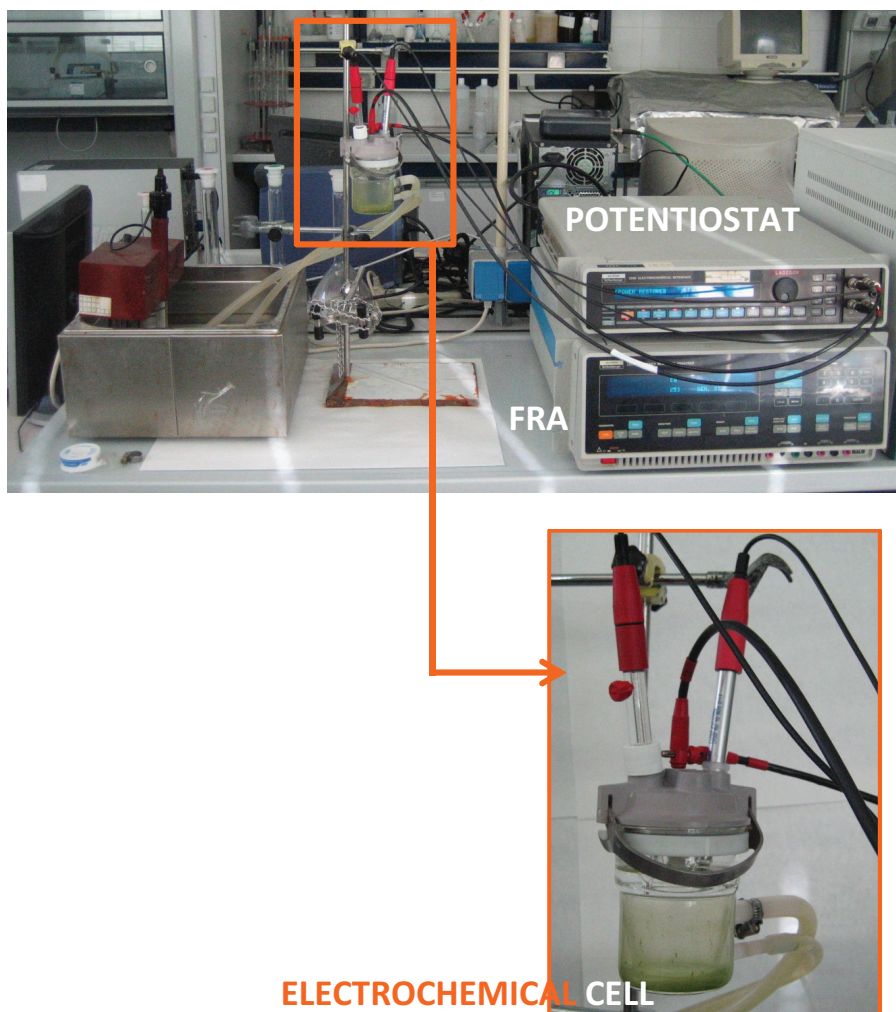


Figure 4.1. Optical images of the microstructures of the (a-a') as-cast CoCrMo alloy and (b-b') after the thermal treatment.

### 4.3. Experimental Set-up

A double-wall three-electrode cell (volume 50 ml) in aerated conditions was used for all the electrochemical measurements. The experimental set-up was shown in **Figure 4.2**. An Ag/AgCl 3-M KCl reference electrode and a platinum wire was used as counter electrode.



**Figure 4.2.** Experimental set-up.



#### CHAPTER 4. Electrochemical characterization of CoCrMo alloy in simulated body fluids

Before each experiment, the samples were mechanically polished (from 1000 to 4000 grit SiC paper), degreased with acetone, washed with pure water and dried with compressed air before use. After cleaning and rinsing the polished sample was assembled into the electrochemical cell that was subsequently filled with the electrolyte. Temperature of the solution was kept at 37°C (human body conditions).

The composition of the electrolytes employed on the electrochemical tests is:

- **NaCl:** 8 g L<sup>-1</sup> of NaCl (0.14 M) is the base solution and the salt is added in order to give conductivity to the solution.
- **NaCl+BSA:** 8 g L<sup>-1</sup> of NaCl and 0.5 g L<sup>-1</sup> of Bovine Serum Albumin (BSA, organic compound).
- **PBS:** 8 g L<sup>-1</sup> of NaCl, 0.25 g L<sup>-1</sup> of KH<sub>2</sub>PO<sub>4</sub> (1 mM), 0.2 g L<sup>-1</sup> of KCl (3 mM) and 1.44 g L<sup>-1</sup> of Na<sub>2</sub>HPO<sub>4</sub> (10 mM) (inorganic species).
- **PBS+BSA:** 8 g L<sup>-1</sup> of NaCl, 0.25 g L<sup>-1</sup> of KH<sub>2</sub>PO<sub>4</sub>, 0.2 g L<sup>-1</sup> of KCl, 1.44 g L<sup>-1</sup> of Na<sub>2</sub>HPO<sub>4</sub> and 0.5 g L<sup>-1</sup> (interaction between organic and inorganic species).
- **Bovine Serum (BS)** solution by SIGMA (which contains 30 wt.% of BSA).

All electrochemical measurements were carried out using a potentiostat Solartron 1286 and Frequency Response Analyser Solartron 1250 (**Figure 4.2**).

## 4.4. Results and Discussion

Two main sections have been considered in this chapter. The first one corresponding to the study of the influence of chemical composition of the electrolyte and the electrode potential and the second one corresponding to the study of the influence of pH and aeration conditions on the electrochemical behaviour of CoCrMo alloys.

### 4.4.1. INFLUENCE OF CHEMICAL COMPOSITION AND APPLIED POTENTIAL

The general electrochemical characterization of the alloy in different simulated body fluids and applied potentials was carried out.

#### EXPERIMENTAL PROCEDURE

Three electrochemical tests were carried out:

1) **Potentiodynamic curves** with the following experimental sequence:

- Measurement of the OCP during 10 minutes. **OCP** value was the extracted parameter and it was obtained by the average value of the OCP in the last minute of the stabilization test where the steady-state value was reached.
- Cathodic cleaning by potentiostatic test at -1.5 V during 5 minutes in order to reduce the oxide already formed on the CoCrMo alloy and to assure good reproducibility of the following measurements.
- Potentiodynamic curves obtained scanning the applied potential from -1.5 to 1.5 V (anodic direction) at the scan rate of  $2 \text{ mV s}^{-1}$  and registering the response in current. According to the  $\tau_v^*$  dimensionless time the scan rate is slow enough and allows to attain a steady state mass (Chapter 3, *Experimental techniques*). The electrochemical parameters extracted from the potentiodynamic curves are: the corrosion potential ( $E_{corr}$ ) and the corrosion current density ( $i_{corr}$ ) obtained by Tafel slope

#### CHAPTER 4. Electrochemical characterization of CoCrMo alloy in simulated body fluids

extrapolation, the passive current density ( $i_p$ ) obtained at a potential of 0.1 V and the breakdown potential ( $E_{br}$ ).

##### 2) Potentiostatic tests:

- Measurement of the OCP during 10 minutes. **OCP** value was the extracted parameter.
- Cathodic cleaning by potentiostatic test at -1.5 V during 5 minutes.
- Potentiostatic test at the applied potentials of -1, -0.5, -0.05, 0.35 and 0.75 V during 1 hour. The applied potentials were selected according to the CoCrMo potentiodynamic curves and within the different potential domains. The aim of applying potentials of the different domain allows one to characterize the interface of the biomaterial/electrolyte when different electrochemical reactions are favoured onto the CoCrMo alloy. For example, the generation of the oxide film is favoured when the potential lies within the passive domain. However, the formation of the passive film was hindered and the reduction of the media was favoured when a potential within the cathodic domain is applied. The extracted parameters were the final current density ( $i_f$ ) or passive current density ( $i_{pp}$ ) when the applied potential favours the passivation of the sample and the electrical charge ( $q$ ). The values of the current density measured at the end of the potentiostatic tests are inversely proportional to the polarization resistance of the alloy.

##### 3) Electrochemical Impedance Spectroscopy (EIS):

- EIS measurements were carried out under potentiostatic conditions (applied potentials: -1, -0.5, -0.05, 0.35 and 0.75 V) according to previous tests. Impedance measurements were performed for 10 frequency decades from 1 mHz to  $10^5$  Hz with an amplitude of  $\pm 10$  mV. The impedance data were analysed with the *Zview 2.70* software package and fitted to the corresponding equivalent electrical circuit. EIS allows one to determine the influence of the physico-chemical properties of the electrolyte (chemical composition, pH, oxygen

content) and the applied potentials on the electrochemical properties of the interface electrolyte/biomaterial.

The reproducibility of the measurements was determined through three repetitions of each electrochemical test.

4.4.1.1. OCP

The temporary evolution of the OCP in simulated body fluids is plotted in **Figure 4.3** and the average OCP values are shown in **Table 4.I**. The evolution with time of the OCP consists in a continuous shifting towards more positive values with time. The positive potential evolution indicates the formation of a protecting passivation layer on the CoCrMo alloy. This behaviour is more noticeable in the non-containing BSA solutions.

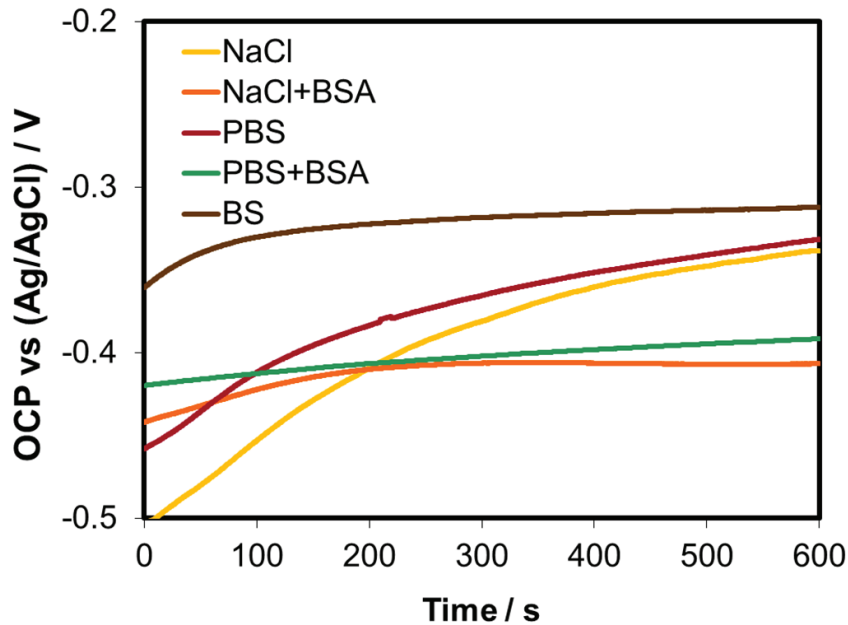


**Figure 4.3.** OCP evolution with time for CoCrMo alloy in all simulated body fluids at pH 7.4 and 37°C.

According to these results, solution chemistry significantly affects OCP of CoCrMo; BSA notably shifts towards more negative values (80 mV) the OCP of the CoCrMo. On the contrary, phosphates slightly increase OCP of the CoCrMo. It is known that BSA could act as cathodic inhibitor on CoCrMo alloys [34], thus shifting their OCP towards lower values while phosphates act as anodic inhibitor [12]. When both compounds are present in the solution, BSA action predominates on the electrochemical behaviour of this alloy. Nevertheless, OCP measurement is not sufficient to determine the real

implication of the BSA and phosphates on the electrochemical behaviour of the alloy and more advanced techniques are required.

**Table 4.I.** Average values of the OCP measurements.

OPEN CIRCUIT POTENTIAL					
SOLUTION	NaCl	NaCl+BSA	PBS	PBS+BSA	BS
OCP (mV)	-334 ± 20	-410 ± 8	-330 ± 10	-392 ± 15	-323 ± 40

#### 4.4.1.2. POTENTIODYNAMIC CURVES

Typical anodic potentiodynamic curves of the CoCrMo in all simulated body fluids are shown in **Figure 4.4**. In addition, the electrochemical parameters extracted from the potentiodynamic curves ( $E_{corr}$ ,  $i_{corr}$ ,  $i_p$  and  $E_{br}$ ) are summarized in **Table 4.II**.

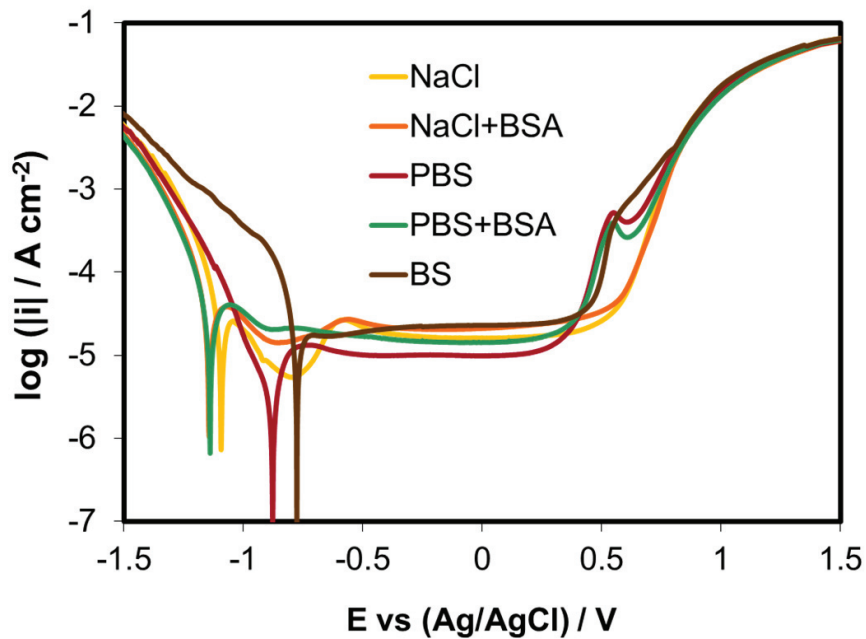


**Figure 4.4.** Potentiodynamic curves for the CoCrMo alloy in different simulated body fluids at 37°C and pH 7.4.

To facilitate interpretation the curves can be divided in four potential domains. The cathodic domain includes potentials below -1.1 V where the current is determined by the reduction of water and, partially, of dissolved oxygen since the curves were obtained under aerated conditions. In this domain BSA slightly diminishes the current while phosphate has no major effect. On the other hand, BS favours the reduction reaction of the media with high values of cathodic current density in the entire domain. The potential domain comprised between -1.2 and -0.5 V is characterized by the transition from cathodic to anodic current at the corrosion potential followed by some fluctuations of the anodic current. The presence of BSA shifts the corrosion

potentials towards more cathodic potentials while phosphate ions have an opposite effect, except in the presence of BSA. Therefore, the BSA determines the electrochemical behaviour of the alloy in this domain since it suppresses the phosphate effect. The third domain corresponds to the passive plateau and ranges from -0.5 up to 0.4 V. Phosphate ions decrease the passive current density while BSA increases it. Finally, the transpassive domain is characterized by the increase in current because of the transpassive dissolution of the chromium oxide as well as water oxidation (when the potential is above the equilibrium potential of water oxidation which corresponds approximately with 0.6 V).

Phosphate-containing solutions (with and without BSA) present a shoulder at approximately 0.6 V. Such effect can be related to the possible formation of ion-phosphate complexes (phosphate-chromium) which can activate transpassive dissolution [10]. Similar results were obtained by Hodgson et al. [11]. After the test, the CoCrMo alloy was uniformly corroded over the entire surface (uniform corrosion). No localized or pitting corrosion was observed on the alloy surface.

The effect of the BSA and phosphates in the potentiodynamic conditions can be observed in the  $E_{corr}$  and  $i_{corr}$  extracted from the anodic curves represented in **Figure 4.4**. Phosphate ions act as cathodic inhibitors as suggested by the shift of the  $E_{corr}$  towards more anodic potentials and the decrease of the  $i_{corr}$  when comparing the values in NaCl and PBS solutions (displacement of the anodic Tafel slope).

On the other hand, BSA suppresses the effect of the phosphates on the CoCrMo corrosion behaviour. BSA acts as cathodic inhibitor according to the decrease of the cathodic current observed in **Figure 4.4**. This behaviour can be explained by the presence of the adsorbed BSA that may impede the access of the oxidant to the metallic surface. In NaCl and PBS solutions, BSA displaces the  $E_{corr}$  towards more cathodic potentials and increases the  $i_{corr}$ . This behaviour suggests that BSA also acts accelerating the anodic reaction. BSA can bind to metal ions and transport them away from the solution/passive film interface, thus encouraging further dissolution [35]. Therefore, BSA has a double antagonistic role, cathodic inhibitor and anodic catalyser.



The effect of the BS on the electrochemical behaviour of the alloy was noticeable. The species of the BS favoured the acceleration of the cathodic reaction since an increase of the current density in the entire domain was registered. This effect produced a displacement of the  $E_{corr}$  towards more anodic values. No apparent modification on the anodic reaction was observed. In addition, the formation of the ion-complexes was as well observed in the transpassive domain by means of the apparition of the peak at 0.65 V. Due to the complex formulation of the BS it is difficult to determine the implication of the different compounds on the electrochemical behaviour of the alloy.

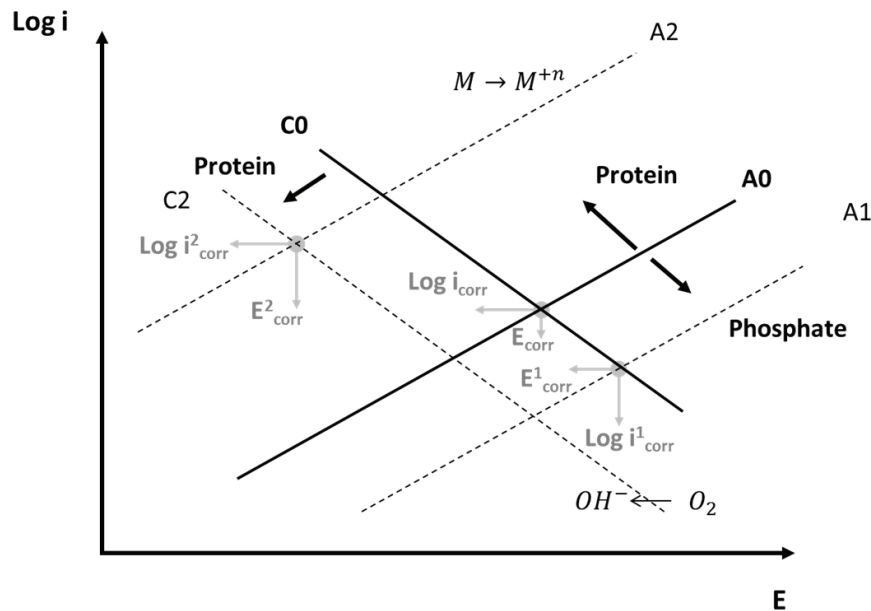


**Figure 4.5.** Mixed potential theory applied to interpret the effect of BSA and phosphates on CoCrMo corrosion potential and corrosion current density. Phosphate ions act as anodic inhibitor (displacement of the anodic branch **A0** to **A1**). The BSA acts as a cathodic inhibitor (from **C0** to **A2**) but can accelerate the anodic oxidation of the metal by binding metal ions (from **A0** to **A2**).

The Evans diagram of the mixed potential represented in **Figure 4.5** explains the combined effect of phosphate and BSA on the polarization curves of the CoCrMo alloy. The graph is semiempirical because it is built adopting the Tafel slopes corresponding

to the anodic dissolution and cathodic reactions. The presence of BSA increases the dissolution rate of the metal (from **A0** to **A2**) but at the same time reduces the cathodic current (from **C0** to **C2**). Close to the  $E_{corr}$ , the two effects compensate each other to some extent; at more anodic potentials the contribution of the cathodic current becomes negligible and BSA essentially accelerates corrosion. Phosphate adsorption decreases the anodic reaction rate (from **A0** to **A1**). Because of competitive adsorption of BSA molecules and phosphate ions, the BSA replaces adsorbed phosphate ions and thus accelerates the anodic reaction.

**Table 4.II.** Electrochemical parameters of the CoCrMo alloy in simulated body fluids.

<b>ELECTROCHEMICAL PARAMETERS</b>					
<b>SOLUTION</b>	<b>NaCl</b>	<b>NaCl+BSA</b>	<b>PBS</b>	<b>PBS+BSA</b>	<b>BS</b>
$E_{corr}$ (mV)	-1092 ± 20	-1147 ± 20	-887 ± 5	-1139 ± 10	-777 ± 10
$i_{corr}$ ( $\mu\text{A cm}^{-2}$ )	9.6 ± 1	11.5 ± 0.5	2.1 ± 0.1	11.6 ± 0.1	9.3 ± 0.7
$i_p$ ( $\mu\text{A cm}^{-2}$ )	16.2 ± 0.8	20.9 ± 1.1	10.2 ± 0.6	14.4 ± 0.6	22.9 ± 1.2
$E_{pr}$ (mV)	517 ± 12	562 ± 15	327 ± 21	378 ± 26	437 ± 25
$b_a$ (mV)	157 ± 5	130 ± 12	110 ± 20	189 ± 18	243 ± 30
$b_c$ (mV)	-83 ± 2	-75 ± 7	-156 ± 18	-86 ± 7	-85 ± 5

#### 4.4.1.3. POTENTIOSTATIC TESTS

Potentiostatic measurements were carried out in order to evaluate the effect of potential on the corrosion kinetics of the CoCrMo alloy. Thus, potentials lying within the four potential domains were selected: -1 V for the cathodic domain, -0.5 V for the anodic-cathodic transition domain, -0.05 V and 0.35 V for the passive domain and 0.75 V for the transpassive domain. The selected potentials used for carrying out the potentiostatic tests in all simulated body fluids were specified in **Figure 4.6**.

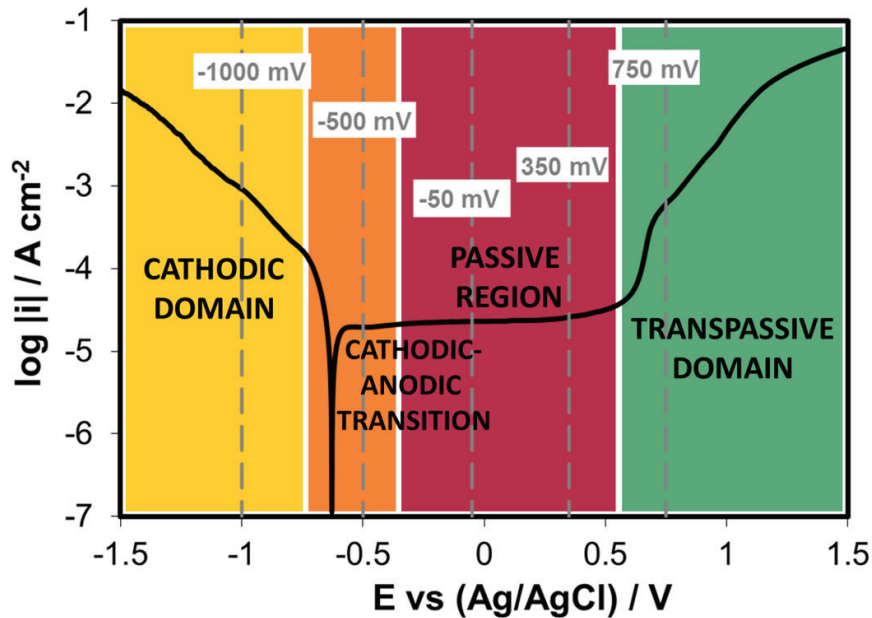


**Figure 4.6.** Typical potentiodynamic curve of a CoCrMo alloy with the selected applied potentials for the potentiostatic and EIS tests.

The temporary evolution of the current density was represented for each applied potential in all simulated body fluids in order to evaluate the influence of the chemical composition of the media in the different electrochemical reactions.

#### A) CATHODIC DOMAIN

At -1 V, potential which lies within the cathodic domain, the overall current is dominated by the cathodic reaction as consequence of reduction of water and dissolved oxygen (Figure 4.7). The values of the  $i_f$  and  $q$  obtained from the potentiostatic tests are summarized in Table 4.III. For this reason the current density was negative from the beginning of the test. The same behaviour was observed by Hodgson et al. [11] when applied a potential under similar conditions in a CoCrMo alloy.

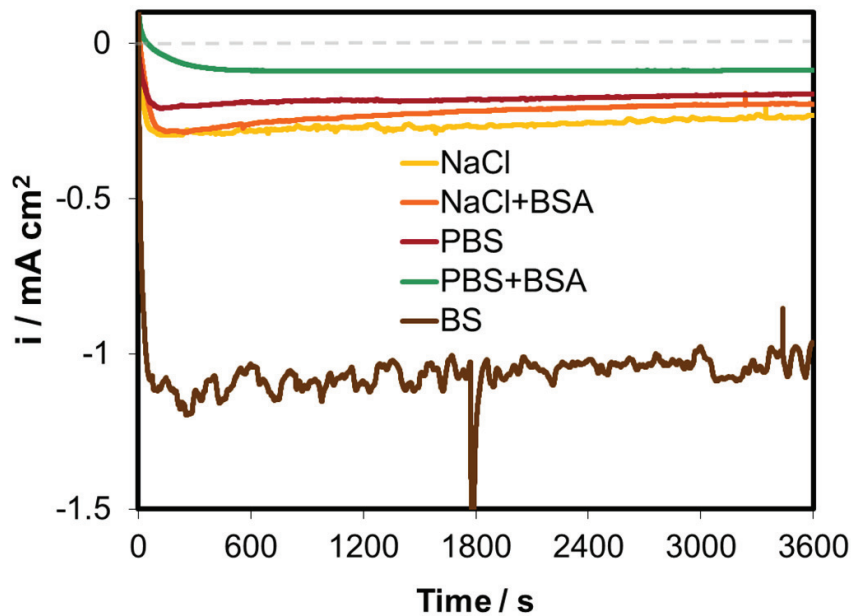


Figure 4.7. Potentiostatic measurements of the CoCrMo alloy after 1 hour of immersion at -1 V in all simulated body fluids.

It is observed that the BS favours the reduction reaction obtaining the highest values in the  $i_f$  ( $-0.97 \text{ mA cm}^{-2}$ ) and the cathodic electrical charge ( $-3828 \text{ mC cm}^{-2}$ ).

The cathodic inhibition effect of the BSA, previously described in the potentiodynamic curves, is also observed in these potentiostatic tests. In the BSA-containing solutions a decrease of the  $i_f$  is observed: from  $-0.23$  to  $-0.20 \text{ mA cm}^{-2}$  in saline solution and from

**CHAPTER 4.** Electrochemical characterization of CoCrMo alloy in simulated body fluids

-0.16 to -0.09 mA cm<sup>-2</sup> in phosphate solution. According to these results, the presence of phosphate ions in the solution also decreased the  $i_f$  values. Although the cathodic inhibition effect of the phosphate ions is not observed in the potentiodynamic curves, the potentiostatic tests clearly show that the phosphate ions can act reducing the cathodic current density probably by adsorption.

**Table 4.III.** Electrochemical parameters extracted from the potentiostatic tests at -1 V of CoCrMo alloy in simulated body fluids.

<b>ELECTROCHEMICAL PARAMETERS</b>					
<b>SOLUTION</b>	<b>NaCl</b>	<b>NaCl+BSA</b>	<b>PBS</b>	<b>PBS+BSA</b>	<b>BS</b>
$i_f$ (mA cm <sup>-2</sup> )	-0.23 ± 0.01	-0.20 ± 0.02	-0.16 ± 0.01	-0.09 ± 0.00	-0.97 ± 0.10
$q$ (mC cm <sup>-2</sup> )	-943 ± 50	-801 ± 25	-645 ± 35	-300 ± 12	-3828 ± 120

## B) CATHODIC-ANODIC TRANSITION

The potentiostatic tests carried out at -0.5 V in all simulated body fluids are shown in the **Figure 4.8**. When the selected potential belongs to the cathodic-anodic transition (-0.5 V) a change in the sign of the current density takes place. Initially, an abrupt increase in the current density is observed before current stabilization as a consequence of the passive film formation. After certain time the current density becomes negative which means that the reduction reaction is favoured on the CoCrMo alloy. The values of the final current density reached and the electrical charge (separated in the cathodic and anodic charge) were summarized in **Table 4.IV**.

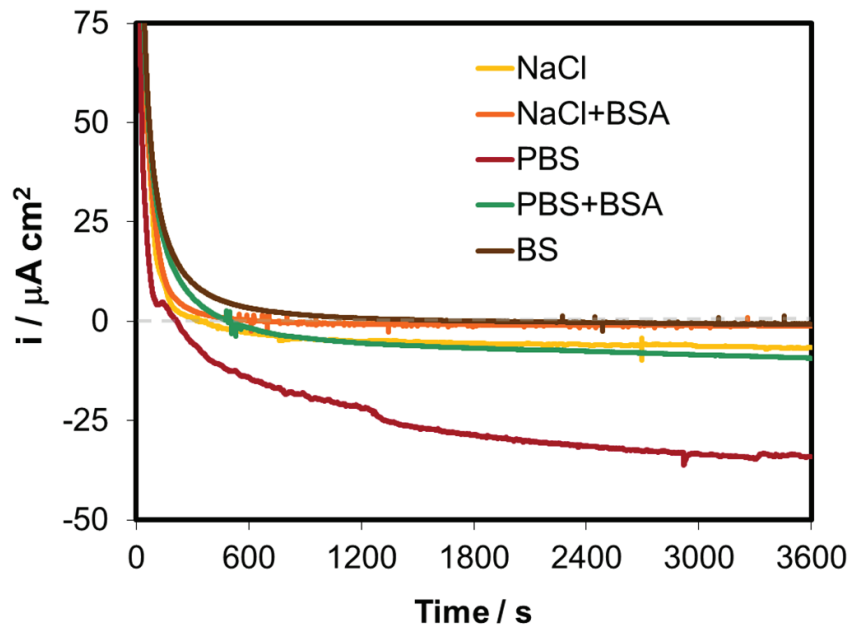


**Figure 4.8.** Potentiostatic measurements of the CoCrMo alloy after 1 hour of immersion at -0.5 V in all simulated body fluids.

**Table 4.IV.** Electrochemical parameters extracted from the potentiostatic tests at -0.5 V of CoCrMo alloy in simulated body fluids.

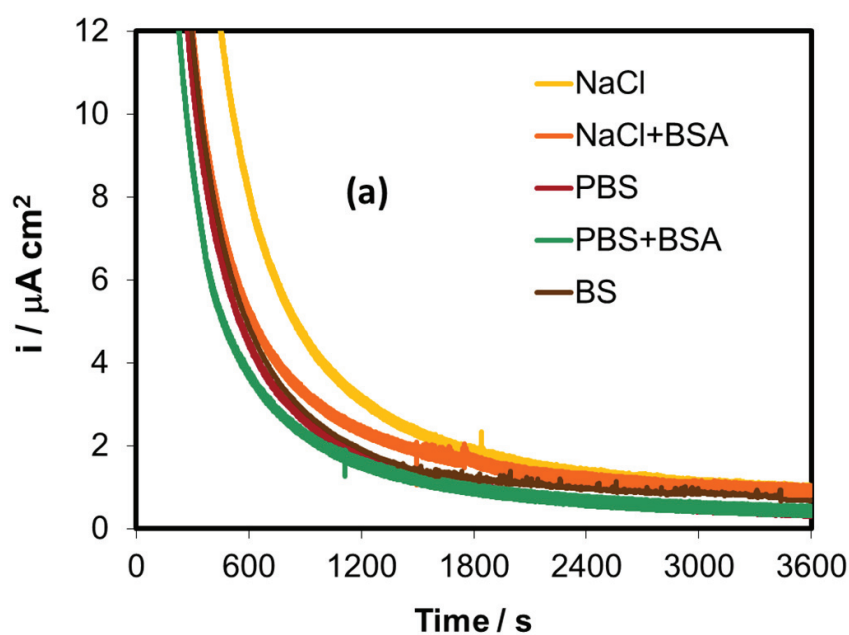
ELECTROCHEMICAL PARAMETERS					
SOLUTION	NaCl	NaCl+BSA	PBS	PBS+BSA	BS
$i_f (\mu\text{A cm}^{-2})$	$-6.7 \pm 0.2$	$-1.2 \pm 0.1$	$-33.7 \pm 0.5$	$-9.2 \pm 0.3$	$-0.7 \pm 0$
$q_+ (\text{mC cm}^{-2})$	$14.4 \pm 1.2$	$12.8 \pm 0.7$	$7.1 \pm 0.4$	$15.0 \pm 2.1$	$20.8 \pm 1.5$
$q_- (\text{mC cm}^{-2})$	$-17.1 \pm 1.5$	$-2.5 \pm 0.3$	$-88.3 \pm 10.1$	$-20.7 \pm 2.1$	$-0.8 \pm 0$

The BSA displaces the inversion of the current density sign towards higher immersion times (around 700 s). This displacement was enhanced in presence of BS (1850 s) where the highest value of anodic charge ( $20.8 \text{ mC cm}^{-2}$ ) was registered during the potentiostatic test. Similar behaviour was obtained for the CoCrMo alloy in NaCl+BSA solution.

The highest cathodic current density is reached in the PBS solution ( $-33.7 \mu\text{A cm}^{-2}$ ) which can be explained by the displacement of the  $E_{corr}$  towards more anodic potentials in the potentiodynamic curve (**Figure 4.4**). Thus, in presence of phosphates the electrochemical reactions at -0.5 V corresponds to the cathodic domain generating high values of cathodic charge ( $-88.3 \text{ mC cm}^{-2}$ ). This behaviour can be explained because of the phosphate ions act as catalyser of water reduction into hydrogen [36]. However, the presence of BSA supresses this effect and the value of the cathodic  $i_f$  considerably diminishes in the test carried out in PBS+BSA ( $-9.2 \mu\text{A cm}^{-2}$ ).

### C) PASSIVE DOMAIN

In order to characterize the electrochemical behaviour of the alloy under passive conditions two potentials lying within the passive domain were selected. The potentials were -0.05 and 0.35 V which corresponds to the lower and higher passive domain respectively. These potentiostatic tests in all simulated body fluids were shown in **Figure 4.9 (a)** and **(b)**. The values of the  $i_{pp}$  registered at both potentials were summarized in **Table 4.V**. The current transient at the beginning of the test is typical from a passivation process under potentiostatic conditions. When applying a passive potential, the current density increases abruptly until a maximum value and then exponentially diminishes until reaching a constant value. Once the material is passivated, the value of the current density remains constant and stable ( $i_{pp}$ ). The main difference in the current measurements between both potentials was observed in the current transient and in the final value. Generally, higher values of  $i_{pp}$  and  $q$  were registered for the potentiostatic tests carried out at the potential of 0.35 V in all solutions.





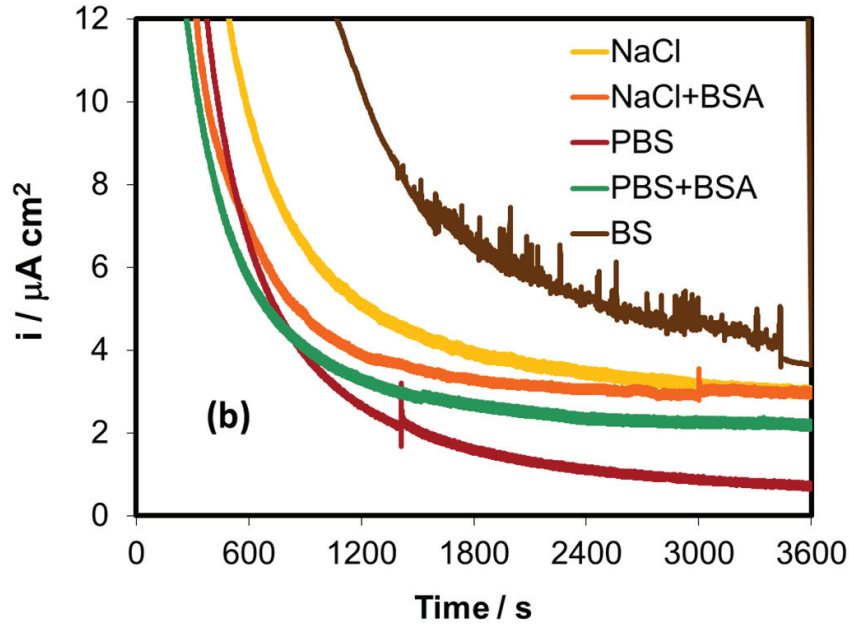


Figure 4.9. Potentiostatic measurements of the CoCrMo alloy after 1 hour of immersion at (a) -0.05 V and (b) 0.35 V in all simulated body fluids.

Table 4.V. Electrochemical parameters extracted from the potentiostatic tests at -0.05 and 0.35 V of CoCrMo alloy in simulated body fluids.

ELECTROCHEMICAL PARAMETERS						
SOLUTION	PASSIVE POTENTIAL	NaCl	NaCl+BSA	PBS	PBS+BSA	BS
$i_{pp}$ ( $\mu\text{A cm}^{-2}$ )	-0.05 V	$0.91 \pm 0.05$	$0.84 \pm 0.05$	$0.34 \pm 0.02$	$0.30 \pm 0.01$	$0.67 \pm 0.15$
	0.35 V	$2.95 \pm 0.10$	$2.95 \pm 0.12$	$0.74 \pm 0.07$	$2.29 \pm 0.31$	$12.17 \pm 1.20$
$q$ ( $\text{mC cm}^{-2}$ )	-0.05 V	$47.5 \pm 0.5$	$34.2 \pm 0.7$	$22.7 \pm 0.5$	$18.9 \pm 1.2$	$25.3 \pm 0.4$
	0.35 V	$60.3 \pm 0.6$	$45.3 \pm 1.2$	$37.6 \pm 1.0$	$29.3 \pm 3.2$	$137.1 \pm 20.1$

The  $i_{pp}$  values reached in the potentiostatic tests (Table 4.V) lie within the typical average values of the bulk CoCrMo alloy presented in a CoCrMo alloy Round Robin [37].

At both potentials, phosphate ions act decreasing the value of the  $i_{pp}$ . Nevertheless, the behaviour of the BSA depends on the potential and varies with solution chemistry. At -0.05 V, BSA slightly decreases the values of the  $i_{pp}$  and the  $q$  with and without presence of phosphate ions. However, the opposite effect is observed at 0.35 V where the value of the  $i_{pp}$  considerably increases in presence of phosphates. These results demonstrated that the effect of the BSA adsorption under passive conditions depends on the surface properties (applied potential) and on the interaction of the compounds present in the electrolyte (phosphates).

The behaviour of the CoCrMo alloy in presence of BS also varies with the applied passive potential. At -0.05 V, the low value of  $i_{pp}$  and  $q$  shows that the BS acts blocking the surface and increasing the corrosion resistance of the alloy. Nevertheless, at 0.35 V the high values of passive current density during the potentiostatic test indicate that the BS favours the passive dissolution of the alloy. The highest values of  $i_{pp}$  ( $12.17 \text{ mA cm}^{-2}$ ) and  $q$  ( $131.1 \text{ mC cm}^{-2}$ ) were obtained in this BS solution.

D) TRANSPASSIVE DOMAIN

The potentiostatic tests carried out at the transpassive potential of 0.75 V in all simulated body fluids are plotted in the **Figure 4.10**. In this domain high positive current densities were measured. It can be observed an initial anodic current peak at the beginning of the test and an stabilization before 600 s with the progressive increase of the current density during the potentiostatic test. An exception to this behaviour was observed in the test carried out in BS where a huge increase of the current was detected after the first anodic current peak. At this potential the anodic dissolution of the oxide layer took place since high values of current density was registered. According to Hodgson et al. [11] two parallel reactions take place on the surface of the material: the passivation (initial current peak) and the anodic reaction of chromium species ( $\text{Cr}^{+6}$ ) determined by the continuous increase of the current after the first anodic current peak.

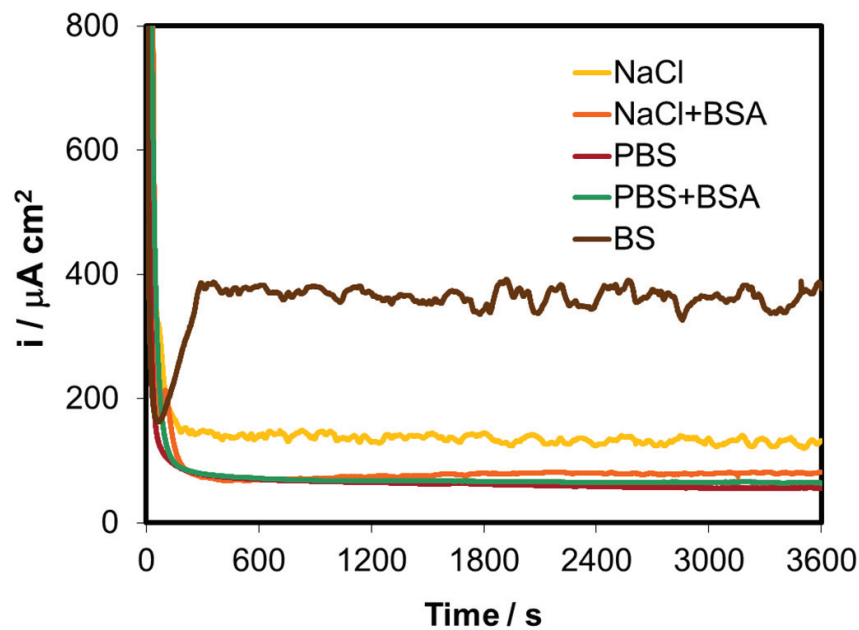


**Figure 4.10.** Potentiostatic measurements of the CoCrMo alloy after 1 hour of immersion at 0.75 V in all simulated body fluids.

The  $i_f$  and  $q$  obtained after 1 hour of immersion at the transpassive potential in all simulated body fluids were summarized in **Table 4.VI**.

According to these results, it is possible to observe that the adsorbed species (BSA and phosphates) hindered the transpassive oxidation of the oxide film (lower values of  $i_f$ ). This behaviour was enhanced in PBS containing solutions probably because of complex-phosphate formation. As already commented in the potentiodynamic curves, at this potential, the generation of metal complexes was favoured.

On the other hand, the chemical composition of the BS has an opposite effect favouring the transpassive oxidation. In this solution, high values of  $i_f$  ( $377 \mu\text{A cm}^{-2}$ ) and  $q$  ( $1303 \text{ mC cm}^{-2}$ ) were obtained.

**Table 4.VI.** Electrochemical parameters extracted from the potentiostatic tests at 0.75 V of CoCrMo alloy in simulated body fluids.

ELECTROCHEMICAL PARAMETERS					
SOLUTION	NaCl	NaCl+BSA	PBS	PBS+BSA	BS
$i_f (\mu\text{A cm}^{-2})$	$132 \pm 10$	$81 \pm 4$	$56 \pm 3$	$64 \pm 8$	$377 \pm 28$
$q (\text{mC cm}^{-2})$	$583 \pm 35$	$417 \pm 25$	$262 \pm 12$	$318 \pm 15$	$1303 \pm 120$

#### 4.4.1.4. ELECTROCHEMICAL IMPEDANCE SPECTROSCOPY

Electrochemical impedance spectroscopy was used to investigate the film/electrolyte-interface on the CoCrMo alloy in different simulated body fluids. EIS was measured under potentiostatic conditions at the same applied potentials of the previous potentiostatic tests. The impedance spectra, in form of Nyquist diagrams and Bode plots, are shown at each applied potential and all simulated body fluids.

##### A) CATHODIC DOMAIN

The EIS spectra obtained at the cathodic potential of -1 V are shown in the Nyquist diagram (**Figure 4.11(a)**) and Bode plot (**Figure 4.11(b)**). This cathodic potential favours the reduction reaction of the media (mainly water and different compounds present in the BS).

From the impedance spectra, the presence of two time constants were clearly observed in all simulated body fluids which are well differentiated in the Nyquist diagram by two semicircles and by the consequent slope change in the Bode plots (representation of the impedance magnitude). Two *RC* circuits in series were proposed to model the impedance spectra (**Figure 3.10(b)**, Chapter 3). The first time constant (outer, higher frequencies) is attributed to the double layer composed by the charge transfer resistance ( $R_{out}$ )/double layer capacitance ( $C_{out}$ ) parallel combination while the second time constant (inner, lower frequencies) is related to the oxide film formed on the CoCrMo alloy represented by the resistance oxide ( $R_{in}$ )/capacitance ( $C_{in}$ ) in parallel combination.

It is important to note that although the cathodic potential hindered the formation of the oxide film, the time constant resistance obtained at low frequencies indicates that this potential is not sufficient to reduce all the oxide film previously formed on the CoCrMo alloy during the sample stabilization at OCP.

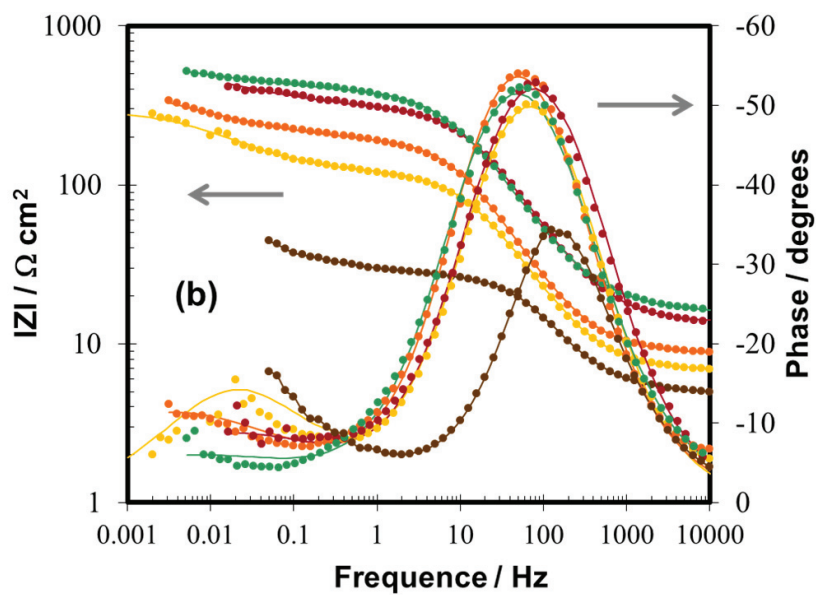
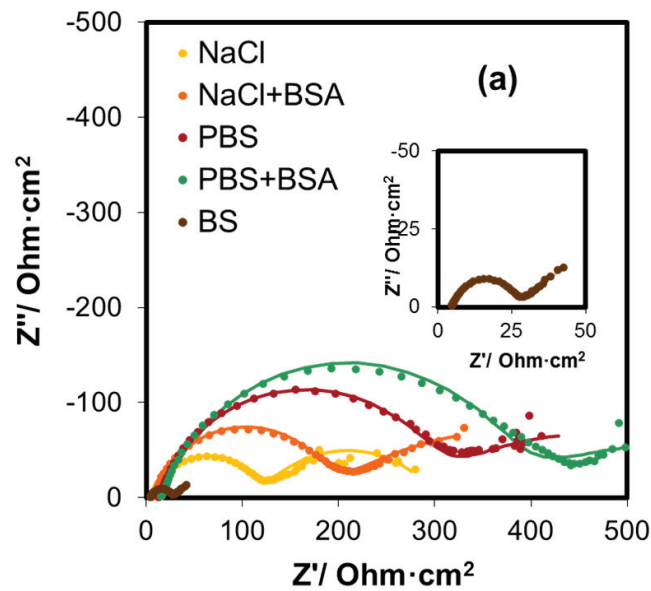


**Figure 4.11.** (a) Nyquist diagrams and (b) Bode plots of the CoCrMo alloys after 1 hour of immersion at -1 V (cathodic domain) in simulated body fluids at 37°C and pH 7.4.

#### CHAPTER 4. Electrochemical characterization of CoCrMo alloy in simulated body fluids

In the EEC the *constant phase element (CPE)* is included to replace the ideal capacitor considering the non-ideal behaviour of the capacitive elements.

The EIS spectra obtained in BS show a *Warburg-like behaviour*. The impedance data were fitted to the equivalent circuit presented in **Figure 4.12** which is modified from the previous one (**Figure 3.10(b)**) including the Warburg element into the circuit. The elements of the equivalent circuit proposed are  $R_s$  (solution resistance),  $CPE_{out}$  (constant phase element of the double layer),  $R_{out}$  (charge transfer resistance of the outer layer) and  $W$  (Warburg element) related to mass transport limitation by diffusion [38-41]. The high frequencies loop can be attributed to the charge transfer which takes place at the interface determining the impedance. The low frequencies loop is relative to the diffusion phenomena of dissolved oxygen from the electrolyte to the interface. The Warburg element indicates mass transport limitation by the dominate diffusion process.

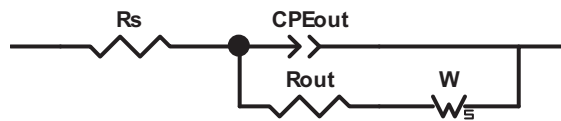


**Figure 4.12.** Equivalent Electrical Circuit for the analysis of impedance spectra of CoCrMo alloy under cathodic conditions in BS.

The theoretical simulated impedance parameters for the CoCrMo alloy under cathodic conditions in simulated body fluids were computed and are summarized in **Table 4.VII**. In addition, the fitted spectra are represented over the experimental data in **Figure 4.11** for each simulated body fluid in solid lines. The superposed representations and the low error values ( $\chi^2 \leq 10^{-4}$ ) corroborate the good fitting of the experimental data.

**Table 4.VII.** Equivalent Electrical circuit parameters of CoCrMo alloy in the studied solutions under cathodic conditions (-1 V) at 37°C and pH 7.4.

<b>ELECTROCHEMICAL PARAMETERS</b>					
<b>-1 V</b>					
	<b>NaCl</b>	<b>NaCl+BSA</b>	<b>PBS</b>	<b>PBS+BSA</b>	<b>BS</b>
$R_s (\Omega \text{ cm}^2)$	6.5 ± 0.2	8.8 ± 0.7	12.0 ± 1.4	16 ± 1.4	5.2 ± 0.4
$R_{out} (\Omega \text{ cm}^2)$	172 ± 15	341 ± 88	671 ± 90	626 ± 90	23 ± 3
$CPE_{out} (\Omega^{-1} \text{ s}^n \text{ cm}^{-2})10^6$	34.3 ± 3.5	23.1 ± 0.7	11.1 ± 2.7	20.8 ± 5.2	277 ± 25
$n_{out}$	0.63 ± 0.01	0.44 ± 0.01	0.45 ± 0.01	0.51 ± 0.05	0.84 ± 0.01
$C_{out} (\mu\text{F cm}^{-2})$	13.8 ± 1.7	2.8 ± 0.6	1.2 ± 0.2	9.5 ± 3	76.6 ± 15
$R_{in} (\Omega \text{ cm}^2)$	137 ± 36	169 ± 5	287 ± 5	609 ± 100	249 ± 2.1
$CPE_{in} (\Omega^{-1} \text{ s}^n \text{ cm}^{-2})10^6$	224 ± 37	191 ± 14	98 ± 1	135 ± 24	-
$n_{in}$	0.83 ± 0.02	0.87 ± 0.01	0.84 ± 0.01	0.80 ± 0.05	-
$C_{in} (\mu\text{F cm}^{-2})$	108.4 ± 8.1	111.7 ± 5.3	48.1 ± 1.4	70.9 ± 12.9	-
$W-R (\Omega \text{ cm}^2)$	-	-	-	-	91 ± 26

The low values of  $R_{in}$  indicate that the oxide film was partially reduced during the pre-conditioning cathodic potentiostatic test. In presence of BSA the Polarization Resistance ( $R_p$ ) of the alloy and  $C_{out}$  decreased one order of magnitude with respect to the results obtained in NaCl solution. These results are in good agreement with the potentiostatic measurements where a decrease of the current density was observed at -1 V. Thus, it can be concluded that the protein adsorption hindered the reduction reaction evolution acting as a cathodic inhibitor. In addition, the inhibition effect of phosphates can be also observed by the huge increase of the  $R_{out}$  and the decrease of the  $C_{out}$  which is enhanced when both species (BSA and phosphates) are present in the solution. On the other hand, the  $R_p$  decreases in BS since the reduction reaction was favoured although the process was limited by diffusion. In the potentiostatic test, the presence of BS favoured the reduction reaction giving high values of current density which indicated low resistance of electron flow through the CoCrMo alloy interface with respect the other studied solutions. Therefore, in BS the charge transfer reaction is faster and favoured by the media; however the accessibility of oxidant and/or the migration of the reduced species into the bulk solution are slower which limits the electrochemical reaction on the electrode surface.



#### B) CATHODIC-ANODIC TRANSITION

The EIS results obtained at the transition potential between cathodic-anodic domains are represented in **Figure 4.13**. The two time constants are clearly observed for the spectra obtained at -0.5 V therefore the EEC in **Figure 3.10(b)** (Chapter 3) was used to interpret the impedance results. **Table 4.VIII** shows the electrical parameters obtained after fitting the experimental data to the proposed model.

The EIS spectra obtained in PBS are in good agreement with the potentiostatic test since the lowest value of  $R_p$  and the highest value of cathodic  $i_f$  were reached respectively.

The impedance spectra obtained in BS shows that probably different electrochemical mechanism occurs on the electrode surface in comparison with the other studied solutions. The second time constant (inner layer) is two orders of magnitude higher than the first time constant (outer layer) which indicates that the limiting process was related to the inner layer reactions.

According to the parameters of the **Table 4.VIII** the main differences between the CoCrMo alloy behaviour in all solutions are in terms of the inner layer. Thus, a thinner passive layer was obtained after the potentiostatic test at -0.5 V which is reflected by the high value of  $C_{in}$  in comparison with the standard capacitance values of passive layers [14,38,42]. This decrease of the oxide film thickness could be due to its electrochemical reduction.

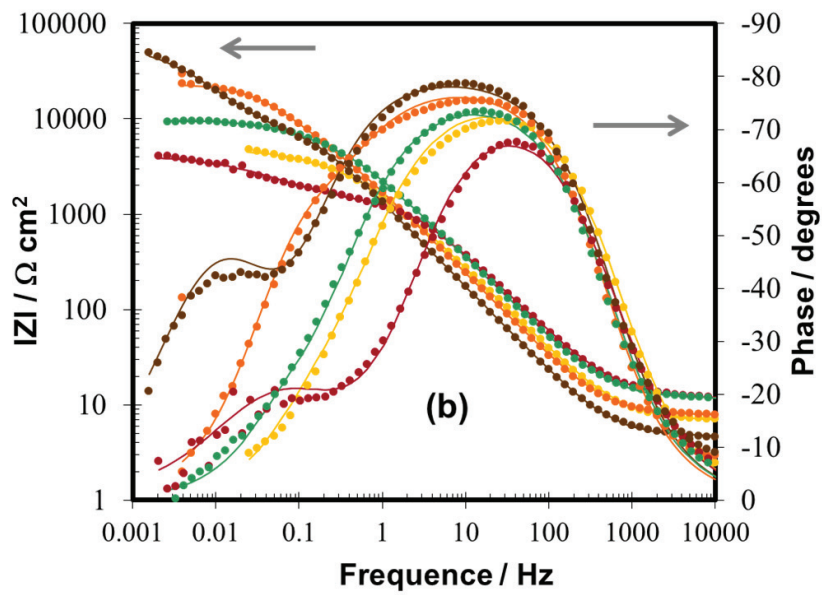
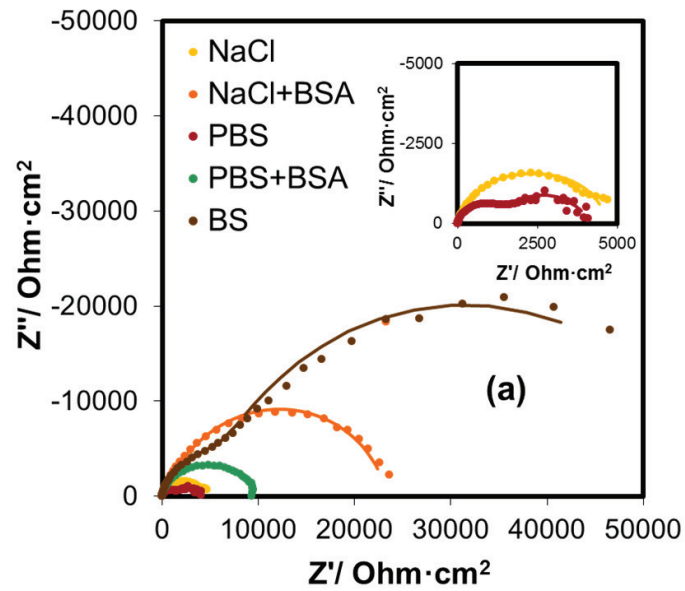


Figure 4.13. (a) Nyquist diagrams and (b) Bode plots of the CoCrMo alloys after 1 hour of immersion at -0.5 V (cathodic-anodic transition) in simulated body fluids at 37°C and pH 7.4.

**Table 4.VIII.** Equivalent electrical circuit parameters of CoCrMo alloy in the studied solutions in the cathodic-anodic transition domain (-0.5 V) at 37°C and pH 7.4.

ELECTROCHEMICAL PARAMETERS					
-0.5 V					
	NaCl	NaCl+BSA	PBS	PBS+BSA	BS
$R_s (\Omega \text{ cm}^2)$	7.2 ± 0.5	8.1 ± 0.1	12.7 ± 1.5	12.3 ± 0.9	5.2 ± 0.7
$R_{out} (\text{k}\Omega \text{ cm}^2)$	2.1 ± 0.2	1.4 ± 0.2	3.9 ± 0.0	3.8 ± 0.3	5.8 ± 0.5
$CPE_{out} (\Omega^{-1} \text{ s}^n \text{ cm}^{-2})10^6$	761 ± 100	271 ± 58	1259 ± 23	1138 ± 525	188 ± 4
$n_{out}$	0.86 ± 0.04	0.86 ± 0.02	0.67 ± 0.02	0.92 ± 0.02	0.92 ± 0.01
$C_{out} (\mu\text{F cm}^{-2})$	325 ± 39	107 ± 43	164 ± 28	756 ± 309	103 ± 13
$R_{in} (\text{k}\Omega \text{ cm}^2)$	2.8 ± 0.1	14.9 ± 9.7	1.4 ± 0.1	7.2 ± 1.7	43.2 ± 13.2
$CPE_{in} (\Omega^{-1} \text{ s}^n \text{ cm}^{-2})10^6$	126 ± 7	171 ± 5	75 ± 4	91 ± 2	586 ± 82
$n_{in}$	0.85 ± 0	0.89 ± 0.02	0.86 ± 0.01	0.84 ± 0.01	0.83 ± 0.01
$C_{in} (\mu\text{F cm}^{-2})$	105 ± 8	190 ± 13	52 ± 5	84 ± 5	115 ± 16

In order to verify if the passive film formed on the CoCrMo is reduced when applying a constant potential of -0.5 V long-term tests were done: potentiostatic tests at OCP and at -0.5 V were carried out for 24 hours and EIS tests were carried out after the immersion period of those 24 hours at the selected applied potentials.

**Figure 4.14(a)** shows the impedance results for the CoCrMo alloy in BS at OCP (-0.36 V) and at -0.5 V after 24 hours of immersion. The  $R_p$  of the samples was lower at the applied potential of -0.5 V than at OCP (1.6 and 2.9  $\text{k}\Omega \text{ cm}^2$  respectively). Therefore, it can be concluded that the passive layer was partially reduced at -0.5 V. In addition, the OCP was also measured before and after the long term tests ( $E=-0.5 \text{ V}$ ). **Figure 4.14(b)** shows the OCP evolution during 10 minutes before and after the 24 hours test at -0.5 V. OCP average value at the end of the test was more active than at the beginning, which is in good agreement with the impedance results and the thinning of the passive layer.

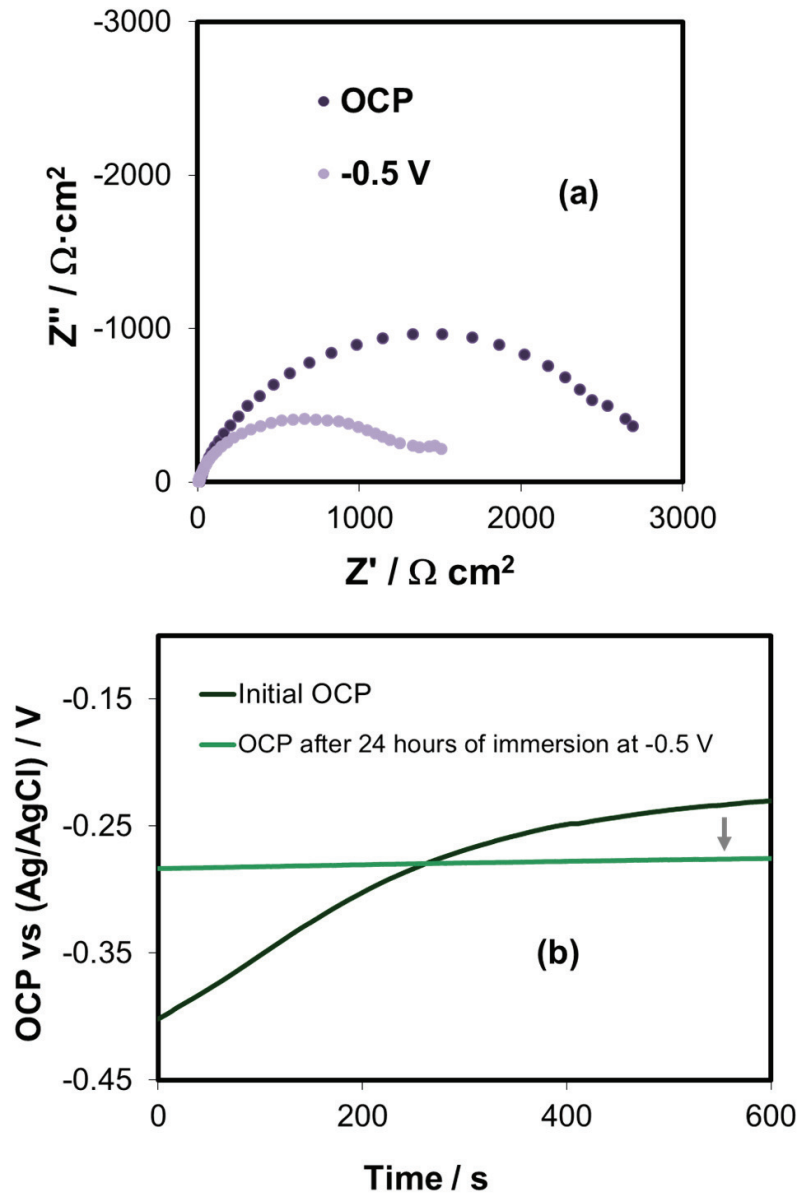


**Figure 4.14.** (a) Nyquist plot at OCP and -0.5 V (transition potential) after 24 h of immersion. (b) Evolution of the OCP before and after the potentiostatic measurements of CoCrMo alloy for 24 h at -0.5 V in bovine serum solution at 37°C and pH 7.4.

#### CHAPTER 4. Electrochemical characterization of CoCrMo alloy in simulated body fluids

These results implies that the reduction process of the oxide layer occurs more intensely in absence of BSA, possibly related to the adsorption of BSA which slows down this reduction reaction. This was corroborated by the increase of the  $R_{in}$  in the tests carried out in presence of protein (from 2.8 to 14.9  $k\Omega\text{ cm}^2$  in saline solutions and from 1.4 to 7.2  $k\Omega\text{ cm}^2$  in phosphate containing solutions). Therefore, the electrical parameters extracted from the EIS data also support the statement that the shift of the current density sign is consequence of the superposing cathodic reaction of the media over the anodic reaction. Under these electrochemical conditions the reduction of the media takes place since the reduction of the Cr present in the oxide film was not thermodynamically favoured [43].

### C) PASSIVE DOMAIN

The impedance spectra obtained under passive conditions at the potential of -0.05 V and 0.35 V in the different simulated body fluids are represented in **Figure 4.15** and **Figure 4.16** respectively. The study of the alloy under passive conditions is the most relevant since CoCrMo alloy is found passivated when implanted into the human body.

Two superposed time constants were observed in the Nyquist diagrams and Bode plots plotted in **Figure 4.15** and **4.16** (only one semi-arc in the Nyquist diagram). Thus, the EEC selected to model the experimental results consist of two subcircuit *RC* disposed in series where each subcircuit *RC* corresponds to one time constant. The outer element is related to the Helmholtz layer on the electrode surface and the inner is related to the oxide film (described in Chapter 3, *Experimental techniques*). The values of the electrical parameters obtained after fitting the experimental results to the selected EEC is shown in **Table 4.IX**. In addition, the polarization resistance ( $R_p$ ) of the CoCrMo alloy in the simulated body fluids at both passive potentials is represented in **Figure 4.17**.

Impedance spectra clearly exhibited a passive behaviour of the alloy reaching values of  $R_p$  between 0.2 and  $1\text{M}\Omega\text{ cm}^2$ . Influence of the chemical composition of the electrolyte and of the applied potential can be observed.

In the passive domain, the EIS spectra showed different features in presence of BSA. BSA shifted the phase angle towards lower frequencies. This behaviour is observed with and without phosphates. In addition, phosphates increased the corrosion resistance of the alloy.

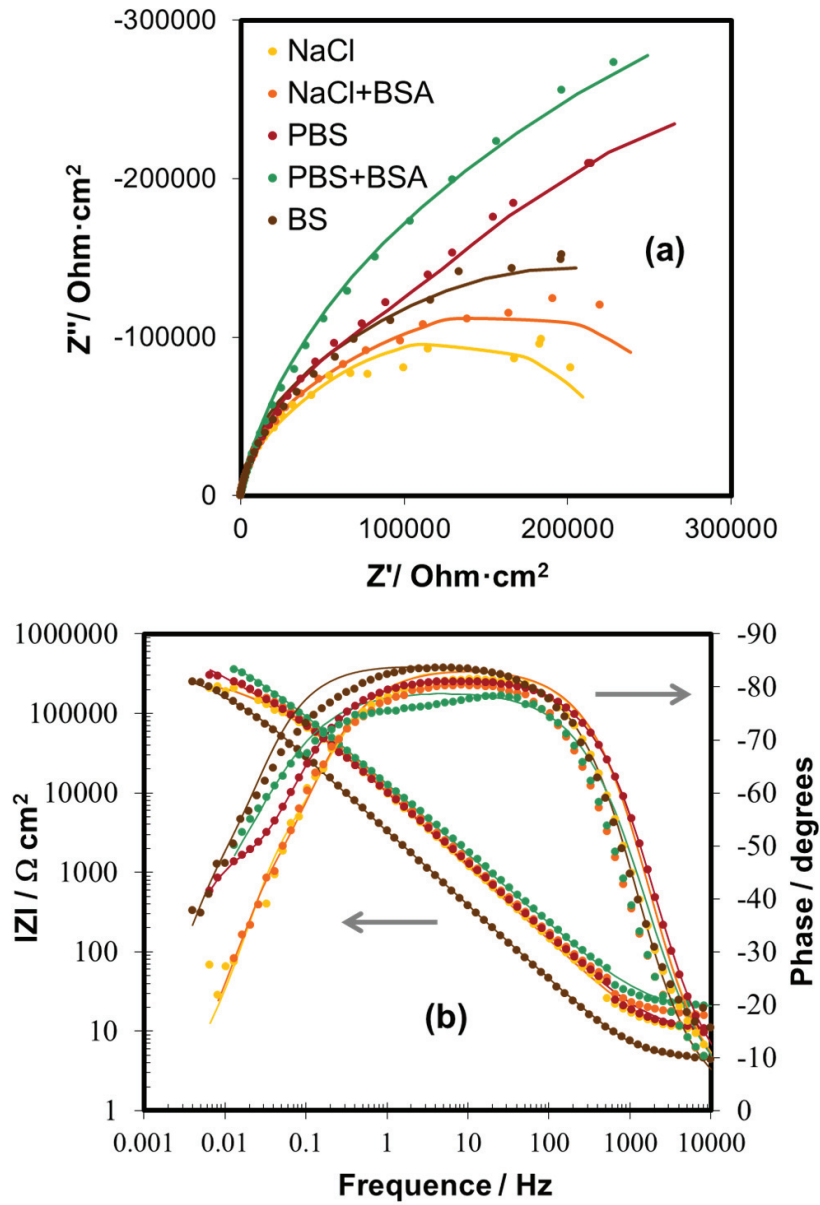


Figure 4.15. (a) Nyquist diagram and (b) Bode plot of the CoCrMo alloy after 1 hour of immersion at -0.05 V in different simulated body fluids at 37°C and pH 7.4.

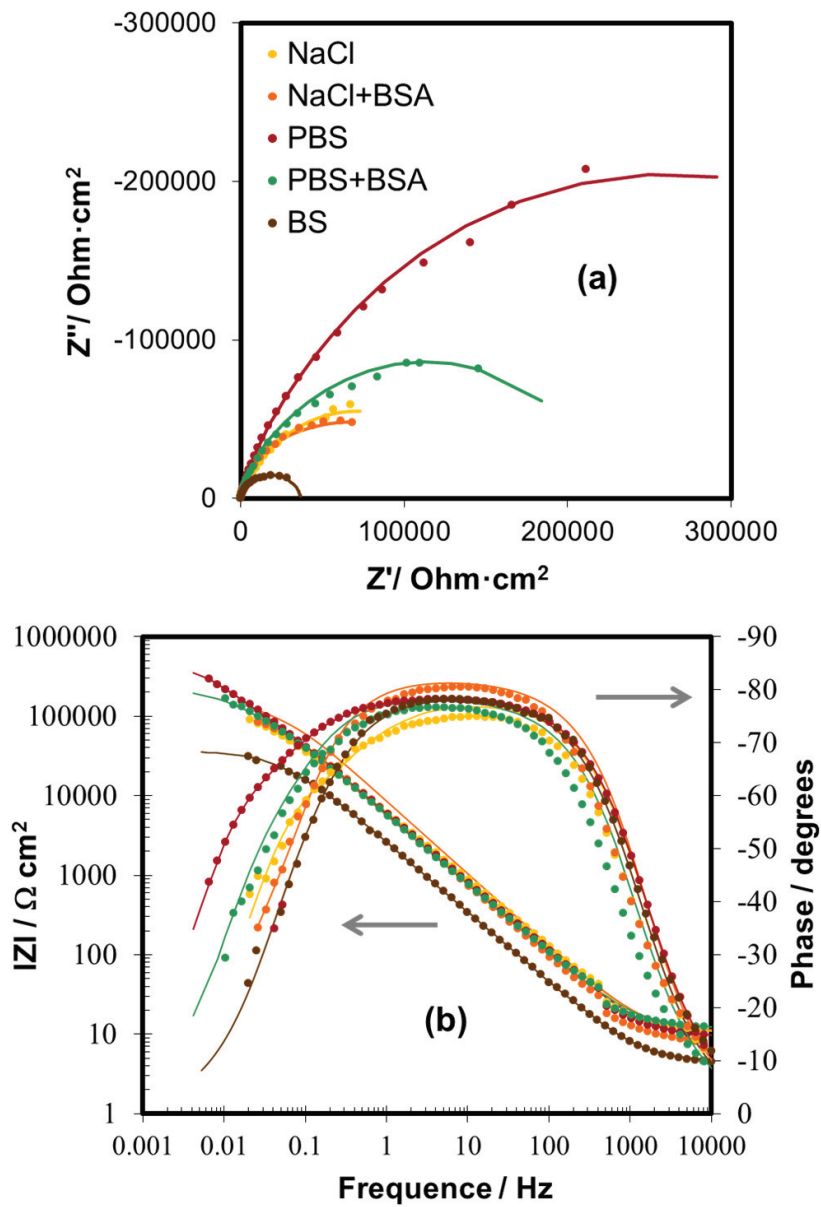


Figure 4.16. (a) Nyquist diagram and (b) Bode plot of the CoCrMo alloy after 1 hour of immersion at 0.35V in different simulated body fluids at 37°C and pH 7.4.



**Table 4.IX.** Equivalent electrical circuit parameters of CoCrMo alloys in the studied solutions at -0.05 and 0.35 V at 37°C and pH 7.4.

ELECTROCHEMICAL PARAMETERS					
-0.05 V					
	NaCl	NaCl+BSA	PBS	PBS+BSA	BS
$R_s (\Omega \text{ cm}^2)$	10 ± 0.0	12.5 ± 0.7	12.5 ± 1.3	20 ± 0	4.3 ± 0.4
$R_{out} (\text{k}\Omega \text{ cm}^2)$	26.3 ± 0.7	32.5 ± 3.4	116.2 ± 5.4	155.0 ± 7.1	27.5 ± 3.5
$CPE_{out} (\Omega^{-1} \text{ s}^n \text{ cm}^2) 10^6$	42.3 ± 0.1	30.4 ± 0.1	36.1 ± 5.2	30.6 ± 0.7	137 ± 20
$n_{out}$	0.98 ± 0.01	0.96 ± 0.04	0.95 ± 0.06	0.92 ± 0.05	0.99 ± 0.00
$C_{out} (\mu\text{F cm}^2)$	34.7 ± 1.9	21.3 ± 0.6	26.3 ± 2.1	15.8 ± 0.6	127.1 ± 0.5
$R_{in} (\text{k}\Omega \text{ cm}^2)$	210 ± 5	214 ± 19	527 ± 38	739 ± 12	249 ± 2.1
$CPE_{in} (\Omega^{-1} \text{ s}^n \text{ cm}^2) 10^6$	48 ± 1	12.5 ± 4	8.8 ± 0.2	8.5 ± 2	15.5 ± 2.2
$n_{in}$	0.91 ± 0	0.86 ± 0.07	0.90 ± 0.02	0.86 ± 0.02	0.90 ± 0.00
$C_{in} (\mu\text{F cm}^2)$	13.3 ± 0.3	14.1 ± 0.9	10.8 ± 0.5	11.3 ± 3.0	19.2 ± 1.2
0.35 V					
	NaCl	NaCl+BSA	PBS	PBS+BSA	BS
$R_s (\Omega \text{ cm}^2)$	10 ± 0	11.5 ± 2.1	9.5 ± 0.7	12 ± 2	3.5 ± 1
$R_{out} (\text{k}\Omega \text{ cm}^2)$	16.1 ± 1.5	30.8 ± 2.3	61.8 ± 10	8.3 ± 3	4.6 ± 0.5
$CPE_{out} (\Omega^{-1} \text{ s}^n \text{ cm}^2) 10^6$	202.1 ± 38.3	38.8 ± 0.0	122.0 ± 4.4	135.1 ± 1.6	246.0 ± 3.0
$n_{out}$	0.91 ± 0.06	0.98 ± 0.01	0.92 ± 0.08	0.93 ± 0.07	0.96 ± 0.07
$C_{out} (\mu\text{F cm}^2)$	127.5 ± 32.1	33.2 ± 0.4	81.0 ± 7.0	97.2 ± 8.1	176.5 ± 9.2
$R_{in} (\text{k}\Omega \text{ cm}^2)$	141 ± 12	118 ± 2	493 ± 15	206 ± 8	34 ± 2.1
$CPE_{in} (\Omega^{-1} \text{ s}^n \text{ cm}^2) 10^6$	10.2 ± 0.3	9.6 ± 1.1	7.1 ± 0.7	9.7 ± 1.3	40 ± 2
$n_{in}$	0.87 ± 0.01	0.87 ± 0.00	0.87 ± 0.02	0.92 ± 0.02	0.89 ± 0.02
$C_{in} (\mu\text{F cm}^2)$	10.8 ± 0.2	10.6 ± 1.3	8.9 ± 1.0	10.9 ± 0.5	41.6 ± 3.2

At -0.05 V the main differences in the EIS are observed in the outer layer where capacitance ( $C_{out}$ ) and resistance ( $R_{out}$ ) significantly varies depending on the chemical composition of the solution. It is well known that BSA and phosphate ions are adsorbed onto the metal surface [14,44,45] which modifies the electrical properties of the outer layer of the alloy (**Table 4.IX**). The presence of BSA and phosphates decreases the capacitance of the outer layer in comparison with the obtained in NaCl. In addition, when both species are present in the solution, the capacitance  $C_{out}$  lies between the extreme values observed in the NaCl+BSA and the PBS solution. The adsorption of the different species increases the thickness of the double layer taking into account the **equation (3.31)** (Chapter 3, *Experimental techniques*) which inversely relates the capacitance with the thickness of the passive layer. Higher thickness of the double layer was obtained in the tests carried out in presence of BSA solutions;

probably due to the fact that this molecule presents larger size than the ionic or inorganic species (NaCl and phosphate ions). Although BSA increases the values of the  $R_{out}$  (from 26.3 to 32.5  $k\Omega\text{ cm}^2$ ), under these potentiostatic conditions the BSA has a small effect in the polarization resistance of the alloy, increasing slightly the  $R_p$  values from 236.3 to 246.5  $k\Omega\text{ cm}^2$  in NaCl and NaCl+BSA respectively. On the contrary, phosphate ions have a major effect in terms of resistance increasing the  $R_{out}$  one order of magnitude (116  $k\Omega\text{ cm}^2$ ) and the  $R_p$  twice the obtained in NaCl (643.2  $k\Omega\text{ cm}^2$ ), **Figure 4.17**. This effect can be explained by a phosphate rich layer covering the electrode surface which blocks the mass transport of oxygen and/or of reaction products to and/or from the electrode surface. Potentiodynamic curves and potentiostatic tests are in good agreement with these results since the lowest values of  $i_p$  and  $i_{pp}$  respectively were obtained in PBS solutions for the CoCrMo alloy.

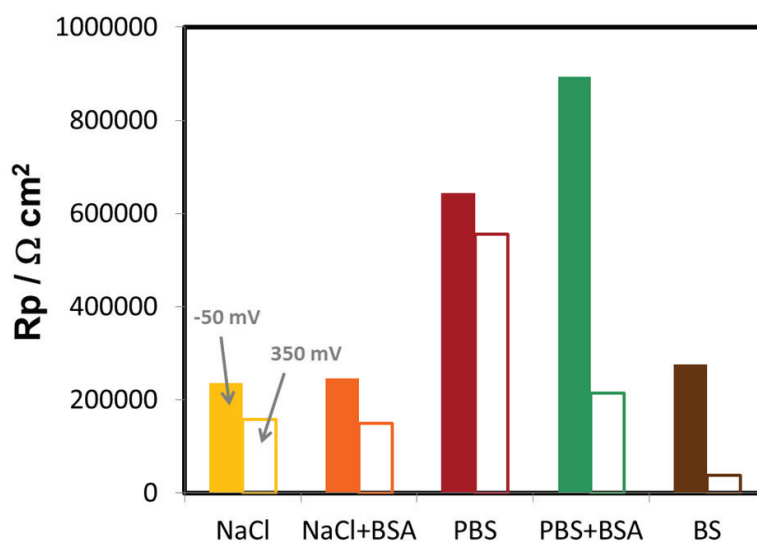


**Figure 4.17.** Polarization resistance of CoCrMo alloy in the studied solutions at -0.05 V and 0.35 V at 37°C and pH 7.4.

#### CHAPTER 4. Electrochemical characterization of CoCrMo alloy in simulated body fluids

These results also support the competitive adsorption between phosphate ions and BSA taking place on the CoCrMo alloy electrode surface observed by Igual and Mischler [14]. They confirmed that the competition of both species for adsorption is favoured because of at pH 7.4 BSA and phosphates are negatively charged.

With respect to the influence of the BS in the outer layer, the complex formulation of the BS makes difficult to determine the implication of specific compounds on the corrosion behaviour of the alloy. The value of the  $R_p$  ( $276 \text{ k}\Omega \text{ cm}^2$ ) obtained in BS lies between the values obtained in the saline and phosphate solutions which indicates the possible formation of a biofilm blocking the surface and hindering the passive dissolution of the alloy. Furthermore, the high  $C_{out}$  and low  $R_{out}$  values indicate that this adsorbed layer is thinner and less resistant than the layer obtained in BSA and PBS solutions. This behaviour can be explained by the adsorption of certain compounds present in the BS which can take up first the active sites on the CoCrMo alloy surface.

The electrical parameters corresponding to the inner layer ( $C_{in}$ ,  $R_{in}$ ) are slightly solution-dependent. Only a slight increase in  $R_{in}$  was observed in presence of phosphates. Furthermore, the values of the thickness obtained from the  $C_{in}$  (applying the **equation (3.31)** and taking the relative dielectric constant  $\epsilon=10$  for oxide films) correspond well with the oxide film thickness obtained under the same electrochemical conditions by other authors [10,11,14]. At -0.05 V, the thickness of the oxide film lies between 1.5 and 2 nm.

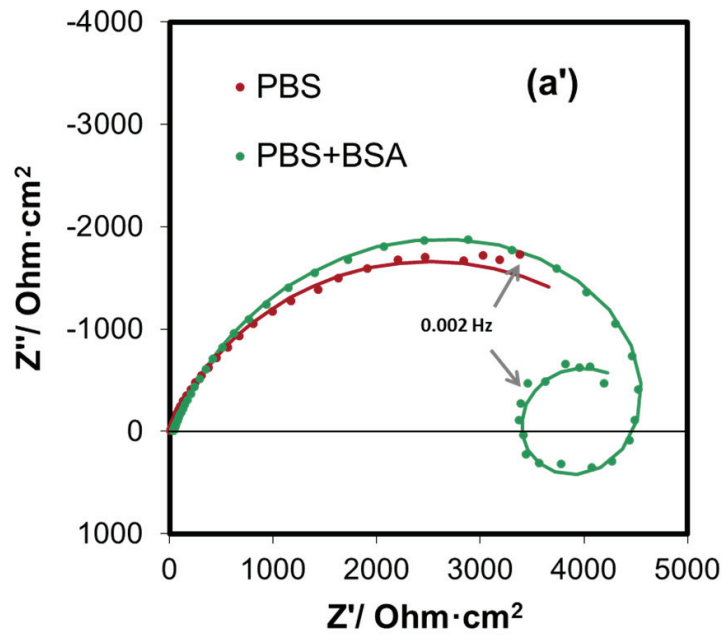
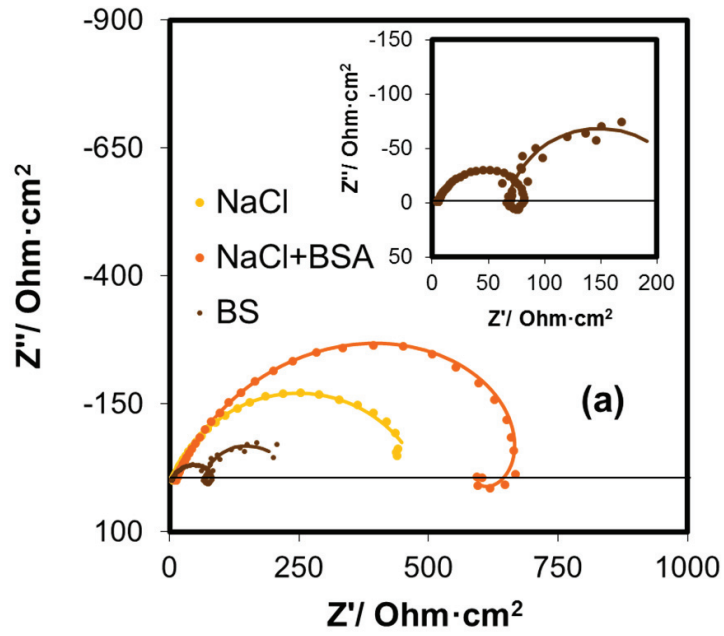
The spectra and the electrical parameters obtained at 0.35 V show some differences compared to the results obtained at -0.05 V. On the one hand, lower values of  $R_p$  were obtained at 0.35 V in all studied solutions which is in good agreement with the highest values of current density obtained at this potential in the previous potentiodynamic curves and potentiostatic tests. In addition, differences in the inner layer were also detected: the capacitance values of the inner layer ( $C_{in}$ ) decreased at higher passive potentials (0.35 V). This behaviour can be due to the thicker passive film formed at higher applied potentials under potentiostatic conditions (between 2.5-4 nm) [10,46] characterized by lower protectiveness. This fact is corroborated by the lower values of  $n$  which indicate the generation of an oxide film less homogeneous at 0.35 V than the

one formed at -0.05 V. The electrical parameters of the outer layer were also affected by the applied potential, obtaining lower  $R_{out}$  and higher  $C_{out}$  values at 0.35 V. This can be related to the different properties of the double layer depending on the applied potential [41].

Different behaviour of BSA was observed at 0.35 V. While BSA slightly shifted the  $R_p$  value towards more resistive values at -0.05 V, the opposite effect was registered at 0.35 V. Furthermore, this effect was more pronounced in presence of phosphates where a huge decrease of the  $R_p$  was obtained (from 555 k $\Omega$  cm<sup>2</sup> in PBS to 214 k $\Omega$  cm<sup>2</sup> in PBS+BSA). At this potential, the BSA suppresses the blocking effect of the phosphates favouring the passive dissolution of the alloy. The same behaviour was observed in the impedance spectra obtained in BS where the lowest values of the  $R_p$  were measured.

#### D) TRANSPASSIVE DOMAIN

**Figure 4.18** shows the impedance spectra at the applied potential of 0.75 V (transpassive domain). Nyquist diagram with lower and higher resistance (semicircle) in the impedance spectra are plotted separated in **Figure 4.18(a)** and **Figure 4.18(a')**. In addition, the magnitude and phase of the Bode plots are represented in the **Figure 4.18(a)** and **Figure 4.18(a)** respectively. In the transpassive domain, the EIS data present complex spectra highly influenced by the chemical composition of the simulated body fluid. An inductive loop is observed at lower frequencies in some spectra which is more visible in certain simulated body fluids. The generation of this loop can be attributed to instabilities of the system as consequence of adsorption-desorption phenomena onto the alloy surface since it only appears in protein containing solutions [47]. In the spectra obtained in non-containing protein solution, a semicircle in the Nyquist diagram is observed in the same complex domain without interception with the x-axes. Therefore, different EECs were used to model the electrochemical behaviour of the CoCrMo in the transpassive domain depending on the electrolyte.



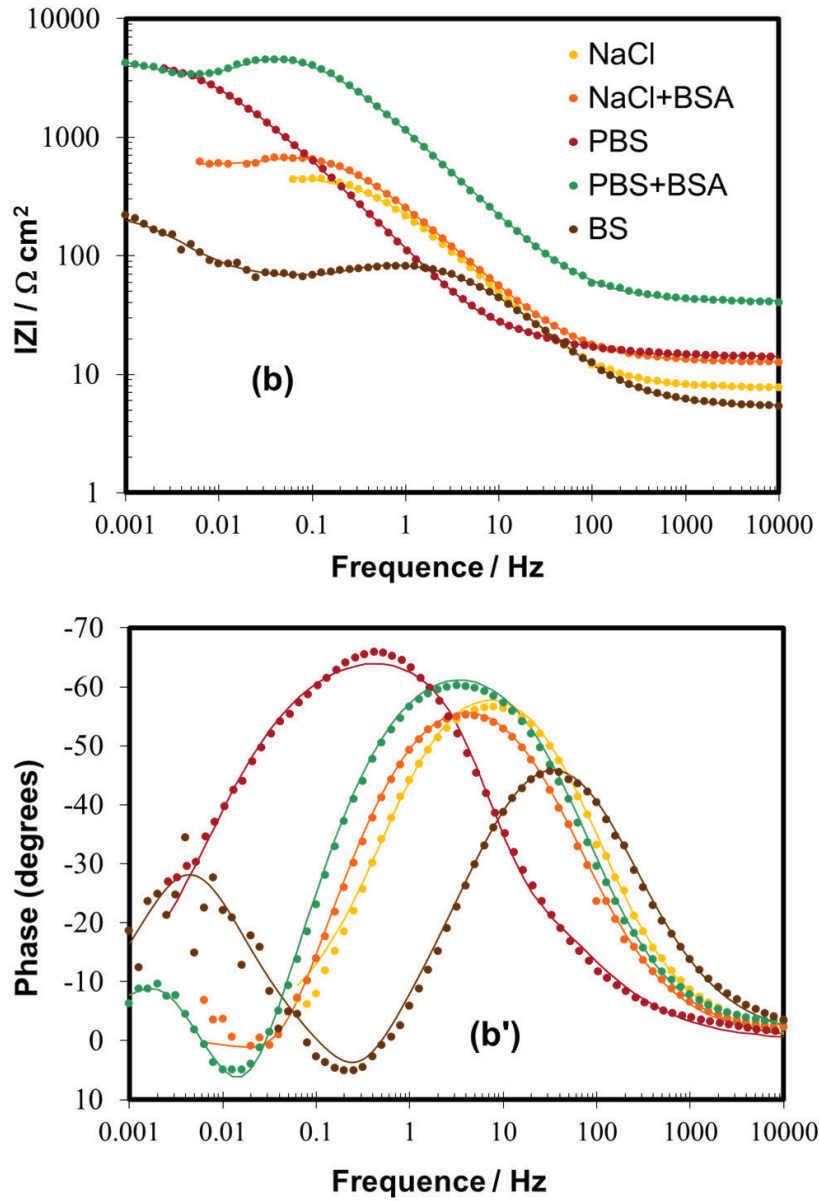
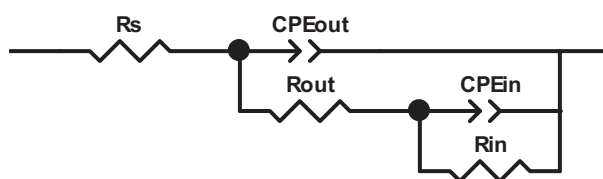


Figure 4.18. (a-a') Nyquist diagram and (b-b') Bode plot of the CoCrMo alloy after 1 hour of immersion at 0.75 V in different simulated body fluids at 37°C and pH 7.4.

In PBS, the spectrum clearly shows two time constants which can be detected by a change in the phase angle (Bode plot, **Figure 4.18(b')**). Thus, the EEC proposed (represented in **Figure 4.19**) was slightly modified from the EEC used to model the passive alloy because of an inhomogeneous oxide film was formed on the CoCrMo alloy due to the transpassive dissolution.



**Figure 4.19.** Equivalent electrical circuit for the analysis of the impedance spectra in simulated body fluids without presence of protein.

In this EEC,  $CPE_{out}$  represents the capacity of the metal/film/electrolyte interface,  $R_{out}$  is the outer layer resistance,  $CPE_{in}$  is related to the capacitance of the inner layer and  $R_{in}$  the inner oxide layer resistance. This EEC is commonly used to model the EIS spectra obtained in porous or inhomogeneous passive alloys [48-51].

In order to fit the experimental spectra obtained in NaCl, the previous EEC was simplified. In this case, the loop at lower frequencies was slightly formed and the system became rapidly instable at higher frequencies. Thus, the EEC employed consists in the same EEC proposed in **Figure 4.19** without the subcircuit  $RC$  related to the inner layer. Therefore, only the electrical parameters related to the double layer can be analyzed with the EIS data obtained in NaCl.

In the protein-containing solutions the behaviour of the system was characterized by a high frequency capacitive loop related to the charge transfer due to the dissolution of the metal as a result of the anodic applied potential, an inductive loop at medium frequency and a semi-arc obtained at the lowest frequencies which indicates the presence of an inner surface film. The EEC proposed is shown in **Figure 4.20**. Other authors have used the same electrical circuit for passive alloys [52]. The circuit consists of the following elements:  $CPE_{out}$  represents the capacity of the metal/film/electrolyte



**CHAPTER 4.** Electrochemical characterization of CoCrMo alloy in simulated body fluids

interface,  $R_{out}$  is the outer layer resistance and the  $RL$  element (resistance and inductance) is attributed to the relaxation of the corrosion products on the electrode surface [39,52],  $CPE_{in}$  is related to the capacitance of the inner layer and  $R_{in}$  the inner oxide layer resistance.

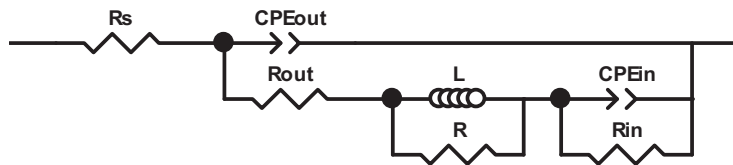


**Figure 4.20.** Equivalent electrical circuit for the analysis of the impedance spectra in simulated body fluids in presence of protein.

An inductive loop is clearly observed at lower frequencies in the impedance spectra obtained in BSA containing solutions. However, the impedance data related to the inner layer (second time constant) was not detected in the spectrum obtained in the NaCl+BSA solution. Thus, in order to fit the experimental results obtained in NaCl+BSA, the EEC proposed in the **Figure 4.20** was simplified and the subsystem  $RC$  related to the inner element was removed.

The values of the electrical parameters extracted for the CoCrMo alloy in the different simulated body fluids were summarized in **Table 4.X**.

**Table 4.X.** Equivalent circuit parameters of CoCrMo alloys in the studied solutions at 0.75 V at 37°C and pH 7.4.

<b>ELECTROCHEMICAL PARAMETERS</b>					
<b>0.75 V</b>					
	<b>NaCl</b>	<b>NaCl+BSA</b>	<b>PBS</b>	<b>PBS+BSA</b>	<b>BS</b>
$R_s (\Omega \text{ cm}^2)$	7.9 ± 0.2	10.3 ± 4	12.7 ± 1.8	41 ± 10	5.2 ± 0.3
$R_{out} (\Omega \text{ cm}^2)$	478 ± 6	524 ± 91	27 ± 9	3142 ± 70	60 ± 1
$CPE_{out} (\Omega^{-1} \text{ s}^n \text{ cm}^{-2})10^6$	824 ± 6	887 ± 41	1580 ± 282	194 ± 25	762 ± 3
$n_{out}$	0.78 ± 0.02	0.76 ± 0.01	0.70 ± 0.04	0.78 ± 0.02	0.77 ± 0.01
$C_{out} (\mu\text{F cm}^{-2})$	191 ± 30	190 ± 20	134 ± 50	49 ± 3	136 ± 11
$L (\text{H cm}^2)$	-	600 ± 41	-	15771 ± 97	11 ± 2
$R (\Omega \text{ cm}^2)$	-	178 ± 68	-	2353 ± 56	24 ± 4
$R_{in} (\text{k}\Omega \text{ cm}^2)$	-	-	4.1 ± 0.9	1.5 ± 0.2	0.2 ± 0.0
$CPE_{in} (\Omega^{-1} \text{ s}^n \text{ cm}^{-2})10^3$	-	-	0.475 ± 0.012	57.2 ± 0.4	279 ± 16
$n_{in}$	-	-	0.95 ± 0.00	0.98 ± 0.01	0.88 ± 0.00
$C_{in} (\text{mF cm}^{-2})$	-	-	0.396 ± 0.014	63.6 ± 0.5	468 ± 26

The highest values of  $R_p$  were obtained for the tests carried out in presence of phosphate with values of 4 k $\Omega \text{ cm}^{-2}$  in PBS and 7 k $\Omega \text{ cm}^{-2}$  in PBS+BSA. These values are one order of magnitude higher with respect to the other solutions. These results show that the phosphate adsorption on the CoCrMo alloy surface hindered the transpassive dissolution of the alloy.

In addition, in the PBS+BSA solution the lowest value of  $C_{out}$  and the highest value of  $R_{out}$  confirmed that a thicker resistive layer was adsorbed on the oxidized surface. In addition, the large  $L$  value supports that the adsorption process under these conditions was quite relevant.

Optical images were obtained on the CoCrMo alloy after the potentiostatic test under transpassive conditions (**Figure 4.21**). It is observed that the transpassive dissolution of the alloy become an inhomogeneous surface revealing the carbides of the alloy. Preferential dissolution at grain boundaries was observed. These images support the EEC selected in order to fit the experimental results.

**CHAPTER 4.** Electrochemical characterization of CoCrMo alloy in simulated body fluids

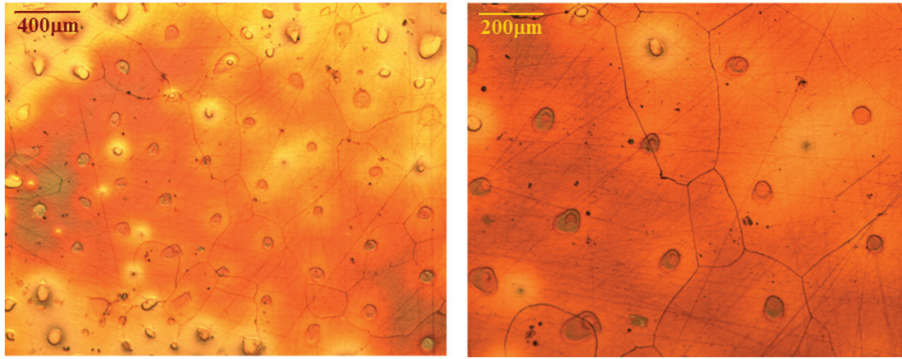


**Figure 4.21.** Optical images of the CoCrMo alloy after the potentiostatic test at 0.75 V in bovine serum at 37°C and pH 7.4.

#### **4.4.2. INFLUENCE OF pH AND AERATION CONDITIONS OF THE SIMULATED BODY FLUIDS**

The main objective of this section is to elucidate the effect of the pH on the electrochemical behaviour of CoCrMo alloy in simulated body fluids by means of the conventional electrochemical techniques (OCP, potentiodynamic curves, potentiostatic tests and EIS). PBS with and without the addition of BSA was employed as simulated body fluids in order to study the effect of the protein on the electrochemical behaviour of the alloy. It is well known that the global charge of the protein changes with the pH, taking negative charge for values of pH above its isoelectric point (*pI*) and positive charge for more acidic pH. The value of the *pI* for the BSA corresponds to 4.7-4.9 [53,54] in water at 25°C. In addition, with the objective of determining the influence of the oxygen presence on the electrochemical response of the alloy aeration conditions were controlled.

##### **4.4.2.1. EXPERIMENTAL SEQUENCE**

The same experimental set-up already described was used in this section. The working electrode (CoCrMo alloy) was mounted as a rotating disc electrode (RDE) and the rotation speed was fixed at 1000 rpm. Furthermore, the nitrogen and oxygen were purged into the cell during the test in order to control the aeration (deoxygenated/oxygenated).

PBS was used to carry out the experiments in order to avoid possible pH variations in the solution during the test. The selected pH to carry out the experimental tests were pH 3 (acidic), pH 7.4 (body conditions) and pH 10 (alkaline). BSA concentration was fixed at 0.5 g L<sup>-1</sup>. A pH-electrode was introduced into the cell in order to detect any pH changes during the electrochemical test.

#### CHAPTER 4. Electrochemical characterization of CoCrMo alloy in simulated body fluids

Two electrochemical tests were carried out:

- 1) Potentiodynamic curves with the following experimental sequence:
  - Measurement of the OCP during 10 minutes;
  - Cathodic cleaning by potentiostatic test at -1.5V during 5 minutes adding the BSA at the end of the potentiostatic measurement (reaching a BSA concentration of  $0.5 \text{ g L}^{-1}$  into the electrolyte);
  - Potentiodynamic curves performed by scanning the applied potential from -1.5 and moved in the anodic direction to 1.5 V at the scan rate of  $1 \text{ mV s}^{-1}$ .
  
- 2) Potentiostatic tests+EIS
  - Measurement of the OCP during 10 minutes;
  - Cathodic cleaning by potentiostatic test at -1.5 V during 5 minutes;
  - Potentiostatic test at the passive potential of -0.05 V during 1 hour. The applied potential was selected within the passive potential domain according to the CoCrMo potentiodynamic curves.
  - EIS measurements at -0.05 V potentiostatic conditions (constant potential) corresponding to the previous test.

The same electrochemical parameters previously described were extracted from the experimental results (**Section 4.4.1**)

The reproducibility of the measurements was determined through three repetitions of each electrochemical test.

#### 4.4.2.2. RESULTS

Different phosphate species are predominant depending on the solution pH which can be extracted from their equilibrium diagram. **Figure 4.22** shows the equilibrium diagrams of the phosphate species and the concentration of those compounds at different pH according to the following equilibrium acidic constants ( $K_H$ ) of the phosphoric acid.

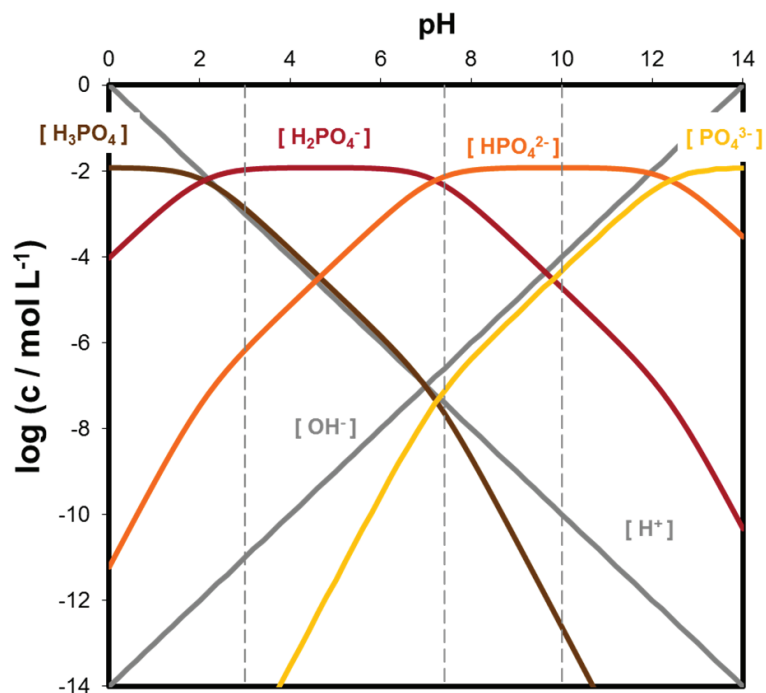


**Figure 4.22.** Equilibrium diagram of the species in the PBS solutions at different pH, where C is the molar concentration of the species.

**CHAPTER 4.** Electrochemical characterization of CoCrMo alloy in simulated body fluids

The electrochemical reaction of phosphates on CoCrMo was measured to be slower than the acidic-base equilibria. Consequently, the concentration of the different phosphate species was supposed to be controlled by the acidic-base equilibria (4.1), (4.2), (4.3) (expressed as dissociation reactions) and the corresponding acidic constants of deprotonation equilibrium are given in equations (4.4), (4.5), (4.6).

$$K_{H1} = \frac{[H_2PO_4^-] \cdot [H^+]}{[H_3PO_4]} \quad (4.4)$$

$$K_{H2} = \frac{[HPO_4^{2-}] \cdot [H^+]}{[H_2PO_4^-]} \quad (4.5)$$

$$K_{H3} = \frac{[PO_4^{3-}] \cdot [H^+]}{[HPO_4^{2-}]} \quad (4.6)$$

**Table 4.XI** summarizes the concentration of the phosphate species, the  $H^+$  and  $OH^-$  at different solution pH according to the corresponding equilibria. It is possible to observe that the highest  $[H_2PO_4^-]$  is found in the PBS solution at pH 3 while  $[HPO_4^{2-}]$  is the most concentrated phosphate specie at pH 7.4 and pH 10.  $[H_3PO_4]$  is negligible at these pH values.

**Table 4.XI.** Molar concentration of the species in PBS solutions at different pH

CONCENTRATION (M)			
SPECIES	pH 3	pH 7.4	pH 10
$H^+$	$1 \cdot 10^{-3}$	$4 \cdot 10^{-8}$	$1 \cdot 10^{-10}$
$OH^-$	$1 \cdot 10^{-11}$	$2.5 \cdot 10^{-7}$	$1 \cdot 10^{-4}$
$PO_4^{-3}$	$3 \cdot 10^{-16}$	$8 \cdot 10^{-8}$	$5 \cdot 10^{-5}$
$HPO_4^{-2}$	$7 \cdot 10^{-7}$	$7 \cdot 10^{-3}$	$1 \cdot 10^{-2}$
$H_2PO_4^-$	$1 \cdot 10^{-2}$	$4.6 \cdot 10^{-3}$	$2 \cdot 10^{-5}$
$H_3PO_4$	$1.5 \cdot 10^{-3}$	$2.6 \cdot 10^{-8}$	$2.6 \cdot 10^{-13}$

### A) OPEN CIRCUIT POTENTIAL MEASUREMENTS

The OCP was measured for 10 minutes at the beginning of each electrochemical test. In all cases, the OCP increases with time which indicates the spontaneous formation of a protective passive layer in the PBS solution according to the previously obtained results. **Figure 4.23** shows the average value of the OCP measurements and their corresponding standard deviation. These OCP values were extracted from the measurements of the last minute of the test although the steady-state was not completely reached.

OCP values decrease with the solution pH and are higher in the oxygen saturated solution ( $O_2$ ) than in the deoxygenated solution ( $N_2$ ). Indeed in the oxygen-containing solutions OCP linearly decreases with the pH increase. On the other hand, in the deoxygenated solutions, OCP significantly drops from pH 3 to pH 7.4 and at higher solution pH OCP values remain approximately constant.

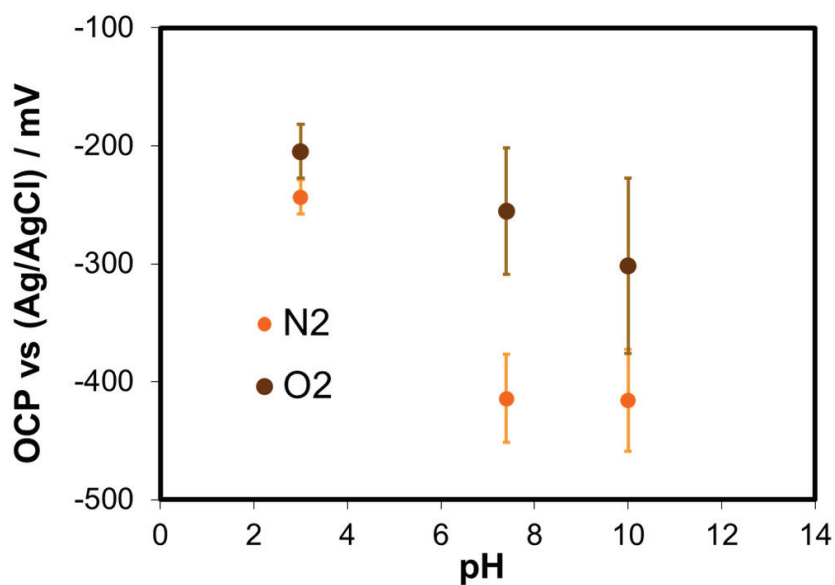


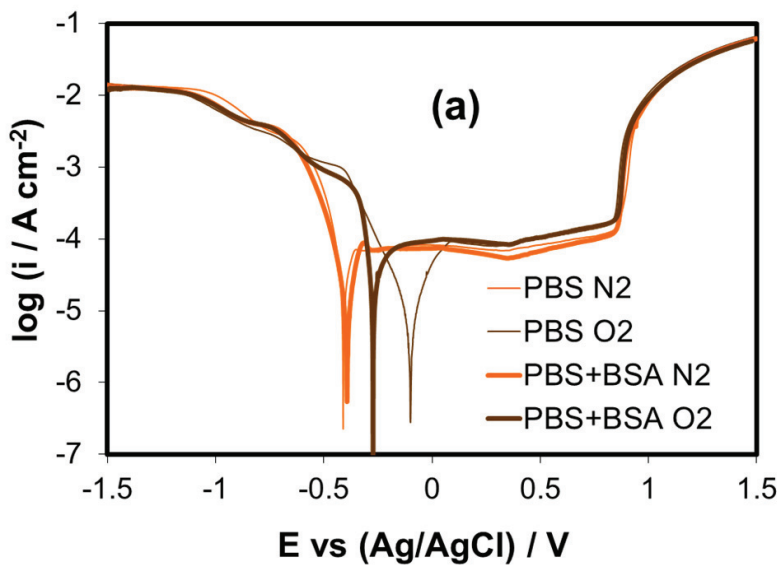
**Figure 4.23.** Average values of OCP measurements of CoCrMo alloy in PBS solutions at different pH and 37°C.



**B) POTENTIODYNAMIC POLARIZATION CURVES**

The effect of oxygen content and BSA addition on the general electrochemical behaviour of the CoCrMo was studied by means of potentiodynamic measurements. **Figure 4.24** shows the potentiodynamic curves of CoCrMo rotating disk in the PBS solutions with and without BSA under aerated ( $O_2$ ) and deaerated ( $N_2$ ) conditions at **(a)** pH 3, **(b)** pH 7.4 and **(c)** pH 10.

The typical potential domains of the potentiodynamic curves of the CoCrMo alloy, already described in **Figure 4.3**, are observed: the cathodic, the cathodic-anodic transition, the passive and the transpassive domain. Electrochemical parameters were extracted from the potentiodynamic curves and they are summarized in **Table 4.XII**. The values of the passive current density ( $i_p$ ) were extracted from the polarization curves at the applied potential of 0.25 V (potential lying within the passive region).



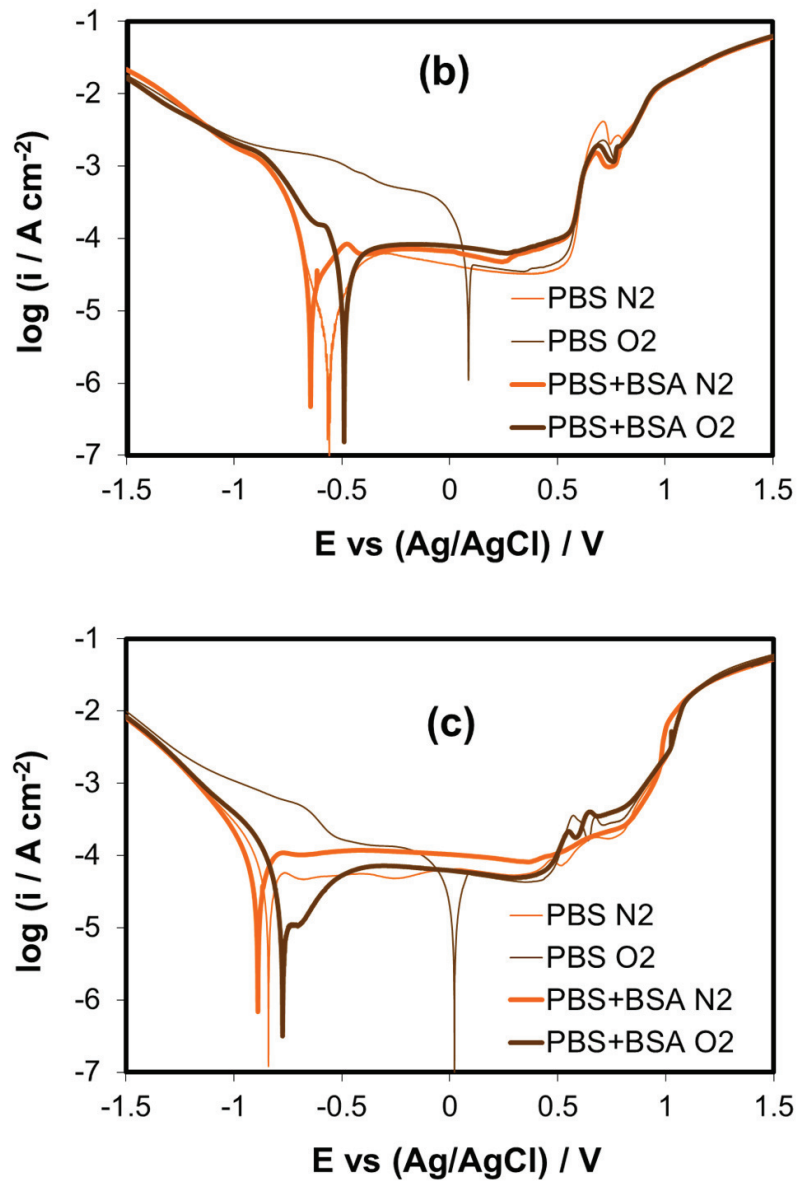
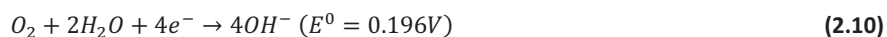
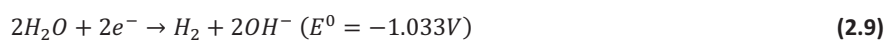
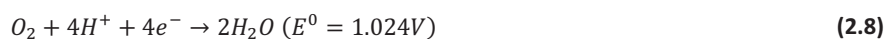


**Figure 4.24.** Potentiodynamic curves of CoCrMo alloy rotating disk in PBS solutions with and without BSA in aerated (O<sub>2</sub>) and deaerated (N<sub>2</sub>) conditions at (a) pH 3, (b) pH 7.4 and (c) pH 10 at 37°C.

**Table 4.XII.** Electrochemical parameters extracted from the potentiodynamic curves of the CoCrMo alloy in simulated body fluids at 37°C and pH 3, 7.4 and 10.

ELECTROCHEMICAL PARAMETERS					
SIMULATED BODY FLUID	AERATION	$E_{corr}$ (mV)	$i_{corr}$ ( $\mu\text{A}/\text{cm}^2$ )	$i_p$ ( $\mu\text{A}/\text{cm}^2$ )	$E_{br}$ (mV)
<b>pH 3</b>					
PBS	N <sub>2</sub>	-389 ± 40	26.5 ± 5.0	68.6 ± 6.1	807 ± 24
	O <sub>2</sub>	-99 ± 1	5.5 ± 0.5	100.6 ± 2.6	832 ± 1
PBS+BSA	N <sub>2</sub>	-407 ± 20	14.0 ± 2.1	75.7 ± 5.3	846 ± 6
	O <sub>2</sub>	-255 ± 25	24.7 ± 0.8	81.5 ± 4.1	848 ± 3
<b>pH 7.4</b>					
PBS	N <sub>2</sub>	-569 ± 4	10.8 ± 0.7	34.1 ± 2.7	521 ± 30
	O <sub>2</sub>	87 ± 11	16.5 ± 0.7	35.0 ± 3.5	519 ± 9
PBS+BSA	N <sub>2</sub>	-617 ± 42	12.1 ± 2.1	60.9 ± 2.3	513 ± 24
	O <sub>2</sub>	-513 ± 32	11.7 ± 1.6	81.6 ± 3.0	549 ± 4
<b>pH 10</b>					
PBS	N <sub>2</sub>	-829 ± 15	26.9 ± 2.2	59.6 ± 4.7	683 ± 25
	O <sub>2</sub>	25 ± 6	24.6 ± 1.1	59.2 ± 5.1	429 ± 4
PBS+BSA	N <sub>2</sub>	-882.5 ± 9	26.2 ± 0.1	117.3 ± 11.9	751 ± 9
	O <sub>2</sub>	-650 ± 56	8.9 ± 3.0	89.7 ± 3.3	453 ± 29

In the cathodic domain the current density was determined by the reduction of water in deoxygenated test (nitrogen purge) and by the dissolved oxygen and water in the electrochemical tests carried out in oxygen saturated conditions. The typical reduction reactions that take place in the cathodic domain depend on the solution pH and aeration conditions. According to these physical parameters the likely reactions produced on the cathodic domain are described (*Introduction*, Chapter 1):



The reactions (2.7) and (2.8) consist of the electrochemical reactions of hydrogen ion favoured in acidic media in deoxygenated solution and oxygen saturated solution respectively. In oxygenated solutions either reaction (2.7) or reaction (2.8) are possible, but it can be assumed that under the real conditions the reaction (2.8) is

more favoured. The reaction (2.9) and (2.10) show the reduction reaction of water in neutral and alkaline media. The reaction (2.10) can occur via two pathways depending on the nature of the metal substrate and the presence or absence of an oxide film [55].

Anodic polarisation curves of CoCrMo alloy obtained at pH 3 are shown in **Figure 4.24(a)**. Main differences between the curves were observed in the cathodic domain at low overpotentials while the passive and transpassive domains are slightly affected by the presence of the BSA and the aeration conditions. In absence of oxygen, PBS(N<sub>2</sub>) and PBS+BSA(N<sub>2</sub>), there is no effect of the BSA in the potentiodynamic curves. In presence of oxygen (PBS(O<sub>2</sub>) and PBS+BSA(O<sub>2</sub>)), BSA shifts the corrosion potential towards lower values (potentials from -99 to -255 mV), increases the corrosion current density (from 5.5 to 24.7  $\mu\text{A cm}^{-2}$ ) and decreases the passive current density (from 100.6 to 81.5  $\mu\text{A cm}^{-2}$ ). According to these results it can be concluded that, in acidic media, BSA mainly acts over the oxygen reduction reaction.

With respect to the effect of the aeration conditions, presence of oxygen increases the corrosion potential and increases or decreases the corrosion current density of the CoCrMo alloy depending on the solution chemistry, **Table 4.XII**.

**Figure 4.24(b)** shows the potentiodynamic curves of the CoCrMo alloy in PBS solutions with saturated oxygen and without oxygen, in presence and in absence of BSA at a neutral pH of 7.4. BSA affects the electrochemical behaviour of the CoCrMo in those PBS solutions, especially in presence of oxygen presence. The addition of BSA decreases the cathodic current density and shifts the  $E_{corr}$  towards more cathodic potentials where a displacement of 0.5 V was observed in the case of oxygen containing solutions due to the fact that the cathodic reaction is controlled by diffusion (PBS(O<sub>2</sub>) solutions without BSA). In this potential range, the current density was independent of the applied potential which shows that the cathodic reaction is limited by the transport of the oxygen. Under these conditions BSA also increases the passive current density in the oxygen and nitrogen containing solutions. In previous studies, similar effect of BSA was observed in neutral media (pH 7.4) without controlling the aeration conditions [14].

#### CHAPTER 4. Electrochemical characterization of CoCrMo alloy in simulated body fluids

In the transpassive domain, which is characterized by the increase in current density due to transpassive dissolution of the chromium oxide as well as water oxidation, a formation of phosphate-chromium ion complexes are shown according to the current density peak observed at 0.6 V [56,57]. The release and dissolution of metal ions may be favoured by the formation of metallic complexes that activates transpassive dissolution [10,58,59].

In the PBS solution at pH 7.4, the main phosphate species are  $\text{HPO}_4^{-2}$  and  $\text{H}_2\text{PO}_4^-$  which can be adsorbed on the CoCrMo surface and form a passive layer which contains phosphate compounds. After an equilibrium time (OCP measurement) BSA is added to the surface and attached to the passive layer, thus blocking the access of the oxidant species to the metallic surface. Finally, at pH 7.4, the aeration effect in PBS+BSA solution is small and oxygen slightly increases the corrosion potential and the corrosion current density of the CoCrMo alloy.

**Figure 4.24(c)** shows the typical anodic polarization curves of CoCrMo obtained at pH 10. Considerably influence of oxygen was observed on the general electrochemical behaviour of the alloy in the PBS solution (without BSA). The most important effect is the displacement towards higher values of the  $E_{corr}$  due to the oxidant effect of the oxygen. This effect produces an increase of the current density in the whole cathodic domain, which is enlarged, from -1.5 V to 0 V. According to the reduction reactions proposed in neutral and alkaline media, the increase of the cathodic current density is related to the four-electron process in presence of oxygen in comparison with the two-electron process in its absence (reaction **(2.10)** and reaction **(2.8)** respectively). In addition, the plateau observed in  $\text{PBS}(\text{O}_2)$  indicates that the cathodic reaction is also limited by the transport of oxygen.

In the transpassive domain, the presence of oxygen may favour the formation of other different metallic complexes observed by two peaks in the current density response. The oxygen displaces the value of  $E_{corr}$  around 1 V towards more anodic potentials (from -829 to 25 mV) and the  $E_{br}$  from 683 to 429 mV. In oxygenated solutions, the transpassive domain starts at lower potentials and it is possible to distinguish two anodic peaks. Several authors [60] have related this response to the formation of

metal complexes that activate transpassive dissolution. In this case, the dissolution of the alloying elements forming complexes with phosphates is favoured in alkaline media.

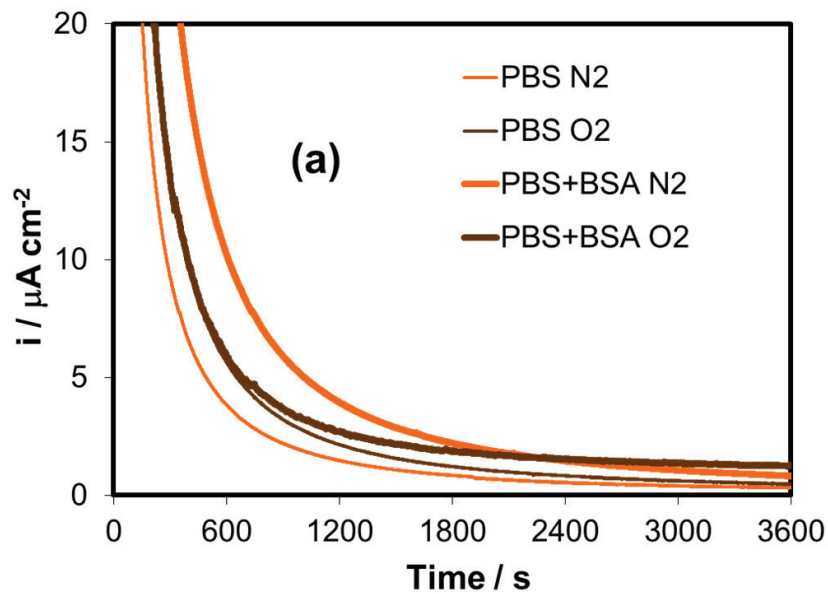
On the other hand, BSA shifts the corrosion potential towards lower values and the oxygen effect is hindered. One may conclude that the main action of BSA in neutral and alkaline media was on the oxygen reaction since suppresses the oxygen transport limitation occurring in the  $\text{PBS}(\text{O}_2)$  solution.

Finally the pH was observed to decrease the cathodic current density thus shifting the cathodic reduction reaction to higher potentials when pH decreases.

C) POTENTIOSTATIC TESTS

Figure 4.25 shows the current evolution at an applied passive potential on the CoCrMo alloy in the simulated body fluids at different solution pH and under different aeration conditions.

In all cases an exponential recovery of the current density with time can be observed after the abrupt increase when applying the constant potential which is characteristic for passivation phenomena [11]. This behaviour was previously observed in the general characterization of the CoCrMo alloy under passive conditions (section 4.4.1). Steady state values ( $i_{pp}$ ) and electrochemical charge exchange ( $q$ ) during the potentiostatic tests are summarized in Table 4.XIII and represented as a function of the pH in the Figure 4.26.



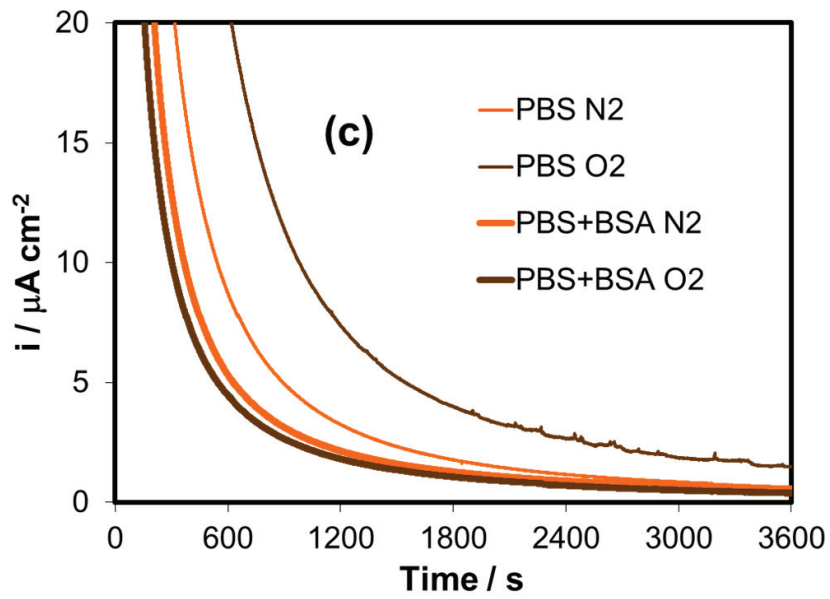
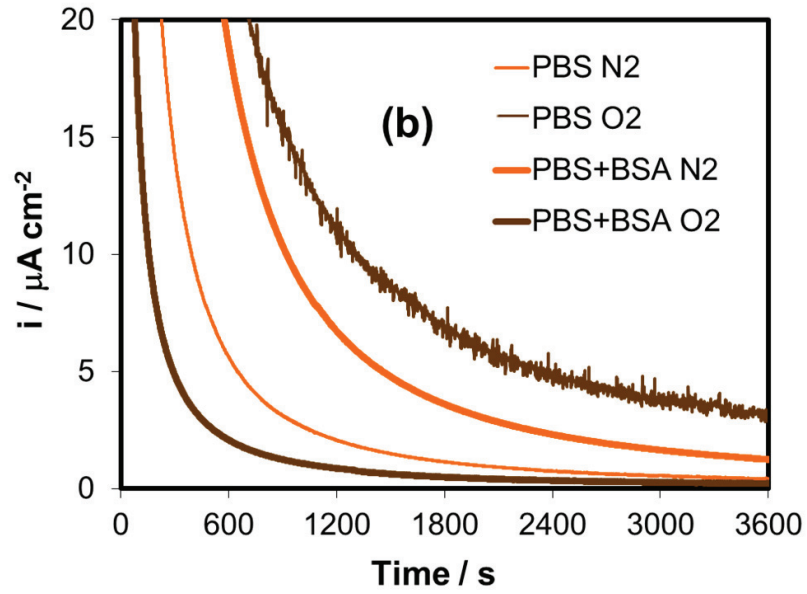


Figure 4.25. Potentiostatic tests of CoCrMo alloy in PBS and PBS+BSA solutions under aerated and deaerated conditions at (a) pH 3, (b) pH 7.4 and (c) pH 10.



**CHAPTER 4.** Electrochemical characterization of CoCrMo alloy in simulated body fluids

In the acidic media, presence of oxygen increases the steady value of the passive current density and the electrochemical charge in all PBS solutions. On the contrary, in neutral and alkaline PBS solutions, oxygen increases the electrochemical charge in the non-containing BSA solution while it decreases the charge in the BSA solution (more noticeable at neutral pH). The same effect is observed in the steady value of the passive current density. At this pH, the lowest value of  $q$  was obtained in the test carried out in PBS+BSA oxygenated solutions.

With respect to the influence of pH, only in PBS solutions, without the addition of BSA, the electrochemical charge linearly increases with the solution pH (**Figure 4.26**).

**Table 4.XIII.** Passive current density ( $i_{pp}$ ) and electrochemical charge ( $q$ ) in the potentiostatic tests at -0.05 V of the CoCrMo alloy in simulated body fluids at 37°C and pH 3, 7.4 and 10.

<b>ELECTROCHEMICAL PARAMETERS</b>			
<b>SOLUTION</b>	<b>AERATION</b>	$i_{pp}$ ( $\mu\text{A cm}^{-2}$ )	$q$ ( $\text{mC cm}^{-2}$ )
<b>pH 3</b>			
PBS	N <sub>2</sub>	0.33 ± 0.02	34.8 ± 2.1
	O <sub>2</sub>	0.48 ± 0.03	51.2 ± 0.9
PBS+BSA	N <sub>2</sub>	0.83 ± 0.02	53.4 ± 3.4
	O <sub>2</sub>	1.26 ± 0.12	87.9 ± 2.3
<b>pH 7.4</b>			
PBS	N <sub>2</sub>	0.40 ± 0.03	56.3 ± 1.9
	O <sub>2</sub>	2.81 ± 0.25	160.9 ± 3.2
PBS+BSA	N <sub>2</sub>	1.25 ± 0.17	198.4 ± 1.2
	O <sub>2</sub>	0.23 ± 0.05	20.2 ± 0.6
<b>pH 10</b>			
PBS	N <sub>2</sub>	0.62 ± 0.09	81.6 ± 2.0
	O <sub>2</sub>	1.47 ± 0.25	242.2 ± 6.2
PBS+BSA	N <sub>2</sub>	0.55 ± 0.01	53.4 ± 2.5
	O <sub>2</sub>	0.37 ± 0.02	34.7 ± 3.2

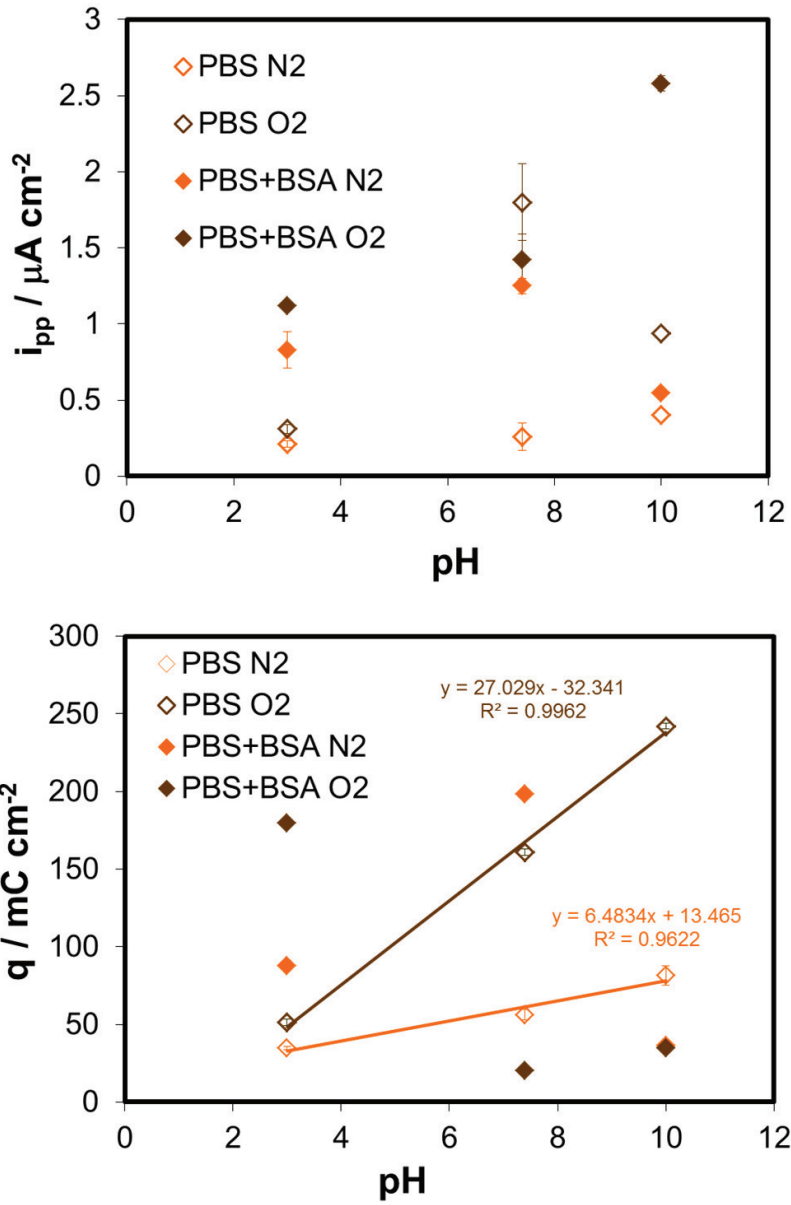


**Figure 4.26.** (a) Steady state values of passivation current density ( $i_{pp}$ ) and (b) electrochemical charge exchange ( $q$ ) during the potentiostatic tests at different pH in the studied simulated body fluids.

#### D) ELECTROCHEMICAL IMPEDANCE SPECTROSCOPY

EIS was employed to investigate the film/electrolyte-interface on the CoCrMo alloys in PBS solutions at different pHs and aeration conditions. EIS was measured under potentiostatic conditions and the corresponding results are shown in **Figures 4.27-4.29** by means of Nyquist diagrams and Bode plots.

Two time constants can be clearly distinguished in the impedance spectra as previously observed in the CoCrMo alloy characterization under passive conditions. According to this behaviour, the same EEC was taken to model the experimental data (i.e. two subsystems *RC* in series) since the system presents similar properties [14,38]. The EEC used for the CoCrMo alloy under passive conditions, its physical description and the characterization of the electrical elements was described in the Chapter 3 (*Experimental techniques*) and in the passive characterization of the alloy (**section 4.3.1**).

The theoretical simulated impedance parameters for the tested alloy under different solution pH, aeration conditions and electrolyte composition are computed and summarized in **Table 4.IX**. In order to validate these parameters, after doing the experimental data fitting to the EEC, two considerations were taken into account: the Chi-squared values ( $\chi^2$ ) obtained with the fitting was suitable low ( $\chi^2 \leq 10^{-4}$ ) and the errors associated with each element were lower than 5 %.

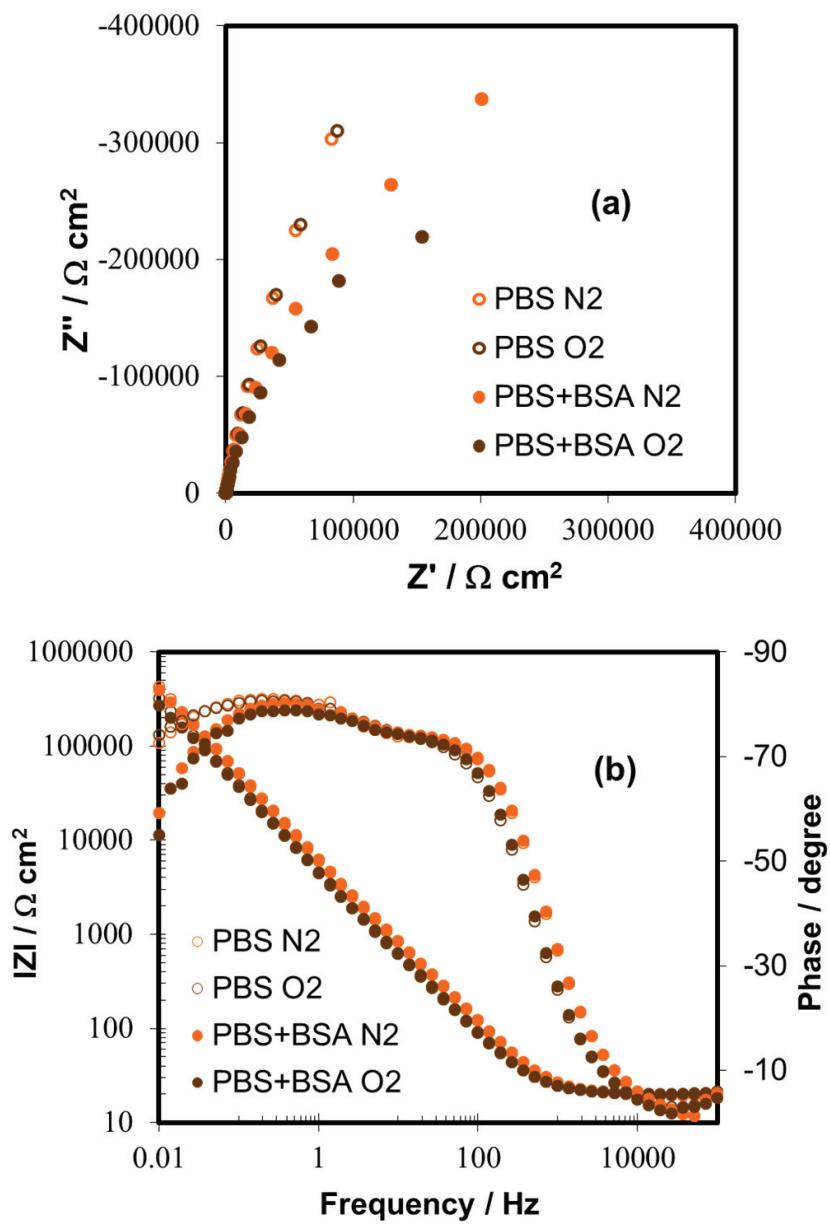


Figure 4.27. (a) Nyquist diagram and (b) Bode plot of the CoCrMo alloy at an applied potential of -0.05 V in PBS and PBS+BSA solution under aerated and deaerated conditions at pH 3.

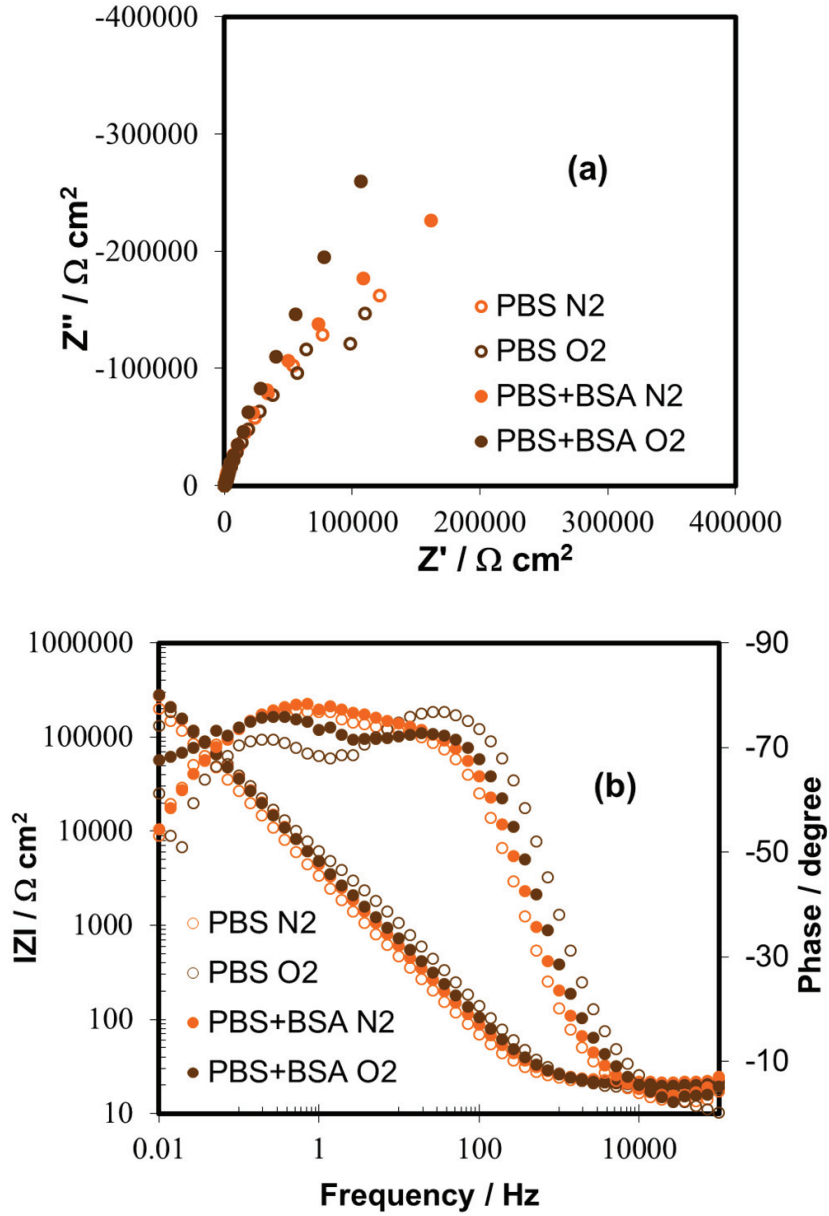


Figure 4.28. (a) Nyquist diagram and (b) Bode plot of the CoCrMo alloy at an applied potential of  $-0.05 \text{ V}$  in PBS and PBS+BSA solution under aerated and deaerated conditions at **pH 7.4**.

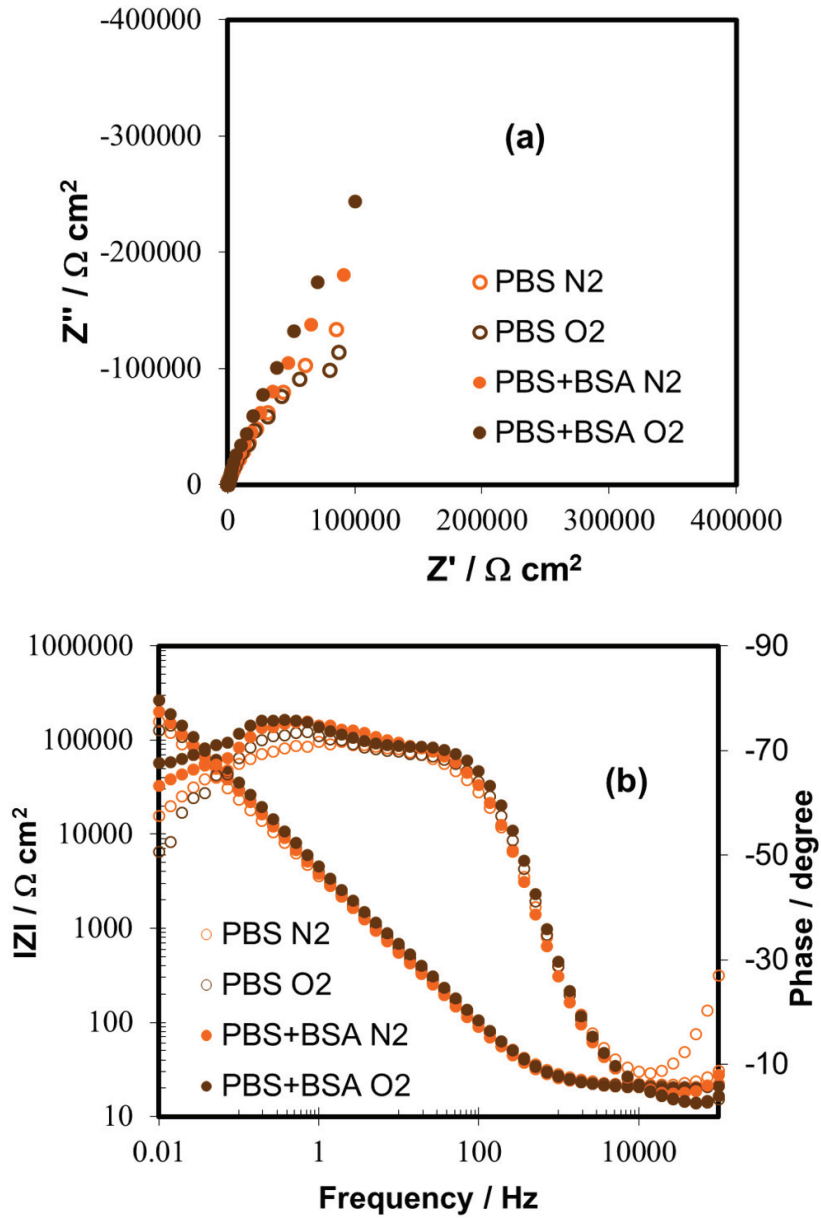


Figure 4.29. (a) Nyquist diagram and (b) Bode plot of the CoCrMo alloy at an applied potential of  $-0.05 \text{ V}$  in PBS and PBS+BSA solution under aerated and deaerated conditions at **pH 10**.

#### CHAPTER 4. Electrochemical characterization of CoCrMo alloy in simulated body fluids

**Figure 4.27(a-b)** shows the impedance results in the PBS solutions and pH 3. BSA decreases the polarization resistance of the CoCrMo alloy in all the PBS solutions. On the other hand, aeration conditions have small effect on the passive dissolution resistance of the CoCrMo alloy in the PBS solutions (slightly decreases  $R_p$ ). The aeration conditions affect the double layer capacitance by increasing the capacitance values of the inner and outer layer in the oxygen-containing solutions.

**Figure 4.28(a-b)** shows the impedance results in the PBS solutions and pH 7.4. In this case, BSA effect is clearly observed and generates an increase in the passive dissolution resistance. Aeration effect at this pH is related to the chemical composition of the solution. Oxygen decreases the polarization resistance in the PBS solution while it increases the polarization resistance in the PBS+BSA solution. On the other hand, oxygen decreases the capacitance of the double layer in both solutions (with the exception of the test carried out in PBS where the capacitance value remains almost constant).

Finally the impedance results in PBS solutions and pH 10 are represented in **Figure 4.29(a-b)** and they show similar trend as the one observed at pH 7.4: BSA increases the polarization resistance of CoCrMo alloy under passive conditions and oxygen increases or decreases that polarization resistance in PBS+BSA and PBS solutions respectively.

In general the pH increase produces a decrease in the  $R_p$  and an increase of  $C_{in}$ .

**Table 4.XIV.** Equivalent circuit parameters of CoCrMo alloys in the studied solutions at -0.05 V at 37°C and different pH under aerated and deaerated conditions.

<b>ELECTROCHEMICAL PARAMETERS</b>				
<b>pH 3</b>				
	<b>PBS</b>		<b>PBS+BSA</b>	
	<b>N<sub>2</sub></b>	<b>O<sub>2</sub></b>	<b>N<sub>2</sub></b>	<b>O<sub>2</sub></b>
$R_s$ ( $\Omega$ cm <sup>2</sup> )	12 ± 1	13 ± 0.3	13 ± 0.5	13 ± 2
$R_{out}$ (k $\Omega$ cm <sup>2</sup> )	20 ± 5	14 ± 2	17 ± 3	16 ± 10
$CPE_{out}$ ( $\Omega^{-1}$ s <sup>n</sup> cm <sup>-2</sup> )10 <sup>6</sup>	214 ± 14	406 ± 21	239 ± 9	350 ± 8
$n_{out}$	0.82 ± 0.02	0.79 ± 0.01	0.83 ± 0.01	0.82 ± 0.02
$C_{out}$ ( $\mu$ F cm <sup>-2</sup> )	57 ± 6	99 ± 5	72 ± 3	105 ± 2
$R_{in}$ (M $\Omega$ cm <sup>2</sup> )	1.23 ± 0.03	1.07 ± 0.05	0.57 ± 0.03	0.36 ± 0.02
$CPE_{in}$ ( $\Omega^{-1}$ s <sup>n</sup> cm <sup>-2</sup> )10 <sup>6</sup>	48 ± 1	63 ± 4	46 ± 3	64 ± 2
$n_{in}$	0.93 ± 0.02	0.93 ± 0.02	0.92 ± 0.03	0.92 ± 0.02
$C_{in}$ ( $\mu$ F cm <sup>-2</sup> )	65 ± 1	87 ± 6	62 ± 4	85 ± 3
<b>pH 7.4</b>				
	<b>PBS</b>		<b>PBS+BSA</b>	
	<b>N<sub>2</sub></b>	<b>O<sub>2</sub></b>	<b>N<sub>2</sub></b>	<b>O<sub>2</sub></b>
$R_s$ ( $\Omega$ cm <sup>2</sup> )	14 ± 0	11 ± 0.3	14 ± 0.2	18 ± 1
$R_{out}$ (k $\Omega$ cm <sup>2</sup> )	17 ± 9	83 ± 5	11 ± 6	177 ± 25
$CPE_{out}$ ( $\Omega^{-1}$ s <sup>n</sup> cm <sup>-2</sup> )10 <sup>6</sup>	906 ± 12	83 ± 3	594 ± 25	55 ± 2
$n_{out}$	0.71 ± 0.01	0.96 ± 0	0.75 ± 0.01	0.85 ± 0.06
$C_{out}$ ( $\mu$ F cm <sup>-2</sup> )	148 ± 2	62 ± 2	116 ± 5	28 ± 1
$R_{in}$ (M $\Omega$ cm <sup>2</sup> )	0.48 ± 0.02	0.22 ± 0.03	0.38 ± 0.01	0.47 ± 0.01
$CPE_{in}$ ( $\Omega^{-1}$ s <sup>n</sup> cm <sup>-2</sup> )10 <sup>6</sup>	63 ± 4	59 ± 1	64 ± 5	44 ± 0
$n_{in}$	0.92 ± 0	0.87 ± 0.03	0.92 ± 0.01	0.9 ± 0.01
$C_{in}$ ( $\mu$ F cm <sup>-2</sup> )	85 ± 8	86 ± 1	85 ± 0	51 ± 0
<b>pH 10</b>				
	<b>PBS</b>		<b>PBS+BSA</b>	
	<b>N<sub>2</sub></b>	<b>O<sub>2</sub></b>	<b>N<sub>2</sub></b>	<b>O<sub>2</sub></b>
$R_s$ ( $\Omega$ cm <sup>2</sup> )	13 ± 0.5	13 ± 0.7	13 ± 0.3	21 ± 1
$R_{out}$ (k $\Omega$ cm <sup>2</sup> )	22 ± 9	13 ± 10	5 ± 11	23 ± 5
$CPE_{out}$ ( $\Omega^{-1}$ s <sup>n</sup> cm <sup>-2</sup> )10 <sup>6</sup>	886 ± 21	366 ± 18	875 ± 17	212 ± 3
$n_{out}$	0.72 ± 0.03	0.8 ± 0.03	0.75 ± 0.01	0.85 ± 0.01
$C_{out}$ ( $\mu$ F cm <sup>-2</sup> )	155 ± 4	95 ± 5	182 ± 4	99 ± 2
$R_{in}$ (M $\Omega$ cm <sup>2</sup> )	0.26 ± 0.01	0.16 ± 0	0.36 ± 0.01	0.47 ± 0.02
$CPE_{in}$ ( $\Omega^{-1}$ s <sup>n</sup> cm <sup>-2</sup> )10 <sup>6</sup>	96 ± 0	79 ± 1	82 ± 5	44 ± 2
$n_{in}$	0.84 ± 0.02	0.87 ± 0.02	0.87 ± 0.04	0.9 ± 0
$C_{in}$ ( $\mu$ F cm <sup>-2</sup> )	177 ± 0	116 ± 2	135 ± 8	105 ± 5



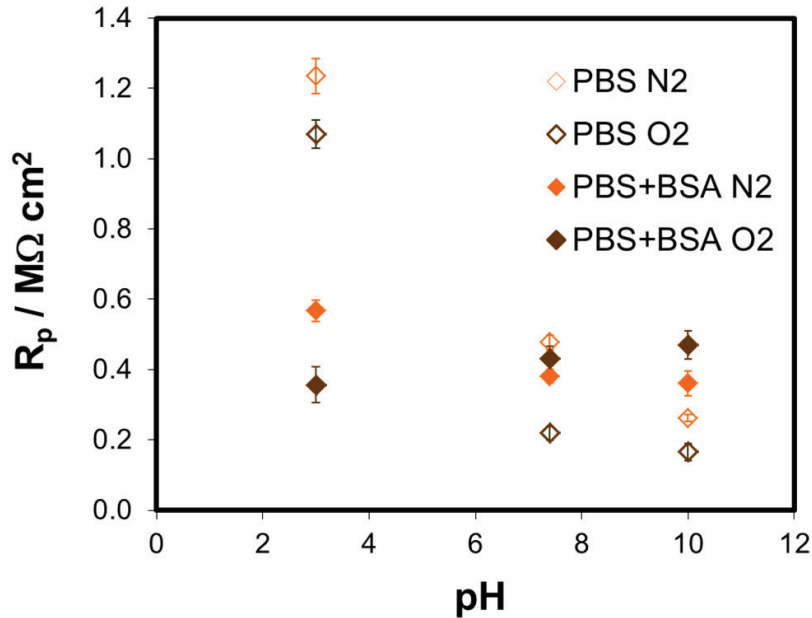


**Figure 4.30.** Polarization resistance of the interface biomaterial/body fluid in the simulated body fluids under aerated and deaerated conditions and different pH at 37°C.

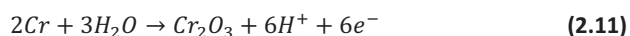
#### 4.4.2.3. DISCUSSION

##### A) INFLUENCE OF pH

In the passive domain, the polarization resistance of the CoCrMo alloy in the PBS solutions decreases with the increase of the solution pH, **Figure 4.30**. In principle, the local alkalinity leads to the formation of insoluble oxides, hydroxides or oxi-hydroxides [55] but solution chemistry also plays a role in the passivation mechanisms of the metallic alloys. According to the equilibrium reactions of the phosphate species shown in **Figure 4.22** it is possible to observe that the highest  $\text{H}_2\text{PO}_4^-$  concentration is found in PBS solution at pH 3. The highest resistance to passive dissolution was also found in pH 3 and it is known that the activity of the cobalt oxide decreases in presence of  $\text{NaH}_2\text{PO}_4$  due to the formation of an insoluble cobalt phosphate [39,61]. Several authors [10-12,39] demonstrated that the major species dissolving from the CoCrMo

alloy is Co, apart from the transpassive region where all alloying elements dissolve according to the composition of the alloy [11]. The same effect of this phosphate compound has been found on the chromium [62]. Therefore one may conclude that the responsible ion for the highest resistance to passive dissolution of CoCrMo passivation is the  $\text{H}_2\text{PO}_4^-$  which mainly precipitates in form of cobalt phosphate ( $\text{Co}(\text{H}_2\text{PO}_4)_2$ ). These metallic phosphates formed on the CoCrMo alloy have been previously analysed [63] and they contribute to diminish the rate of the passive dissolution of the biomaterial by blocking the electronic transfer through the passive film.

Due to hydrolysis, the action mechanism of orthophosphates is pH-dependent and only when  $[\text{HPO}_4^{2-}] < [\text{PO}_4^{3-}]$  do ionic forms display inhibitive activity in alkaline solutions [64]. It is then reasonable to accept that in the present case, with  $[\text{HPO}_4^{2-}] > [\text{PO}_4^{3-}]$  the protective oxide films by the “pore plugging” [64] mechanism stabilized by phosphates are not the mechanisms by which CoCrMo passivates and adsorption followed by precipitation is the main mechanism governing the passive dissolution of the alloy and thus is highly influenced by solution chemistry and physico-chemical properties of the solution (i.e. pH). Therefore, although CoCrMo passivity is mainly due to the chromium oxide formation, according to the **reaction (2.11)** [38], the solution properties modify the role of the other alloying elements and determines the mechanisms of the anodic and the cathodic reactions.



On the other hand BSA competes with phosphates for adsorption [14]; but in acidic solutions the BSA adsorption may be limited by the charge effects (BSA is positively charged in this acidic solution). It is worth to note here that due to the different charge of the species presents in solution, for the BSA (positive) and phosphates (negative), phosphate species could be predominantly adsorbed in the metallic surface in the solutions at pH below the isoelectric point (pI) for BSA, 4.7-4.9 [53,54].

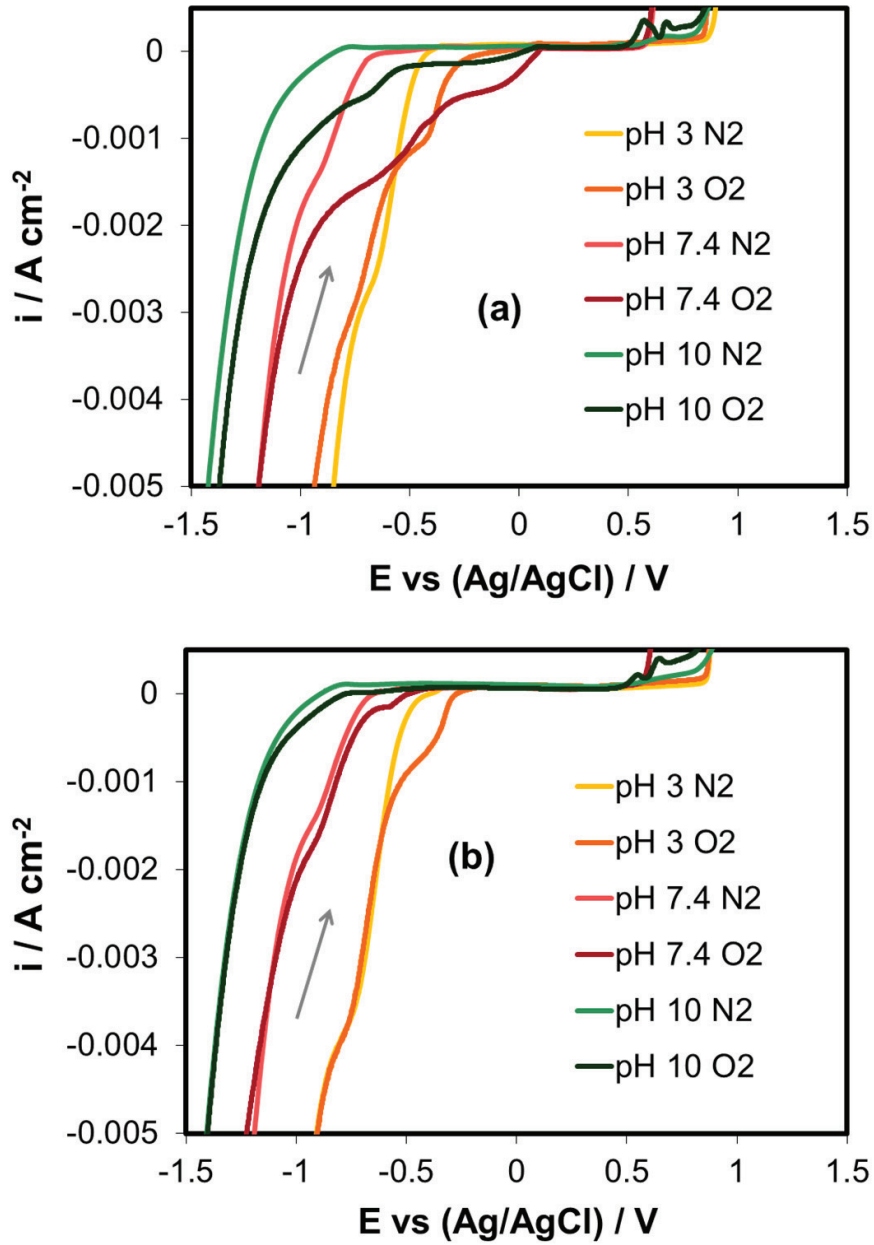
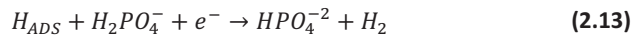
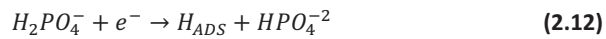


Figure 4.31.  $i$ - $E$  curves of CoCrMo rotating disk in PBS solution with and without BSA in aerated conditions at different pHs and 37°C: (a) PBS (N<sub>2</sub>) and (O<sub>2</sub>), (b) PBS+BSA (N<sub>2</sub>) and (O<sub>2</sub>).

In neutral and alkaline media, when  $H_2PO_4^-$  concentration diminishes and BSA adsorption is facilitated by its negative charge, polarization resistance of CoCrMo in PBS and PBS+BSA solutions are similar and only in the solutions at pH 10, polarization resistance in PBS+BSA is higher than the one obtained in PBS.

Therefore, precipitation of phosphate compounds involving  $H_2PO_4^-$  is the main phenomenon that affects the corrosion mechanism in the passive domain of CoCrMo alloys.

With respect to the effect of pH on the anodic-cathodic transition and the cathodic domain, *i-E* representations of the potentiodynamic curves are shown in **Figure 4.31**. At each studied pH in the present work, the potential at which cathodic reaction initiates shifts towards more negative values with the pH increase. Specifically in the PBS+BSA solutions, the cathodic reaction rate decreases with the increase in the solution pH. While in the PBS solutions at pH 3 the cathodic current density is lower than at pH 7.4 at low overpotentials. This phenomenon, in which the cathodic reaction is suppressed at pH 3 and according to the mixed-potential theory, means that the anodic reaction of the alloys could also be suppressed due to the  $H_2PO_4^-$  compound precipitation. When the applied potential exceeds -0.5 V, the hydrogen evolution starts from water reduction at lower reaction rates with the pH increase. It is also important to note that phosphate species act as catalyser of water reduction into hydrogen and the global reaction may be considered as reversible (**reactions (2.12) and (2.13)**).



Therefore,  $H_2PO_4^-$  also contributes to the highest reduction reaction rate at the lowest pH and the corrosion mechanism seems much complicated because  $H_2PO_4^-$  would contribute to both the anodic dissolution reaction of the alloy and to the hydrogen evolution reaction in different ways, depending on the solution pH. Similar results were found by Kurosaki et al. when analysing the electrochemical behaviour of iron in PBS solutions [36]. On the other hand, in the range of  $pH > 5$ , the reduction of water molecule with the participation of  $H_2PO_4^-$  is predominant in the hydrogen evolution

reaction and this would explain the lower overpotential for the hydrogen reduction in neutral and alkaline solution pH.

#### B) INFLUENCE OF BSA

According to the potentiodynamic curves shown in **Figure 4.24**, influence of BSA on the electrochemical behaviour of CoCrMo alloy depends on the pH. It slightly affects the electrochemical response of the system in acidic solutions while it interferes in the cathodic reactions and in the anodic behaviour in neutral and alkaline solutions.

In acidic conditions it has been shown that  $\text{H}_2\text{PO}_4^-$  is mainly adsorbed and it forms a precipitate on the CoCrMo surface while BSA remains in the solution, therefore, there is a significant effect of the protein in this acidic condition, **Figure 4.24(a)**. Frateur et al. [65] also studied the adsorption process of BSA on passivated chromium and concluded that their results depend strongly on the dimensions of the protein that are taken into account at given a pH.

On the contrary, in neutral and basic media, BSA competes for adsorption on the metallic surface and reduces the cathodic reaction rate of the oxidant (water and dissolved oxygen) [14]. BSA acts as a barrier to the electronic transference at the interface biomaterial/body fluid which impedes the access of the oxidant to the CoCrMo surface. Therefore, the cathodic current densities in  $\text{N}_2$  and  $\text{O}_2$  atmospheres are very similar at pH 7.4 in BSA-containing solution, **Figure 4.24(b)**. In the PBS solutions at pH 10, **Figure 4.24(c)**, BSA also adsorbs on the electrode surface thus hindering the oxygen reduction reaction. This mechanism explains the higher resistance to the passive dissolution at that pH when compared to the non-containing BSA solutions. When no oxygen is present in the solution, the effect of BSA is only observed in the water reduction and therefore potentiodynamic curves are very similar at high cathodic overpotential than those measured without BSA.

It is possible to observe in **Figure 4.31** that the polarization resistance of the alloy under passive conditions does not strongly depend on the solution pH in the PBS+BSA solutions. Therefore one may conclude that an applied passive potential BSA adsorbs

on the alloy surface competing with phosphate compounds and depending on the nature of those compounds the final effect of the protein consists on either enhancing or blocking the passive dissolution. BSA effect is detrimental when substituting  $\text{H}_2\text{PO}_4^-$  sites (BSA decreases the resistance of CoCrMo to passive dissolution in acidic PBS solutions) but it increases the resistance when substituting  $\text{HPO}_4^{2-}$  sites (BSA slightly increases the resistance to passive dissolution in pH 7.4 and 10). In the PBS solution at pH 10 the highest concentration of the phosphate species in the solution is  $\text{HPO}_4^{2-}$ , **Figure 4.22**, which despite adsorbing on the CoCrMo surface does not strongly block the passive dissolution of the alloy. Therefore the resistance to passive dissolution is also given by the effect of the adsorbed BSA which enhances this resistance when compared to the PBS+BSA solution.

### C) INFLUENCE OF AERATION

Effect of aeration was clearly observed in the OCP results, **Figure 4.23**, which shows a positive shift of CoCrMo OCP towards more positive values in oxygen-containing solutions, particularly in neutral and basic solutions. Presence of oxygen enhances barrier film formation and increases electrode passivity [66], however, when analysing the CoCrMo in PBS solutions under well-established electrochemical conditions (at an applied passive potential) the effect of oxygen consists on decreasing the resistance of CoCrMo alloy to passive dissolution (**Figure 4.30**). Only in presence of BSA oxygen reduces the electrochemical charge measured during the potentiostatic tests, **Table 4.XIII**.

Phosphates are oxygen-dependent inhibitors [64], and thus their rate of action can ultimately be determined by the rate of oxygen diffusion to the surface, especially after the metal itself has consumed most of the oxygen in its own oxidation. The decrease in polarization resistance of the interface biomaterial/body fluid in the present case is due to the fact that  $\text{H}_2\text{PO}_4^-$  does not need oxygen to be adsorbed on the metallic surface and thus acting in the same way independently on the aeration conditions. Indeed oxygen has a detrimental effect on the passive dissolution of the CoCrMo alloy when compared to the oxygen-free solutions in all the studied

**CHAPTER 4. Electrochemical characterization of CoCrMo alloy in simulated body fluids**

conditions. This fact may be explained by the acceleration of oxidation kinetics produced under oxygenated conditions which increases the electrochemical reaction rates.

#### 4.5. Conclusions

Electrochemical techniques (open circuit potential, potentiodynamic and potentiostatic measurements and electrochemical impedance spectroscopy) were employed to characterize the electrochemical behaviour of CoCrMo biomedical alloy in different simulated body fluids. Influence of chemical composition of the electrolyte, pH, aeration and electrochemical conditions (i.e. applied potential) on the corrosion behaviour of CoCrMo alloys was analyzed. Thus, the main conclusions of the study are summarized as follows:

1. The main corrosion mechanism of the CoCrMo alloy is the passive dissolution. In addition, the electrochemical reactions occurring in the interface of the CoCrMo alloy oxide film/electrolyte are strongly dependent on the potential electrode. The adsorption of BSA take place on the CoCrMo alloy surface modifying the oxide film properties.
2. EIS has demonstrated to be a useful tool to analyse the corrosion behaviour of CoCrMo alloys as well as to study the modification of the passive film properties depending on the applied potential under potentiostatic conditions. The impedance spectra were described in terms of a simple equivalent circuit consisting of two serial *RC* circuits corresponding to the inner passive oxide layer and to the outer adsorbed layer. The model was found consistent with dc electrochemical results.
3. Electrochemical interface varies depending on the applied potential and chemical composition of the electrolyte. The cathodic domain is related to the reduction reaction which is limited by diffusion in presence of BS. In the active-passive transition two times constants can be clearly distinguished related to the initial reduction of the oxide film which is more enhanced in presence of phosphates. At an applied passive potential two times constants superposed also appears with high values of polarization resistances, characteristics of the passive conditions. Finally, at higher anodic potentials electrochemical measurements are typical of the oxidation reaction, where the impedance



#### CHAPTER 4. Electrochemical characterization of CoCrMo alloy in simulated body fluids

spectra show at lowest frequencies an inductive loop characteristic of adsorption process.

4. Adsorption of phosphates reduces the corrosion rate of the alloy while BSA acts in different ways. Under potentiodynamic conditions, BSA acts as cathodic inhibitor impeding the access of the oxidant to the metallic surfaces and accelerating the anodic reaction. Under potentiostatic conditions, at lower applied passive potentials BSA increases the corrosion resistance (blocking the surface) while at higher passive potentials the opposite effect is obtained (increase of the passive dissolution). In both cases, BSA effect on the passive film was enhanced in presence of phosphates.
5. The results show that the general corrosion behaviour of CoCrMo alloy depends on the solution pH. Thus, the effect of BSA and the aeration conditions are related to that pH value. In all tests, the cathodic current density is determined by the reduction of water and/or reduction of oxygen which depends on the pH and O<sub>2</sub> content.
6. At pH 3 no influence of BSA was observed in deoxygenated solutions which implies that BSA acts over the oxygen reduction reaction in acidic media. A noticeable influence of BSA addition was observed at pH 7.4 (mainly in aerated conditions). In the oxygen content solution, the cathodic reaction is mass transport limited. Finally, at pH 10, the influence of BSA was similar than in neutral solutions. Thus, in neutral and alkaline solutions BSA suppress mass transport limitation produced by the excess of oxygen in the electrolyte.
7. Under passive conditions, H<sub>2</sub>PO<sub>4</sub><sup>-</sup> favours the formation of passivating compounds which improves the resistance of the CoCrMo alloy to passive dissolution. Therefore, when the concentration of the H<sub>2</sub>PO<sub>4</sub><sup>-</sup> increases (when pH decreases), the polarization resistance of the alloy also increases.
8. BSA adsorbs on the metallic surface and competes with the different phosphates species for this adsorption thus enhancing or reducing the passive dissolution of the alloy depending on the solution pH. BSA effect is detrimental

when substituting  $\text{H}_2\text{PO}_4^-$  sites (pH 3) but it increases the CoCrMo resistance when substituting  $\text{HPO}_4^{2-}$  sites (pH 7.4 and pH 10).

9. Oxygen effect depends on the pH of the PBS solution but reduces the passive dissolution resistance of the alloy in all the studied conditions.

#### 4.6. References

- [1] W. P. Ren, D. C. Markel, R. Zhang, X. Peng, B. Wu, H. Monica, P. H. Wooley, *Biomaterials* 27 (2006) 5161-5169.
- [2] K. S. Katti, *Colloids and Surfaces B: Biointerfaces* 39 (2004) 133-142.
- [3] J. J. Jacobs, J. L. Gilbert, R. M. Urban, *Journal of Bone and Joint Surgery-American Volume* 80A (1998) 268-282.
- [4] M. A. Germain, A. Hatton, S. Williams, J. B. Matthews, M. H. Stone, J. Fisher, E. Ingham, *Biomaterials* 24 (2003) 469-479.
- [5] Y. Okazaki, E. Gotoh, *Biomaterials* 26 (2005) 11-21.
- [6] A. Masse, M. Bosetti, C. Buratti, O. Visentin, D. Bergadano, M. Cannas, *Journal of Biomedical Materials Research Part B-Applied Biomaterials* 67B (2003) 750-757.
- [7] J. H. Dumbleton, M. T. Manley, *Journal of Arthroplasty* 20 (2005) 174-188.
- [8] T. Hanawa, *Materials Science and Engineering: C* 24 (2004) 745-752.
- [9] E. Codaro, P. Melnikov, I. Ramires, A. Guastaldi, *Russian Journal of Electrochemistry* 36 (2000) 1117-1121.
- [10] I. Milosev, H.-H. Strehblow, *Electrochimica Acta* 48 (2003) 2767-2774.
- [11] A. W. E. Hodgson, S. Kurz, S. Virtanen, V. Fervel, C.-O. A. Olsson, S. Mischler, *Electrochimica Acta* 49 (2004) 2167-2178.
- [12] T. Hanawa, S. Hiromoto, K. Asami, *Applied Surface Science* 183 (2001) 68-75.
- [13] Y.-S. Li, K. Wang, P. He, B. X. Huang, P. Kovacs, *Journal of raman spectroscopy* 30 (1999) 97-103.
- [14] A. Igual Muñoz, S. Mischler, *Journal of the Electrochemical Society* 154 (2007) C562-C570.
- [15] I. Milosev, H. H. Strehblow, *Journal of biomedical materials research* 52 (2000) 404-412.
- [16] Y. Yan, A. Neville, D. Dowson, *Tribology International* 40 (2007) 1492-1499.
- [17] F. Contu, B. Elsener, H. Böhni, *Corrosion Science* 47 (2005) 1863-1875.
- [18] A. Sargeant, T. Goswami, *Materials & Design* 28 (2007) 155-171.
- [19] F. Watari, A. Yokoyama, M. Omori, T. Hirai, H. Kondo, M. Uo, T. Kawasaki, *Composites Science and Technology* 64 (2004) 893-908.

- [20] A. Ithurbide, I. Frateur, A. Galtayries, P. Marcus, *Electrochimica Acta* 53 (2007) 1336-1345.
- [21] J.F.Foster, V.M.Rosenoer, M.Oratz, M.A.Rothschild, *Albumin Structure, Function and Uses*, in: 1997, 53.
- [22] Zhijun Bai, Jeremy L.Gilbert, *ASM Handbook. Corrosion: Environments and Industries* 13C (2009) 837-852.
- [23] J. L. Gilbert and J. J. Jacobs, *The mechanical and electrochemical processes associated with taper fretting crevice corrosion: A review*, 1997.
- [24] S. E. Moulton, J. N. Barisci, A. Bath, R. Stella, G. G. Wallace, *Journal of Colloid and Interface Science* 261 (2003) 312-319.
- [25] S. Virtanen, I. Milosev, E. Gomez-Barrena, R. Trebse, J. Salo, Y. T. Kontinen, *Acta Biomaterialia* 4 (2008) 468-476.
- [26] H. H. Hassan, M. A. Amin, S. Gubbala, M. K. Sunkara, *Electrochimica Acta* 52 (2007) 6929-6937.
- [27] K. S. Raja, D. A. Jones, *Corrosion Science* 48 (2006) 1623-1638.
- [28] A. Foelske, H.-H. Strehblow, *Surface and Interface Analysis* 29 (2000) 548-555.
- [29] J. J. Jacobs, R. M. Latanision, R. M. Rose, S. J. Veeck, *Journal of Orthopaedic Research* 8 (1990) 874-882.
- [30] J. Cawley, J. E. P. Metcalf, A. H. Jones, T. J. Band, D. S. Skupien, *Wear* 255 (2008) 999-1006.
- [31] H. S. Dobbs, J. L. M. Robertson, *Journal of Materials Science* 18 (1983) 391-404.
- [32] H. E. Placko, S. A. Brown, J. H. Payer, *Journal of biomedical materials research* 39 (1998) 292-299.
- [33] V.Amigó Borrás, A.Paolini, J.F.Moreno Ballester, A.Vicente Escuder, F.Romero Sanchís. Estudio de la Influencia de los tratamientos térmicos de la microdureza y microestructura de aleaciones Co-Cr-Mo. *National Congress of Mechanical Properties of Solids*, 487-496. 2002.
- [34] S. Hiromoto, E. Onodera, A. Chiba, K. Asami, T. Hanawa, *Biomaterials* 26 (2005) 4912-4923.
- [35] A. C. Lewis, M. R. Kilburn, P. J. Heard, T. B. Scott, K. R. Hallam, G. C. Allen, I. D. Learmonth, *Journal of Orthopaedic Research* 24 (2006) 1587-1596.
- [36] M. Kurosaki, M. Seo, *Corrosion Science* 45 (2003) 2597-2607.

**CHAPTER 4. Electrochemical characterization of CoCrMo alloy in simulated body fluids**

- [37] A. Igual Muñoz and S. Mischler, Inter-laboratory study on electrochemical methods for the characterisation of CoCrMo biomedical alloys in simulated body fluids, European Federation of Corrosion by Maney Publishing on behalf of The Institute of Materials, Minerals & Mining, 2011.
- [38] A. Kocijan, I. Milosev, D. K. Merl, B. Pihlar, *Journal of Applied Electrochemistry* 34 (2004) 517-524.
- [39] M. Metikos-Hukovic, Z. Pilic, R. Babic, D. Omanovic, *Acta Biomaterialia* 2 (2006) 693-700.
- [40] S. R. Taylor, E. Gileadi, *Corrosion* 51 (1995) 664-672.
- [41] D. Landolt, *Corrosion and surface chemistry of metals*, 2007.
- [42] S. Karimi, T. Nickchi, A. Alfantazi, *Corrosion Science* 53 (2011) 3262-3272.
- [43] Marcel Pourbaix, *Atlas of electrochemical Equilibria in Aqueous Solutions*, 1974.
- [44] D. Sun, J. A. Wharton, R. J. K. Wood, *Wear* 267 (2009) 1845-1855.
- [45] D. Sun, J. A. Wharton, R. J. K. Wood, *Wear* 267 (2009) 52-60.
- [46] A. W. Hodgson, S. Mischler, B. Von Rechenberg, S. Virtanen, *Proceedings of the Institution of Mechanical Engineers Part H-Journal of Engineering in Medicine* 221 (2007) 291-303.
- [47] J. R. Scully, D. C. Silverman, and M. W. Kending, *Electrochemical impedance. Analysis and interpretation*, Philadelphia (United States of America), 1993.
- [48] I. Milosev, T. Kosec, H. H. Strehblow, *Electrochimica Acta* 53 (2008) 3547-3558.
- [49] M. E. P. Souza, M. Ballester, C. M. A. Freire, *Surface and Coatings Technology* 201 (2007) 7775-7780.
- [50] P. Girault, J. L. Grosseau-Poussard, J. F. Dinhut, L. Marechal, *Nuclear Instruments and Methods in Physics Research Section B: Beam Interactions with Materials and Atoms* 174 (2001) 439-452.
- [51] Y. F. Kao, T. D. Lee, S. K. Chen, Y. S. Chang, *Corrosion Science* 52 (2010) 1026-1034.
- [52] K. C. Emregül, A. A. Aksüt, *Corrosion Science* 42 (2000) 2051-2067.
- [53] P. G. Righetti, T. Caravaggio, *Journal of Chromatography A* 127 (1976) 1-28.
- [54] M. A. Khan, R. L. Williams, D. F. Williams, *Biomaterials* 20 (1999) 631-637.
- [55] F. J. Presuel-Moreno, M. A. Jakab, J. R. Scully, *Journal of the Electrochemical Society* 152 (2005) B376-B387.

- [56] I. Catelas, A. Petit, H. Vali, C. Fragiskatos, R. Meilleur, D. J. Zukor, J. Antoniou, O. L. Huk, *Biomaterials* 26 (2005) 2441-2453.
- [57] C. J. L. Silwood, M. Grootveld, *Journal of Inorganic Biochemistry* 99 (2005) 1390-1400.
- [58] A. Ouerd, C. Alemany-Dumont, B. Normand, S. Szunerits, *Electrochimica Acta* 53 (2008) 4461-4469.
- [59] D. Sun, J. A. Wharton, R. J. K. Wood, L. Ma, W. M. Rainforth, *Tribology International* 42 (2009) 99-110.
- [60] A. Kocijan, I. Milosev, B. Pihlar, *Journal of Materials Science-Materials in Medicine* 15 (2004) 643-650.
- [61] M. Metikos-Hukovic, R. Babic, *Corrosion Science* 49 (2007) 3570-3579.
- [62] C. Tkaczyk, O. L. Huk, F. Mwale, J. Antoniou, D. J. Zukor, A. Petit, M. Tabrizian, *Biomaterials* 30 (2009) 460-467.
- [63] A. C. Lewis, P. J. Heard, *Journal of Biomedical Materials Research Part A* 75A (2005) 365-373.
- [64] J. Sinko, *Progress in Organic Coatings* 42 (2001) 267-282.
- [65] I. Frateur, J. Lecoeur, S. Zanna, C. O. A. Olsson, D. Landolt, P. Marcus, *Electrochimica Acta* 52 (2007) 7660-7669.
- [66] W. A. Badawy, M. M. El-Rabiee, N. H. Helal, H. Nady, *Electrochimica Acta* 56 (2010) 913-918.

## CHAPTER 5: MECHANISMS OF BSA ADSORPTION

---

### 5.1. Introduction

Proteins are relatively large biomolecules and have a tendency to accumulate at the interface between solutions and solid surfaces [1,2]. The adsorption of proteins at interfaces is a widespread phenomenon in both natural and man-made systems. Protein adsorption occurs when any protein-containing fluid comes into contact with a foreign surface. There has been considerable interest in the interfacial behaviour of proteins in the human body as a result of problems associated with bacterial growth [3,4] and metal dissolution [5-7]. In the field of biomaterials and medical implants, it is widely accepted that one of the initial events that significantly influences biocompatibility is the nearly instantaneous adsorption of proteins from biological fluids onto biomaterial surfaces. This adsorbed protein film may be beneficial for certain biomedical applications where the immobilization of specific proteins and enzymes is necessary or desirable, such as in the case of immunoassays and biosensors [8]; on some metallic materials and alloys even the adsorption process reduces the corrosion rate [9].

However, for serum-contacting medical devices (including implants), the complex layer of adsorbed plasma proteins is generally unfavourable and could potentially lead to major complications including microbial infections [10]. As consequence of this process, on some metal surfaces an accelerated metal ion release rate was obtained [6,7,11].

The enhancement of dissolution rate in the presence of proteins can be explained by the formation of biofilm or complexes between metal ions and proteins. Although the biofilm also lubricates the surface, the total material degradation was increased due to increased corrosion [5,6,12,13].

Several studies have been made on the interaction of proteins with metal surfaces to determine the molecular conformation or orientation of the adsorbed molecules. It was found that the interactions between proteins and surfaces, resulting in adsorption, can be affected by a number of factors, such as temperature, conformation of the protein in solution and its bulk concentration, pH, ionic strength, and the surface properties of the material onto which adsorption occurs [1,14].

Electrochemical studies have been carried out on the adsorption of serum proteins [15] on titanium and titanium oxides [1,16], stainless steels [17-20] and platinum [21]; however, no literature has been found on the behaviour of serum protein adsorption on CoCrMo alloys. Once implanted and exposed to the aggressive body environment (biological fluids in the body contain water, salt, dissolved oxygen, bacteria, proteins and various ions such as chloride and hydroxide), CoCrMo tends to corrode over time and metal ions become clinically harmful resulting in a lack of biocompatibility of the implant [22]. Indeed, correlations between metal release from CoCrMo hip joint implants and their clinical behaviour could be established in in-vivo studies involving animal and human patients experiments [23-26]. Other studies confirmed that electrochemical corrosion caused loss of biocompatibility and failure of CoCrMo implants [27-30]. Despite the clinical relevance of the corrosion of CoCrMo implant alloys, the involved phenomena are still little understood and few studies are available on this topic.



## CHAPTER 5. Mechanisms of BSA adsorption

The objective of this chapter is to elucidate the mechanism of BSA adsorption onto CoCrMo biomedical alloy using electrochemical techniques. Electrochemical parameters obtained from the electrochemical tests allow one to determine the adsorption isotherms, surface concentration of adsorbed protein, surface affinity of the protein, Gibbs free energy, enthalpy and entropy of adsorption process. The effect of surface condition (passivation time) on the adsorption mechanisms of BSA on a CoCrMo biomedical alloy was analysed. This study provides a better understanding of the interfacial behaviour of the biomaterial in contact with the BSA (model protein) under different physical and chemical conditions.

## **5.2. Thermodynamical characterization of the BSA adsorption on CoCrMo surface**

### **5.2.1. SIMULATED BODY FLUIDS**

Solutions of bovine serum albumin, BSA, (from Merck Fraction V) were prepared by dissolving different amounts of protein in 0.14 M NaCl solution adjusting the pH at 7.4 with the addition of NaOH concentrated. In order to analyse the adsorption mechanism of the protein 5, 20, 50 and 500 mg L<sup>-1</sup> BSA were added to the NaCl electrolyte. Although these solutions are not buffered, the pH was controlled with a pH-meter during the experiment which revealed that no significant variations in the solution pH were produced. All chemicals were of analytical grade and doubly distilled grade water was employed in the preparation of the solutions. The solutions were preheated at 298, 313, 323 and 333 K before carrying out the electrochemical experiments and temperatures were maintained during the experimental test.

### **5.2.2. ELECTROCHEMICAL MEASUREMENTS**

The electrochemical tests conducted for the thermodynamic characterization was potentiodynamic curves and electrochemical impedance spectroscopy (EIS). All measurements were carried out using a potentiostat Solartron 1287. The same three-electrode electrochemical setup included a platinum wire as counter electrode and a Ag/AgCl (3M KCl) reference electrode was employed in this study (Chapter 3). Previously heated electrolyte solutions were poured at the corresponding test temperatures (298, 313, 323 and 333 K) into the double wall cell heated through water circulation. All experiments were carried out under aerated conditions.

## EXPERIMENTAL PROCEDURE

Two electrochemical tests were carried out:

1) **Potentiodynamic curves** with the following experimental sequence:

- Cathodic cleaning by potentiostatic test at -1.5 V during 5 minutes.
- Measurement of the OCP during 60 minutes. **OCP** value was extracted as the average value of the OCP in the last minute.
- Potentiodynamic curves starting 0.2 V below the OCP scanning in the anodic direction until 1.5 V at the scan rate of  $2 \text{ mV s}^{-1}$ . In order to analyse the thermodynamic behaviour of the adsorption process  $E_{corr}$ ,  $i_{corr}$ ,  $i_p$  (at 0.1 V) and  $E_{br}$  were extracted.

2) **OCP+EIS**

- Cathodic cleaning by potentiostatic test at -1.5 V during 5 minutes.
- Measurement of the OCP during 60 minutes. **OCP** value was extracted as the average value of the OCP in the last minute.
- EIS measurements under open circuit conditions. Measurements have been performed starting from 1 mHz up to  $10^5$  Hz, at 10 data cycles/decade with an AC amplitude of  $\pm 10$  mV.

In order to verify the reproducibility of the measurements three repetitions of each test were carried out.

### 5.2.3. EXPERIMENTAL RESULTS

#### A) OPEN CIRCUIT POTENTIAL

OCP values are summarized in **Table 5.1**. In these experiments a continuous increase of the OCP with time until reaching a stable value is also observed (**Figure 5.1**). This trend indicates the continuous and quasi-stable passivation of the CoCrMo alloy in all BSA solutions and temperatures.

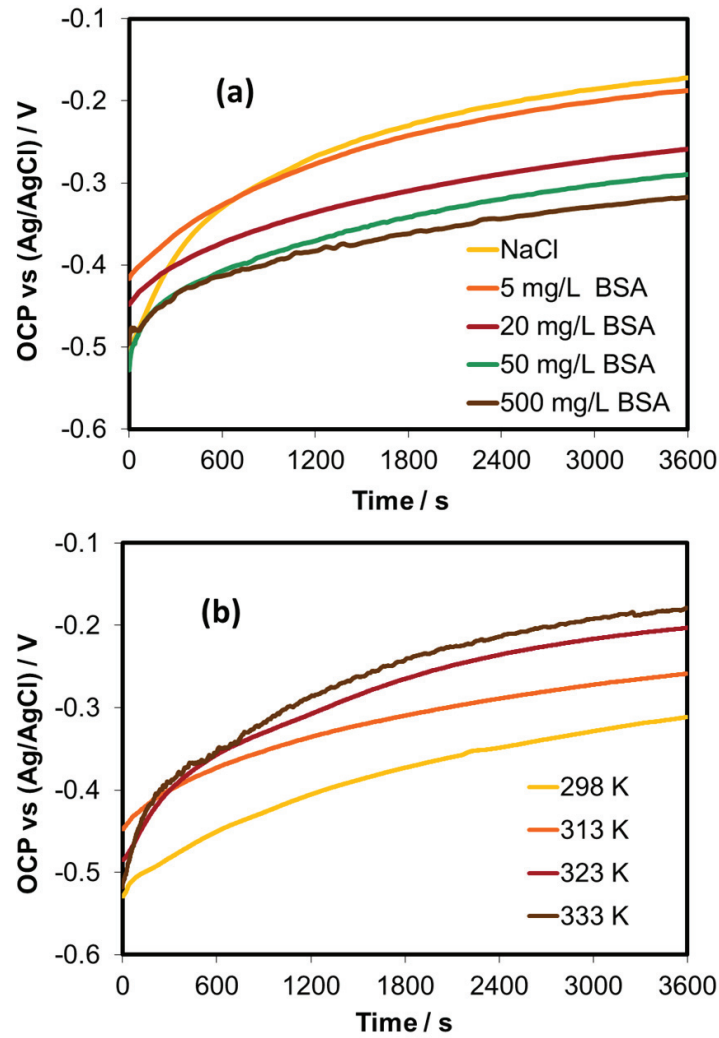


**Figure 5.1.** Open Circuit Potential evolution during 1 hour (a) at 313K in 0.14 M NaCl solution with different BSA additions and (b) in 0.14 M NaCl+20 mg L<sup>-1</sup> of BSA at different temperatures.

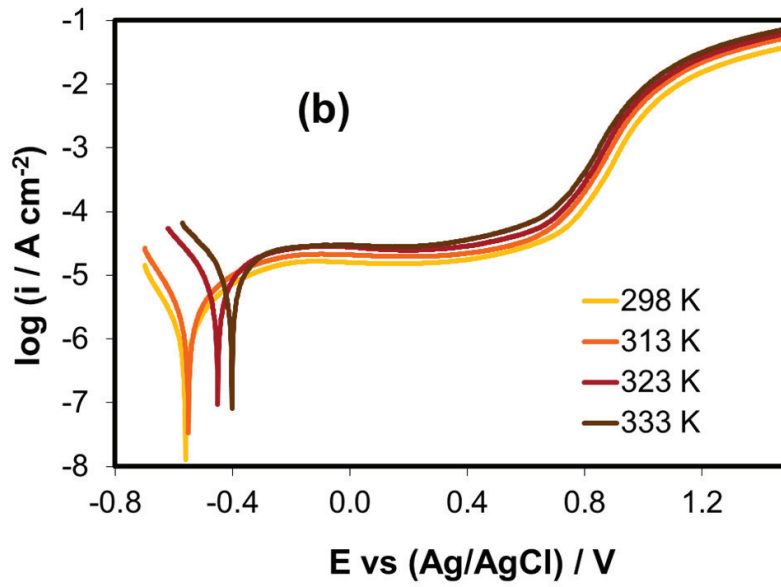
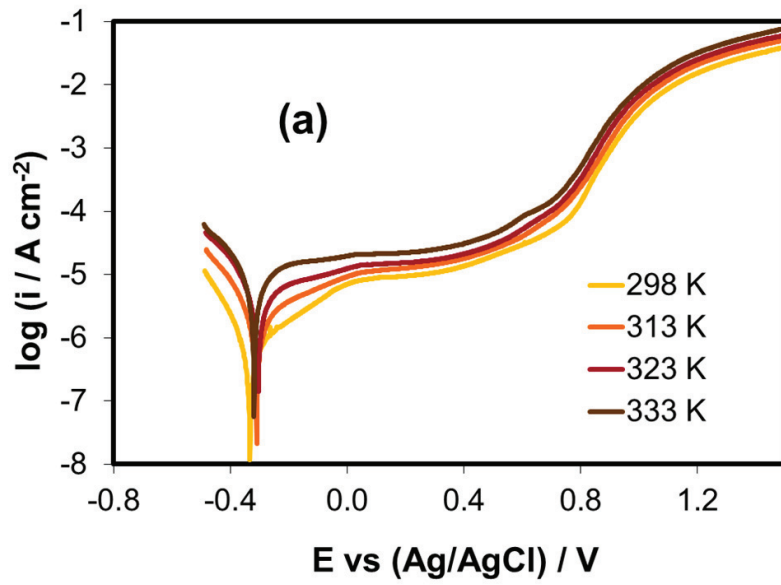
The increase of BSA concentration generally shifts the OCP towards more cathodic potentials (**Figure 5.2(a)**) at all temperatures with respect to the control value (saline medium) which can be related to the enhancement of the anodic reaction by the binding of proteins and metal ions [31]. The standard deviation associated with the OCP values shows the good reproducibility of the experimental OCP obtained for each experimental condition.

A displacement of the OCP towards nobler values with temperature was observed for the biomedical alloy in NaCl solution and BSA-containing solutions at concentrations below  $500 \text{ mg L}^{-1}$  (**Figure 5.2(b)**) where temperature has the opposite effect. At higher temperatures a stabilization of the OCP values was observed. Nevertheless, in the NaCl solution with  $500 \text{ mg L}^{-1}$  of BSA the decrease of potential with temperature is almost linear, reaching for all temperatures the lowest values of OCP at this BSA concentration.

## B) POTENTIODYNAMIC CURVES

Anodic polarization curves of CoCrMo obtained at different temperatures in NaCl and BSA-containing solutions are shown in **Figure 5.2**. Four characteristic potential domains can be also distinguished in these potentiodynamic curves. A short cathodic domain can be observed at potentials below  $E_{corr}$  at which the current density is given by the reduction of water and partially dissolved oxygen. The transition from cathodic to anodic current at the corrosion potential lies between -0.2 and -0.5 V. The passive domain is extended in a broad range of potentials (from -0.4 up to 0.5 V) which is wider at lower temperatures. Finally, the transpassive domain shows a current increase above 0.5 V due to the transpassive dissolution of oxides and water oxidation.

The electrochemical parameters extracted from the anodic potentiodynamic curves are shown in **Table 5.I**. Corrosion potential ( $E_{corr}$ ) and corrosion current density values ( $i_{corr}$ ) were obtained using the Tafel analysis at the different temperatures (see *Experimental Techniques*, Chapter 3). In all cases charge transfer was assumed and lineal extrapolation of cathodic and anodic curves was carried out around  $E_{corr} \pm 0.1$  V. In general, corrosion potentials shift towards more anodic potential values and breakdown potentials ( $E_{br}$ ) decrease with temperature. No significant influence of temperature was observed on  $i_{corr}$  values in solutions with BSA from 0 to 20 mg L<sup>-1</sup> (in low protein concentrations). However, when the BSA concentration was above 20 mg L<sup>-1</sup>,  $i_{corr}$  significantly increased at the studied range of temperatures. On the other hand, when the concentration of BSA increased until 500 mg L<sup>-1</sup> an  $i_{corr}$  decrease was observed at all temperatures. This phenomenon was also observed in the passive current density ( $i_p$ ). The low standard deviation associated with the values of the electrochemical parameters demonstrates the good reproducibility of the experimental potentiodynamic curves obtained in all experimental conditions and their good consistency. The variation of the  $i_{corr}$  and the  $i_p$  with temperature and BSA concentration was represented in **Figure 5.3** where the described trend can be clearly observed.



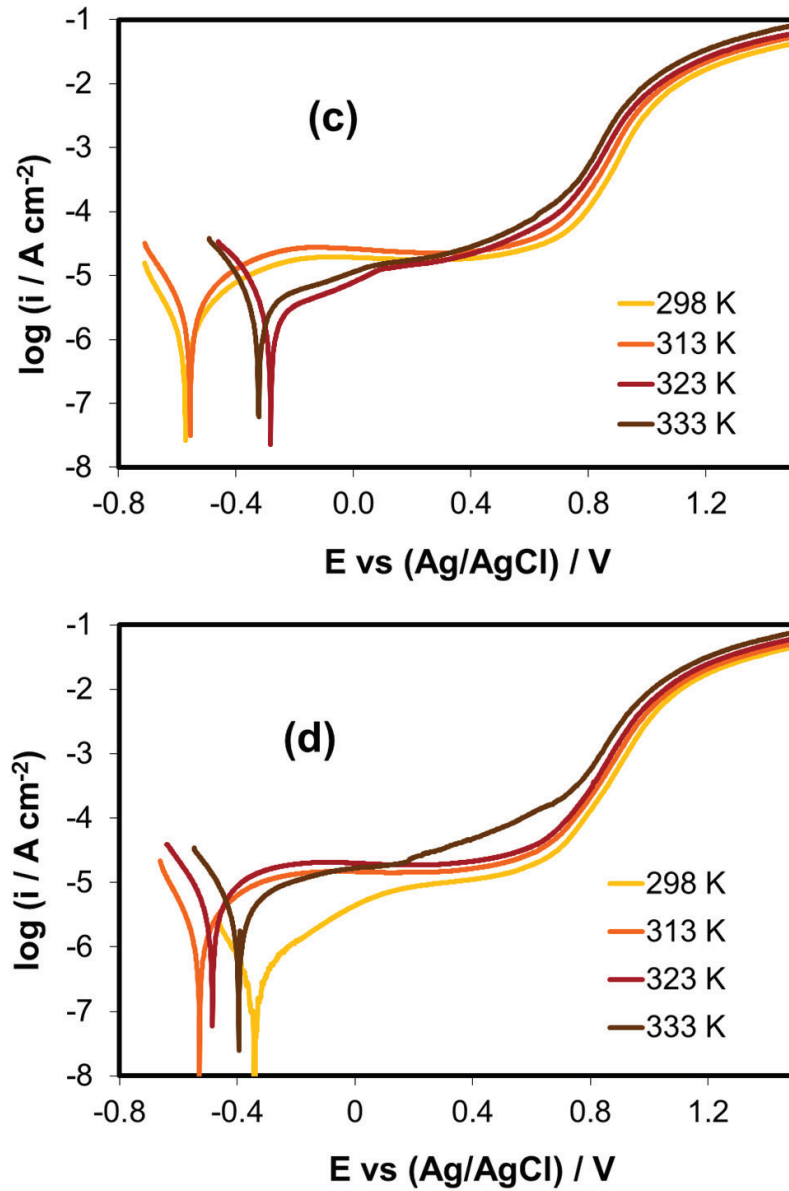


Figure 5.2. Potentiodynamic curves of CoCrMo alloy in 0.14 M solutions with (a) 5 mg L<sup>-1</sup>, (b) 20 mg L<sup>-1</sup>, (c) 50 mg L<sup>-1</sup> and (d) 500 mg L<sup>-1</sup> of BSA at different temperatures.



**Table 5.I.** Electrochemical parameters of the CoCrMo alloy in saline solutions without and with BSA additions at different temperatures and pH 7.4.

<b>ELECTROCHEMICAL PARAMETERS</b>					
<i>T</i> (K)	<i>OCP</i> (mV)	<i>i<sub>corr</sub></i> ( $\mu\text{A cm}^{-2}$ )	<i>E<sub>corr</sub></i> (mV)	<i>i<sub>p</sub></i> ( $\mu\text{A cm}^{-2}$ )	<i>E<sub>br</sub></i> (mV)
<b>NaCl</b>					
298	-259 ± 4	0.09 ± 0.01	-420 ± 14	6.5 ± 0.2	817 ± 13
313	-196 ± 22	0.20 ± 0.05	-315 ± 25	9.0 ± 0	775 ± 25
323	-155 ± 25	0.43 ± 0.05	-158 ± 2	10.8 ± 0.3	728 ± 15
333	-135 ± 2	0.70 ± 0.10	-210 ± 30	21.1 ± 1.2	675 ± 8
<b>NaCl + 5 mg L<sup>-1</sup> BSA</b>					
298	-263 ± 5	0.12 ± 0.02	-333 ± 17	9.1 ± 0.3	779 ± 21
313	-202 ± 32	0.18 ± 0.02	-310 ± 19	12.1 ± 0.1	727 ± 16
323	-180 ± 36	0.35 ± 0.07	-304 ± 24	14.8 ± 0.5	696 ± 7
333	-187 ± 12	0.37 ± 0.15	-319 ± 86	21.1 ± 0.6	639 ± 5
<b>NaCl + 20 mg L<sup>-1</sup> BSA</b>					
298	-293 ± 30	0.16 ± 0.03	-561 ± 23	15.2 ± 1.1	789 ± 12
313	-261 ± 16	0.21 ± 0.03	-550 ± 19	19.6 ± 0.7	747 ± 15
323	-181 ± 22	0.44 ± 0.05	-451 ± 23	25.1 ± 0.6	721 ± 21
333	-160 ± 26	0.49 ± 0.09	-402 ± 32	27.9 ± 1.2	682 ± 5
<b>NaCl + 50 mg L<sup>-1</sup> BSA</b>					
298	-311 ± 11	2.10 ± 0.10	-572 ± 19	17.6 ± 0.8	792 ± 2
313	-264 ± 28	3.87 ± 0.15	-556 ± 18	22.4 ± 1.2	748 ± 2
323	-243 ± 17	5.40 ± 0.55	-283 ± 7	23.2 ± 0.9	704 ± 1
333	-239 ± 22	6.90 ± 0.30	-322 ± 30	27.8 ± 1.3	641 ± 15
<b>NaCl + 500 mg L<sup>-1</sup> BSA</b>					
298	-303 ± 15	0.90 ± 0.01	-339 ± 6	9.5 ± 0	782 ± 17
313	-320 ± 19	2.30 ± 0.17	-528 ± 17	14.3 ± 0.4	747 ± 18
323	-312 ± 6	4.90 ± 0.30	-484 ± 44	18.6 ± 0.6	725 ± 12
333	-345 ± 14	5.53 ± 0.25	-395 ± 13	20.1 ± 1.0	567 ± 4

The role of BSA on the electrochemical behaviour of CoCrMo alloy was described in the Chapter 4 and also previously reported by Igual and Mischler [31]. BSA acts as inhibitor of the cathodic reaction and accelerates the anodic reaction. The inhibition effect can be explained by the presence of adsorbed BSA that may impede the access of the oxidant to the metallic surface [32]. On the other hand, the adsorption of the protein can bind to metal ions and transport them away from the solution/passive film interface [5,16,31,33]. Under the considered experimental conditions (potentiodynamic conditions), according to *OCP*, *i<sub>corr</sub>* and *i<sub>p</sub>* results, the presence of protein leads to the formation of a passive film less noble and less protective than in the saline solution. This is corroborated by the increase in *i<sub>corr</sub>* (above 20 mg L<sup>-1</sup>) and *i<sub>p</sub>* parameters with BSA respect to the NaCl solution.

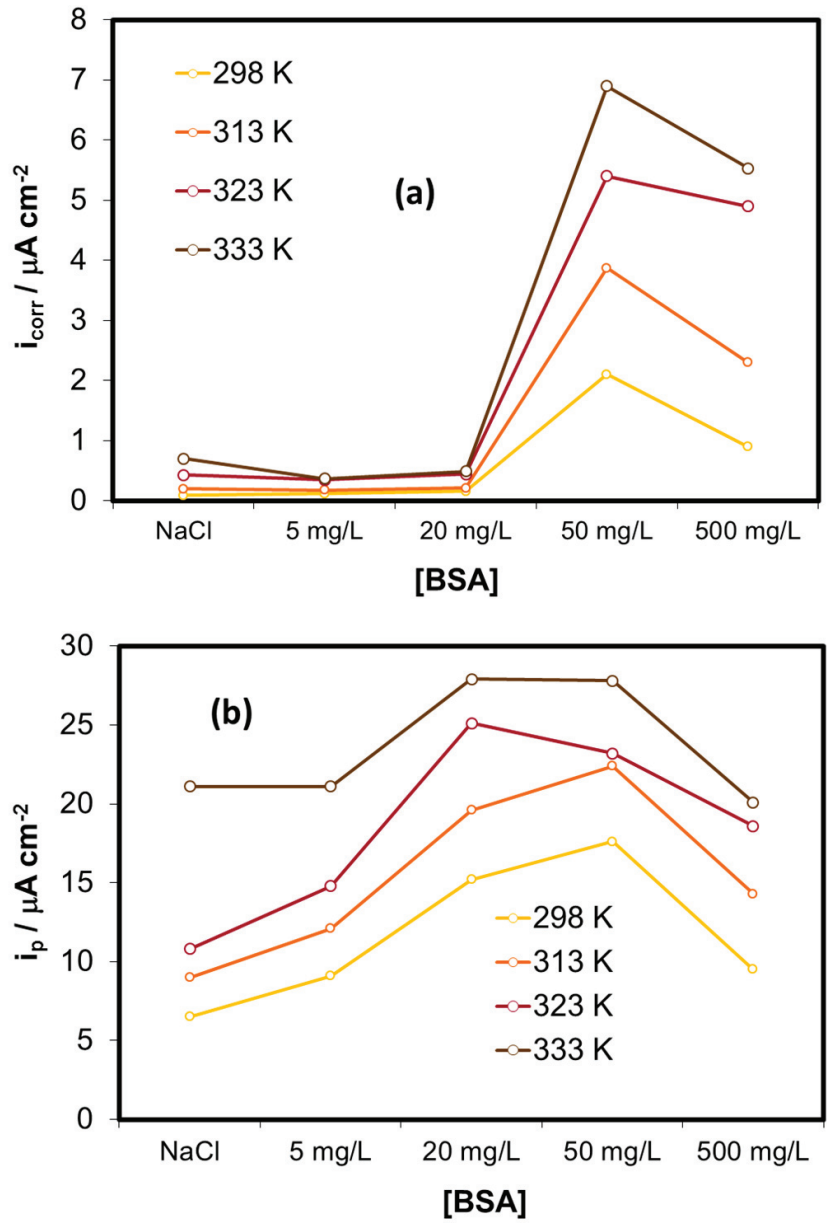


**Figure 5.3.**  $i_{corr}$  and  $i_p$  extracted from the potentiodynamic curves for the CoCrMo alloy at different temperatures and BSA concentrations.

This behaviour can be described through the Evans diagrams represented in **Figure 5.4**. In this graph, the double action (role of cathodic inhibitor and anodic catalyser) of BSA on CoCrMo alloys is described in NaCl solutions with 50 and 500 mg L<sup>-1</sup> of BSA. First of all, at low BSA concentration (represented in **Figure 5.4(a)**), the addition of BSA reduces the cathodic reaction rate (displaces the cathodic Tafel slope towards lower current density values, from **C0** to **C1**) and on the other hand BSA increases the dissolution rate (displacement of the anodic Tafel slope towards higher current density values, from **A0** to **A1**). The higher values of  $i_{corr}$  denote that the latter predominates over the cathodic reaction. At higher BSA concentrations (500 mg L<sup>-1</sup>) the following electrochemical effects can be observed, **Figure 5.4(b)** and **5.4(c)**; stronger inhibition effect on the cathodic reaction (independently on the temperature) and lower increase of the dissolution rate with respect to the NaCl solution with 50 mg L<sup>-1</sup> of BSA.

**Figure 5.4(b)** shows the influence of high BSA concentrations (500 mg L<sup>-1</sup>) at lower temperatures (between 298 and 313 K) by means of the Evans diagrams. In this diagram the cathodic Tafel slope is displaced towards lower current density values (from **C0** to **C2**), reaching values of current density lower than the obtained in 50 mg L<sup>-1</sup> of BSA (comparing **C1** with **C2**). According to these results, the cathodic inhibition process is favoured with the increase of the BSA addition. On the other hand, the displacement of the anodic Tafel slope is towards higher current density values (from **A0** to **A2**); however this increase is lower in the highest BSA-containing solutions (from **A1** to **A2**). These results indicate the loss of catalytic effect of the BSA on the anodic reaction in solutions with 500 mg L<sup>-1</sup> of BSA when compared to 50 mg L<sup>-1</sup>, probably related to the blocking effect of the protein as stated by Afonso et al [34]. Furthermore, the increase of the BSA concentration can limit the diffusion of oxygen onto the surface affecting the stability of the passive layer which depends on the availability of oxygen and/or acts like a barrier, i.e. increasing the corrosion resistance [35].

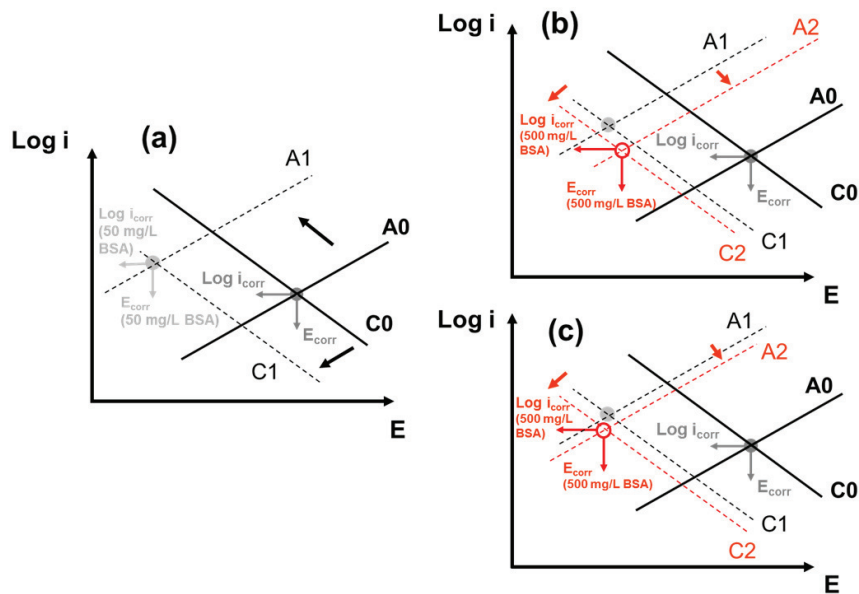


**Figure 5.4.** Mixed potential theory applied to interpret the effect of BSA concentration on CoCrMo corrosion potential and corrosion current density. **(a)** Influence of BSA concentration ( $50 \text{ mg L}^{-1}$ ) on cathodic/anodic Tafel slopes of CoCrMo biomedical alloy. **(b)** Influence of BSA concentration ( $500 \text{ mg L}^{-1}$ ) at 298-313K. **(c)** Influence of BSA concentration ( $500 \text{ mg L}^{-1}$ ) at 323-333K.

**Figure 5.4(c)** shows the influence of high BSA concentrations ( $500 \text{ mg L}^{-1}$ ) at higher temperatures (between 323 and 333 K) by means of the Evans diagrams. In this case, the displacement of the cathodic Tafel slope (**C2**) has the same magnitude than in **Figure 5.4(b)**. It can be concluded that, in the whole range of studied temperatures, the BSA adsorption acts as inhibitor of the cathodic reaction independently of the temperature range (similar displacement of the cathodic slope in all cases). However, although the displacement of the anodic slope follows the same trend with BSA concentration (increases the current density values (from **A0** to **A2**)), the change with respect to **A1** is not significant. Thus, at higher temperatures, no significant changes in the kinetics of the anodic reaction are obtained even at high BSA concentrations which could be related to the BSA denaturation.

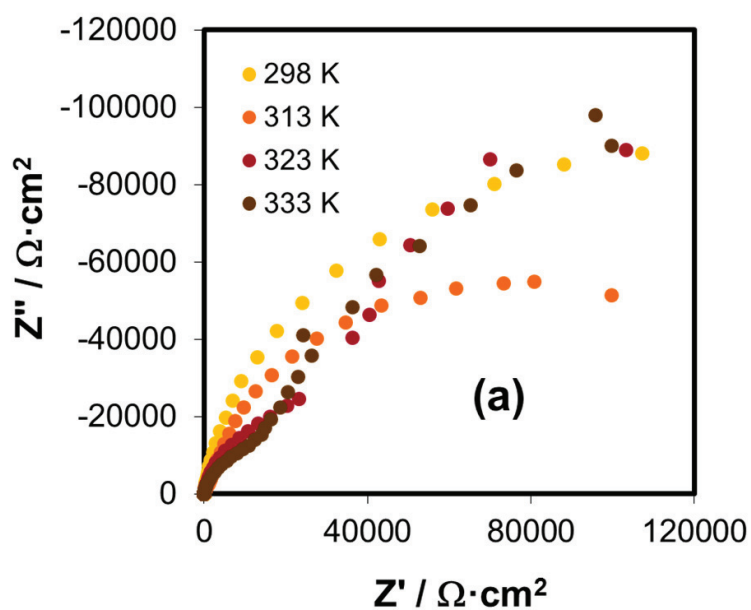
## CHAPTER 5. Mechanisms of BSA adsorption

The main conclusions extracted from the Evans diagrams (**Figure 5.4**) are the following: BSA acts as cathodic inhibitor (diminishing the cathodic reaction rate). This behaviour is more noticeable at lower BSA concentrations since no differences are observed in NaCl solutions with 50 and 500 mg L<sup>-1</sup> of BSA. On the other hand, BSA catalyses the anodic reaction since it increases the anodic reaction rate but the effect depends on the BSA concentration and the temperature.

### C) ELECTROCHEMICAL IMPEDANCE SPECTROSCOPY

Electrochemical impedance spectroscopy was employed to investigate the film/electrolyte-interface on the CoCrMo alloy. EIS was measured at OCP. At this potential the spontaneous formation of the oxide layer on the metal surface is observed in all cases (OCP shifted towards more positive values with time) and the final values of the OCP achieved after one hour of immersion lied within the passive domain of the alloy (**Figure 5.2**). This corroborates again the spontaneity of the passivity process of the CoCrMo biomedical alloy.

Examples of the impedance spectra at OCP are shown in **Figure 5.5** and **Figure 5.6** in form of Nyquist diagrams (**Figure 5.5(a)**) and **Figure 5.6**) and Bode plots (**Figure 5.5(b)**).



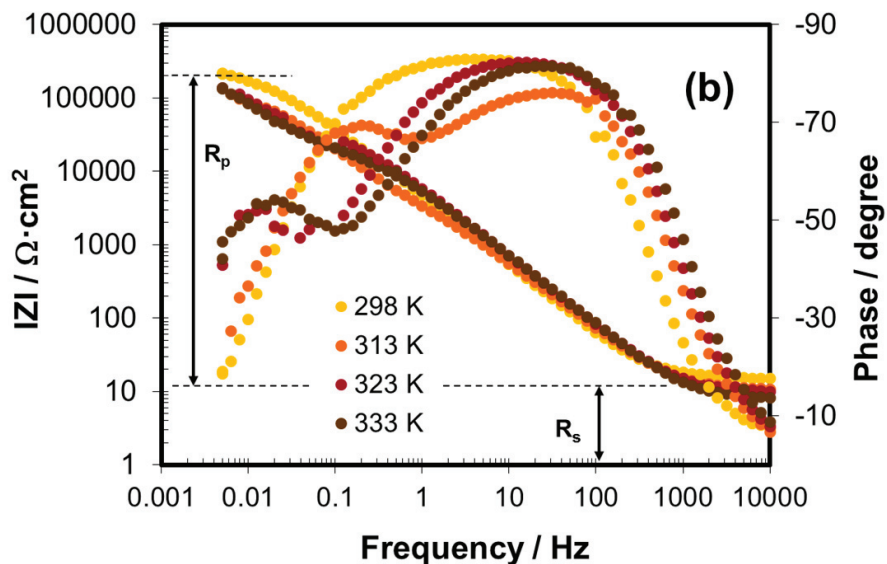


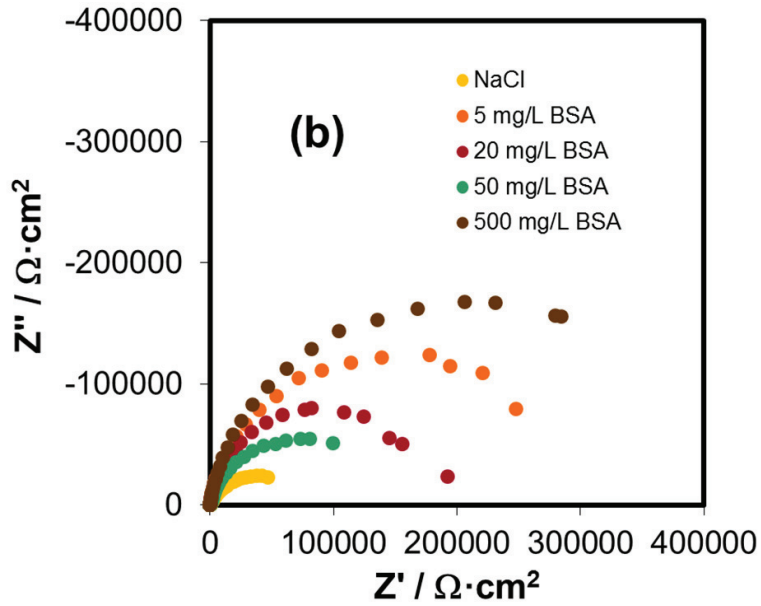
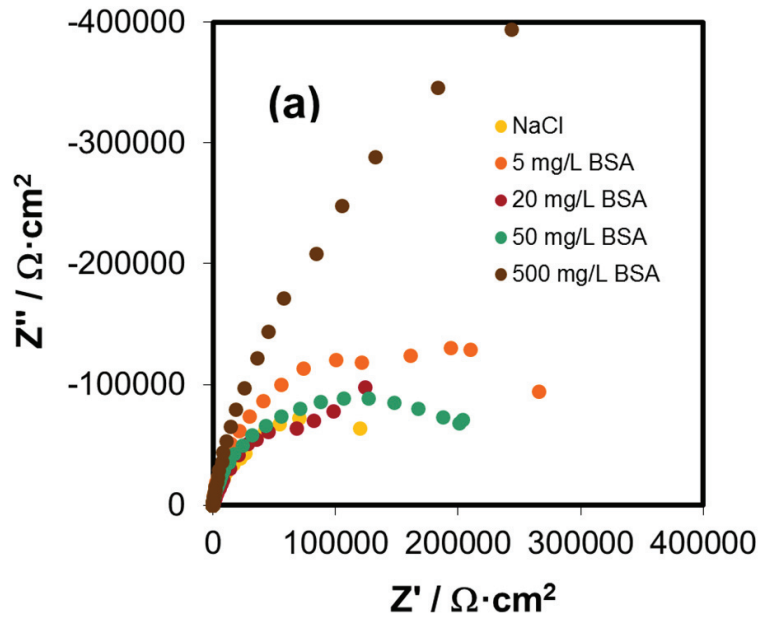
**Figure 5.5.** (a) Nyquist diagrams and (b) Bode plots of the CoCrMo alloy after 1h of immersion at OCP in NaCl + 50 mg L<sup>-1</sup> BSA at different temperature and pH 7.4.

Three distinctive segments of the spectra depending on the frequency range are observed. The solution resistance ( $R_s$ ) obtained at the highest frequencies (where the absolute impedance curve is almost independent of the frequency and the phase angle value approaching 0°) decreases with temperature. At the lower medium-frequency region, a quite linear relationship can be observed between the absolute impedance and the frequency with a slope close to -1 and the phase angle approximately -80°. Capacitive behaviour of the electrode/electrolyte interface can be observed in this frequency region. In the low-frequency region, the resistive behaviour of the electrode is not visible; i.e. the region where the absolute impedance is independent of the frequency ( $DC$  limit) is not attained. In addition, it is also interesting to note that the capacitive region starts at rather lower frequencies and extends deep into the low-frequency region (**Figure 5.5**). In all cases temperature shifted the Bode plot towards higher frequencies. Furthermore, at higher temperatures two time constants can be clearly distinguished.

The Nyquist plots of the CoCrMo alloy at each temperature and BSA solutions are represented in **Figure 5.6**. The EIS diagrams exhibit the expected passive state shape characterized by high impedance values with capacitive behaviour [36-38]. In general, BSA increased the diameter of the semicircles which is related to the increase in the charge transfer resistance.

Two overlapped time constants can be considered in the impedance spectra shown in **Figure 5.6**. The first corresponding to an outer layer (attributed to the presence of inhomogeneous passive film and to the passive dissolution of the passive layer) and the second related to the oxide film formed on the CoCrMo alloy. The EEC used to model the experimental EIS data consist of two sub-circuits  $RC$  in series (described in Chapter 3, *Experimental techniques*). Thus, one time constant is attributed to the oxide resistance ( $R_{in}$ )/capacitance ( $C_{in}$ ) parallel combination across the oxide and the second is attributed to the charge transfer resistance ( $R_{out}$ )/double layer capacitance ( $C_{out}$ ) parallel combination [31]. The electrical parameters obtained after fitting the experimental data to the proposed EEC are summarized in **Table 5.II**.





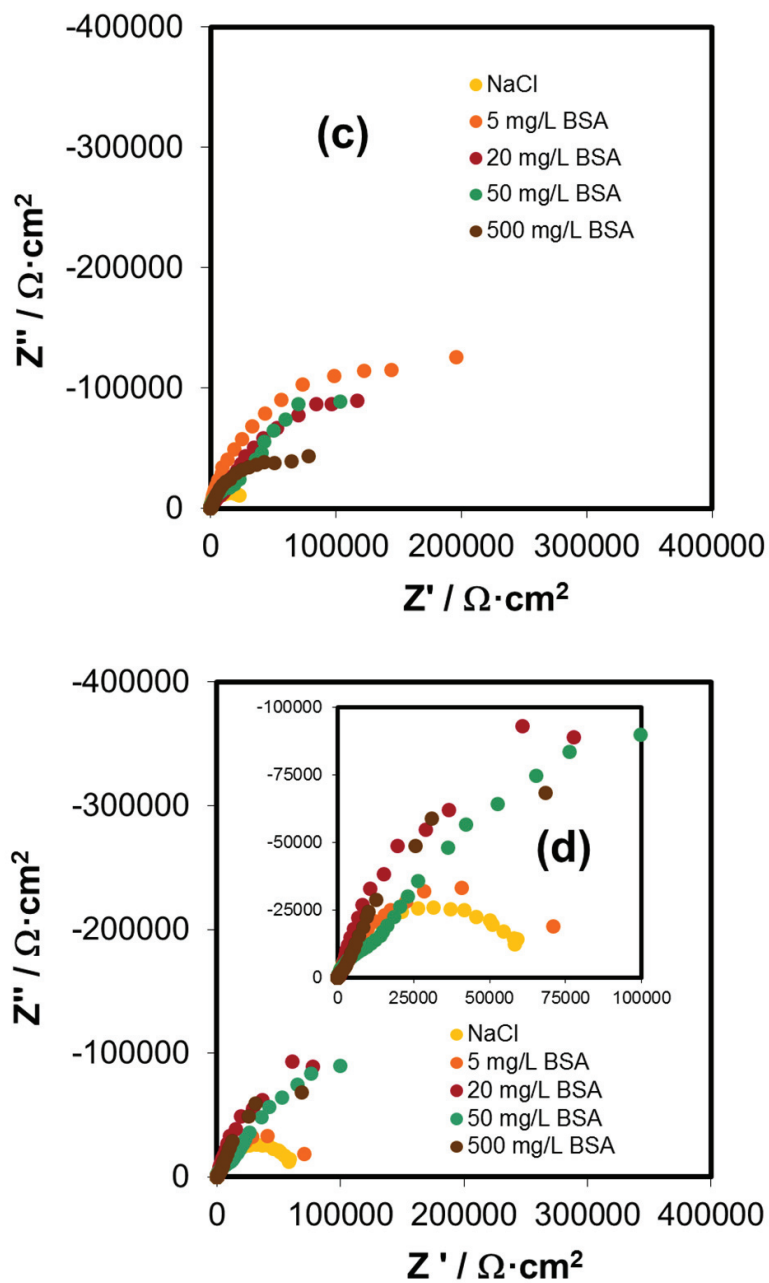


Figure 5.6. Nyquist diagrams and of CoCrMo alloy at OCP in 0.14 M NaCl solution with several BSA additions at different temperatures (a) 298, (b) 313, (c) 323 and (d) 333K.

**Table 5.II.** Equivalent Electrical Circuit parameters of CoCrMo alloys in the studied solutions at OCP at 37°C and different pH under aerated and deaerated conditions.

ELECTROCHEMICAL PARAMETERS					
298 K					
	NaCl	5 mg L <sup>-1</sup>	20 mg L <sup>-1</sup>	50 mg L <sup>-1</sup>	500 mg L <sup>-1</sup>
$R_s$ ( $\Omega$ cm <sup>2</sup> )	18 ± 4	15.5 ± 0.5	13.5 ± 0.5	15 ± 0	14 ± 2
$R_{out}$ (k $\Omega$ cm <sup>2</sup> )	62.2 ± 5.5	58.1 ± 10.0	59.0 ± 3.2	72.4 ± 5.3	87.2 ± 4.0
$CPE_{out}$ ( $\Omega^{-1}$ s <sup>n</sup> cm <sup>-2</sup> )10 <sup>6</sup>	220 ± 40	249 ± 35	259 ± 42	346 ± 33	325 ± 40
$n_{out}$	0.98 ± 0.01	0.99 ± 0.00	0.98 ± 0.04	0.99 ± 0.00	0.99 ± 0.00
$C_{out}$ ( $\mu$ F cm <sup>-2</sup> )	200 ± 40	235.5 ± 35	231 ± 42	328 ± 30	307 ± 38
$R_{in}$ (k $\Omega$ cm <sup>2</sup> )	156 ± 70	259 ± 64	254 ± 50	222 ± 30	420 ± 35
$CPE_{in}$ ( $\Omega^{-1}$ s <sup>n</sup> cm <sup>-2</sup> )10 <sup>6</sup>	39 ± 23	35 ± 5	38 ± 16	41 ± 5	38 ± 3
$n_{in}$	0.90 ± 0.03	0.93 ± 0.01	0.93 ± 0.05	0.92 ± 0.00	0.93 ± 0.01
$C_{in}$ ( $\mu$ F cm <sup>-2</sup> )	48 ± 18	42 ± 5	47 ± 14	50 ± 5	50 ± 3
313 K					
	NaCl	5 mg L <sup>-1</sup>	20 mg L <sup>-1</sup>	50 mg L <sup>-1</sup>	500 mg L <sup>-1</sup>
$R_s$ ( $\Omega$ cm <sup>2</sup> )	11 ± 1	12 ± 0	12 ± 0	10.5 ± 0.5	12 ± 1
$R_{out}$ (k $\Omega$ cm <sup>2</sup> )	58 ± 2	54 ± 5	56 ± 2	34 ± 11	37 ± 6
$CPE_{out}$ ( $\Omega^{-1}$ s <sup>n</sup> cm <sup>-2</sup> )10 <sup>6</sup>	150 ± 95	160 ± 16	205 ± 15	256 ± 17	179 ± 14
$n_{out}$	0.98 ± 0.00	0.99 ± 0.00	0.99 ± 0.00	0.99 ± 0.00	0.99 ± 0.01
$C_{out}$ ( $\mu$ F cm <sup>-2</sup> )	131 ± 50	150 ± 16	193 ± 15	241 ± 17	168 ± 14
$R_{in}$ (k $\Omega$ cm <sup>2</sup> )	108 ± 0	275 ± 37	173 ± 34	192 ± 87	283 ± 85
$CPE_{in}$ ( $\Omega^{-1}$ s <sup>n</sup> cm <sup>-2</sup> )10 <sup>6</sup>	59 ± 1	51 ± 4	47 ± 8	55 ± 18	45 ± 7
$n_{in}$	0.92 ± 0.00	0.93 ± 0.00	0.92 ± 0.00	0.90 ± 0.04	0.88 ± 0.01
$C_{in}$ ( $\mu$ F cm <sup>-2</sup> )	70 ± 1	63 ± 3	57 ± 8	75 ± 17	60 ± 7
313 K					
	NaCl	5 mg L <sup>-1</sup>	20 mg L <sup>-1</sup>	50 mg L <sup>-1</sup>	500 mg L <sup>-1</sup>
$R_s$ ( $\Omega$ cm <sup>2</sup> )	9 ± 0	9 ± 0.7	10 ± 2.5	10 ± 1.4	10 ± 0.8
$R_{out}$ (k $\Omega$ cm <sup>2</sup> )	54 ± 3	40 ± 14	36 ± 7	18 ± 5	20 ± 6
$CPE_{out}$ ( $\Omega^{-1}$ s <sup>n</sup> cm <sup>-2</sup> )10 <sup>6</sup>	110 ± 2	119 ± 13	121 ± 62	129 ± 25	101 ± 11
$n_{out}$	0.99 ± 0.00	0.98 ± 0.01	0.97 ± 0.02	0.99 ± 0.00	0.95 ± 0.03
$C_{out}$ ( $\mu$ F cm <sup>-2</sup> )	103 ± 2	103 ± 12	96 ± 60	120 ± 23	70 ± 11
$R_{in}$ (k $\Omega$ cm <sup>2</sup> )	60 ± 10	266 ± 60	167 ± 60	118 ± 57	133 ± 50
$CPE_{in}$ ( $\Omega^{-1}$ s <sup>n</sup> cm <sup>-2</sup> )10 <sup>6</sup>	65 ± 21	67 ± 5	60 ± 22	52 ± 8	49 ± 17
$n_{in}$	0.90 ± 0.10	0.91 ± 0.01	0.90 ± 0.01	0.90 ± 0.02	0.88 ± 0.04
$C_{in}$ ( $\mu$ F cm <sup>-2</sup> )	81 ± 3	133 ± 11	156 ± 56	229 ± 20	195 ± 10
333 K					
	NaCl	5 mg L <sup>-1</sup>	20 mg L <sup>-1</sup>	50 mg L <sup>-1</sup>	500 mg L <sup>-1</sup>
$R_s$ ( $\Omega$ cm <sup>2</sup> )	8 ± 0.4	8.5 ± 0.4	8.5 ± 2	7.5 ± 1	9 ± 0
$R_{out}$ (k $\Omega$ cm <sup>2</sup> )	16 ± 5	7 ± 4	9 ± 4	4 ± 1	7 ± 3
$CPE_{out}$ ( $\Omega^{-1}$ s <sup>n</sup> cm <sup>-2</sup> )10 <sup>6</sup>	96 ± 30	116 ± 3	103 ± 20	147 ± 40	79 ± 27
$n_{out}$	0.86 ± 0.07	0.86 ± 0.06	0.93 ± 0.10	0.94 ± 0.05	0.89 ± 0.01
$C_{out}$ ( $\mu$ F cm <sup>-2</sup> )	29 ± 17	38 ± 2	61 ± 17	94 ± 32	32 ± 22
$R_{in}$ (k $\Omega$ cm <sup>2</sup> )	44 ± 7	66 ± 2	86 ± 7	79 ± 10	87 ± 14
$CPE_{in}$ ( $\Omega^{-1}$ s <sup>n</sup> cm <sup>-2</sup> )10 <sup>6</sup>	69 ± 23	85 ± 30	94 ± 24	134 ± 30	109 ± 30
$n_{in}$	0.90 ± 0.01	0.82 ± 0.06	0.84 ± 0.10	0.81 ± 0.06	0.85 ± 0.05
$C_{in}$ ( $\mu$ F cm <sup>-2</sup> )	81 ± 20	133 ± 26	156 ± 17	229 ± 28	195 ± 27

**Figure 5.7** shows the values of the electrical parameters corresponding to the outer layer ( $R_{out}$  and  $CPE_{out}$ ) as a function of BSA concentration.  $R_{out}$  slightly decreased with BSA concentration below  $50 \text{ mg L}^{-1}$  and the lowest value of  $R_{out}$  was reached in the NaCl solutions with  $50 \text{ mg L}^{-1}$  of BSA. Temperature decreased  $R_{out}$  values, indeed  $R_{out}$  was comprised between 0 and  $20 \text{ k}\Omega \text{ cm}^2$  at 333K.  $CPE_{out}$  presented the same tendency with temperature than  $R_{out}$ ;  $CPE_{out}$  diminished from 298 to 323 K and remained constant above 333 K.  $CPE_{out}$  increased with BSA concentration below  $50 \text{ mg L}^{-1}$  (in  $50 \text{ mg L}^{-1}$   $CPE_{out}$  showed the maximum value).

**Figure 5.8** shows the  $CPE_{in}$  and  $R_p$  values as a function of BSA concentration and temperature. In general,  $CPE_{in}$  values slightly decreased with BSA concentration from 298 to 323 K and the opposite effect was observed at 333K. In addition, at this temperature, the value of the phase element increased one order of magnitude compared to the other temperatures. With respect to the  $R_p$  values, in general, the addition of BSA increased the values of this resistance at all temperatures; the increase is more noticeable in  $500 \text{ mg L}^{-1}$  of BSA. Furthermore temperature strongly decreases the  $R_p$  values.

The capacitance values were determined following the procedure described in the EIS section of the Chapter 3 (*Experimental techniques*) and they are shown in the **Figure 5.9**. The trend of the capacitance was similar to the CPE since the  $n$ -values are quite similar for all the fitting results of the impedance spectra. Differences between  $C_{out}$  are observed for the temperatures 323 and 333K which were practically equal in terms of  $CPE_{out}$ . The decrease of the  $C_{out}$  with the temperature can be related to the formation of a thicker outer layer (adsorbed layer) at higher temperatures in the studied temperature range.

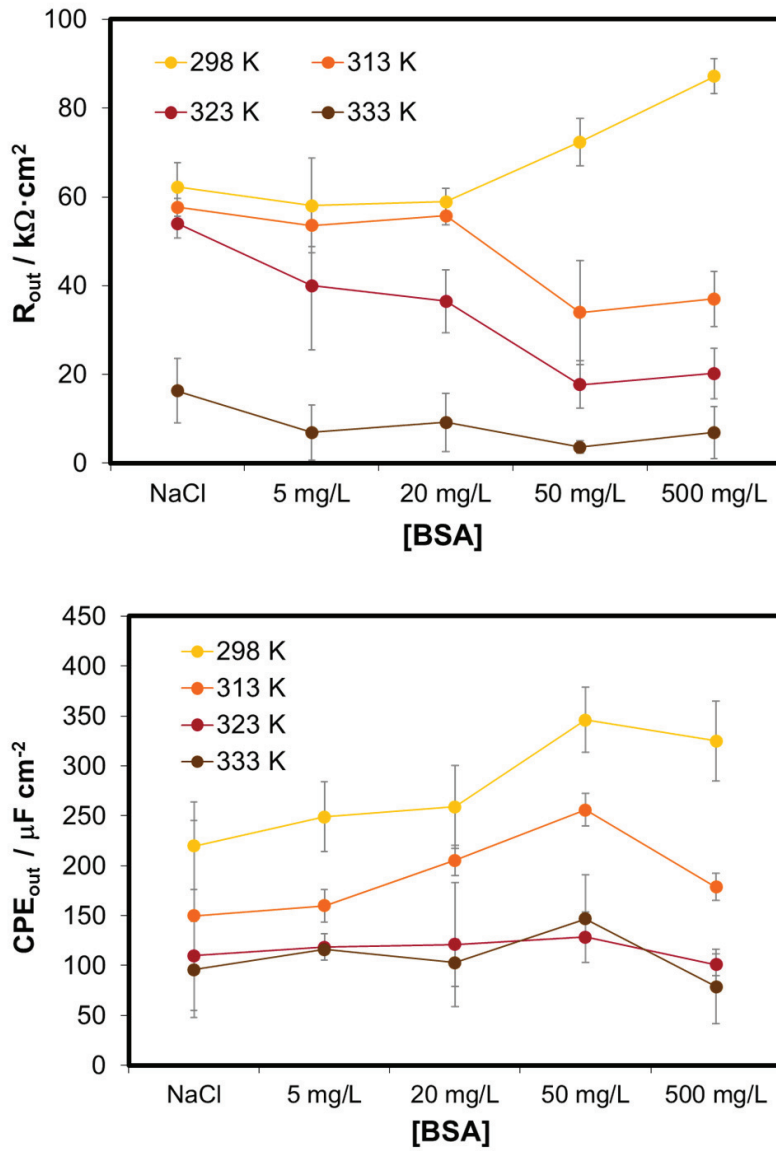


**Figure 5.7.** Equivalent circuit parameters of the outer layer ( $R_{out}$  and  $CPE_{out}$ ) according to the electrical circuit proposed for the analysis of the impedance spectra. Influence of BSA concentrations at different temperatures.

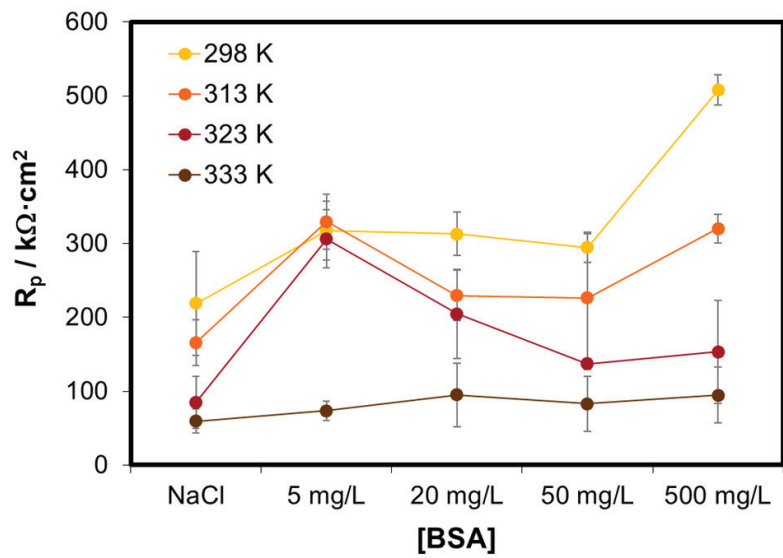
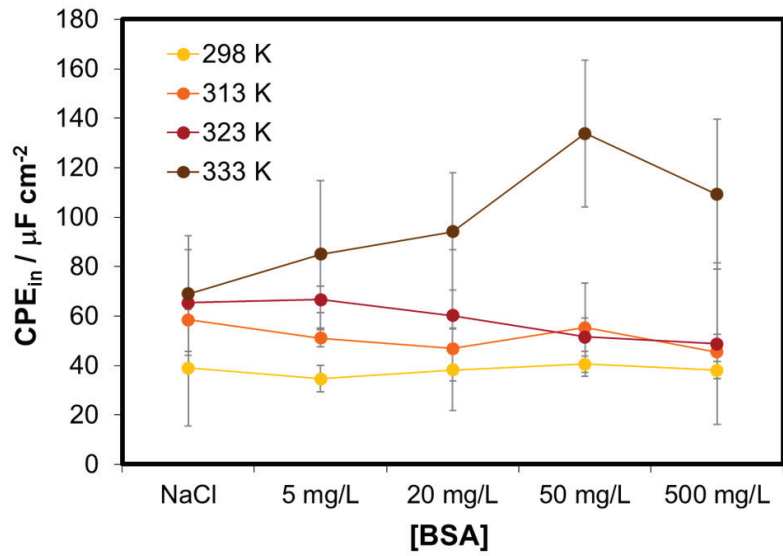


**Figure 5.8.**  $CPE_{in}$  and  $R_p$  according to the electrical circuit proposed for the analysis of the impedance spectra. Influence of BSA concentrations at different temperatures.

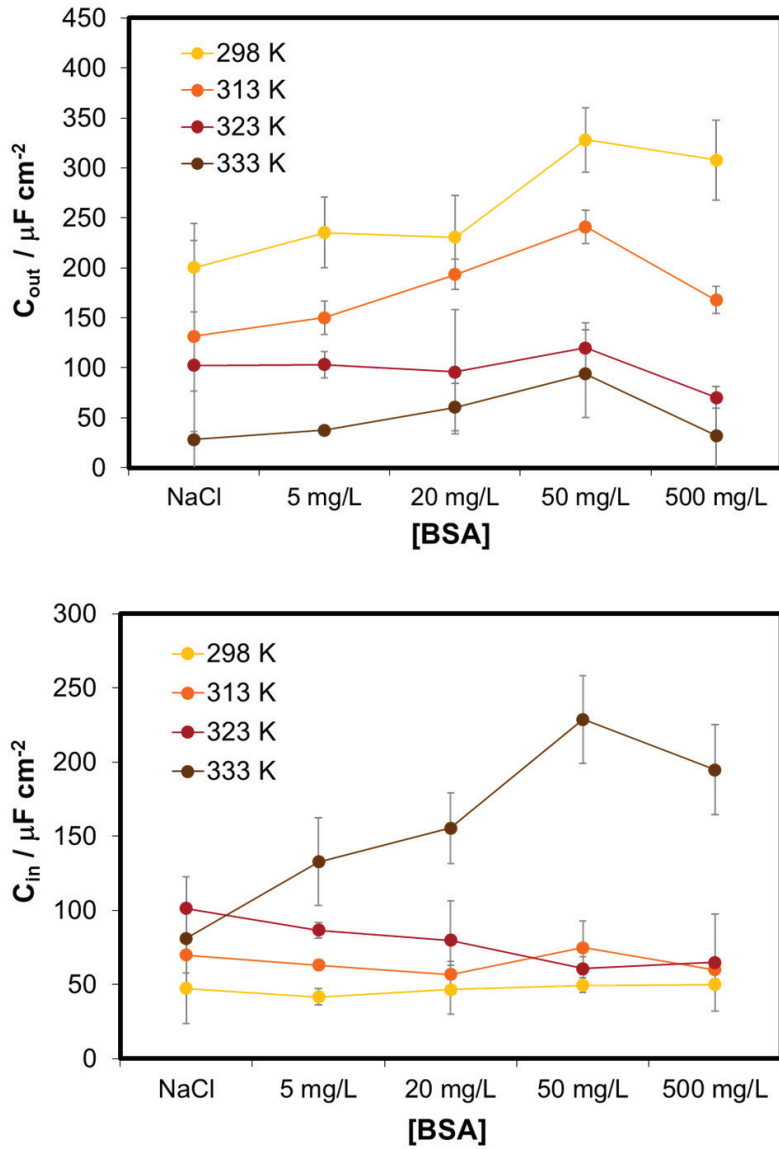


Figure 5.9.  $C_{out}$  and  $C_{in}$  values of the CoCrMo alloy interface at OCP at different temperatures and BSA solutions after fitting the experimental impedance spectra to the EEC proposed.

There is an effect of BSA concentration on the outer layer of the passive film. BSA increased the  $C_{out}$  values and significantly decreased the  $R_{out}$  values (except at 298K). This behaviour was already observed by Igual and Mischler [31]. Opposite effect of BSA on the outer parameters were obtained in NaCl solutions with 500 mg L<sup>-1</sup> of BSA; in this case  $C_{out}$  decreased and  $R_{out}$  increased with respect to the NaCl solution with 50 mg L<sup>-1</sup> of BSA. These results confirm the increase of the thickness of the outer layer of the passive film in solutions with higher BSA additions and the blocking of the mass transport from the electrode surface (by covering the electrode surface).

The  $C_{in}$  values corresponding to the inner layer of the passive film were influenced by the presence of BSA (**Figure 5.9**). Similar results were obtained by Igual and Mischler [31] and they suggested that the protein modifies the nature of the inner layer of the passive film at OCP. It is important to highlight the influence of BSA on the  $C_{in}$  values at 333K; related to the strong influence of BSA (in denatured state) on the passive film formation. The  $R_p$  values (**Figure 5.8**) can be related to the amount of protein adsorbed onto the electrode surface [39]. This fact explains the increase of  $R_p$  with BSA concentration (enhanced to 500 mg L<sup>-1</sup>).

The degree of surface coverage ( $\theta$ ) of the metal surface by an adsorbed protein at each temperature can be quantified by the  $R_p$  values using the following equation [40]:

$$\theta = \frac{R_{p(NaCl+BSA)} - R_{p(NaCl)}}{R_{p(NaCl+BSA)}} \quad (5.1)$$

where  $R_{p(NaCl+BSA)}$  is the polarization resistance obtained by the EIS spectra at different BSA concentration while  $R_{p(NaCl)}$  corresponds to the polarization resistance in NaCl solution without BSA (blank solution). According to the obtained results, the coverage of the CoCrMo alloy surface by the BSA at different BSA concentrations and temperatures was represented in **Figure 5.10**.



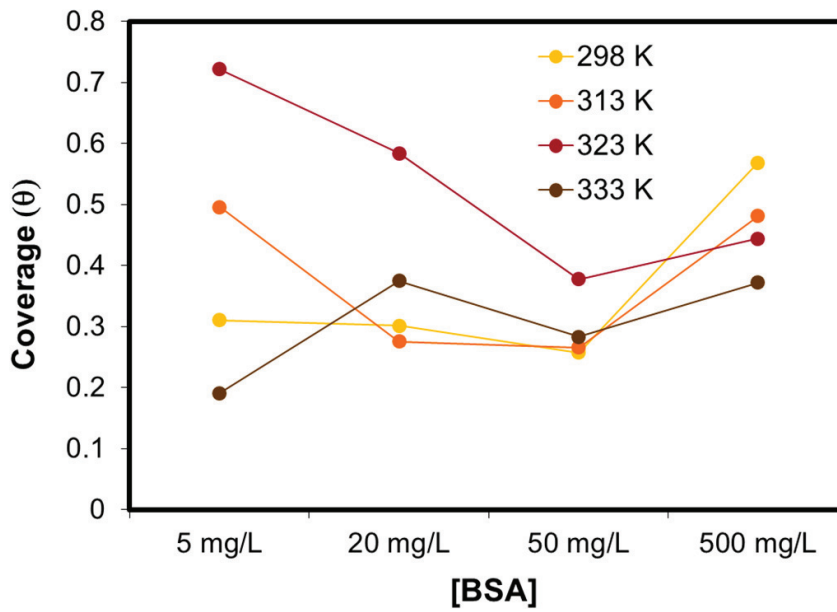


**Figure 5.10.** Degree of surface coverage of the CoCrMo alloy surface by BSA adsorption at OCP at different temperatures and BSA solutions after fitting the experimental impedance spectra to the proposed EEC.

At low temperatures (298 and 313K) the coverage remains practically constant with a value around 0.3 and only increasing in 500 mg L<sup>-1</sup> to values between 0.5-0.6. At 323K a significant increase in the surface coverage value was observed. The conformation rearrangements of the protein occurs with the temperature [41] which can be modified the surface coverage. Nevertheless, lower surface coverage values at 333K were related to the denaturation of the protein. It is worth to note that under this studied conditions the surface coverage is lower than 1 and therefore the surface is not completely covered by a protein monolayer.

#### 5.2.4. INFLUENCE OF TEMPERATURE. ARRHENIUS EQUATION.

The effect of temperature on the electrochemical behaviour of the CoCrMo biomedical alloy has been done with the electrochemical parameters extracted from the potentiodynamic curves and impedance data. Corrosion and passive current density increased with temperature which is related to the increase of corrosion rate and the generation of a less protective oxide film (**Figure 5.3**). Furthermore, temperature diminished the passive domain and favoured transpassivity at lower potential (**Figure 5.2**). Results from potentiodynamic measurements are consistent with EIS results. The main effect of temperature on EIS data was the significant decrease of  $R_p$  values, which produced a higher passive dissolution rate of CoCrMo. Furthermore, the marked increase of the  $C_{in}$  values in the experiments carried out at 333K indicated the diminution of the thickness of the inner passive layer according to **equation (3.31)** which inversely relates the capacitance value with the thickness of the represented layer (*Experimental techniques*, Chapter 3). Although these results suggest a decrease in thickness of the inner oxide layer with temperature, the total oxide film will be thicker because of the lowest values of  $C_{out}$  registered at higher temperature in the CoCrMo alloy. Therefore, according to the EIS parameters, the increase of the temperature provides an increase of the total oxide film thickness. H. Mishina et al. [42] observed that denaturation of BSA begins to occur at approximately 323-328 K. The results obtained at 333K can also be related to this denaturation process of the protein, which generates an important decrease of  $R_{out}$ .

In order to explain the effect of temperature on the corrosion behaviour of CoCrMo alloy Evans diagrams are employed (**Figure 5.11**). According to this representation temperature increases the dissolution rate of the metal (from **A0** to **A1**) and favours cathodic reaction kinetics (from **C0** to **C1**). Therefore, the increase in temperature gives an excess energetic to the system that favours the kinetics of the anodic and cathodic reaction, thus increasing both,  $E_{corr}$  and  $i_{corr}$ .

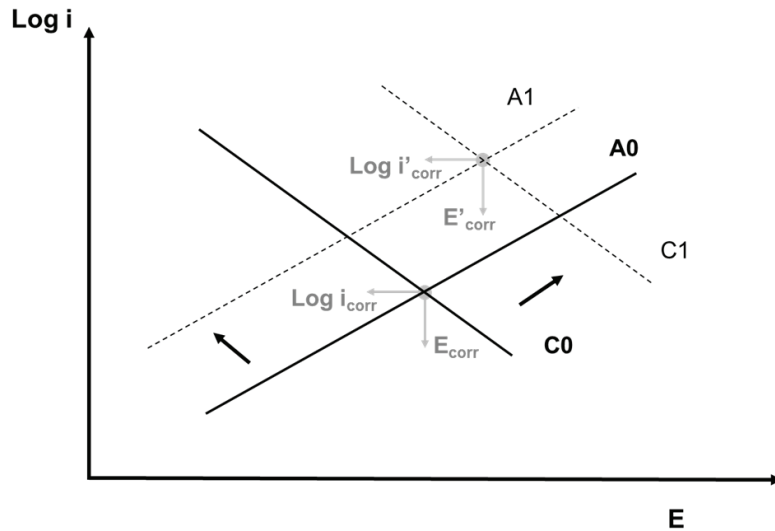


**Figure 5.11.** Mixed potential theory applied to interpret the effect of the temperature on the CoCrMo corrosion potential and corrosion current density.

The polarization curves of the CoCrMo alloy indicated that the corrosion process is accompanied by charge transfer overpotential, i.e. **activation type** [35]. The activation energy of the corrosion process was obtained from the linear variation of the rate of the metal dissolution reaction assigned as the corrosion current density,  $i_{corr}$ , with the temperature, which obeys the **Arrhenius equation** [43]. This linear relation is represented as:

$$i_{corr} = A_{Ar} \cdot e^{\frac{-E_a}{RT}} \quad (5.2)$$

where  $i_{corr}$  ( $A \text{ cm}^{-2}$ ) is the corrosion current density,  $E_a$  ( $J \text{ mol}^{-1}$ ) is the activation energy of corrosion,  $T$  (K) is the temperature,  $R$  ( $J \text{ mol}^{-1} \text{ K}^{-1}$ ) is the gas constant and  $A_{Ar}$  is a pre-exponential factor. The **equation (5.1)** can be rewritten as follows:

$$\frac{d \ln i_{corr}}{d \left( \frac{1}{T} \right)} = - \frac{E_a}{R} \quad (5.3)$$

Logarithmic values of  $i_{corr}$  can be represented versus  $1/T$  and one should obtain a linear dependence. The linear plots of the alloy in the different solutions are represented in **Figure 5.11**. The corrosion rate of CoCrMo increases in all solutions with an increase in

temperature. The slope of the line gives the activation energy for the process in the temperature range from 298 to 333 K and the values are summarized in **Table 5.III**.

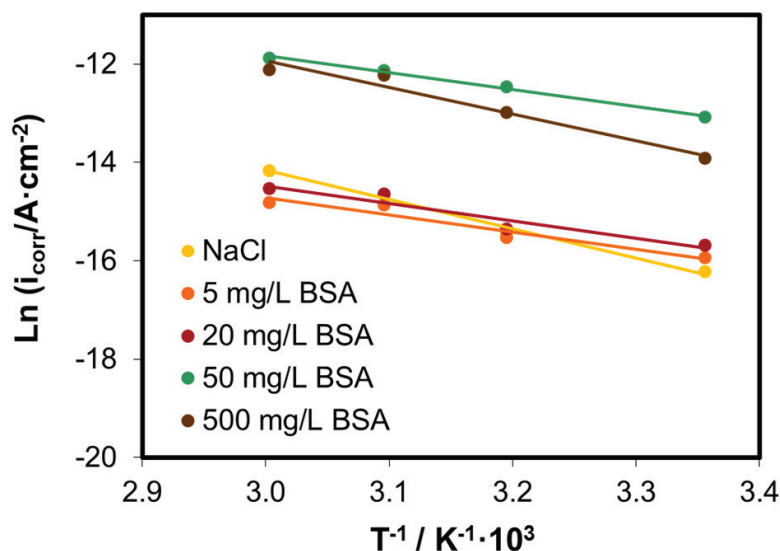


**Figure 5.12.** Effect of temperature on the corrosion rate of CoCrMo alloy in 0.14 M NaCl and different BSA additions, *Arrhenius plot*.

The highest activation energy was obtained in NaCl solution,  $49.2 \text{ kJ mol}^{-1}$  and it decreased when adding 5, 20 and 50  $\text{mg L}^{-1}$  BSA to around  $28 \text{ kJ mol}^{-1}$ . Hence the addition of BSA to the saline solution caused a decrease in the corrosion activation energy of  $21 \text{ kJ mol}^{-1}$ . This indicates that the adsorption of BSA molecules onto the CoCrMo surface occurred by a charge transfer mechanism, probably by **chemisorption** [44]. Thus, adsorption of the protein on the CoCrMo surface and subsequent formation of a complex with the metal ions from the passive oxide film (most likely Cr and Co) reduced the activation energy and enhanced the corrosion rate of the alloy [20,45].

However when the concentration of the BSA increased to the highest value ( $500 \text{ mg L}^{-1}$ ) the activation energy increased again. All electrochemical parameters are in good agreement with these results, since at  $500 \text{ mg L}^{-1}$   $i_{corr}$  and  $i_p$  decreased and the  $R_p$  significantly increased.

Corrosion current density ( $i_{corr}$ ) can also be related to the  $R_p$  through the well-known **Stern-Geary equation**:

$$i_{corr} = \frac{b_a b_c}{2.303(b_a + b_c)} \cdot \frac{1}{R_p} \quad (5.4)$$

where  $b_a$  and  $b_c$  (V decade<sup>-1</sup>) are the anodic and cathodic Tafel slopes respectively which are defined in the Chapter 3 in the **equation (3.7)** and **(3.8)**. As already stated, the dependence of the rate of a corrosion process on temperature has been described using the Arrhenius equation, **equation (5.1)**. Applying logarithms to **equation (5.1)** and substituting  $i_{corr}$  by **equation (5.3)** one obtains the following expression:

$$\ln \frac{R_p}{T} = \frac{E_a}{R} \cdot \frac{1}{T} + constant \quad (5.5)$$

where the constant includes  $A$ ,  $R$ ,  $F$ ,  $\alpha_a$  and  $\alpha_c$ . Therefore a plot of  $\ln(R_p/T)$  against  $1/T$  gives a straight line, from which a corrosion activation energy  $E_a$  can be calculated from the slope.  $R_p$  values were extracted from the impedance data. **Figure 5.13** shows the Arrhenius plots for the CoCrMo electrode immersed in the protein-free saline solution and in the saline solution containing different amount of BSA.

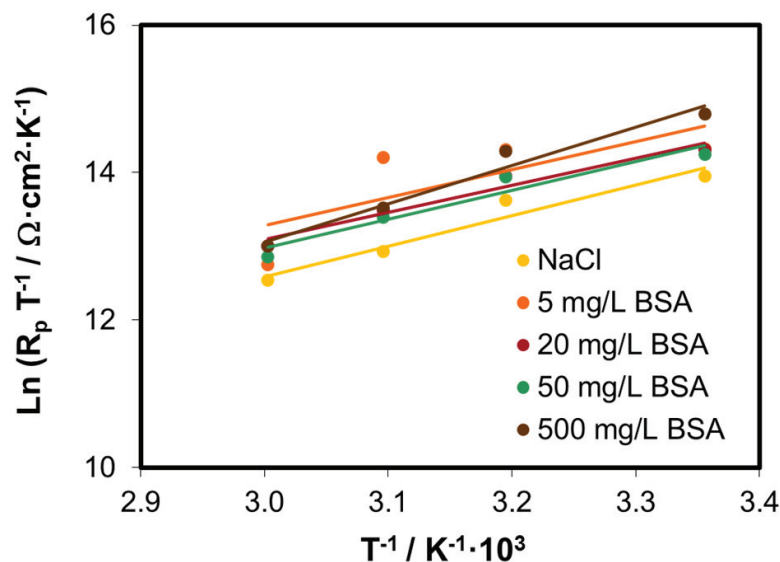


**Figure 5.13.** Effect of temperature on the charge transfer resistance of CoCrMo alloy in 0.14 M NaCl and different BSA additions, *Arrhenius plot*.

The corrosion rate of CoCrMo increased in all solutions with temperature. The activation energies calculated from the slopes of the lines were shown in **Table 5.III**. Hence, the addition of BSA to the saline solution caused a decrease in the corrosion activation energy of  $3 \text{ kJ mol}^{-1}$ . This decrease is considerably lower than that obtained from the potentiodynamic curves. However, this corroborates that the adsorption of BSA molecules onto the CoCrMo surface occurred by a *charge transfer mechanism*. Difference in  $E_a$  obtained by different electrochemical techniques can be explained if one takes into account the different electrochemical conditions under which AC and DC results are obtained. EIS tests were carried out under OCP conditions where the alloy is under its passive state. Therefore, the corrosion mechanism analysed in those EIS tests is the passive dissolution, which essentially differs from the active dissolution defined by the  $i_{corr}$  parameter obtained from DC results.

In good agreement with the results obtained from the potentiodynamic curves, activation energy from impedance data presented the highest value in the NaCl solution with 500 mg L<sup>-1</sup> of BSA.

**Table 5.III.** Activation energy values obtained from the potentiodynamic curves and EIS results on a CoCrMo alloy at temperatures from 298 to 333 K in different NaCl solutions.

ACTIVATION ENERGY ( $\text{kJ mol}^{-1}$ )		
Solution	Potentiodynamic curves	EIS
NaCl	49.4	34.5
NaCl + 5 $\text{mg L}^{-1}$ BSA	28.8	31.5
NaCl + 20 $\text{mg L}^{-1}$ BSA	29.5	30.5
NaCl + 50 $\text{mg L}^{-1}$ BSA	28.3	32.6
NaCl + 500 $\text{mg L}^{-1}$ BSA	45.2	43.1

Possibly, this behaviour could be related to the precipitation of the protein or their deposition onto the material surface that cause the loss bind of the protein to metal and difficult transport of the metallic ions away from the solution/passive film interface. The inhibition of the electrochemical reaction by covering the electrode surface and blocking the mass transportation of oxygen and/or reaction products to and/or from the electrode surface could explain the increase of activation energy. This behaviour is also confirmed by these  $i_p$  values, where a decrease of the current density was obtained when the concentration was increased from 50 to 500  $\text{mg L}^{-1}$  of BSA. The equivalent circuit parameters related with the outer layer ( $R_{out}$  and  $CPE_{out}$ ) are in good agreement with this behaviour. According to those results an increase of the thickness and resistance of the adsorbed layer are obtained at 500  $\text{mg L}^{-1}$ . Furthermore, an enhancement of  $R_p$  was attained at this BSA concentration.

In any case, it is clearly observed the different electrochemical behaviour in high and low BSA containing solutions. Afonso et al. [34] obtained similar results when analysing the influence of BSA on the anodic dissolution of chromium contained in UNS S31254 stainless steel in chloride environments. They observed two different behaviour depending on the BSA concentration; at lower BSA concentration the complexing effect of BSA was predominant and favoured metal dissolution while at higher BSA concentrations the predominant effect was the adsorption of the protein on the surface.

### 5.2.5. INFLUENCE OF BSA CONCENTRATION ON THE PASSIVE BEHAVIOUR. LANGMUIR ISOTHERM.

In order to analyse the influence of BSA concentration on the electrochemical behaviour of CoCrMo, the dependence of the polarization resistance,  $R_{p,c}^{-1}$  versus BSA concentration was plotted in the whole range of investigated temperatures (Figure 5.14).

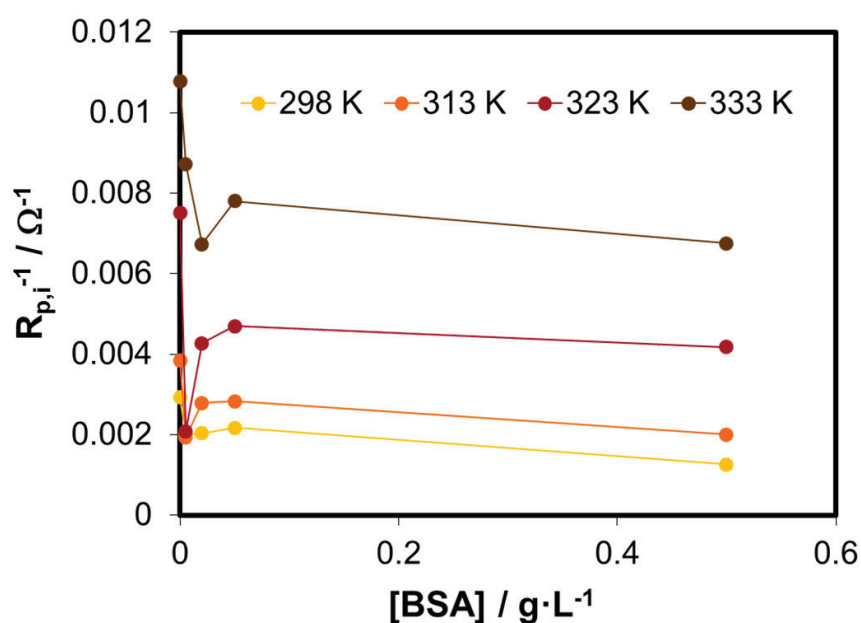


**Figure 5.14.** Adsorption isotherm of BSA onto the CoCrMo electrode in 0.14 M NaCl solution (pH 7.4) at different temperatures.

Temperature caused a significant decrease in the polarization resistance (shown as an increase in  $R_{p,c}^{-1}$ ). BSA additions also produced an increase in the polarization resistance until a plateau level was attained in 50 mg L<sup>-1</sup> BSA. **Figure 5.14** shows that the polarization resistance, and hence corrosion current density ( $i_{corr} \propto R_{p,i}^{-1}$ , **equation(5.3)**), depends on the BSA concentration. Therefore, the magnitude of the corrosion current density, after being corrected for the current density recorded in the



protein-free solution ( $R_{p,0}$ ) for each incremental addition of protein ( $R_{p,i}$ ) by the expression ( $R_{p,c}^{-1} = R_{p,i}^{-1} - R_{p,0}^{-1}$ ), can be correlated to the surface concentration of BSA, i.e.  $R_{p,c}^{-1} \propto \Gamma$ . Some isotherms have been used in order to characterize the adsorption of the BSA onto CoCrMo surface. Nevertheless, the isotherm that better describes this adsorption process is the **Langmuir isotherm** (equation (1.11), Introduction). Equation (1.11) can be rearranged to give:

$$\frac{c}{\Gamma} = \frac{1}{B_{ADS}\Gamma_{max}} + \frac{c}{\Gamma_{max}} \quad (5.6)$$

A plot of  $c/\Gamma$  versus concentration should yield a straight line with parameters  $\Gamma_{max}$  and  $B_{ADS}$  derived from the slope and intercept, respectively. The dependence of  $c \cdot R_{p,c}$  versus BSA concentration in the solution was also found to be linear (Figure 5.15), over the investigated temperature range.

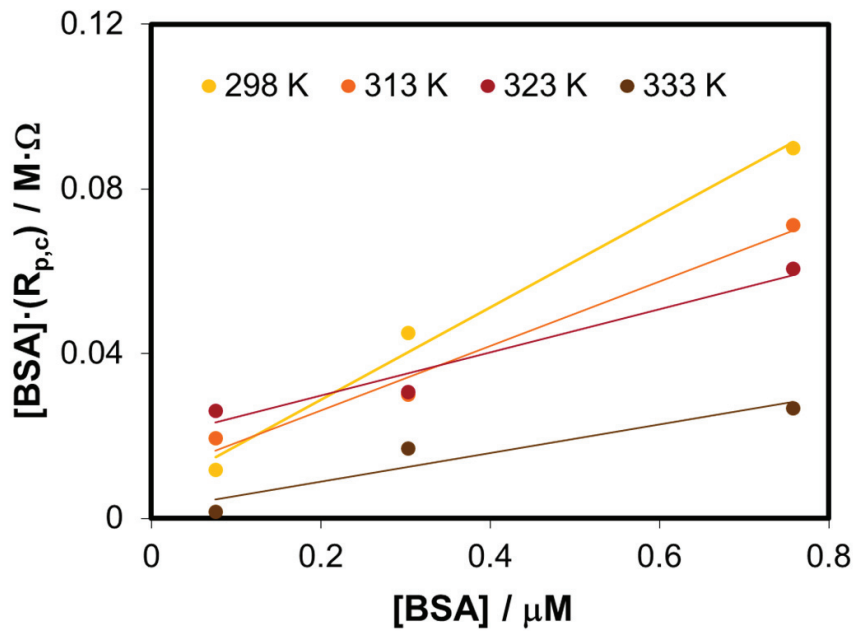


Figure 5.15. Langmuir adsorption isotherm presented in a linearized form, according to equation (5.6) for BSA adsorbed onto the CoCrMo alloy in 0.14 M NaCl solution (pH 7.4) at different temperatures.

The good agreement between the experimental and simulated values showed that the Langmuir isotherm could be successfully used to describe the adsorption of BSA onto CoCrMo surface. Therefore,  $\Gamma_{max}$  and  $B_{ADS}$  values were obtained from the linear regression in **Figure 5.15** and they are summarized in **Table 5.IV**. Saturated surface concentration,  $\Gamma_{max}$ , increased with temperature, while the affinity of the adsorbate towards adsorption,  $B_{ADS}$ , decreased between 298-323 K and then increased at 333 K. This increase in adsorption likely results from a higher affinity of the denatured structure of the BSA molecule in the bulk solution for the surface, possibly resulting in multilayer adsorption. At temperatures above 333 K thermal denaturation and unfolding of BSA begins [42,46]. The increase in surface concentration of BSA could be related to the reversible partial unfolding that occurs between 313-323 K in the bulk solution. Similar results were obtained by Jackson et al [16] when studying the adsorption behaviour of several (serum) proteins on titanium.

The parameter  $B_{ADS}$ , which reflects the affinity of the adsorbate molecules toward adsorption sites at a constant temperature, could be presented as:

$$B_{ADS} = \frac{1}{c_{solvent}} \exp\left(\frac{-\Delta G_{ADS}}{RT}\right) \quad (5.7)$$

where  $R$  ( $\text{J mol}^{-1} \text{K}^{-1}$ ) is the gas constant,  $T$  (K) the temperature  $\Delta G_{ADS}$  ( $\text{J mol}^{-1}$ ) the Gibbs free energy of adsorption, and  $c_{solvent}$  the molar concentration of a solvent, which in this case is the water ( $c_{H_2O} = 55.5 \text{ mol dm}^{-3}$ ).

From the  $1/R_{p,c(max)}$ , which is proportional to  $\Gamma_{max}$ , calculated from the slope of the line in **Figure 5.14**, and the value for  $B_{ADS}$  determined from the intercept, the  $\Delta G_{ADS}$  values were calculated for the series of temperatures for BSA using **equation (5.6)** and they are summarized in **Table 5.IV**.

**Table 5.IV.** Saturated surface concentrations, affinity constants and standard Gibbs free energies for BSA on CoCrMo obtained from impedance measurements at various temperatures

THERMODYNAMICAL PARAMETERS			
$T$ (K)	$\Gamma_{max}$ ( $\text{M}\Omega^{-1}$ )	$B_{ADS} \cdot 10^{-7}$ ( $\text{dm}^3 \cdot \text{mol}^{-1}$ )	$\Delta G_{ADS}$ ( $\text{kJ} \cdot \text{mol}^{-1}$ )
298	8.9	1.8	-51.3
313	12.8	0.7	-51.6
323	18.9	0.3	-50.6
333	28.8	1.7	-57.2

The Gibbs free energy of adsorption of BSA,  $\Delta G_{ADS}$ , onto CoCrMo surface in saline solutions at different temperatures was calculated and represented in **Figure 5.16**. At 298 K the Gibbs free energy of adsorption of BSA onto CoCrMo surface has a value of  $-51.29 \text{ kJ mol}^{-1}$ . Such a high value indicates strong adsorption of BSA onto the CoCrMo surface, i.e. **chemisorption**. This confirmed our previous conclusions drawn from the difference in the corrosion activation energies caused by the addition of BSA to the solution (Arrhenius plot, **Figure 5.11**). With an increase in temperature from 298 to 333 K, the negative Gibbs free-energy value also increased, but at 323 K dropped down. The decrease in the  $B_{ADS}$  and  $\Delta G_{ADS}$  at 323 K is in good agreement with similar observations already reported in the literature [45] and could be related to structural changes in the protein. On the other hand, the increase of the constant  $B_{ADS}$  at 333K indicates high increase in the affinity of BSA towards adsorption sites at the CoCrMo surface. According to Jackson et al. [16] the increase in adsorption likely results from a higher affinity of the denatured structure of the BSA molecule in the bulk solution for the surface (resulting in a multilayer adsorption).

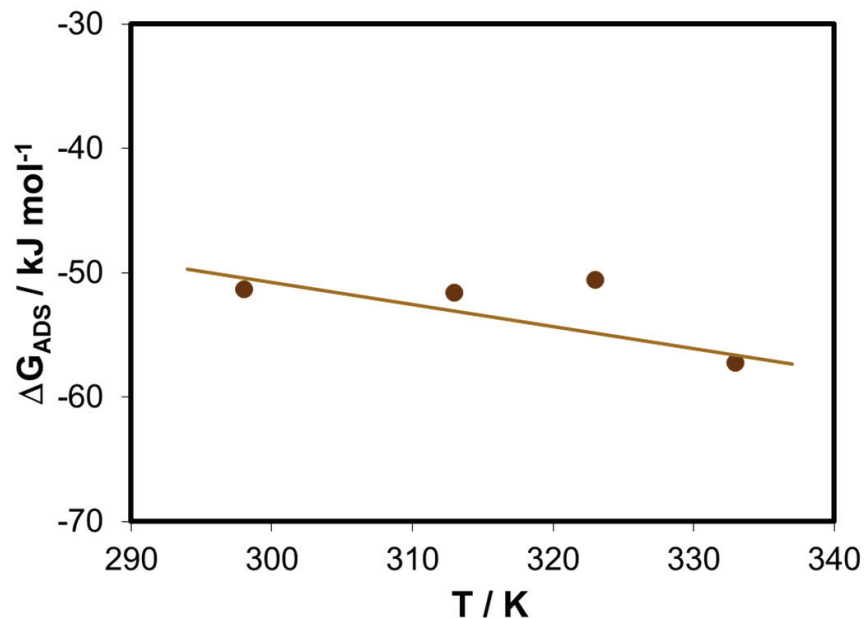


**Figure 5.16.** Dependence of the Gibbs energy of adsorption on the temperature for BSA onto CoCrMo surface in NaCl solution (pH 7.4) calculated from Electrochemical Impedance Spectroscopy data.

From the plot which shows the dependence of  $\Delta G_{ADS}$  with temperature, **Figure 5.16**, the enthalpy,  $\Delta H_{ADS}$ , and entropy  $\Delta S_{ADS}$  values for BSA were calculated. The slope of the line yielded the value of entropy  $\Delta S_{ADS} = 176 \text{ J mol}^{-1} \text{ K}^{-1}$  and the enthalpy of adsorption was calculated from the intercept  $\Delta H_{ADS} = 2.04 \text{ kJ mol}^{-1}$ . The positive enthalpy value  $\Delta H_{ADS}$  shows that the adsorption of BSA onto the CoCrMo surface is an **endothermic process**. However, from the calculated thermodynamic values the gain in **entropy** actually represents the **driving force** for the adsorption of the protein onto the CoCrMo surface [33]. The  $T\Delta S_{ADS}$  product ranges from 52 to 58  $\text{kJ mol}^{-1}$ , depending on the temperature, which is considerably higher than the enthalpy value. The structure, and hence dimensions of the molecule, changes when the protein adsorbs onto a surface. The induced structural changes can lead to a considerably entropy gain, which appears to be the driving force for adsorption of BSA. It has been shown in the literature [16] that proteins with low native-state stabilities possess a strong driving

## CHAPTER 5. Mechanisms of BSA adsorption

force for adsorption related to breakdown of native tertiary and partially secondary structure; in other words, adsorption is driven by an increase in the conformational entropy of the protein. Large positive entropy values could arise from the unfolding of protein molecules upon adsorption.

This study is in good agreement with previous contributions related to the adsorption of BSA onto passive alloys [16,20]. Based on them and according to our results, it can be confirmed that the adsorption of BSA on CoCrMo alloys follows the ***Langmuir isotherm***.

### **5.3. Influence of the BSA on CoCrMo passivated surfaces**

#### **5.3.1. INTRODUCTION**

Passivity and adsorption mechanisms determine the electrochemical behaviour of the CoCrMo alloy in biosystems. The adsorption of the protein was analysed simultaneously to passivation of the alloy since the protein was present in the electrolyte at the beginning of the different electrochemical test. In this section, both mechanisms have been evaluated separately by studying the adsorption mechanism of the BSA under different passive conditions of the CoCrMo alloy (different passive potential and passivation time).

#### **5.3.2. ELECTROCHEMICAL MEASUREMENTS**

The experimental set-up was the same conventional three-electrode electrochemical cell with a platinum wire as a counter electrode and a Ag/AgCl (3M KCl) reference electrode. The main difference with the previous tests was that the working electrode was mounted as a rotating disk electrode (RDE) with the rotation speed fixed at 1000 rpm. The hydrodynamic conditions of the working electrode induce a flux in the electrolyte which provides uniform mass transport rate over the entire electrode surface [47]. Thus, the diffusion layer thickness does not depend on the radius and the steady-state current is controlled by the solution flow rather than diffusion. In this study, aliquots of BSA were added into the solution after passivation of the samples during different periods of time in order to analyse the effect of BSA adsorption on passivated CoCrMo surfaces. Therefore, the hydrodynamic conditions of the system also allow the homogenization of the solutions after BSA additions.



**Figure 5.17.** Experimental set-up with the working electrode mounted in a rotating disk electrode (RDE).

Initially, with the aim of determining the mechanisms of the BSA adsorption process on the CoCrMo alloy behaviour, a general electrochemical characterization of the alloy was carried out through classical potentiodynamic experiments. The potential scan was realized from an applied potential of  $-1.5\text{ V}$  and moved into the anodic direction to  $1.5\text{ V}$  at a scan rate of  $2\text{ mV s}^{-1}$ . The simulated body fluids used for the potentiodynamic test were PBS and PBS with the addition of  $100\text{ mg L}^{-1}$  of Bovine Serum Albumin (BSA).

Two different electrochemical tests were carried out in order to study the BSA adsorption: tests under open-circuit conditions and potentiostatic tests at an applied passive potential ( $-0.05\text{ V}$ ). The latter applied potential was selected following the

initial CoCrMo characterization (Chapter 4). The samples were immersed in PBS saline solution for different time periods (5, 15, 25, 55, 85 and 115 minutes). After the immersion times under both electrochemical conditions (OCP and -0.05 V), one aliquot of BSA was added in the electrochemical cell reaching a concentration of 100 mg L<sup>-1</sup> of BSA into the solution. When the BSA was added to the solution, the OCP and the current density evolution at  $E_{\text{applied}} = -0.05 \text{ V}$  was measured for 20 minutes. EIS measurements were carried out at the end of the OCP measurements and at the end of the potentiostatic tests in order to characterize the electrolyte/metal interface. Analogous tests (OCP, potentiostatic and EIS) were carried out without the addition of the BSA and under the same potential conditions (OCP and -0.05 V). In all cases, EIS measurements were performed starting from 1 mHz up to 10<sup>5</sup> Hz, at 10 cycles dec<sup>-1</sup> with an AC amplitude of  $\pm 10 \text{ mV}$ . The buffer solution was used in this study in order to avoid problems with the modification of the pH when the injection of BSA was carried out into the electrolyte.



## 5.3.3. POTENTIODYNAMIC CURVES

Figure 5.18 shows two potentiodynamic curves of the CoCrMo in PBS solution with and without BSA. The BSA adsorption modifies the electrochemical properties of the alloy under the studied conditions, in good agreement with previous results and works [31]. BSA modifies the cathodic-anodic transition by decreasing the corrosion potential ( $E_{corr}$ ) and decreasing the current density in the cathodic domain. BSA also acts in the passive domain of the alloy. In the PBS solution, the passivation domain of the alloy is extended from -0.75 to 0.5 V; this domain increases from -1 to 0.5 V when the BSA is added. Furthermore, the value of the passivation current density ( $i_p$ ) is higher in presence of BSA, which increases from  $2.77 \mu\text{A cm}^{-2}$  to  $3.99 \mu\text{A cm}^{-2}$  (these values are obtained at a passive potential of -0.05 V).

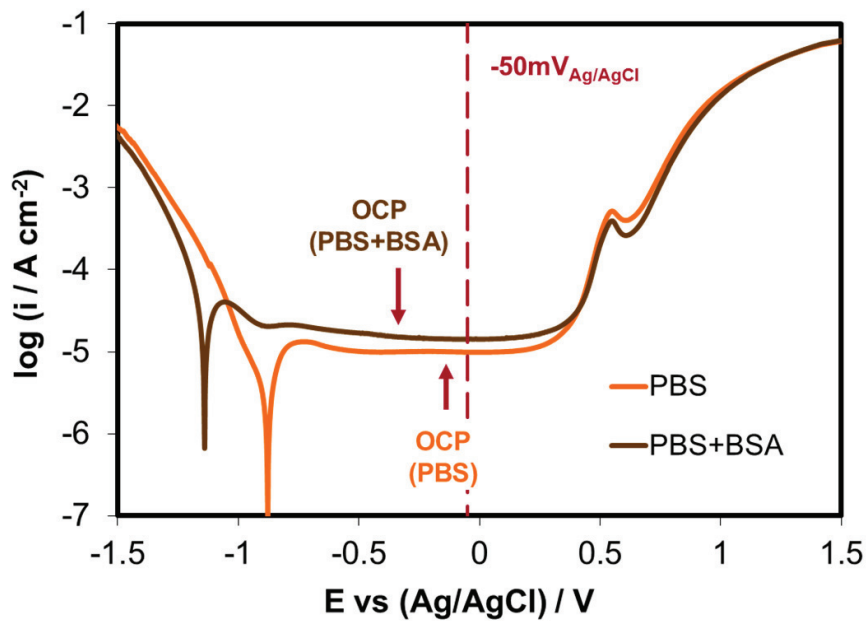


Figure 5.18. Potentiodynamic curves of the CoCrMo alloy in PBS and PBS+BSA at 37°C and pH 7.4. Arrows indicate the open circuit values of the alloy in PBS and PBS+BSA solution.

It is possible to observe in **Figure 5.18** that OCP values measured in PBS and PBS+BSA solutions as well as the selected applied potential of -0.05 V lied within the passive domain of the CoCrMo alloy in both electrolytes (PBS and PBS+BSA).

## 5.3.4. OCP

Figure 5.19 shows the time evolution of the OCP measurement of the CoCrMo alloy in PBS solution, which consisted in a continuous shift towards more positive values. BSA injection was added after different immersion periods and indicated in the figure with arrows.

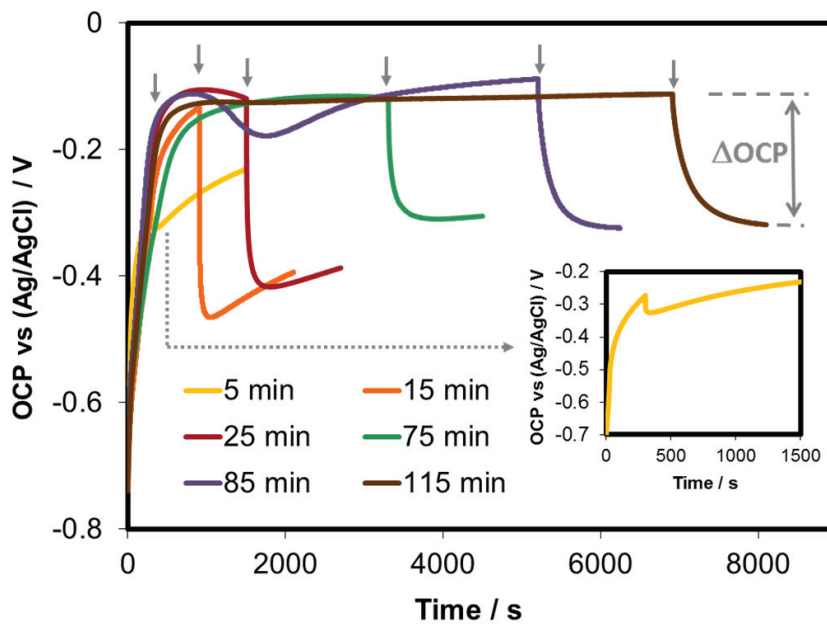


Figure 5.19. OCP evolution of the CoCrMo alloy before and after BSA addition (indicated by arrows) in PBS solution at 37°C and pH 7.4. The last 20 min corresponds to the effect of BSA on the OCP values.

The positive evolution of the OCP at the beginning of the tests indicates the formation of the protecting passive layer on the biomaterial surface. Several studies have reported that the composition of the passive film formed on the CoCrMo alloys is predominantly  $\text{Cr}_2\text{O}_3$  oxide with some minor contribution of other oxides (Co- and Mo-oxides, especially if the film is air formed) [30,48-50].

In all cases, when adding the BSA to the solution, OCP dropped and, depending on the immersion time, they tended to increase again. When the immersion time increased above 60 minutes, OCP values exponentially decreased after BSA addition reaching a final constant value of OCP.

BSA addition produced a change on the electrochemical reactions (taking place on the interface biomaterial/body fluid cathodic and anodic reaction) at OCP. The displacement of the equilibrium potential was described previously in **Figure 5.4** by means of Evans diagrams. According to the obtained results, the OCP shift towards more negative values was related to the double role of BSA adsorption on CoCrMo surface: inhibitor of the cathodic process (impeding the access of the oxidant to the metallic surface) as well as accelerator of the anodic reaction [30,48,51].

In order to analyse the effect of BSA addition on the OCP evolution, the last 20 minutes of each test are represented in **Figure 5.20**. The passivation of the sample did not reach a complete steady state (OCP was continuously changing with time) before the BSA injection; therefore the evolution of the OCP may be influenced by the synergy of the passivation and adsorption processes. After long passivation times (above 75 minutes), no apparent modification in the kinetic mechanisms of adsorption was observed; indeed, in terms of OCP variation after BSA addition, values of  $0.636 \text{ mV min}^{-1}$  ( $\pm 0.36 \text{ mV min}^{-1}$ ) were measured in the last minute of the experiments. However, the direct measure of the OCP is not enough for evaluating the electrochemical properties of the system and thus EIS analysis were carried out.

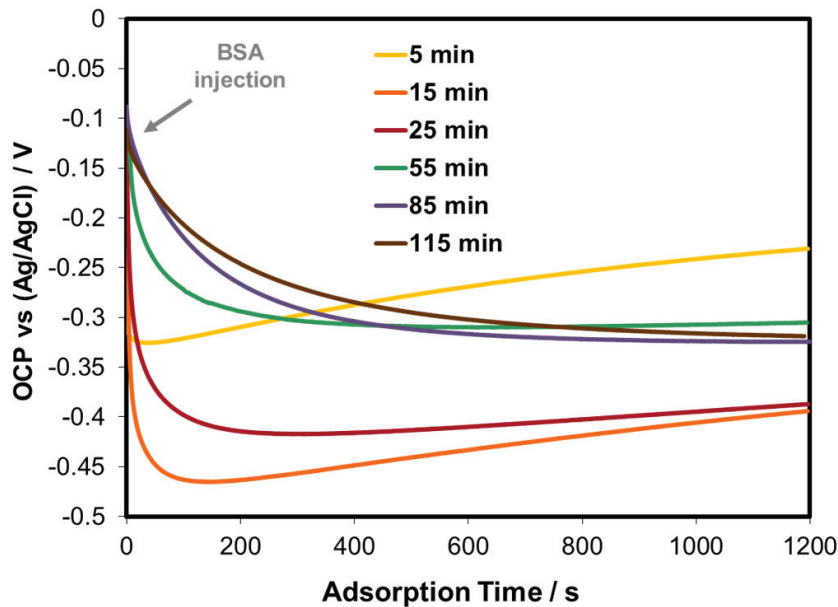


**Figure 5.20.** OCP evolution of the CoCrMo alloy after BSA injection after different immersion times in PBS solution at 37°C and pH 7.4.

According to **Figure 5.20**, the difference between the initial and final values of the OCP just before and after BSA injection respectively were extracted. These variations in the OCP values ( $\Delta OCP$ ) are represented in **Figure 5.21** as a function of the passivation time. In **Figure 5.19** an example of the  $\Delta OCP$  value extraction is shown. It can be observed that  $\Delta OCP$  decreases with the passivation time for immersion periods above 20 minutes. Therefore the effect of the BSA adsorption on CoCrMo surface decreases when passivation time increases. For short passivation times (5-10 minutes), CoCrMo surface was not stabilized (OCP continued significantly increasing) and thus effect of BSA strongly competes with the passive film formation. At higher passivation time lower variation of the OCP was registered, with a lower value of standard deviation associated. In these cases, it can be considered that the major effect on the OCP variation is due to BSA adsorption.

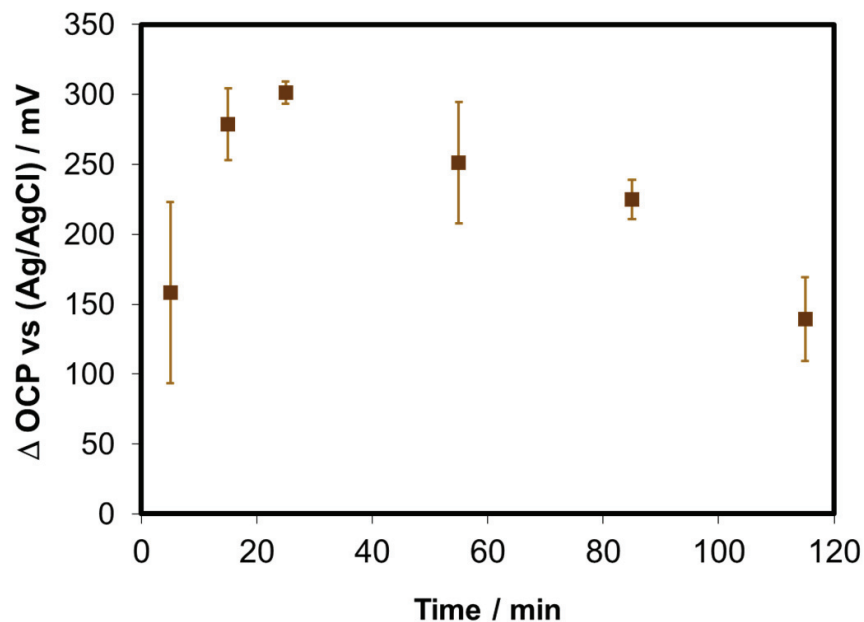


**Figure 5.21.** Difference between the initial and final value of the OCP measurements of the CoCrMo alloy before and after the BSA addition in PBS solution at 37°C and pH 7.4.

The characterization of the biomaterial/electrolyte interface and the adsorption process was done through EIS measurements carried out after 20 minutes of the BSA addition. **Figure 5.22** shows the EIS diagrams (in form of Nyquist diagrams and Bode plots) after the BSA addition and different immersion times (passivation at OCP). Furthermore, analogous electrochemical tests without BSA addition were carried out. In both cases, the EIS diagrams exhibit a typical passive state shape characterized by high impedance values with non-ideal capacitive behaviour [36-38,52-54].

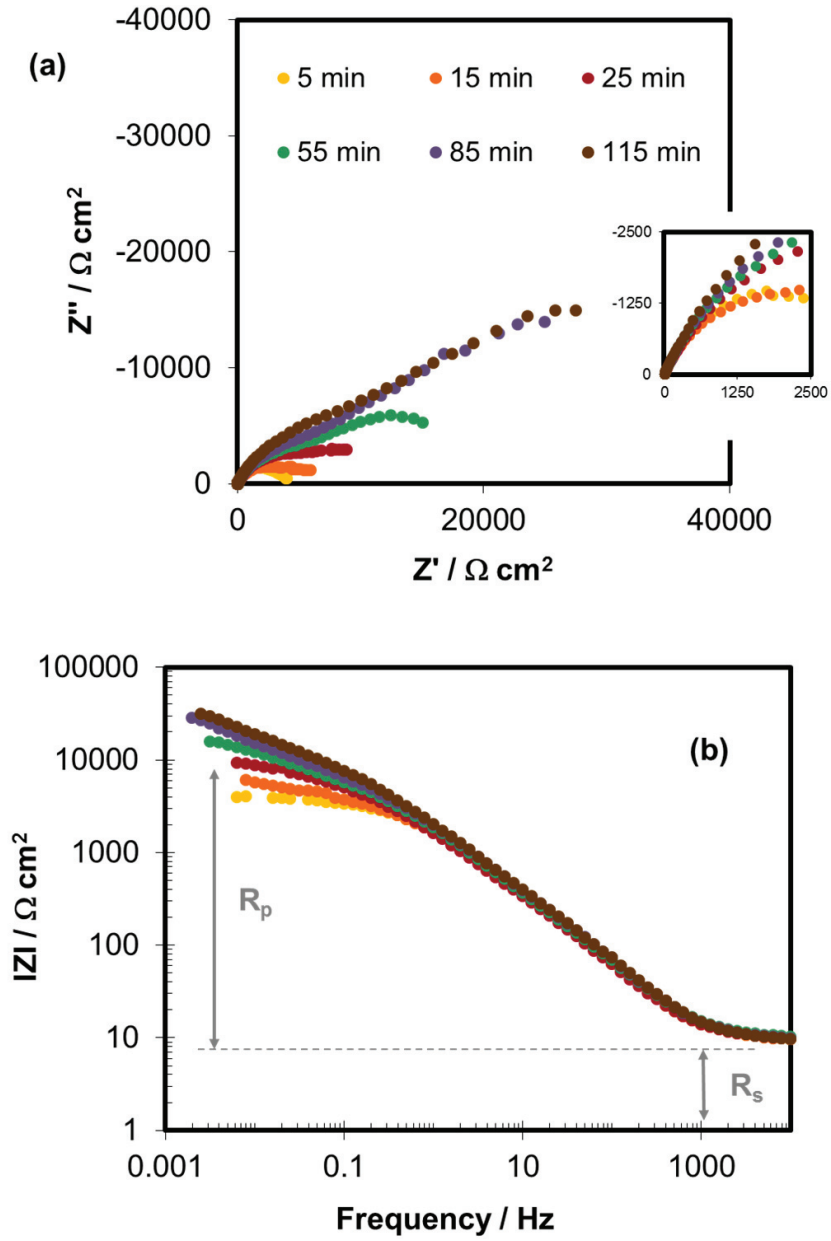


**Figure 5.22.** (a) Nyquist diagrams and (b) Bode plots (impedance modulus) of the CoCrMo alloy at OCP after different immersion times and 20 min after BSA addition in PBS solution at 37°C and pH 7.4.

The theoretical impedance parameters obtained from the electrochemical tests (with and without BSA addition) after fitting the EIS spectra with the EEC proposed in the Chapter 3 (two  $RC$  groups disposed in series) are summarized in **Table 5.V**. According to these results, the main difference between the impedance tests carried out in presence and absence of BSA was obtained in the total resistance values (the  $R_p$  values decreased with the BSA addition). These results suggested that BSA modify the electrochemical properties of the passive film in PBS solution. Igual et al. [31] obtained similar results, working at OCP, and they explained that the presence of the protein displaces the phosphate molecules thus suppressing the protective effect of phosphates. The high  $R_p$  values in the PBS solution (without BSA addition) is probably due to the fact that the phosphates formed a layer covering the electrode surface and blocking the mass transport of oxygen and/or of reaction products to and/or from the electrode surface; BSA is less efficient in reducing the reaction rate because its larger size does not allow the formation of the compact film [31].

Furthermore, it is observed that the  $R_p$  in PBS solutions continuously increases with time. However, when the protein was added into the solution the continuous increase of the  $R_p$  values is stopped. Thus, the adsorption of the protein displacing the phosphate ions can act blocking the surface which hinders the continuous increase of the  $R_p$  of the CoCrMo alloy with time. These results demonstrate that the electrochemical behaviour of the alloy depends on when the protein is added, i.e. passivation with BSA (PBS+BSA) or adding the BSA under the passivated surface of the CoCrMo in PBS.



**Table 5.V.** Equivalent electrical circuit parameters of the CoCrMo alloy at different passivation time in PBS solution with and without BSA addition at 37°C and pH 7.4.

<b>EQUIVALENT ELECTRICAL CIRCUIT PARAMETERS</b>							
Passivation time (min)	$R_s$ ( $\Omega \text{ cm}^2$ )	$CPE_{out}$ ( $\Omega^{-1} \text{ s}^n \text{ cm}^2$ ) $10^6$	$n_{out}$	$R_{out}$ ( $\text{k}\Omega \text{ cm}^2$ )	$CPE_{in}$ ( $\Omega^{-1} \text{ s}^n \text{ cm}^2$ ) $10^6$	$n_{in}$	$R_{in}$ ( $\text{k}\Omega \text{ cm}^2$ )
<b>BSA</b>							
5	9	153	0.83	1	193	0.79	3
15	9	150	0.78	3	911	0.77	3.3
25	9.5	144	0.77	4.3	830	0.77	7
55	9	130	0.78	5	692	0.76	16
85	8.5	127	0.78	6	633	0.75	19
115	9	122	0.78	7.7	399	0.9	26
<b>without BSA</b>							
25	8	125	0.79	6	575	0.84	12
35	8	110	0.80	4.5	530	0.81	7.6
45	9	97	0.82	3.8	650	0.78	23
75	8	126	0.80	9.7	953	0.81	54
105	8.5	106	0.79	11	783	0.85	40
135	8	120	0.80	11.5	992	0.80	65

**Table 5.VI.**  $C_{out}$  and  $C_{in}$  values of the CoCrMo alloy interface at OCP obtained after different periods of immersion times.

<b>CAPACITANCE</b>					
<b>BSA</b>			<b>without BSA</b>		
Passivation time (min)	$C_{out}$ ( $\mu\text{F cm}^{-2}$ )	$C_{in}$ ( $\mu\text{F cm}^{-2}$ )	Passivation time (min)	$C_{out}$ ( $\mu\text{F cm}^{-2}$ )	$C_{in}$ ( $\mu\text{F cm}^{-2}$ )
5	39	167	25	1265	530
15	23	1265	35	1406	650
25	20	1406	45	1478	953
55	19	1478	75	1450	783
85	18	1450	105	519	992
115	18	519	135	167	575

Furthermore, the results shown in **Table 5.V** and **5.VI** suggest that the passivation time has an effect on the properties (composition, morphology) of the inner layer of the passive film. A diminution of the  $C_{in}$  values ( $519 \mu\text{F cm}^2$ ) was observed when the passivation time is 115 minutes, which implies an increase in thickness of the passive layer. Hodgson et al. [30] also studied, at a fixed potential, the impedance spectra of a CoCrMo alloy and they observed qualitatively an increase of the polarization resistance of the alloy with time.

The high values obtained for the inner layer capacitance diverge from those obtained previously and in previous works [31]; two main reasons are responsible of this fact, the electrochemical and the rotating conditions used in this study (the values of the present work have been obtained under OCP and using a RDE 1000 r.p.m. instead of applying a constant passive potential under static conditions). Mainly because of the non-controlled electrochemical conditions (OCP varies with time) these capacitance values lead to an uncertain film thickness calculation. In this sense, **equation (3.31)** may generate unambiguous values of the film thickness because the dielectric properties ( $\epsilon$ ) can be altered by changes in composition or morphology of the film. Several works have been found [55-57] studying the effect of the dielectric constant on the passive film thickness and high capacitance values were related to the alterations caused by passive film composition and morphology on that dielectric properties. Further investigations are needed in order to analyse the influence of dielectric properties of the passive film with time and applied potential.

According to the effect of temperature and BSA concentration on the electrochemical behaviour of the CoCrMo alloy carried out previously, it was confirmed that the BSA adsorption on CoCrMo alloy follows the **Langmuir isotherm (Figure 5.14)**. The surface concentration or amount of protein adsorbed ( $\Gamma$  in  $\text{mol}\cdot\text{cm}^{-2}$ ) can be correlated with the charge transfer resistance related to protein adsorption  $R_{p,c}^{-1}$  [17], i.e.,  $R_{p,c}^{-1}$  proportional to  $\Gamma$ . The  $R_{p,c}^{-1}$  can be calculated by means of the following expression [20]  $R_{p,c}^{-1} = R_{p,i}^{-1} - R_{p,0}^{-1}$ , where  $R_{p,i}$  is the charge transfer resistance obtained after different passivation times and  $R_{p,0}$  is the charge transfer resistance recorded in the protein free-solution. Thus, to investigate the influence of passivation time (at OCP) on

the CoCrMo behaviour, the dependence of the  $R_{p,c}^{-1}$  (proportional to surface concentration) versus immersion time was represented in **Figure 5.23**.

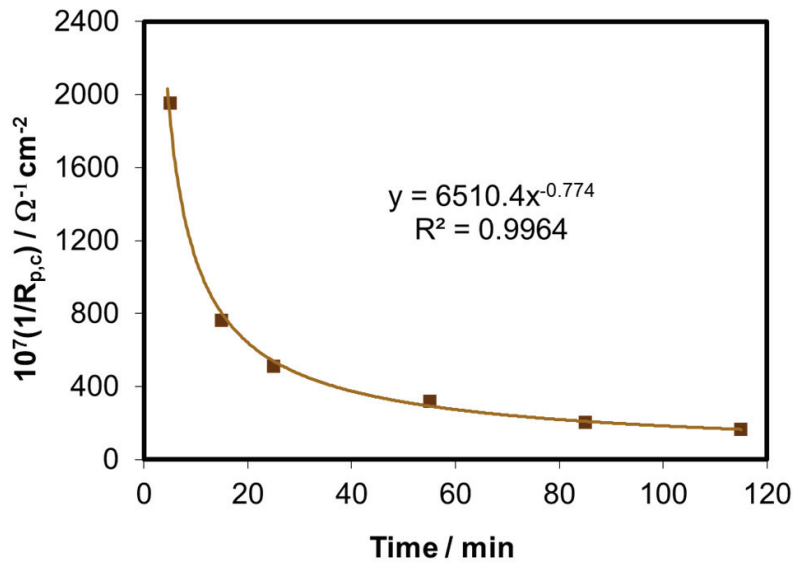


**Figure 5.23.** Evolution of the  $R_p^{-1}$  of the CoCrMo interface after BSA injection at different immersion times in PBS solution at 37°C and pH 7.4.

The amount of adsorbed protein on the CoCrMo surface at OCP depends on the immersion time. Therefore, it can be concluded that the amount of adsorbed BSA potentially decrease with the immersion time although this adsorbed protein remains constant for immersion times above 50 s. These results are in good agreement with the  $\Delta OCP$  represented in **Figure 5.21** where lower influence of the BSA adsorption was detected after longer passivation times. Furthermore, the decrease of the  $C_{out}$  values at higher passivation time (when no apparent modification in the kinetic mechanisms of the adsorption process is detected) corroborates that less amount of protein is adsorbed on the electrode surface.

### 5.3.5. APPLIED PASSIVE POTENTIAL

In order to analyse the effect of the BSA adsorption under different surface conditions a passive potential of -0.05 V was applied on the CoCrMo alloy for different periods of time. The current evolution at the passive applied potential before BSA addition is typical of a passivation process under potentiostatic conditions (Figure 5.24). When applying a passive potential the current density abruptly increases until a maximum value is reached and then diminishes until reaching a constant value (passivation current density,  $i_{pp}$ ) [30] typically of a passivation process (*Experimental techniques*, Chapter 3)

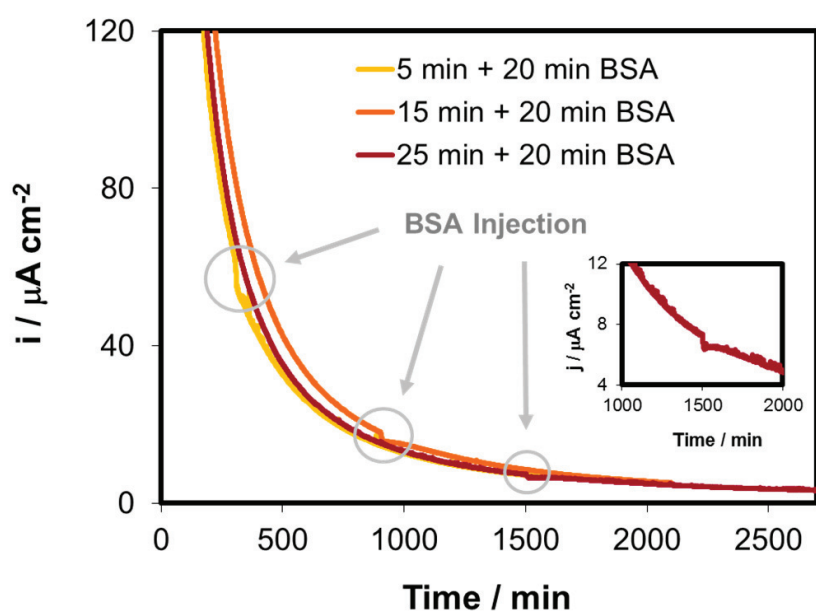


**Figure 5.24.** Current density evolution of the CoCrMo alloy at an applied passive potential of -0.05 V after 5, 15 and 25 min of passivation time and 20 min of BSA addition (arrows indicate the instant of BSA injection) in PBS solution at 37°C and pH 7.4. Inset: enlargement of the current density evolution during BSA addition when the passivation time is 25 min.

The passivation kinetics of the CoCrMo alloy can be expressed by the following expression [58]:

$$i = A_s \cdot t^{-n_s} \quad (5.8)$$

where  $i$  denotes the current density,  $A_s$  is a constant,  $t$  is the time and  $n_s$  is the passivation rate parameter representing the slope of  $\log i$  vs  $\log t$  plot. According to **equation (5.8)** the value of  $n_s$  can be considered an indirect measure of the growth of the oxide film on CoCrMo alloy at applied passive potential. R.F.A. Jardelius-Petterson [59] used the same approach in order to evaluate the passive film growth of stainless steel with different Mo and nitrogen contents.

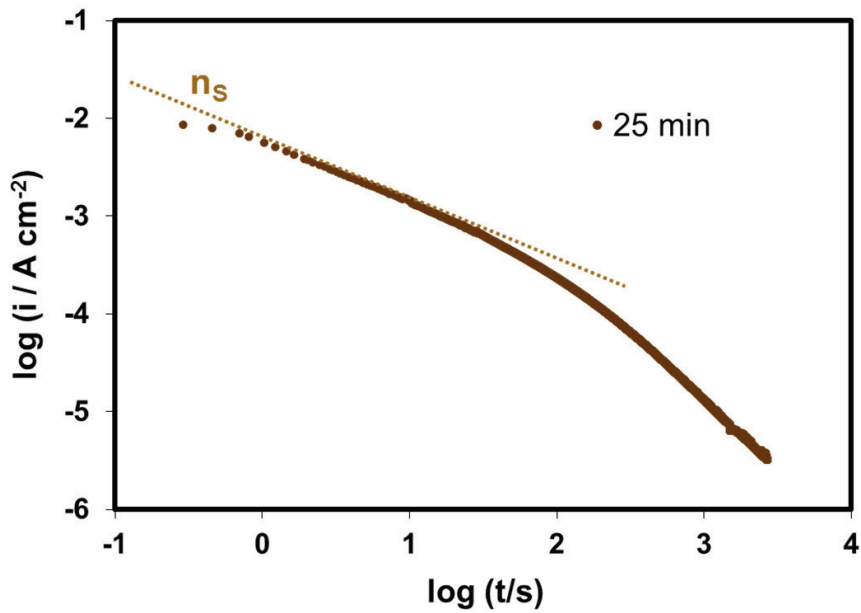


**Figure 5.25.** Decay of the current density with time during passivation of the CoCrMo alloy at an applied passive potential of -0.05 V in PBS solution. Extracted slope ( $n_s$ ) corresponds to the initial passive film growth.

The passivation kinetics of the CoCrMo at the applied passive potential of  $-0.05$  V was analysed by plotting  $\log i$  vs  $\log t$  (**Figure 5.25**). According to **equation (5.8)**, the slope of the linear representation at initial times gives information about the initial passive film growth. Thus, the average value of  $n_s$  is  $0.64 \pm 0.04$ . The low error value shows that the  $n_s$  parameter is a suitable and accurate indicator for characterizing the kinetic growth of the passive film on the alloy at the beginning of the test. This parameter has been extracted from the linear part of the plot showed in **Figure 5.25** and allows one to carry out a numerical quantification of the passive film growth on the alloy. Jae-Bong Lee [58] suggested that the anodic current density evolution can be explained by the fact that the formation rate of the passive oxide film dominated over its dissolution rate. Therefore, the obtained slope is typical for passive films growing without the superimposed dissolution of passive films. Nevertheless, in the next Chapter, the *Electrochemical Quartz Crystal Microbalance* (EQCM) will be used to quantify in real time the passivation kinetics of the CoCrMo alloy in physiological conditions. Therefore, the  $n_s$  value is a first approach that allows one to realize an initial kinetic characterization of the passivation taking place on the electrode surface.

An exponential decrease of the current density can be observed after BSA injection during the potentiostatic tests after passivation times of 5, 15 and 25 minutes (**Figure 5.24**). In the test where the sample was passivated during 5 minutes, an abrupt drop in the current density is observed just after BSA addition (current decay  $8.16 \mu\text{A cm}^{-2}$ ). When the passivation time increased to 15 minutes the current decay was lower ( $3.02 \mu\text{A cm}^{-2}$ ). The current density followed the typical exponential decay of passive surfaces, before and after the BSA addition. However, after 25 minutes of passivation the current density evolution, after BSA addition, is quite different. When the protein was added, the current density dropped ( $2.10 \mu\text{A cm}^{-2}$ ) and then, previous values were recovered. This behaviour was also observed for the test carried out after 55, 85 and 115 minutes of passivation.

**Figure 5.26** shows the evolution of the current density recorded during the last 20 minutes after the BSA addition when the passivation times were 55, 85 and 115 minutes. In these cases, including the test for 25 min, the current density decays when the protein was introduced into the PBS solution and it recovered previous values

afterwards. The recovering of the current density after reaching the minimum value (exponential increase) was modelled by the following equation:

$$i = i_0 \cdot \left( 1 - \exp\left(-\frac{t - t_0}{\tau_1}\right) \right) \quad (5.9)$$

where  $i$  is the current density generated after the BSA addition (in  $\text{A cm}^{-2}$ ),  $i_0$  is the highest value of current density (in  $\text{A cm}^{-2}$ ),  $t_0$  is the time where the current density reaches the lower value after the BSA addition (s),  $t$  is the time (s) and  $\tau_1$  is a time constant associated to the current increase produced as a consequence of BSA adsorption (s).

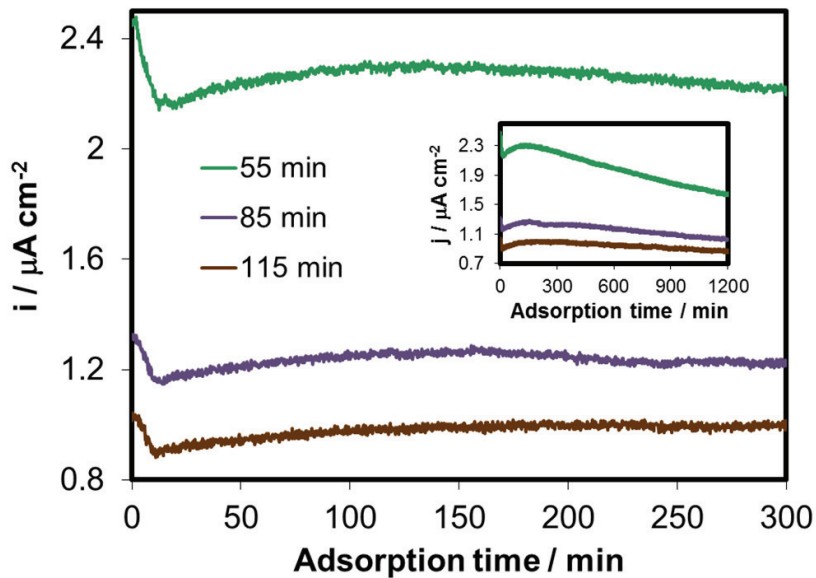


**Figure 5.26.** Evolution of the current density of the CoCrMo alloy after the BSA addition after high passivation times 55, 85 and 115 min (time 0=BSA injection) and at an applied passive potential of -0.05 V in PBS solution at 37°C and pH 7.4.

As an example, **Figure 5.27(a)** shows the evolution of the current density after the BSA addition at a passivation time of 115 minutes and **Figure 5.27(b)** represents the fitting curve using the proposed model in **equation (5.9)** for the repassivation process. In the later graph the values of the current density are expressed as deviation variables, taking the minimum value of the current density (reached after the BSA adsorption) and the time as reference, i.e. null value of current density and time.



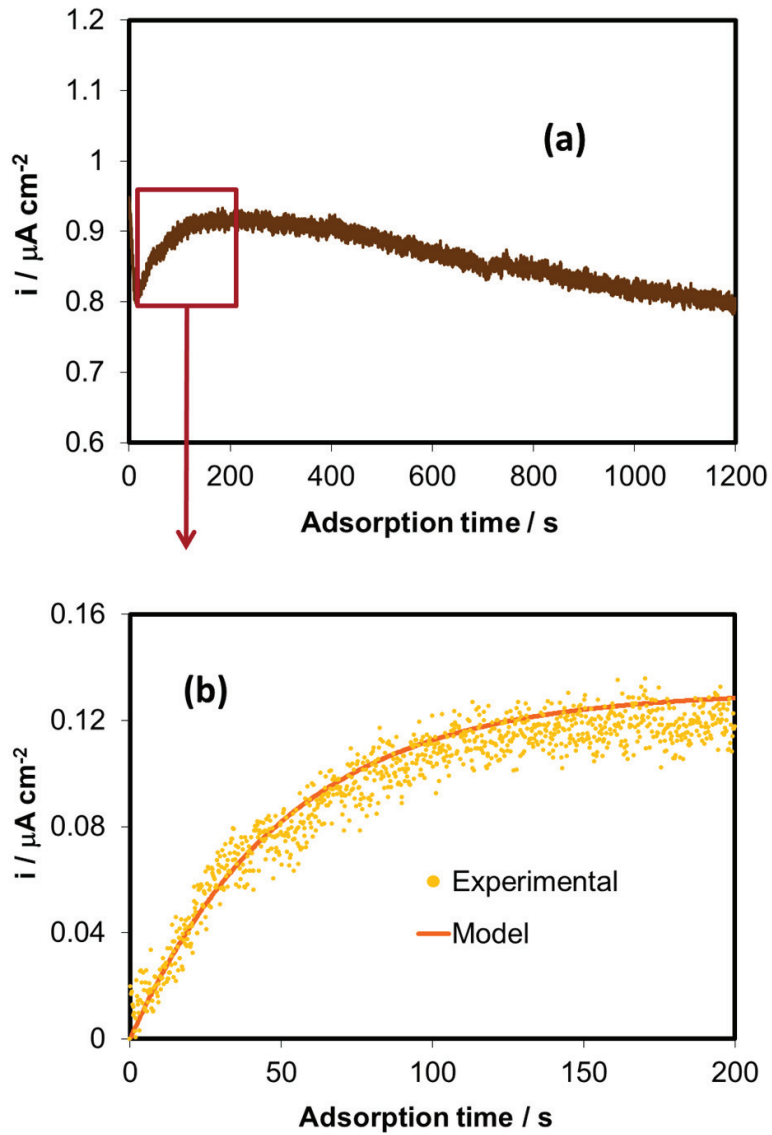


**Figure 5.27.** (a) Evolution of the current density of the CoCrMo alloy at an applied passive potential of -0.05 V after the BSA addition at the passivation time of 115 min. (b) Experimental data for the repassivation process after BSA addition after 115 min of passivation time and fitting curve obtained from equation (5.9).

The time constant values obtained after 25, 55, 85 and 115 minutes of passivation periods according to **equation (5.9)** were extracted and represented in **Figure 5.28** as a function of the passivation times; from this figure, a lineal relationship was obtained. The increase of passivation time generates an increase of the time constants; therefore, the higher the time of passivation, the lower the recovering rate of the current density value after BSA addition. Thus, it can be concluded that the effect of BSA is less pronounced when the passivation time increases under potentiostatic conditions. The stabilization of the passive film reached at higher passivation times might explain the lower influence of the BSA addition and the enhancement in the recovering passive dissolution rate after BSA addition (higher constant time values).

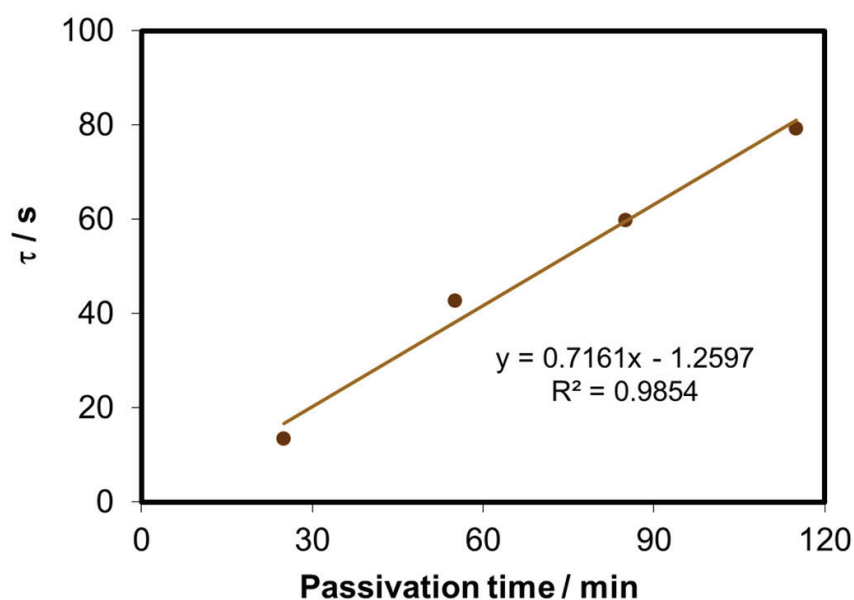


**Figure 5.28.** Time constant values versus passivation time of the  $i$  evolution after the BSA addition.

Different mechanisms of BSA adsorption on passivated surfaces of CoCrMo biomedical alloy, obtained under OCP and applied passive potential, are observed. It is clear that, in both cases, the BSA interacts with the passivated surfaces of CoCrMo modifying the

nature of the passive film by its adsorption. When the protein is added under Open conditions, the OCP shifts towards more cathodic potentials which corroborated the cathodic inhibition and anodic catalytic behaviour of the BSA when is adsorbed on the CoCrMo alloy surface. Thus, BSA can bind to the metal ions and transport them away from the solution/passive film interface encouraging further dissolution which is also corroborated by the decrease of the  $R_p$  values with the BSA addition. On the other hand, when the passivation of the samples was reached under applied potential conditions the current density drops down and it is followed by a recovering of the current density to higher values (reaching similar value of current density before the BSA addition). This effect can be explained by the blocking effect of the mass transport of oxygen and/or of reaction products to and/or from the electrode surface occurred by the BSA adsorption. These statements indicate that the mechanism of BSA adsorption on CoCrMo alloy surface strongly depends on the electrode potential.

Thus, the formation of the passive film may be an important effect on the mechanism of BSA adsorption. Passive film properties depend critically on the formation conditions [60]. The formation of the passive film at OCP involved a slower drift from the cathodic potential to the stabilized OCP potential. Slowly reacting species, such as large BSA molecules, are unlikely to affect the rapid growth of the oxide film during the potential step passivation. BSA has higher probability to interfere with film growth during slow process such as passive film growth at Open-circuit conditions. It is important to specify that the passive conditions were reached by two different ways. The two passivation pathways resulted in significant and reproducible differences in electrochemical measurements.

## 5.4. Conclusions

The interfacial behaviour of BSA on the commercial CoCrMo biomedical alloy surface was studied over the temperature range 298-333 K and at different surface conditions and several passivation times using electrochemical techniques. From the obtained results, the following conclusions are drawn:

1. Electrochemical impedance spectroscopy (EIS) was used in order to characterize the adsorption mechanisms of BSA on the CoCrMo biomedical alloys. The electrode/electrolyte interface and corresponding surface processes were successfully modelled by applying an Equivalent-Electrical-Circuit approach.
2. A charge-transfer resistance value, which represents a direct measure of a corrosion rate, was shown to be very sensitive to the amount of adsorbed protein (surface concentration), thus indicating that the adsorption of the protein (*i*) was accompanied by the transfer of the charge, via chemisorption, and (*ii*) influenced the mechanism and kinetics of the corrosion reaction. This was also apparent from the decrease in the corrosion activation energy, caused by adsorption of the protein. It was shown that BSA exhibits very high affinity towards adsorption at a CoCrMo surface via chemisorption.
3. The adsorption process was modelled using Langmuir adsorption isotherm. The corresponding thermodynamic data was calculated to give the Gibbs free energy, enthalpy and entropy of adsorption. The positive value of enthalpy indicates that excess energetic is involved in the breaking of intramolecular interactions relative to those involved in the formation of protein-metal bonds. However, since the adsorption process was found to be entropically governed, structural unfolding of the protein likely occurs at the electrode surface.
4. At OCP, the surface conditions affect the BSA adsorption kinetics. OCP dropped with the BSA addition. BSA adsorption kinetics was influenced by surface passivation when passivation time was lower than 1 hour. At higher passivation

## CHAPTER 5. Mechanisms of BSA adsorption

times, no apparent modification in the kinetic mechanisms of adsorption was observed. Furthermore the amount of adsorbed BSA decreased with the passivation time on the CoCrMo surface and remains constant for immersion times above 50 s.

5. The effect of the BSA addition at the applied passive potential are found to be dependent on the passivation time. When the passivation time is higher than 15 minutes the recovery of the current density after BSA injection was modelled and it was found a direct correlation between passivation time and time constant of the current density recover (after higher passivation times, slower recovering of the current density values was observed indicating a slower rate of passive dissolution of the CoCrMo alloy).

## 5.6. References

- [1] T. Kopac, K. Bozgeyik, J. Yener, *Colloids and Surfaces A: Physicochemical and Engineering Aspects* 322 (2008) 19-28.
- [2] F. Y. Oliva, L. B. Avalle, O. R. Cámara, C. P. De Pauli, *Journal of Colloid and Interface Science* 261 (2003) 299-311.
- [3] M. A. Khan, R. L. Williams, D. F. Williams, *Biomaterials* 17 (1996) 2117-2126.
- [4] S. Kanagaraja, I. Lundström, H. Nygren, P. Tengvall, *Biomaterials* 17 (1996) 2225-2232.
- [5] S. Virtanen, I. Milosev, E. Gomez-Barrena, R. Trebse, J. Salo, Y. T. Konttinen, *Acta Biomaterialia* 4 (2008) 468-476.
- [6] Y. Yan, A. Neville, D. Dowson, *Tribology International* 40 (2007) 1492-1499.
- [7] N. J. Hallab, K. Mikecz, C. Vermes, A. Skipor, J. J. Jacobs, *Molecular and Cellular Biochemistry* 222 (2001) 127-136.
- [8] P. A. Dimilla, S. M. Albelda, J. A. Quinn, *Journal of Colloid and Interface Science* 153 (1992) 212-225.
- [9] V. Hlady, J. Buijs, *Current Opinion in Biotechnology* 7 (1996) 72-77.
- [10] A. Sargeant, T. Goswami, *Materials & Design* 27 (2006) 287-307.
- [11] F. Watari, A. Yokoyama, M. Omori, T. Hirai, H. Kondo, M. Uo, T. Kawasaki, *Composites Science and Technology* 64 (2004) 893-908.
- [12] J. J. Jacobs, J. L. Gilbert, R. M. Urban, *Journal of Bone and Joint Surgery-American Volume* 80A (1998) 268-282.
- [13] S. G. Steinemann, *Injury-International Journal of the Care of the Injured* 27 (1996) 16-22.
- [14] A. Ithurbide, I. Frateur, A. Galtayries, P. Marcus, *Electrochimica Acta* 53 (2007) 1336-1345.
- [15] K. Nakanishi, T. Sakiyama, K. Imamura, *Journal of Bioscience and Bioengineering* 91 (2001) 233-244.
- [16] D. R. Jackson, S. Omanovic, S. G. Roscoe, *Langmuir* 16 (2000) 5449-5457.
- [17] N. P. Cosman, K. Fatih, S. G. Roscoe, *Journal of Electroanalytical Chemistry* 574 (2005) 261-271.
- [18] S. Omanovic, S. G. Roscoe, *Electrochemical and Solid State Letters* 8 (2005) E12-E15.

## CHAPTER 5. Mechanisms of BSA adsorption

- [19] S. Fukuzaki, H. Urano, K. Nagata, *Journal of Fermentation and Bioengineering* 81 (1996) 163-167.
- [20] S. Omanovic, S. G. Roscoe, *Langmuir* 15 (1999) 8315-8321.
- [21] R. Rouhana, S. M. Budge, S. M. MacDonald, S. G. Roscoe, *Food Research International* 30 (1997) CP1.
- [22] A. Sargeant, T. Goswami, *Materials & Design* 28 (2007) 155-171.
- [23] A. W. Hodgson, S. Mischler, B. Von Rechenberg, S. Virtanen, *Proceedings of the Institution of Mechanical Engineers Part H-Journal of Engineering in Medicine* 221 (2007) 291-303.
- [24] I. Milosev, V. Pisot, P. Campbell, *Journal of Orthopaedic Research* 23 (2005) 526-535.
- [25] Clarke M.T., Lee P.T.H., Arora A., Villar R.N., *Journal of Bone Joint Surgery* 85-B (2003) 913-917.
- [26] Savarino L., Granchi D., Ciapetti G., Cenni E., Greco M., Rotini R., Veronesi C.A., Baldini N., Giunti A., *Journal of biomedical materials research* 66A (2003) 450-456.
- [27] R. W.-W. Hsu, C. C. Yang, C. A. Huang, Y. S. Chen, *Materials Chemistry and Physics* 93 (2005) 531-538.
- [28] L. Reclaru, P. Y. Eschler, R. Lerf, A. Blatter, *Biomaterials* 26 (2005) 4747-4756.
- [29] F. Contu, B. Elsener, H. Bohni, *Journal of the Electrochemical Society* 150 (2003) B419-B424.
- [30] A. W. E. Hodgson, S. Kurz, S. Virtanen, V. Fervel, C.-O. A. Olsson, S. Mischler, *Electrochimica Acta* 49 (2004) 2167-2178.
- [31] A. Igual Muñoz, S. Mischler, *Journal of the Electrochemical Society* 154 (2007) C562-C570.
- [32] X. Cheng, S. G. Roscoe, *Biomaterials* 26 (2005) 7350-7356.
- [33] M. Malmsten, *Journal of Colloid and Interface Science* 207 (1998) 186-199.
- [34] M. L. C. A. Afonso, R. F. V. Villamil Jaimes, E. P. G. ArWas, M. R. Capri, E. Oliveira, S. M. L. Agostinho, *Colloids and Surfaces A: Physicochemical and Engineering Aspects* 317 (2008) 760-763.
- [35] D. Landolt and S. Mischler, *Tribocorrosion of passive metals and coatings*, Woodhead Publishing, 2011.

- [36] M. G. S. Ferreira, J. L. Dawson, *Journal of the Electrochemical Society* 132 (1985) 760-765.
- [37] P. Bommersbach, C. Alemany-Dumont, J. P. Millet, B. Normand, *Electrochimica Acta* 51 (2005) 1076-1084.
- [38] A. C. Bastos, M. G. Ferreira, A. M. Simões, *Corrosion Science* 48 (2006) 1500-1512.
- [39] M. F. Smiechowski, V. F. Lvovich, S. Roy, A. Fleischman, W. H. Fissell, A. T. Riga, *Biosensors and Bioelectronics* 22 (2006) 670-677.
- [40] A. M. Abdel-Gaber, B. A. Abd-El-Nabey, I. M. Sidahmed, A. M. El-Zayady, M. Saadawy, *Corrosion Science* 48 (2006) 2765-2779.
- [41] M. Rabe, D. Verdes, S. Seeger, *Advances in Colloid and Interface Science* 162 (2011) 87-106.
- [42] H. Mishina, M. Kojima, *Wear* 265 (2008) 655-663.
- [43] P.W. Atkins, *Physical Chemistry*, 1994.
- [44] E. Stupniseklisac, M. Metikoshukovic, D. Lencic, J. Vorkapicfurac, K. Berkovic, *Corrosion* 48 (1992) 924-930.
- [45] S. Omanovic, S. G. Roscoe, *Journal of Colloid and Interface Science* 227 (2000) 452-460.
- [46] A. K. Gaigalas, J. B. Hubbard, M. Mccurley, S. Woo, *Journal of Physical Chemistry* 96 (1992) 2355-2359.
- [47] D. Landolt, *Corrosion and surface chemistry of metals*, 2007.
- [48] I. Milosev, H.-H. Strehblow, *Electrochimica Acta* 48 (2003) 2767-2774.
- [49] A. Kocijan, I. Milosev, D. K. Merl, B. Pihlar, *Journal of Applied Electrochemistry* 34 (2004) 517-524.
- [50] T. Hanawa, S. Hiromoto, K. Asami, *Applied Surface Science* 183 (2001) 68-75.
- [51] L. D. Burke, M. E. Lyons, O. J. Murphy, *Journal of Electroanalytical Chemistry* 132 (1982) 247-261.
- [52] A. Igual Muñoz, J. García Antón, J. L. Guiñón, V. Pérez Herranz, *Corrosion Science* 49 (2007) 3200-3225.
- [53] S. L. d. Assis, S. Wolynec, I. Costa, *Electrochimica Acta* 51 (2006) 1815-1819.
- [54] J. Pan, D. Thierry, C. Leygraf, *Electrochimica Acta* 41 (1996) 1143-1153.
- [55] J. J. Gray, C. A. Orme, *Electrochimica Acta* 52 (2007) 2370-2375.



**CHAPTER 5. Mechanisms of BSA adsorption**

- [56] T. P. Cheng, J. T. Lee, W. T. Tsai, *Electrochimica Acta* 36 (1991) 2069-2076.
- [57] K.M.Ismail, S.S.El-Egamy, M.Abdelfatah, *Journal of Applied Electrochemistry* 31 (2001) 663-670.
- [58] J. B. Lee, *Materials Chemistry and Physics* 99 (2006) 224-234.
- [59] R. Jargelius-Pettersson, *Corrosion Science* 41 (1999) 1639-1664.
- [60] I. V. Sieber, H. Hildebrand, S. Virtanen, P. Schmuki, *Corrosion Science* 48 (2006) 3472-3488.



## CHAPTER 6: STUDY OF THE PASSIVATION AND ADSORPTION KINETICS BY EQCM AND XPS

---

### 6.1. Introduction

The EQCM technique has been employed in the study of passive films and electrochemical mechanisms (oxidation and dissolution) of a large number of metals and alloys [1-9], including biomedical relevant metallic materials. Studies of corrosion by EQCM have been carried out on titanium [10-12], stainless steel [6,7] and chromium [13,14]. Frateur et al. [13] studied the adsorption of Bovine Serum Albumin (BSA) on passivated chromium and they observed very fast adsorption kinetics of the BSA on the metallic surface. Ithurbide et al. [14] studied the influence of potential and pH on the adsorption process of albumin on passivated chromium surfaces and the adsorption kinetics was observed to be slightly dependent on the pH in the passive domain.

However, no literature has been found related to the use of EQCM on the corrosion behaviour of CoCrMo alloys. Furthermore, all reported results corresponded to EQCM tests carried out at room temperature (without controlling the temperature). Therefore and according to the large effect that temperature has on the electrochemical and adsorption processes [15], the possibility to extrapolate the obtained results to the in-vivo conditions (37°C) appears problematic.

The main advantage of the EQCM is the possibility to measure the mass changes on an electrode surface in real time with high resolution and sensibility. However, the EQCM is not able to differentiate between the dissolution of the alloy and passive film growth since only the overall mass change occurring on the electrode surface is measured. To get information on the chemical composition and thickness of the passive films, methods of surface analysis such as X-Photoelectron Spectroscopy (XPS) are needed. Thus XPS and EQCM were advantageously combined in the investigation of passivity, in particular for determining the film growth kinetics [7-9,16] of CoCrMo biomedical alloys.

One of the most important biomedical applications of this technique is the real quantification of the total mass that is released from the biomaterial surface and goes into the simulated body fluid. Thus, the loss material rate on real time can be measured by the EQCM.

The aim of the present chapter is the study of the anodic behaviour of a CoCrMo alloy in simulated body fluids at room temperature and at 37°C. For this, the mass change during potential sweeps from a low to a higher passive potential or to transpassive potential were evaluated and correlated to passive film growth. Furthermore, BSA was added into the electrolyte in order to determine the adsorption kinetics and its influence on the rate of passive film growth. Ex-situ XPS analysis were also performed to evaluate the chemical composition and the thickness of the passive film. A quantitative comparison between EQCM and XPS data was carried out.

## 6.2. Experimental

### 6.2.1. QUARTZ CRYSTALS

AT-cut 10MHz quartz crystals (X-tronix, Switzerland) are used for the EQCM studies and served as substrates for depositing the electrodes. The crystals were built up from plates quartz of 14 mm in diameter and 167  $\mu\text{m}$  in thickness (**Figure 6.1**). These crystals contained a thin film electrode on the backside formed by two layers, one of gold (with a thickness of 230 nm) and the second of chromium (20 nm) added to the crystal to avoid delamination. On the opposite side, a 1.45  $\mu\text{m}$  thick CoCrMo layer was deposited by physical vapour depositions (PVD). The latter layer is simultaneously used to drive the crystal of an electric field and to act as working electrode in the electrochemical cell. All the procedure is based on previous publications [9].

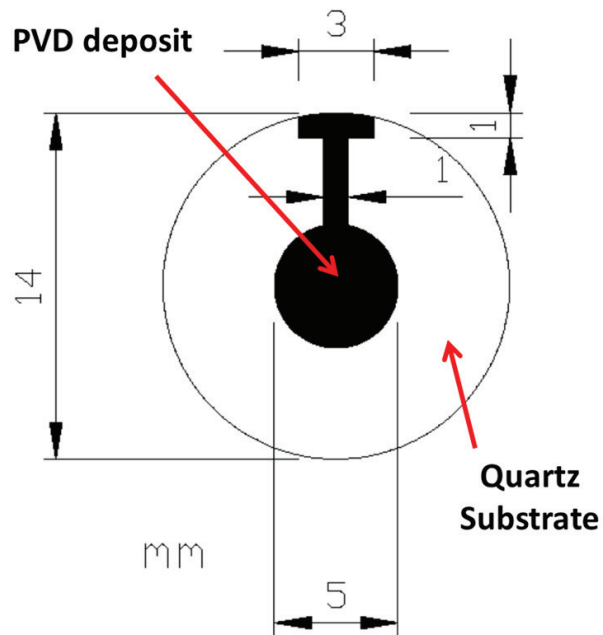


**Figure 6.1.** Design of the PVD deposit on the quartz crystal.

### 6.2.2. PVD DEPOSITS OF CoCrMo LAYERS ON QUARTZ CRYSTALS

The deposition of the metal on the quartz crystals was obtained by physical vapour deposition (PVD) which allows one to obtain thin layers capable of measuring frequency changes as consequence of mass variation on the electrode surface.

The microbalance detects frequencies around 40 kHz of the resonance frequency of the quartz crystal (10 MHz). In order to reach the suitable frequency of the oscillators it is necessary to control the crystal surface and the deposition parameters (potential, power, pressure, load and deposition time). The precise control of these parameters is needed in order to build the oscillators with a fix resonant frequency. In the case of the CoCrMo PVD deposition the desirable value of frequency is reached without previous treatments of the crystal. Thus, the roughness of the crystal is suitable for the deposition without previous chemical etching.

Before the sputter deposition of the CoCrMo on the disk electrode, the quartz crystals were cleaned in an alkaline solution and degreased ultrasonically in iso-propanol for 15 minutes.

The PVD sputter deposition was carried out in an argon atmosphere using a magnetron Edwards ESM 100 PVD chamber equipped with a rotating sample holder (**Figure 6.2**). The rotating part is placed in the top of the system (**Figure 6.2(a)**) which is equipped with 4 holes where the sample holders (masks) are aligned with pins and screwed. **Figure 6.3** (left) shows the masks corresponding to the disc where one of the pieces is used to support the crystal during the deposition and the other (right) contains the pattern in order to reach the final shape of the samples (in form of keyhole). These masks are positioned within the same circle with respect to the axe of rotation. Thus, the equivalent position of all masks allows the same deposition conditions in all the crystals. In addition, the system is equipped with two containers in the bottom part (**Figure 6.2(b)**) where the targets are placed. The target used was a *Stellite 21* which composition was determined by X-Ray Fluorescence (XRF) (Co 60.32 wt.%, Cr 33.84 wt.%, Mo 3.39 wt.%, Fe 1.42 wt.%, Ni 0.53 wt.%).



Figure 6.2. Magnetron Edwards ESM 100 PVD chamber with a (a) rotating part (top) and (b) the containers where the CoCrMo target is placed (bottom).

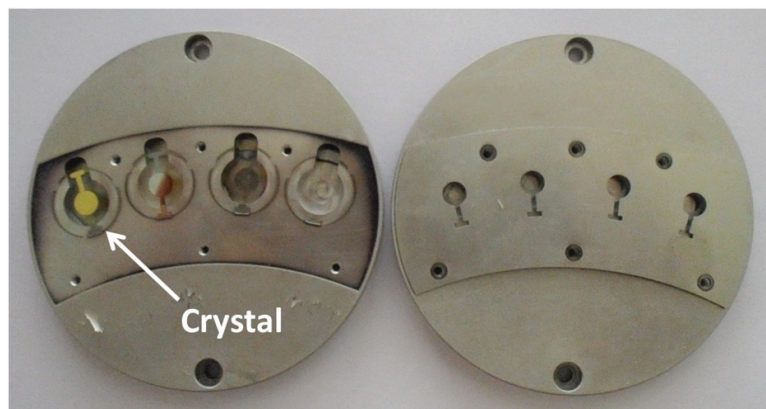


**Figure 6.3.** Images of the ring (left) and disc mask (right) screwed on the PVD sample holder.

The vacuum is reached by decreasing the pressure until  $5 \cdot 10^{-6}$  mbar. The base pressure in the PVD chamber before admitting argon was  $3.2 \cdot 10^{-5}$  mbar, reaching a value of  $10^{-2}$  mbar (pressure during deposition). During the CoCrMo deposition the sample holder was cooled with water with a refrigerant module adapted into the system. Before starting deposition, the substrate surface was cleaned by argon sputtering for 15 minutes. The parameters of the process were: 500 V of Voltage, 355 W of Power, -200 V of bias and 40 minutes of deposition time.

Both sides of the crystal after the PVD process are shown in **Figure 6.4**. The layer of gold (left) is deposited on the crystal by PVD before the CoCrMo deposition (over the Cr layer). This side remains in the ring of the mask during the latter deposition as is represented in **Figure 6.3**. The gold side of the crystal is isolated during the electrochemical measurements and connected to the CoCrMo layer to provide the frequency signal. In the other side **Figure 6.4** (right) the final shape of the CoCrMo deposit is represented and it is simultaneously used to drive the crystal an electric field and to act as working electrode in the electrochemical cell. In order to maintain the same properties in all of the deposits, especially thickness and structure, the deposition properties must be rigorously controlled and maintained between different depositions.



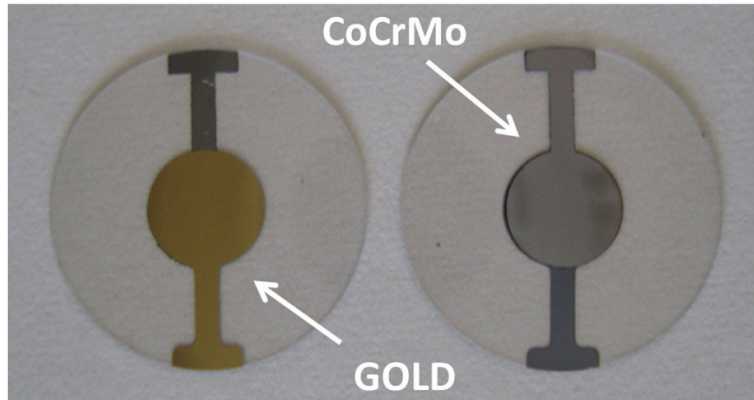


**Figure 6.4.** Image of the ring (left) and disc mask (right) screwed on the PVD sample holder. Quartz crystal with working electrode and back side gold electrode.

When the crystals are placed into the mask, special attention has to be taken in its location. The gold layer on the back side must coincide with the hole of the disc mask since the CoCrMo deposition must be deposited concentrically to the gold layer. Thus, in order to obtain the correct effective area, both circular parts for both metals must be coincident in different sides of the crystals.

The microstructure of the PVD deposits was observed using a JEOL 6300 F scanning electron microscope (SEM). **Figure 6.5(a)** shows that the PVD-coating is compact and dense with a fine-grain structure. The cross section of the **Figure 6.5(b)** shows that the film has a columnar structure with a thickness of 1.45  $\mu\text{m}$ . This structure is related to the columnar growth mode of the deposit previously observed in other deposits of tungsten, stainless steel and chromium [2,8,9].

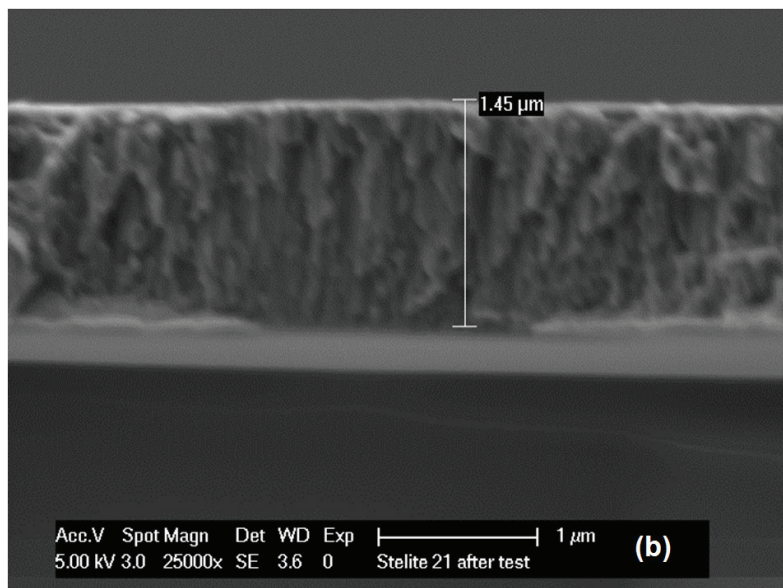
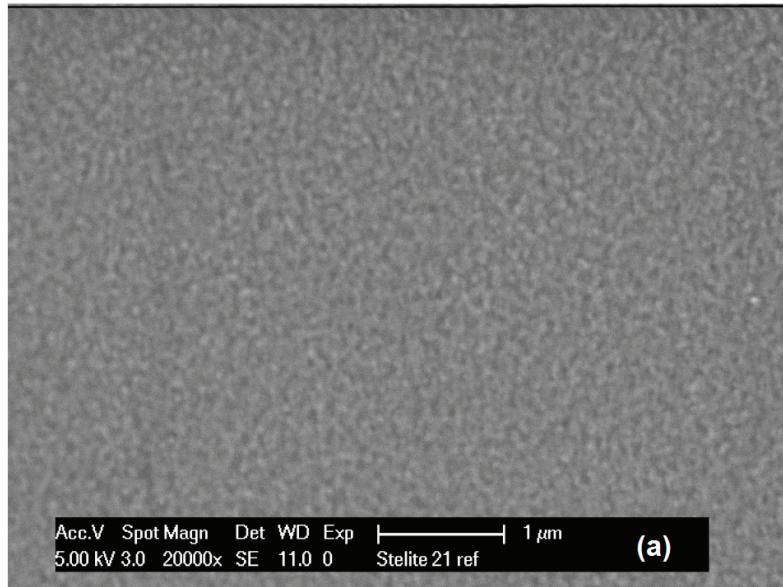


**Figure 6.5.** SEM images of the CoCrMo PVD deposits. **(a)** Surface and **(b)** cross sectional view after fracture.

To minimize interference with the anti-delamination Cr layer, the composition of the PVD layer was measured using EDX instead of XRF. The obtained coating composition (Co 64.87 wt.%, Cr 27.36 wt.%, Mo 5.37 wt.%, Fe 1.55 wt.%, Ni 0.00 wt.%, Si 0.85 wt.%) corresponds well with the target composition and in general with typical biomedical CoCrMo alloys. The presence of a weak Si signal in the coating is likely due to the quartz substrate.

In order to compare the polarization behaviour of the PVD coating to bulk alloys the polarization curve of the coating was graphically compared to published curves [17] in **Figure 6.6**. These curves were obtained with a single biomedical CoCrMo alloy in the same PBS solution. The polarization curve of the PVD coating falls well within the scatter range of the published measurements. This indicates that the results obtained here with the PVD coating are relevant for bulk alloys too.

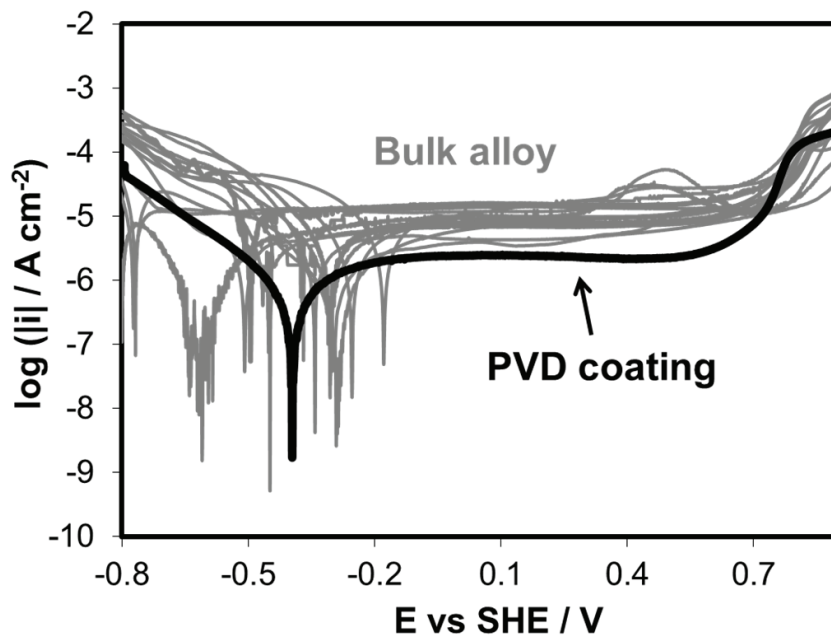


**Figure 6.6.** Comparison of polarization curves obtained with PVD-coating and CoCrMo bulk alloys in PBS solution at 37°C from [17].

### 6.2.3. EXPERIMENTAL SET-UP

**Figure 6.7** schematically shows the EQCM set-up. The oscillatory circuit used was a Maxtek PLO 10i connected to a Fluke PM6680B frequency counter and to a HP 34401 voltmeter (for measuring of the crystal resistance). The electrochemical conditions were controlled using a Schlumberger Solartron 1286 potentiostat. The entire measurement was controlled and data were logged through a National Instruments Labview interface.

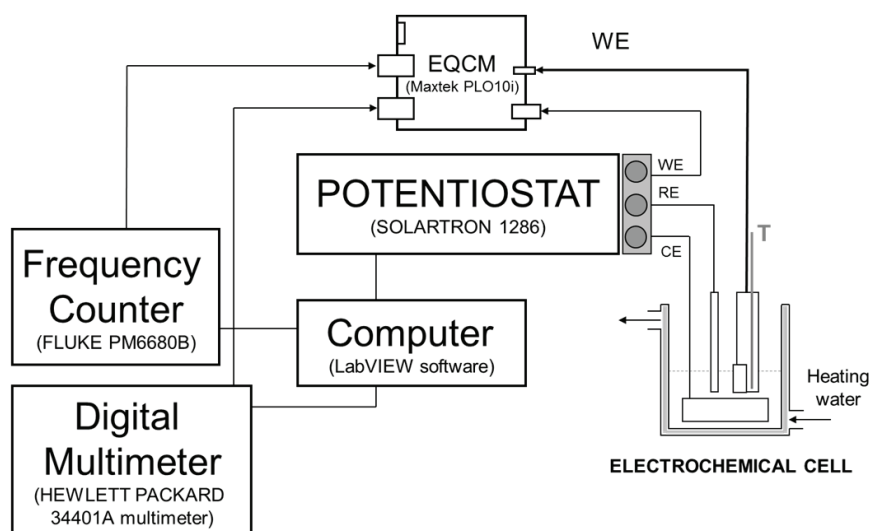


**Figure 6.7.** Schematic EQCM experimental setup.

A double walled three-electrode cell (volume 200 ml) was used for all the electrochemical measurements. An Ag/AgCl (3.5M KCl) reference electrode and a gold wire counter electrode were used. The disposition of the counter electrode in form of spiral permits the correct distribution of the charge during the electrochemical measurements. All potentials are given with respect to the Ag/AgCl electrode. The solution was not deaerated and was kept at room temperature ( $24 \pm 1^\circ\text{C}$ ) or at  $37^\circ\text{C}$  by circulating warm water between the two cell walls. Thus, to avoid thermal variations, related to the different temperature between the electrolyte and the backside of the

quartz electrode, a stabilization time of 30 minutes was imposed before starting the electrochemical experiments.

For the electrochemical experiments the quartz crystals were placed in a vertical Teflon holder previously described by Schmutz et al. [4] and schematically represented in **Figure 6.8**.

A thermocouple introduced in the holder just behind the quartz crystal was used to verify that the temperature had reached a stable value within 30 minutes (Temperature control, **Figure 6.8**). Care was taken to maintain the same height of the working electrode with respect to the electrolyte level (**Figure 6.8**) in all tests since different hydrostatic pressure on the crystal surface may affect the EQCM measurements.

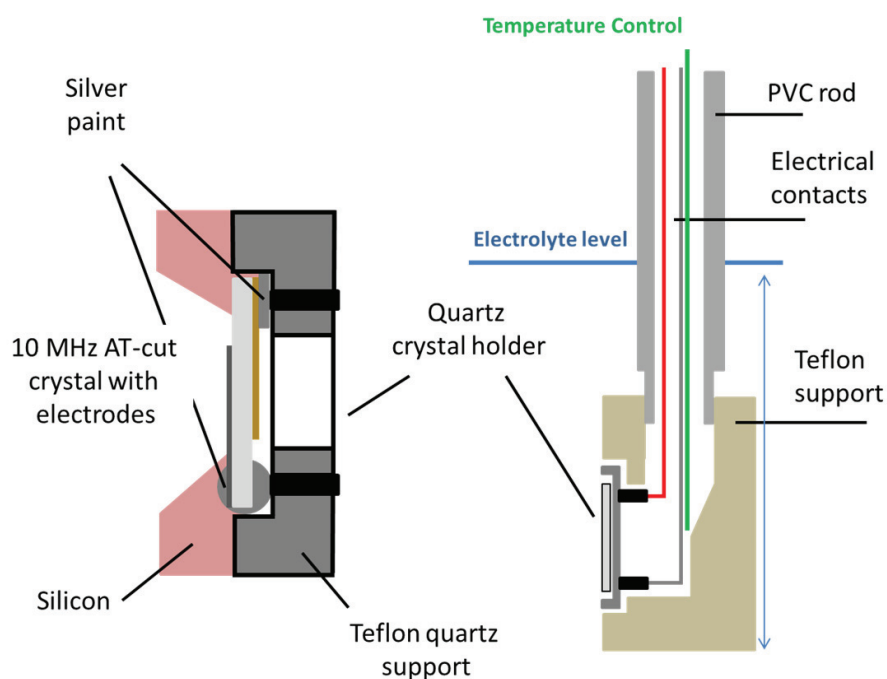


**Figure 6.8.** Scheme of the electrode arrangement used for EQCM experiments: electrode contact (left) and electrode holder (right).

The fixation system of the oscillators has to perform some functions: the system must maintain the perfect isolation of the internal crystal face (back) and the electric contacts, it must not induce strains over the crystal in order to avoid possible variation in the resonance frequency and the configuration design must allow to remove the quartz crystal without damaging the sample for surface analysis. The system configuration used in this work satisfies all these required functions (**Figure 6.8**).

The electrical contact to the working electrode was made by two drops of silver solder isolated from the solution by silicone resin. The silver permits the electric contact between the two faces of the crystal to the electrical connexion. In addition, the silver acts as adhesive of the crystal to the Teflon quartz support. After the crystal fixation, once the silver was dried, silicone (RTV 602, Wacker Chemie) was used to cover the system and was kept during 12 hours approximately. When the silicone was dried, only the conductive area of CoCrMo was exposed. Thus, when the Teflon holder was placed into the electrochemical cell, only this CoCrMo surface was in contact with the electrolyte acting as working electrode. This conductive area has an average value of 23.13 mm<sup>2</sup>.

The crystal surface of the quartz disposed in the fixation system for carry out the electrochemical test is represented in **Figure 6.9**. Three regions can be distinguished: the sensible surface, the conductive surface and the surface covered by the silicon. The sensible and the conductive surfaces are in contact with the electrolyte whereas the surface covered was isolated to the media. The surface sensible to mass variation corresponds to the coincident area between the electrodes at both sides of the quartz crystal (CoCrMo and gold electrodes) represented in **Figure 6.9** by the concentric circle. The value of this surface corresponds to 19.60 mm<sup>2</sup>.

When the silicon is removed, part of the deposited CoCrMo layer was also exposed to the electrolyte which increases the conductive area until 23.13 mm<sup>2</sup>. The ratio between the sensible mass surface and the conductive area is 84 %. The current distribution is admitted constant for the entire surface.

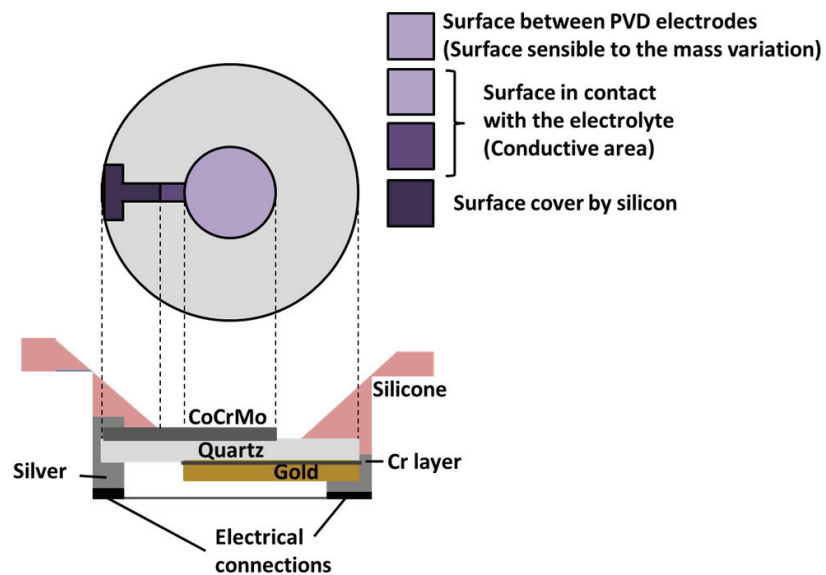


**Figure 6.9.** Electrode surfaces sensible to mass variations within the fixation system of the quartz.

Two electrolytes are used to carry out the experimental test: PBS and PBS with the addition of 500 mg L<sup>-1</sup> of BSA.

**Figure 6.10** shows several images of the different parts of the electrochemical set-up represented schematically in **Figure 6.7**.

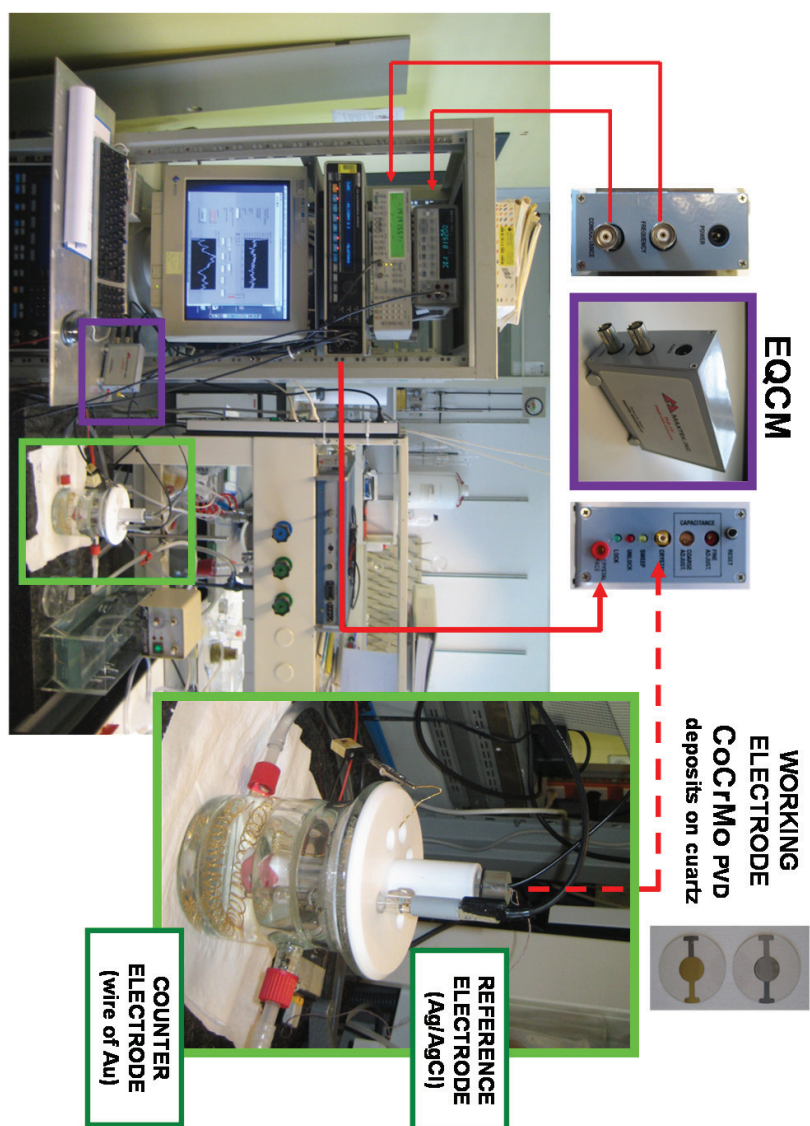


**Figure 6.10.** Images of the experimental set-up used for carrying out the EQCM measurements. The electrochemical cell with the corresponding electrodes is enlarged.



#### 6.2.4. CORRECTION CONSTANT FOR VISCOUS LOADING

The total frequency change ( $\Delta f$ ) obtained in an experimental EQCM measurement is due to the contribution of mass loading ( $\Delta f_m$ ) and the viscous loading ( $\Delta f_v$ ) according to the **equation (6.1)** [18]:

$$\Delta f = \Delta f_m + \Delta f_v \quad (6.1)$$

In the case of ideally smooth surfaces, rigidly attached films and Newtonians fluids, mass loading influences only the resonant frequency, whereas viscous loading affects both the frequency and the quartz crystal resistance near the resonance frequency [18].

The mass loading is only related to changes in the total mass of the quartz due to mass added or removed from the surface. A relationship between the changes in the quartz electrode mass ( $\Delta m$ ) and the frequency shift ( $\Delta f_m$ ) is the Sauerbrey constant which has been described in the Chapter 3 (*Experimental techniques*) by the **equations (3.43)** and **(3.44)**. According to Sauerbrey's theory, the mass sensitivity is only dependent on the quartz properties, not on the added material. Furthermore, the negative sign of the Sauerbrey equation shows an inverse relation between the frequency shift and the mass change on the electrode surface. Thus, a reduction in the resonance frequency is related to mass accumulation on the crystal.

Galliano et al. [18] demonstrated that the viscous loading  $\Delta f_v$  can be accurately corrected in real time by recording the crystal resistance  $\Delta R_{crys}$  since a direct relation between the  $\Delta f_v$  and  $\Delta R_{crys}$  exists according the **equation (6.2)**:

$$\Delta f_v = K_v \cdot \Delta R_{crys} \quad (6.2)$$

Here  $K_v$  is a proportional constant that needs to be calibrated for a given system and temperature.

Water/glycerol solutions with the concentrations of 100, 75, 50 and 25 % (in water volume) were prepared in order to determine the proportionality constant ( $K_v$ ) that allows one to correct the total frequency for viscous loading (**equation (6.2)**). These solutions are chemically inert and do not lead to adsorption on the metal surface and

therefore  $\Delta f_m$  can be neglected [18,19]. Thus, the change in frequency is only related to the viscous load.

**Figure 6.11** shows the frequency variation ( $\Delta f$ ) and the variation of the crystal resistance ( $\Delta R_{crys}$ ) with respect to pure water after immersion of the crystal in the glycerol solutions. A good linear dependence is found in agreement with **equation (6.2)**. The slopes of the linear interpolations give  $K_v$  values of -10.6 and -8.6  $\text{Hz } \Omega^{-1}$  for room temperature and 37°C, respectively. It is important to highlight that all possible variables that can affect the variation of frequency are corrected by this calibration.

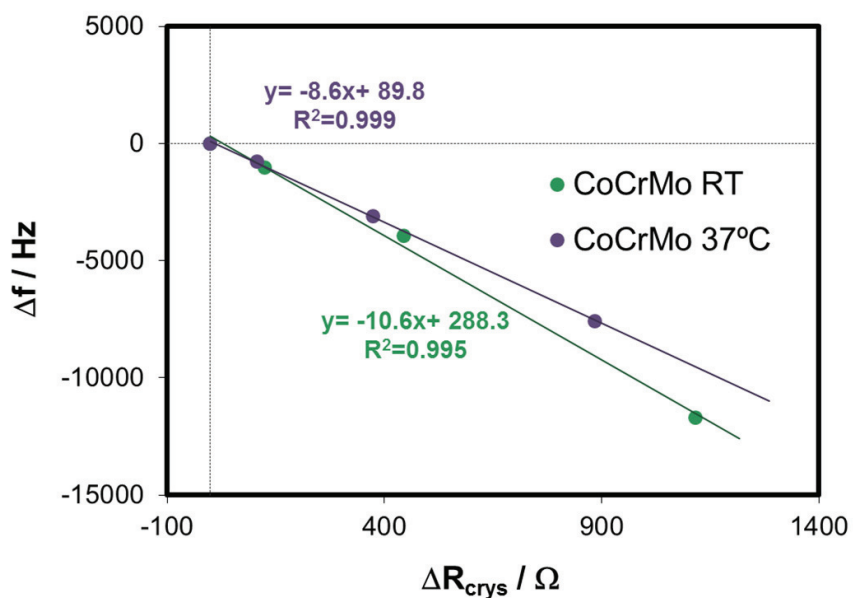


**Figure 6.11.** Variation of the resonance frequency of the quartz crystal electrode as a function of the crystal resistance for the CoCrMo alloy at room temperature and 37°C in solutions of different glycol/water concentration.

The correction for viscous loading is the first step when evaluating the frequency signal obtained after any electrochemical measurement.

### 6.2.5. CALIBRATION OF THE SAUERBREY CONSTANT

The quartz sensitivity factor ( $C_f$ ) in the Sauerbrey equation can be theoretically calculated or experimentally measured. The theoretical values of the  $C_f$  can be obtained using the physical properties of the crystal, however the experimental method obtained by the electrodeposition of copper on a gold electrode at 100 % current efficiency gives more accurate  $C_f$  values [18]. This latter approach was used in this work, **Figure 6.12**.

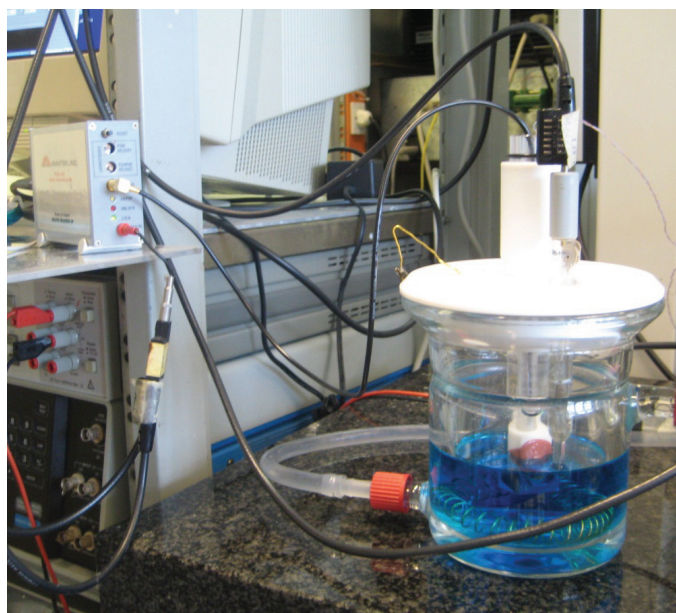


**Figure 6.12.** Experimental cell and EQCM during the calibration of the Sauerbrey constant.

Copper was plated from a solution of 0.5 M  $\text{CuSO}_4$  + 0.5 M  $\text{H}_2\text{SO}_4$  + 1.1 M ethanol at room temperature and 37°C at an applied potential of -0.21 V. Previous studies demonstrated that this process shows a current efficiency of 100 % at this cathodic potential [20,21]. The current density  $i$  and the frequency change  $\Delta f$  due to the electrodeposition were registered during the test (**Figure 6.13**).

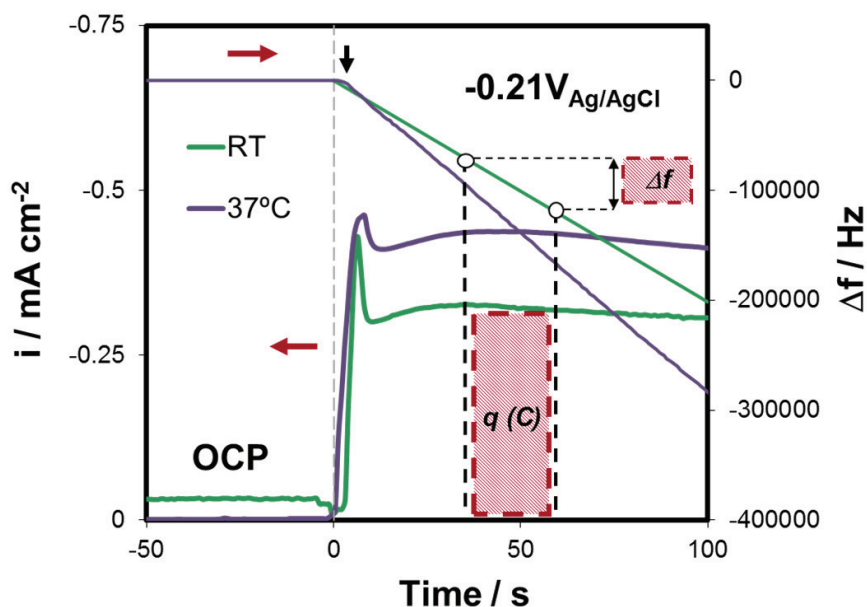


**Figure 6.13.** Current and frequency evolution obtained during the electrodeposition (-0.21 V) of copper on a gold electrode at room temperature (RT) and 37°C.

The contribution of viscous loading was subtracted using the  $K_v$  constant described above (correction for viscous loading). The Sauerbrey constant  $C_f$  was determined using **equation (6.3)**:

$$C_f = -\frac{\Delta f_m}{\Delta m} = -\frac{\Delta f_m}{\frac{q \cdot Mr_{Cu}}{n \cdot F}} \cdot A_{cond} \quad (6.3)$$

where  $q$  is the electrical charge (integrated from the current vs time curves as shown in **Figure 6.13**),  $Mr_{Cu}$  is the atomic mass of copper ( $63.54 \text{ g mol}^{-1}$ ),  $n$  is the charge number or valence of dissolution of the metal (2 in this case),  $F$  is the Faraday constant ( $96485 \text{ C mol}^{-1}$ ) and  $A_{cond}$  is the conductive area in  $\text{cm}^2$  ( $23.13 \text{ mm}^2$ ).

The experimental values of the sensitivity factor ( $C_f$ ) are  $0.20 \pm 0.05$  and  $0.21 \pm 0.01 \text{ Hz cm}^2 \text{ ng}^{-1}$  at room temperature and 37°C, respectively (average values of 3

**CHAPTER 6.** Study of the passivation and adsorption kinetics by EQCM and XPS

independent tests for each temperature). Therefore, at lower temperatures, the same change in frequency corresponds to higher variation in mass on the electrode surface.

#### 6.2.6. ELECTROCHEMICAL TESTS.

Two different electrochemical tests were conducted with the described EQCM set-up: potentiodynamic curves and potential step tests.

The general corrosion behaviour of the CoCrMo alloy was analysed by *potentiodynamic measurements*. Initially, open circuit was measured for 10 min. The scans were started at a cathodic potential of -1 V and moved into the anodic direction up to the transpassive region (limited at a maximum current of 200 mA) at a scan rate of  $1 \text{ mV s}^{-1}$ . The starting potential was selected at -1 V since more cathodic potentials increased the current density which worsened the adhesion properties of the deposit and favoured its breaking-off. These polarization curves are characterized by the simultaneous measurement of the current response and frequency during the scan which allows one to associate the variation of mass on the electrode surface with the different potential domains.

In order to analyse the effect of temperature and the BSA adsorption on the general corrosion behaviour of the CoCrMo alloys, the potentiodynamic curves were carried out under the following experimental conditions: PBS at room temperature, PBS at 37°C and PBS+BSA at 37°C. All experiments were carried out under non deaerated conditions. Electrochemical parameters such as corrosion potential ( $E_{corr}$ ) as well as the passive current density ( $i_p$ ) and the breakdown potential ( $E_{br}$ ) were extracted from the polarization curves. The  $i_p$  was obtained at the passive potential of 0.1 V.

On the other hand, the film growth of the CoCrMo was analysed potentiostatically using *potential step experiments*. These tests consisted in maintaining the potential at -0.05 V for 30 minutes and subsequently increasing it at a fast controlled scan rate (10 and  $100 \text{ mV s}^{-1}$ ) to 0.35 or 0.55 V. The sample was kept at the applied potential for 30 minutes. These potentials have been selected from the potentiodynamic curves in order to study the oxide film growth and dissolution kinetics under passive and transpassive conditions respectively. The response in current and frequency is monitored during the tests. Before the potentiostatic tests, the open circuit potential was measured for 10 min. The use of different potential scan rates allows one to investigate the film response of the alloy to potential changes [8]. Furthermore, a

potential step from OCP to  $-0.05$  V was also performed in order to characterize the oxide film growth before applying the potential ramp. Potential step experiments are schematically represented in **Figure 6.14**.

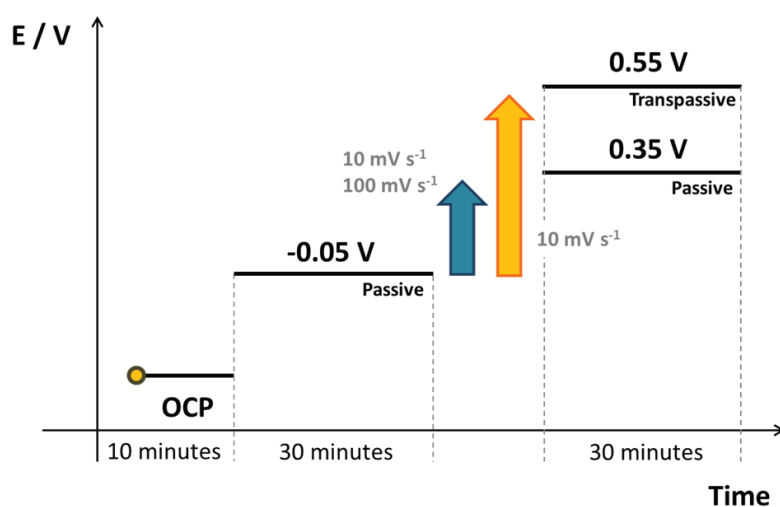


**Figure 6.14.** Potential step measurements (passivation experiments) consisting in maintaining the potential at  $-0.05$  V for 30 minutes and increasing it at a fast controlled scan rate to  $0.35$  V ( $10$  and  $100$   $\text{mV s}^{-1}$ ) or  $0.55$  V ( $10$   $\text{mV s}^{-1}$ ) for 30 minutes. Before the test, OCP was measured during 10 min.

### 6.2.7. X-RAY PHOTOELECTRON SPECTROSCOPY

After the electrochemical experiments the samples were taken out of the cell with the polarization switched on. They were rinsed with water and blow-dry with nitrogen before being stored in a dessicator for at least one week before XPS analysis.

The XPS measurements were performed with a Kratos AXIS ultrahigh resolution spectrometer, using a monochromatic Al  $K_{\alpha}$  X-ray source and a take-off angle of  $0^{\circ}$  with respect to the surface normal. No sputtering was performed prior to analysis. The energy scale was calibrated by fixing the adventitious carbon peak  $285$  eV. The fitting of the XPS-spectra was performed using the commercial software package *CasaXPS*

and the peaks listed in **Table 6.I**. The evaluation procedure included an iterated Shirley procedure for background subtraction. The peak identification was made to obtain a consistent fit at all the investigated potentials. The metal peak positions were allowed to float to compensate for a slight charging in the passive film. For quantification, relative sensitivity factors given by the XPS instrument supplier were used. The passive film thickness was calculated using the intensity ratios of oxidised metal over the metallic signal.

For the quantification of the oxide film thickness, the passive film was divided into an oxide and a covering hydroxide-water layer according to a method previously used [9,22-26]. In presence of BSA, the N peak was included in order to take into account the protein adsorption layer.

**Table 6.I.** XPS peaks considered for fitting the XPS data.

ELEMENT	PEAK	OXIDATION STATE	BINDING ENERGY
Cr	2p <sub>2/3</sub>	Cr	573.8 ± 0.4
		Cr <sup>+3</sup> oxide	+ 2.2
		Cr <sup>+3</sup> hydroxide	+ 3.4
		Cr <sup>+6</sup>	+ 4.9
Co	2p <sub>2/3</sub>	Co	778 ± 0.6
		Co oxidized	+ 2.5
Mo	3d <sub>5/2</sub>	Mo	227.5 ± 0.3
		Mo <sup>+4</sup> oxide	+ 1.5
		Mo <sup>+4</sup> hydroxide	+ 3.4
		Mo <sup>+6</sup>	+ 4.9
O	1s	O <sup>2-</sup>	530.2 ± 0.7
		OH <sup>-</sup>	+ 1.6
		H <sub>2</sub> O	+ 3.0
N	1s	NH	399
		NH <sup>+3</sup>	+ 2.0
		PO <sub>4</sub> <sup>-3</sup>	132.5
P	2p <sub>2/3</sub>	HPO <sub>4</sub> <sup>-2</sup>	+ 1
		H <sub>2</sub> PO <sub>4</sub> <sup>-</sup>	+ 2

Uncertainties are based on 2σ (90% confidence) of 15 measurements. The Co-peak was low in intensity, thus uncertainty is higher. Since oxide peaks were fixed relative to the metal peak, only the relative energy is given [22].



### 6.3. EQCM experiments

In this section, the electrochemical measurements carried out with the EQCM (potentiodynamic curves and potential step tests) and the XPS spectra obtained on the samples after the potential step measurements are shown. In order to clarify the results and its latter discussion, the potential step tests and the XPS section have been divided in two parts, the characterization of the film growth under passive and transpassive conditions.

#### 6.3.1. POTENTIODYNAMIC CURVES

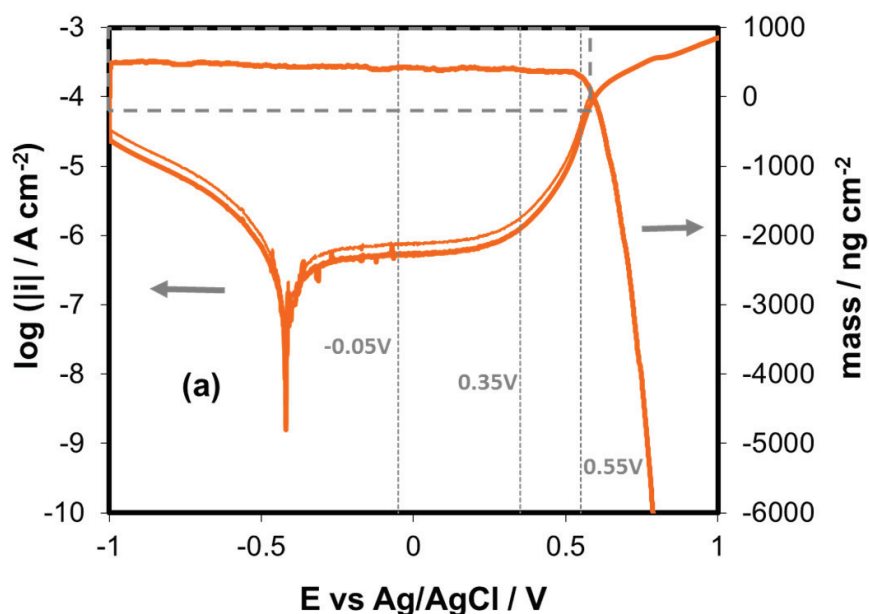
**Figure 6.15** shows the current density evolution and the mass change as a function of the potential sweep carried out in **(a)** PBS at room temperature, **(b)** PBS at 37°C and **(c)** PBS+BSA at 37°C. After the correction for viscous loading, the mass signal was smoothed using a *Savitzky-Golay algorithm* [27].

The cathodic domain below -0.5 V is characterized by a negative current density due to the reduction of dissolved oxygen and partially of water. In this domain, the mass significantly increases at the beginning of the tests in particular at higher temperatures. Indeed, the maximum value of mass reached at 37°C was 760 ng cm<sup>-2</sup> (at -0.8 V) while at room temperature only a maximum of 500 ng cm<sup>-2</sup> (at -0.9 V) was observed. The continuous and slight increase of the mass in this cathodic domain is clearly observed in the enlargements of the mass variation versus potential between -1 V and 0.6 V represented in **Figure 6.16**. This mass increase is likely related to the build up of an oxide film on the CoCrMo alloy surface, which interestingly occurs at relatively large cathodic potentials. However, other phenomena such as adsorption could contribute to the mass increase.

Furthermore, the presence of BSA increases this maximum value of mass in comparison with the maximum values obtained in PBS. Thus, the maximum value of mass value was 2350 ng cm<sup>-2</sup> (at -0.85 V).

The second domain corresponds to the passive plateau which extends over a broad range of potentials (from -0.4 to 0.4 V approximately). In this domain, the current density remains constant and monotonic loss of mass is observed. This behaviour corresponds well to passive dissolution. After the passive domain, the value of the mass reaches the value of 350 ng cm<sup>-2</sup> (in PBS at room temperature), 400 ng cm<sup>-2</sup> (in PBS at 37°C) and 500 ng cm<sup>-2</sup> (in PBS+BSA at 37°C). Therefore, high amount of mass generated at the beginning of the test is dissolved into the electrolyte in the passive domain.

The transpassive domain can be divided in two regions: the first one from approximately 0.4 to 0.6 V and the second from 0.6 to 1 V. The first transpassive region (I) is characterized by an abrupt increase in the current density at around 0.4 V without any significant change in mass loss rate. This potential lies in between the equilibrium potentials of the oxidation of Cr<sup>+3</sup> to Cr<sup>+6</sup> (0.2 V) and of the water oxidation (0.6 V). Therefore this current increase can be attributed to the formation of Cr<sup>+6</sup>.



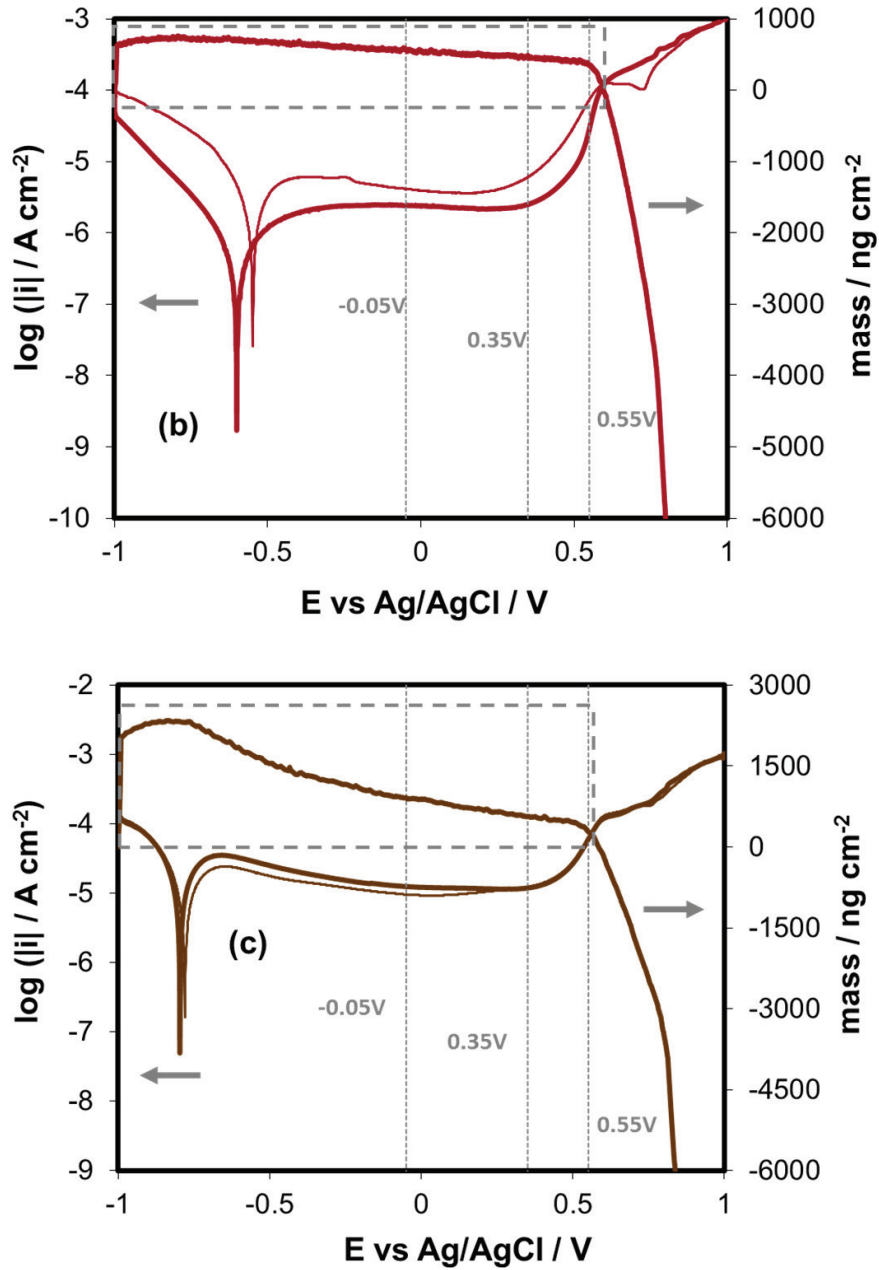
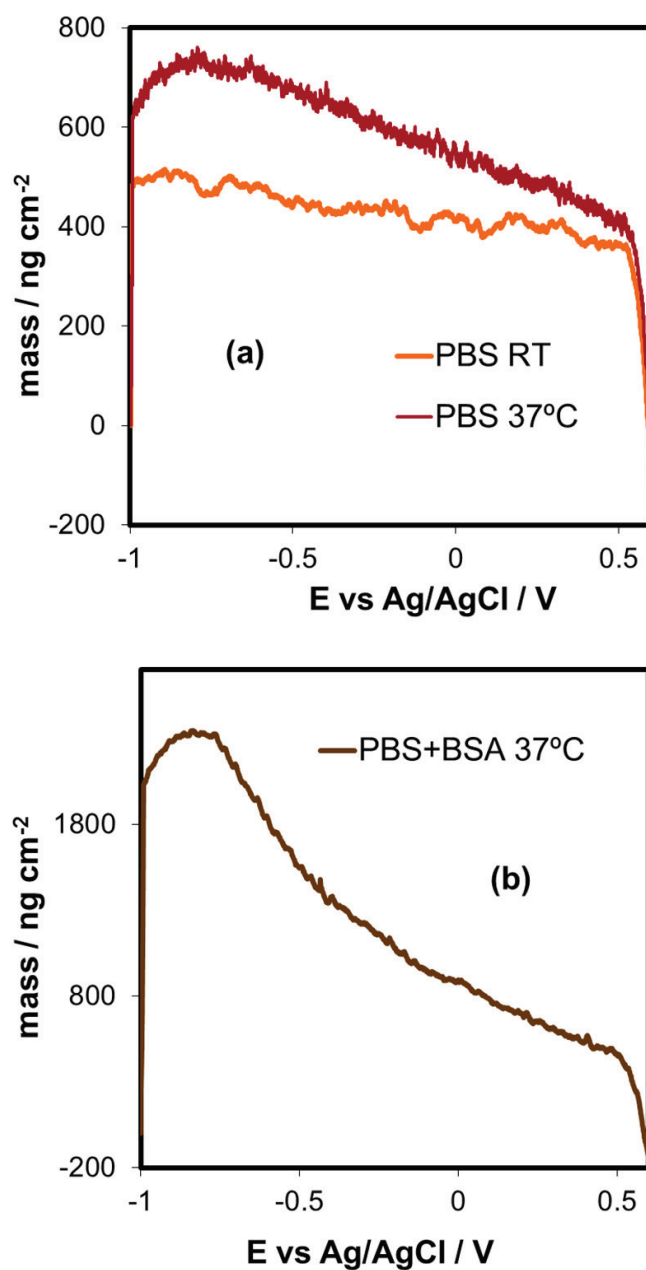


Figure 6.15. Potentiodynamic curve and simultaneous measurement of mass change of the CoCrMo alloy at  $1 \text{ mV s}^{-1}$  (a) in PBS at room temperature, (b) in PBS at  $37^\circ\text{C}$  and (c) in PBS+BSA at  $37^\circ\text{C}$ .



**Figure 6.16.** Enlargement of the mass variation in the active and passive domains of the potentiodynamic curves represented in **Figure 6.15** obtained (a) in PBS at room temperature and 37°C and (c) in PBS+BSA at 37°C.

On the other hand, in the second transpassive region (II), a strong decrease of the mass takes place above 0.6 V due to transpassive dissolution [22]. This potential corresponds to the reversible potential of water and to a change in anodic kinetics characterized by a shoulder in the polarization curve.

Similar transpassive behaviour was reported in a previous EQCM investigation of FeCr alloys in sulphuric acid solutions [5]. These previous and the present findings indicate that oxidation of  $\text{Cr}^{+3}$  to  $\text{Cr}^{+6}$  is not sufficient to trigger transpassive dissolution.

**Table 6.II** summarizes the electrochemical parameters  $E_{corr}$ ,  $i_p$  and  $E_{br}$  extracted from the potentiodynamic curves. At 37°C these values correspond well with the average values obtained under similar conditions in a round robin test carried out using a Co28Cr6Mo bulk alloy [17]. Clearly those parameters are significantly affected by the temperature which shifts  $E_{corr}$  towards lower values and increases  $i_p$  one order of magnitude. This trend in the  $i_p$  parameters was also observed in the temperature study shown in the Chapter 5. The temperature also influences the mass loss. Temperature increases the mass growth at the beginning of the tests (within the cathodic domain) which indicates that passive film thickness increases with temperature. Furthermore, temperature accelerated passive dissolution of the CoCrMo alloys. Indeed, the slope of the mass vs potential curves (**Figure 6.15(a)** and **Figure 6.15(b)**) in the passive domain raises from  $100 \text{ ng cm}^{-2} \text{ V}^{-1}$  at room temperature to  $260 \text{ ng cm}^{-2} \text{ V}^{-1}$  at 37°C.

It is also observed that the BSA affects the values of the extracted electrochemical parameters and the measured mass loss. In presence of BSA, a displacement of the  $E_{corr}$  towards more cathodic potentials and an increase of the current density in the cathodic-anodic transition domain are observed. This corroborates the anodic catalyser behaviour of the BSA under potentiodynamic conditions on the CoCrMo surface. These electrochemical parameters extracted from the curves in the PBS+BSA solution at 37°C (**Table 6.II**) also agrees with the average values obtained in the round robin test carried out using a Co28Cr6Mo bulk alloy with the same BSA concentration and temperature [17]. Furthermore, the BSA adsorption enhanced the loss of mass of the CoCrMo alloy in the passive domain, obtaining a variation of  $1230 \text{ ng cm}^{-2} \text{ V}^{-1}$ .

**Table 6.II.** Electrochemical parameters of the CoCrMo alloy in simulated body fluids at different temperatures.

<b>ELECTROCHEMICAL PARAMETERS</b>				
<b>Electrolyte</b>	<b>Temperature</b>	<b><math>E_{corr}</math> (mV)</b>	<b><math>i_p</math> (<math>\mu\text{A}/\text{cm}^2</math>)</b>	<b><math>E_{br}</math> (mV)</b>
PBS	Room Temperature	$-418 \pm 10$	$0.51 \pm 0.22$	$389 \pm 35$
PBS	37°C	$-575 \pm 54$	$4.46 \pm 1.18$	$406 \pm 21$
PBS+BSA	37°C	$-796 \pm 12$	$12.17 \pm 1.88$	$434 \pm 15$

### 6.3.2. POTENTIAL STEP MEASUREMENTS

Potential step tests were performed in order to characterize the passive film growth of CoCrMo alloys. The following experimental variables were investigated: scan rate, temperature and applied potentials (passive and transpassive potential).

#### A) Passive Domain

The **Figures 6.17-6.20** shows the experimental results obtained during the potential step from -0.05 to 0.35 V in PBS at the scan rates of  $10 \text{ mV s}^{-1}$  at room temperature (**Figure 6.17**), in PBS at the scan rate of  $10 \text{ mV s}^{-1}$  at  $37^\circ\text{C}$  (**Figure 6.18**), in PBS at the scan rate of  $100 \text{ mV s}^{-1}$  at  $37^\circ\text{C}$  (**Figure 6.19**) and in PBS+BSA at the scan rate of  $10 \text{ mV s}^{-1}$  at  $37^\circ\text{C}$  (**Figure 6.20**). The selected potential (0.35 V) corresponds to the passive domain according to the CoCrMo potentiodynamic curves, **Figure 6.15**. The total frequency was measured simultaneously to the total current density. Thus, after correcting the total frequency for viscous loading (**equation (6.1)**) and after applying the Sauerbrey equation (**equations (3.43)** and **(3.44)**) the variation of the total mass measured by EQCM was obtained ( $\text{mass}_{\text{EQCM}}$ ).

**Figures 6.17** and **6.18** show the effect of temperature on the passive film growth. While temperature does not affect the shape of the current transient it influences the total charge and the mass loss. At room temperature the mass loss in the steady state ( $174 \pm 5 \text{ ng cm}^{-2}$ ) is lower than at  $37^\circ\text{C}$  ( $216 \pm 4 \text{ ng cm}^{-2}$ ) while the charge changes from  $1.8 \pm 0.3 \text{ mC cm}^{-2}$  (room temperature) to  $2.9 \pm 0.3 \text{ mC cm}^{-2}$  ( $37^\circ\text{C}$ ).

**Figures 6.18(a)** and **6.19(a)** show the response of the current density when two different scan rates were used. The peak current is higher at  $100 \text{ mV s}^{-1}$  scan rate but the steady-state current density after approximately 500 s ( $0.9 \mu\text{A cm}^{-2}$ ) as well as the total charge ( $3.1 \pm 0.3$  and  $2.8 \pm 0.2 \text{ mC cm}^{-2}$  for 10 and  $100 \text{ mV s}^{-1}$  respectively) are little affected by the scan rate. **Figures 6.18(b)** and **6.19(b)** show the evolution of the mass variation measured during the potentiostatic test at 0.35 V at different scan rates. The mass evolution shows a continuous mass loss (passive dissolution) until approximately 900 s when the mass change reaches a steady-state plateau. The plateau values are  $216 \pm 4$  and  $175 \pm 10 \text{ ng cm}^{-2}$  for the 10 and  $100 \text{ mV s}^{-1}$  scan rates,

respectively. This difference suggests faster passivation at higher scan rate thus yielding less dissolution. The fact that the steady-state is reached earlier at higher scan rate support this hypothesis (**Figures 6.18(b)** and **6.19(b)**).

In **Figure 6.20** the potential step experiment in presence of BSA is shown. The charge ( $3.4 \pm 0.3 \text{ mC cm}^{-2}$ ) and the mass loss ( $245 \pm 21 \text{ ng cm}^{-2}$ ) obtained are slightly higher than the obtained in PBS under the same conditions ( $10 \text{ mV s}^{-1}$  and  $37^\circ\text{C}$ ). This behaviour suggests that the protein favours the passive dissolution of the alloy.

These results are in good agreement with the corrosion characterization of the CoCrMo alloy (Chapter 4) where at  $0.35 \text{ V}$  (upper potential within the passive domain) the addition of BSA favoured the passive dissolution of the alloy under potentiostatic conditions (decrease of  $R_p$  in PBS+BSA in comparison with the obtained in PBS solution).



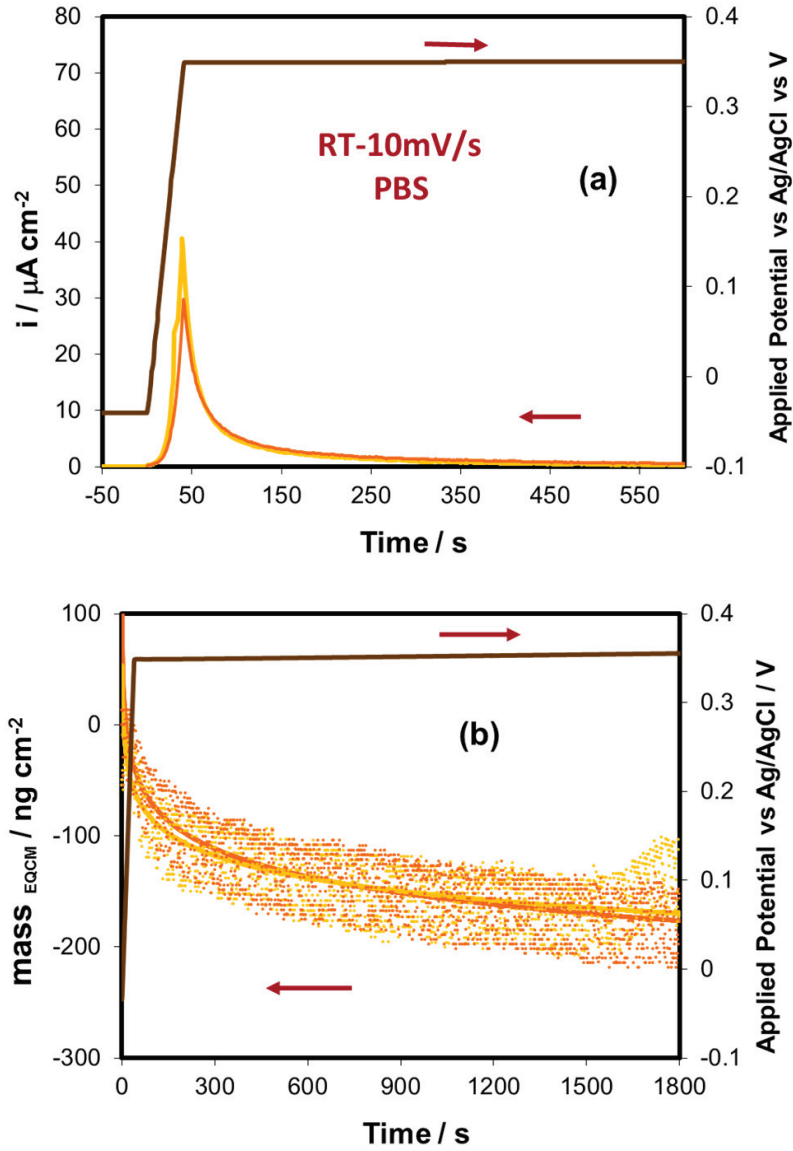


**Figure 6.17.** (a) Current density evolution (b) and mass change measured by the EQCM ( $\text{mass}_{\text{EQCM}}$ ) in potentiostatic tests from -0.05 to 0.35 V of a CoCrMo biomedical alloy in PBS at room temperature and  $10 \text{ mV s}^{-1}$ . Results from two independent tests are shown. Continuous lines corresponds to exponential interpolation of the measurements points.

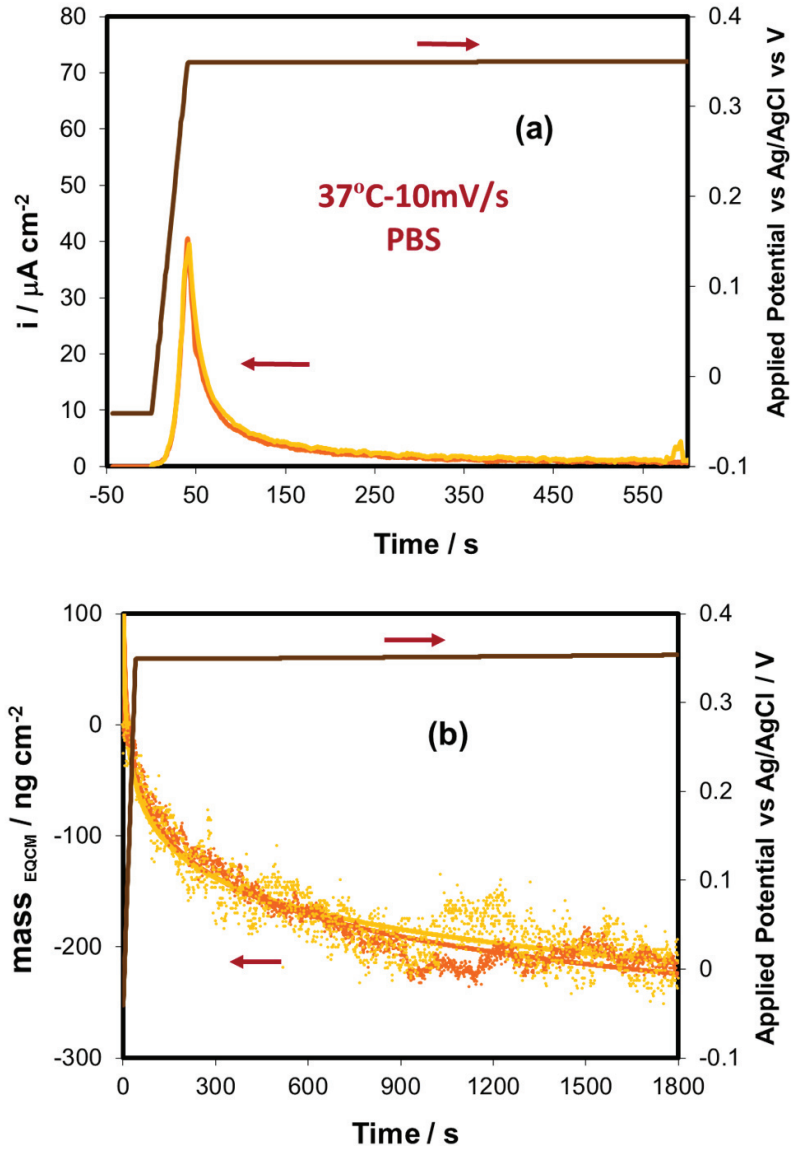


**Figure 6.18.** (a) Current density evolution (b) and mass change measured by the EQCM ( $\text{mass}_{\text{EQCM}}$ ) in potentiostatic tests from -0.05 to 0.35 V of a CoCrMo biomedical alloy in PBS at 37°C and 10  $\text{mV s}^{-1}$ . Results from two independent tests are shown. Continuous lines corresponds to exponential interpolation of the measurements points.

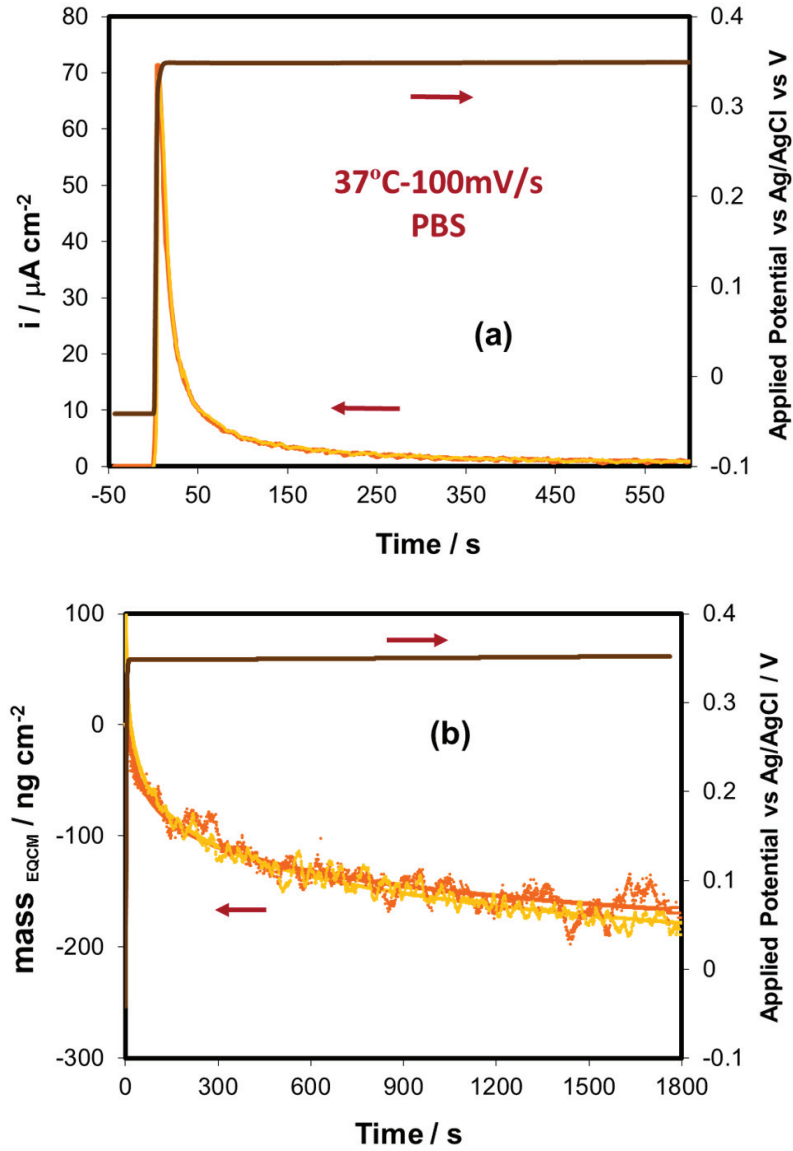


**Figure 6.19.** (a) Current density evolution (b) and mass change measured by the EQCM ( $\text{mass}_{\text{EQCM}}$ ) in potentiostatic tests from -0.05 to 0.35 V of a CoCrMo biomedical alloy in PBS at 37°C and  $100 \text{ mV s}^{-1}$ . Results from two independent tests are shown. Continuous lines corresponds to exponential interpolation of the measurements points.

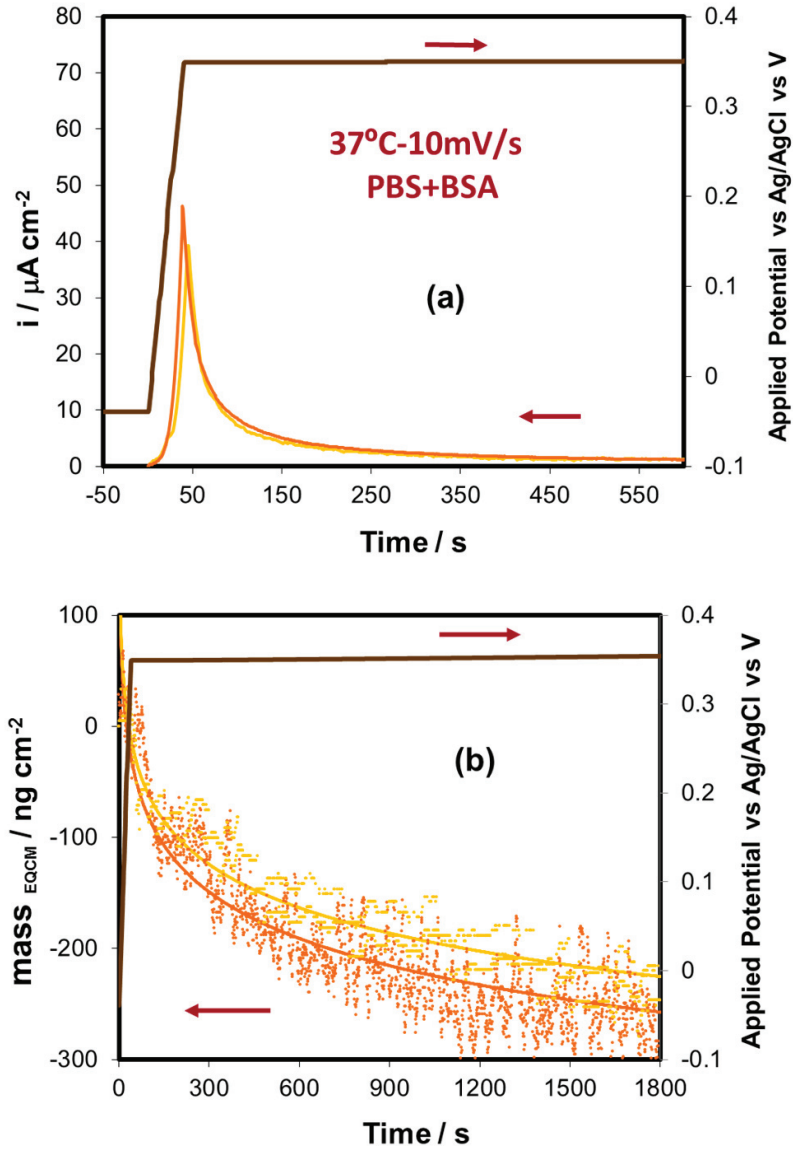


**Figure 6.20.** (a) Current density evolution (b) and mass change measured by the EQCM ( $\text{mass}_{\text{EQCM}}$ ) in potentiostatic tests from -0.05 to 0.35 V of a CoCrMo biomedical alloy in PBS+BSA at 37°C and  $10 \text{ mV s}^{-1}$ . Results from two independent tests are shown. Continuous lines corresponds to exponential interpolation of the measurements points.

### B) Transpassive domain

The results obtained during the potentiostatic test from -0.05 to 0.55 V at  $10 \text{ mV s}^{-1}$  in PBS at room temperature, in PBS at  $37^\circ\text{C}$  and in PBS+BSA at  $37^\circ\text{C}$  has been plotted in **Figure 6.21**. According to the potentiodynamic curves represented in **Figure 6.15** the potential of 0.55 V corresponds to the region (I) of the transpassive domain. The total frequency was measured simultaneously to the total current density.

The response of the current density and the  $\text{mass}_{\text{EQCM}}$  at the applied potential step from -0.05 to 0.55 V (transpassive domain) at room temperature and  $37^\circ\text{C}$  in PBS and PBS+BSA is represented in **Figure 6.21(a)**. After an initial current peak the current stabilizes after approximately 300 s at values of  $32.2$  and  $50.3 \mu\text{A cm}^{-2}$  at room temperature and  $37^\circ\text{C}$ , respectively. A similar transient behaviour was observed by Hodgson et al. [22] on bulk CoCrMo samples passivated at the same potential in buffered 0.14M NaCl solution. In addition, in the **Figure 6.21(b)**, the evolution of the mass loss measured by the EQCM shows a straight line with time. The final mass loss was  $8 \pm 0.7 \mu\text{g cm}^{-2}$  at room temperature and  $12 \pm 2.5 \mu\text{g cm}^{-2}$  at  $37^\circ\text{C}$ . The mass loss at 0.55 V is much larger than at passive potential due to transpassive dissolution that is apparently accelerated at higher temperature. The potential step carried out in presence of BSA was also plotted in **Figure 6.21**. It is observed that the protein addition has no influence on the mass loss kinetics.

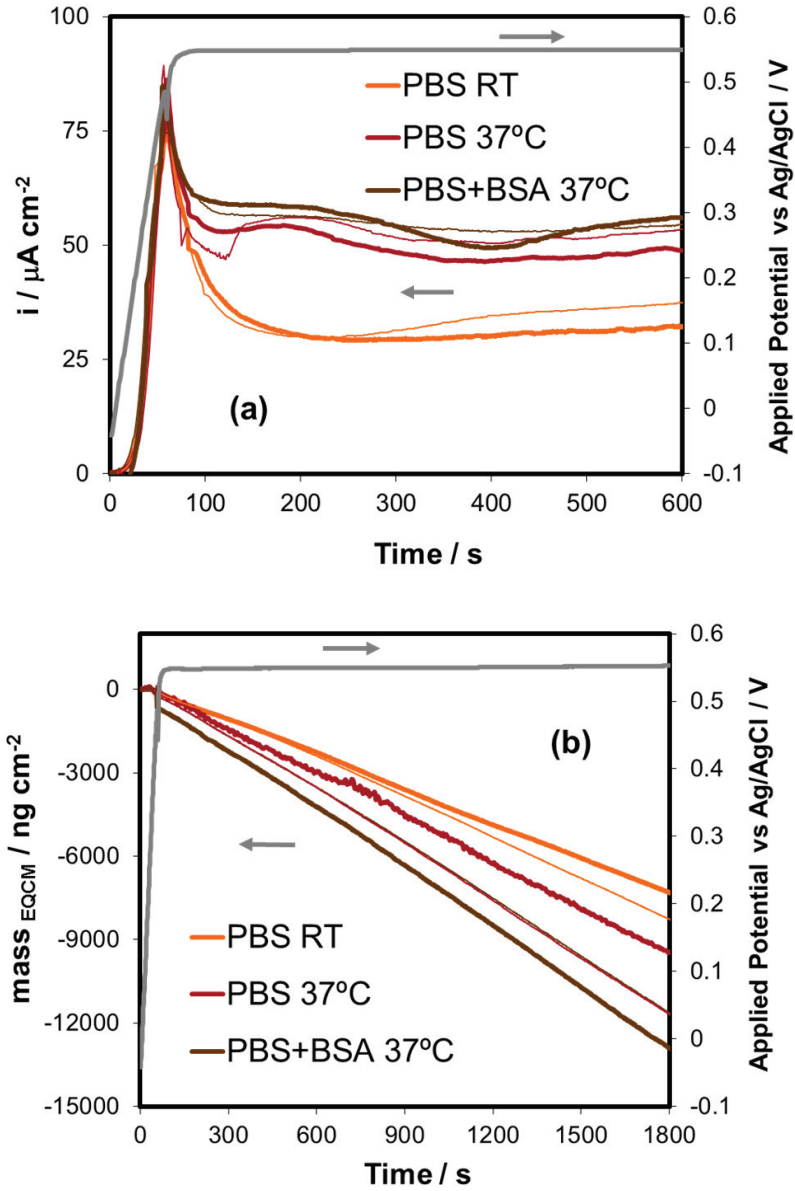


**Figure 6.21.** (a) Current density evolution and (b) mass change measured by the EQCM ( $\text{mass}_{\text{EQCM}}$ ) in potentiostatic tests from -0.05 to 0.55 V of a CoCrMo biomedical alloy at  $10 \text{ mV s}^{-1}$  in PBS at room temperature and 37°C. Two independent tests are shown for each condition.

At this potential, a direct dependence (straight line) of the  $mass_{EQCM}$  and the consumed charge is obtained during the potential step at 0.55 V (Figure 6.22) according to the Faraday's law (equation (3.18), Chapter 3) which adapted for the charge can be rewritten as:

$$m = \frac{M_r \cdot q}{n \cdot F} \quad (6.4)$$

After applying the equation (6.4), an overall value of  $n$  of 4.3 was obtained. This corroborates that under transpassive conditions the mass loss follows the Faraday's law and confirms that the dissolution rate increases due to the dissolution of  $Cr^{+6}$ ,  $Co^{+3}$  and  $Mo^{+6}$  species (Figure 6.22).

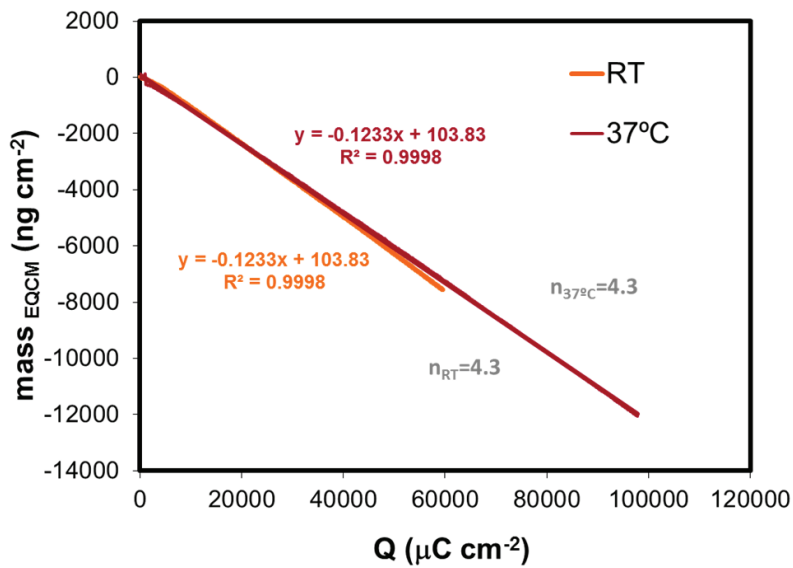


Figure 6.22. Representation of the  $mass_{EQCM}$  versus the charge in order to corroborate the Faraday's law under transpassive conditions (0.55 V) for CoCrMo at room temperature and 37°C.

The parameter  $n=4.3$  was determined by the slope of both lines and is similar at both temperatures which indicates that the oxidized state of the alloying elements is the

same. Thus, taking into account the bulk composition of the CoCrMo alloy, the individual valences  $n_i$  for each element can be extracted:  $n_{Cr}$  and  $n_{Mo}$  are 6 and  $n_{Co}$  is 3. Therefore, this confirms that the dissolution rate increases due to the dissolution of  $Cr^{+6}$ ,  $Co^{+3}$  and  $Mo^{+6}$  species.



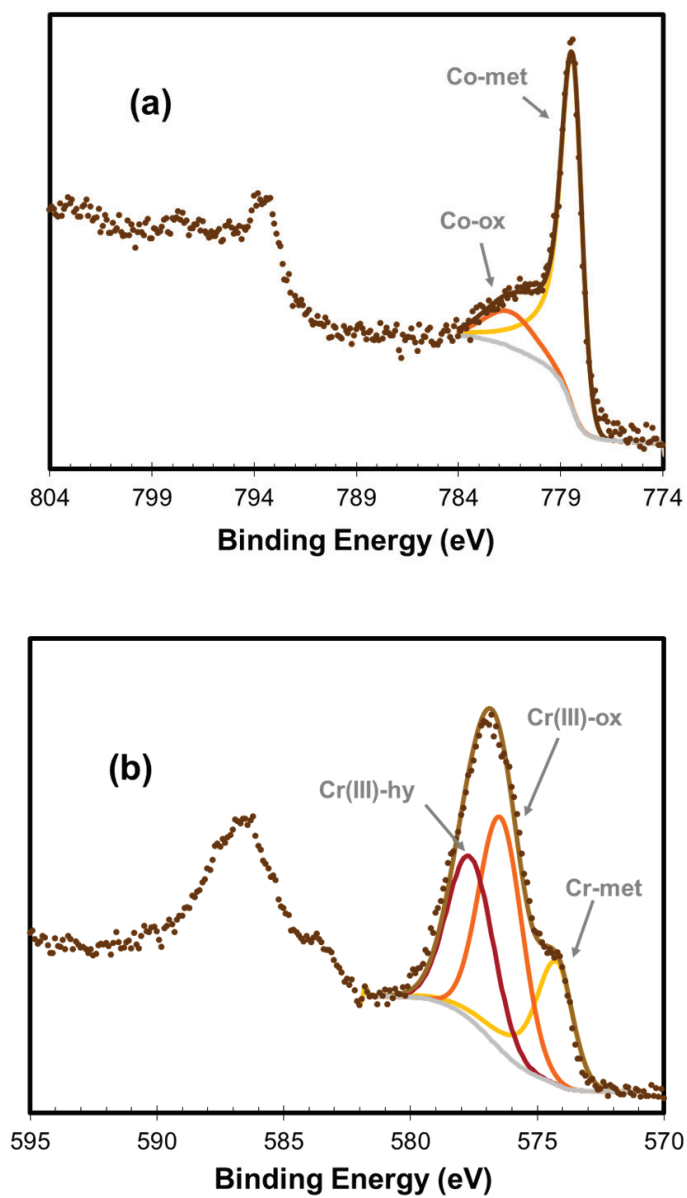
### 6.3.3. XPS ANALYSIS

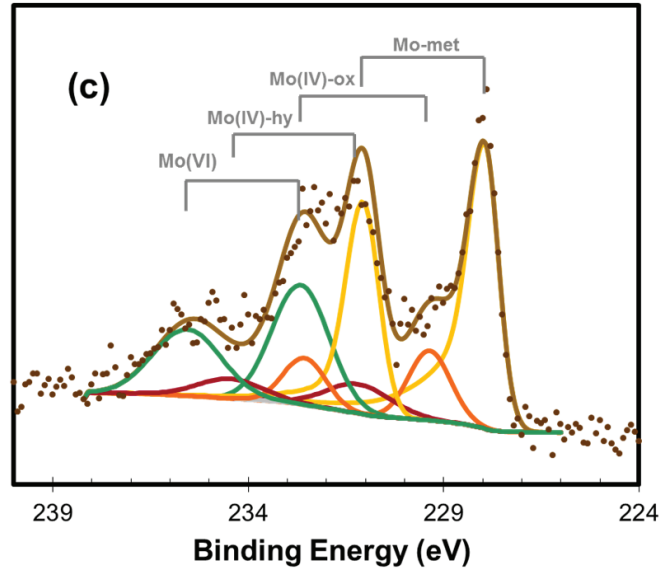
The XPS measurements were used for determining the chemical composition of the passive film, the atomic concentration of the species presents in the oxide film and in the bulk metal and finally, the oxide film thickness. Thus, XPS analysis was performed on samples after the potentiostatic tests under different experimental conditions. In addition, the XPS spectrum was also obtained for the sample polarized after the first step potential (from OCP to -0.05 V) for analysing the variation in thickness and composition between the first and the second potential step (from -0.05 to 0.35 V and from -0.05 to 0.55 V).

The peaks of the alloying elements were deconvoluted according to metallic and oxidized species (**Table 6.1**). **Figure 6.23** shows an example of the deconvolution of **(a)** cobalt (Co2p), **(b)** chromium (Cr2p) and **(c)** molybdenum (Mo3d) of a sample after a potentiostatic step from -0.05 to 0.35 V at the scan rate of  $10 \text{ mV s}^{-1}$  at  $37^\circ\text{C}$ . While the oxidized state significantly contributes to the Cr and Mo signals its contribution to the Co spectrum is very small. All samples suffered carbon adventitious contamination as indicated by the large C peaks situated at 285 eV. On all samples a weak P signal was observed with the maximum intensity at approximately 134 eV indicating the presence of phosphate ions. Adsorption of phosphates from simulated body fluids on the CoCrMo passive films was already reported in the literature [23,28]. The three states  $\text{O}_2^-$ ,  $\text{OH}^-$  and  $\text{H}_2\text{O}$  contributed the O (O1s) peak (**Figure 6.24**).

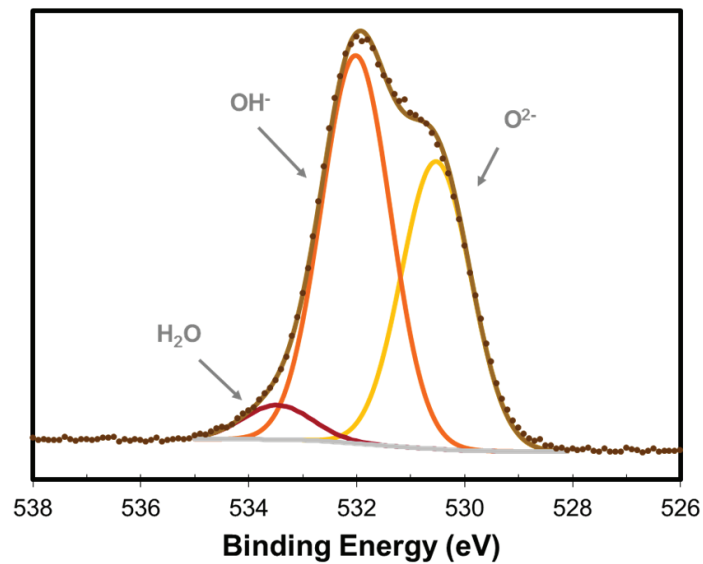
The deconvolution of **(a)** cobalt (Co2p), **(b)** chromium (Cr2p) and **(c)** molybdenum (Mo3d) in a sample measured after potentiostatic step from -0.05 to 0.55 V at the scan rate of  $10 \text{ mV s}^{-1}$  at  $37^\circ\text{C}$  is represented in **Figure 6.25**. The intensity of the oxidized peaks increases considerable in comparison with the peaks obtained under passive conditions (**Figure 6.23**). In addition, metal signal, especially in the Co and Cr spectra, appears strongly attenuated. It is important to highlight the increase in the oxidized states of all alloying elements. The formation of  $\text{Cr}^{+6}$  is detected since the applied potential of 0.55 V is above the transpassive potential of pure chromium. On the other hand, the increase of  $\text{Mo}^{+6}$  is observed in the molybdenum spectra while the  $\text{Mo}^{+4}$  tends to disappear. Thus, Cr and Mo peaks of the spectra correspond well with the

oxidized species deduced by applying the Faraday's law in the potential step tests, Figure 6.22.

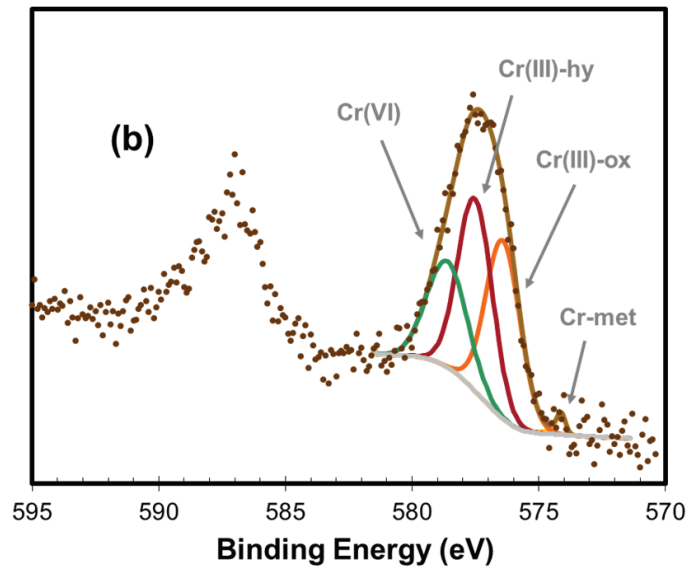
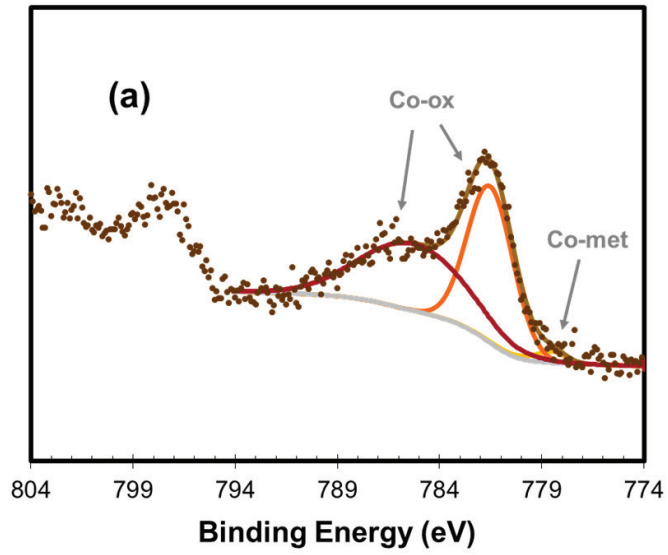




**Figure 6.23.** XPS spectra and the corresponding fitted peaks measured on the CoCrMo alloy after the potentiostatic test from -0.05 to 0.35 V at  $10 \text{ mV s}^{-1}$  in PBS at  $37^\circ\text{C}$ : (a) cobalt, (b) chromium and (c) molybdenum.



**Figure 6.24.** XPS oxygen spectrum and corresponding fitted peaks for the CoCrMo alloy after the potentiostatic test from -0.05 to 0.35 V at  $10 \text{ mV s}^{-1}$  in PBS at  $37^\circ\text{C}$ .



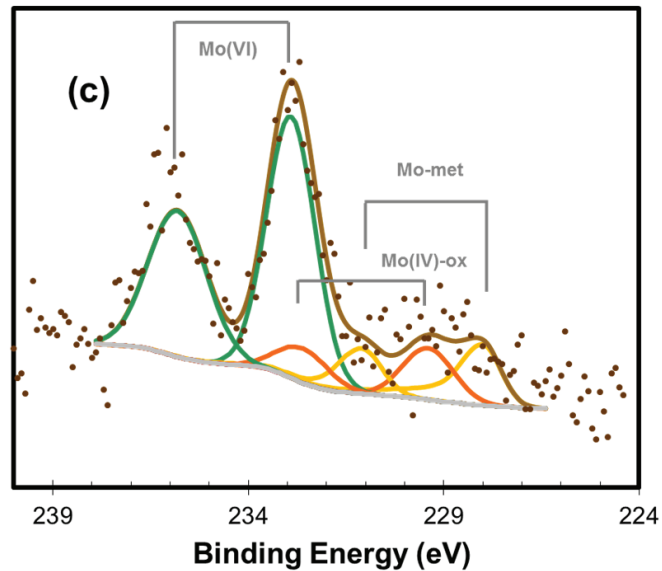


**Figure 6.25.** XPS spectra and the corresponding fitted peaks measured on the CoCrMo alloy after the potentiostatic test from -0.05 to 0.55 V at  $10 \text{ mV s}^{-1}$  in PBS at  $37^\circ\text{C}$ : **(a)** cobalt, **(b)** chromium and **(c)** molybdenum.

The approach developed by Olsson and Landolt [22,24] for characterizing passive films formed in simulated body fluids on CoCrMo alloy was used here for XPS quantification. This approach assumes a four layered structure of the passive surface involving an adsorbed water film, an outermost hydroxide film, an internal oxide film and the underlying metal. By this method it is possible to calculate the film thicknesses and the atomic concentration of the elements in the passive film from the deconvoluted peaks areas from the values of inelastic mean free paths (IMFPs) which were calculated using TPP2 equation [29,30] and from sensitivity factors given by the XPS instrument manufacturer ( $\text{Co}2p_{2/3}$  2.362,  $\text{Cr}2p_{2/3}$  1.583,  $\text{Mo}3d_{5/2}$  2.005,  $\text{C}1s$  0.278,  $\text{O}1s$  0.780). The use of this experimental sensitivity factors has the advantage of considering the contributions of certain features (shake-up, satellites, loss peaks) which are not covered with the theory.

The equations used for the thickness determination are taken for the method developed by Olefjord et al. [25,31] most recently described in detail by Wegrelius [26]. Compared to the standard oxide/metal peak ratio method, they add the possibility of the density of the film to vary with the composition. This leads to a direct iterative procedure for calculating film thickness and composition.

Therefore, the X-Ray induced photoelectron intensity for the oxide film (integrating properly the **equation (3.51)**, Chapter 3) can be obtained by the expression:

$$I_i^{film} = \alpha_{sp} \cdot I_{RX} \cdot c_i^{film} \cdot D^{film} \cdot \lambda_i^{film} \cdot \sigma_i \cdot T(E) \cdot \sin \theta \cdot \left( 1 - \exp\left(\frac{-d^{film}}{\lambda_i^{film} \cdot \sin \theta}\right) \right) \quad (6.5)$$

where  $T(E)$  is the transmission function which is included into the equation in order to take into account the collection efficiency of the electrons sampled by the spectrometer as consequence of the lens functions and energy resolutions and  $D^{film}$  is the density calculated from the concentration and respective oxide density. If the parameter  $Y_i^{film}$  is included in the expression which yields dependent of experimental conditions (including sensitivity factor, transmission and other spectrometer constants) the **equation (6.5)** can be rewrite as follows:

$$I_i^{film} = \alpha_{sp} \cdot c_i^{film} \cdot D^{film} \cdot \lambda_i^{film} \cdot Y_i^{film} \cdot \sin \theta \cdot \left( 1 - \exp\left(\frac{-d^{film}}{\lambda_i^{film} \cdot \sin \theta}\right) \right) \quad (6.6)$$

Correspondingly, the X-Ray photoelectron intensity for a signal from the metal part, attenuated by the oxide layer, is:

$$I_i^{met} = \alpha_{sp} \cdot c_i^{met} \cdot D^{met} \cdot \lambda_i^{met} \cdot Y_i^{met} \cdot \sin \theta \cdot \exp\left(\frac{-d^{met}}{\lambda_i^{met} \cdot \sin \theta}\right) \quad (6.7)$$

The oxide film and metal densities are obtained from the elemental oxide densities:

$$D^{film} = \frac{1}{\sum_{j=1}^N \frac{c_j^{film}}{D_j^{film}}} \quad (6.8)$$

$$D^{met} = \frac{1}{\sum_{j=1}^N \frac{c_j^{met}}{D_j^{met}}} \quad (6.9)$$

Using the intensity ratios it is possible to reduce the **equation (6.6)** for the oxide and for the metal:

$$c_i^{film} = \frac{\frac{I_i^{film}}{\lambda_i^{film} \cdot Y_i^{film} \cdot \left(1 - \exp\left(\frac{-d^{film}}{\lambda_i^{film} \cdot \sin \theta}\right)\right)}}{\sum_{j=1}^N \frac{I_j^{film}}{\lambda_j^{film} \cdot Y_j^{film} \cdot \left(1 - \exp\left(\frac{-d^{film}}{\lambda_j^{film} \cdot \sin \theta}\right)\right)}} \quad (6.10)$$

$$c_i^{met} = \frac{\frac{I_i^{met}}{\lambda_i^{met} \cdot Y_i^{met} \cdot \exp\left(\frac{-d^{met}}{\lambda_i^{met} \cdot \sin \theta}\right)}}{\sum_{j=1}^N \frac{I_j^{film}}{\lambda_j^{met} \cdot Y_j^{met} \cdot \exp\left(\frac{-d^{met}}{\lambda_j^{met} \cdot \sin \theta}\right)}} \quad (6.11)$$

As initializing value, one can start by using the film density for chromium oxide and metal, calculating the concentration sets using **equations (6.10)** and **(6.11)**. The values are then used to find the film thickness  $d^{film}$ :

$$d^{film} = \lambda_i^{film} \cdot \sin \theta \cdot \ln \left( 1 + \frac{I_i^{ox} \cdot D^{met} \cdot \lambda_i^{met} \cdot Y_i^{met}}{I_i^{met} \cdot D^{film} \cdot \lambda_i^{ox} \cdot Y_i^{ox}} \right) \quad (6.12)$$

which can be used to calculate a new set of concentrations and densities. The iteration loop is continued until the film thickness ( $d^{film}$ ) is not changing more than  $1 \cdot 10^{-6} \text{ \AA}$ . The formula converges fast, normally within ten iterations.

Once the composition and thickness of the film is determined by the **equation (6.10)** and **(6.12)**, it is possible to make a split from the O1s peak. The oxide film can be split in an oxide, a hydroxide and a water layer by using the following equations. For the water layer:

$$I_{H_2O} = g \cdot c_{H_2O} \cdot \lambda_0^{film} \cdot \sin \theta \cdot \left( 1 - \exp\left(\frac{-a}{\lambda_0^{film} \cdot \sin \theta}\right) \right) \quad (6.13)$$

For the hydroxide layer:

$$I_{OH^-} = g \cdot c_{OH^-} \cdot \lambda_0^{film} \cdot \sin \theta \cdot \left( \exp\left(\frac{-a}{\lambda_0^{film} \cdot \sin \theta}\right) - \exp\left(\frac{-b}{\lambda_0^{film} \cdot \sin \theta}\right) \right) \quad (6.14)$$

And for the oxide layer:

$$I_{ox} = g \cdot c_{ox} \cdot \lambda_0^{film} \cdot \sin \theta \cdot \left( \exp\left(\frac{-b}{\lambda_0^{film} \cdot \sin \theta}\right) - \exp\left(\frac{-d}{\lambda_0^{film} \cdot \sin \theta}\right) \right) \quad (6.15)$$

In these equations  $g$  corresponds to a common spectrometer constant,  $a$  is the thickness of the water layer,  $b$  is the sum of the water and hydroxide layer and  $d$  is the total thickness of the oxide, hydroxide and water layers. The schematic representation of the layers considered in these calculations is represented in **Figure 6.26**.

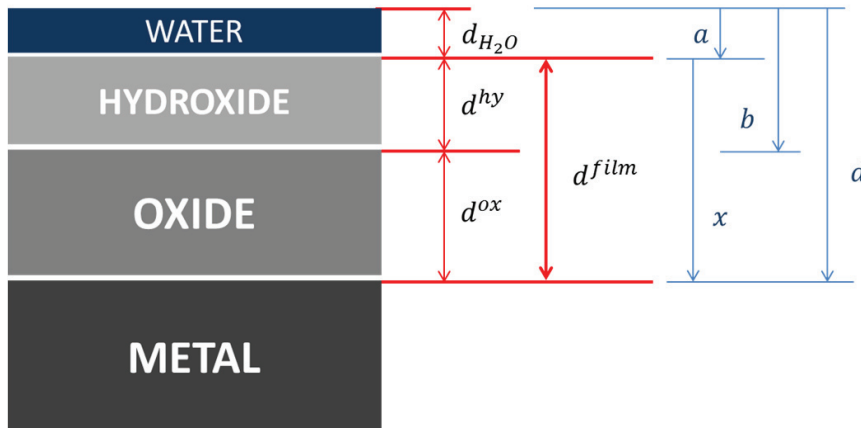


**Figure 6.26.** Scheme of the different layers and their respective thicknesses. The overall film thickness is taken as the sum of the oxide and hydroxide layers. The water and other layers present on the surface are not considered part of the film, as they would not be expected to contain any cations. The definitions to the right are used in **equations (6.13)-(6.20)** for splitting the oxide film into sublayers.



To solve this equation system, it is practical to consider the ratios:

$$k_1 = \frac{1 - \exp\left(\frac{-a}{\lambda_0^{film} \cdot \sin \theta}\right)}{\exp\left(\frac{-a}{\lambda_0^{film} \cdot \sin \theta}\right) - \exp\left(\frac{-b}{\lambda_0^{film} \cdot \sin \theta}\right)} = \frac{c_{OH^-} \cdot I_{H_2O}}{c_{H_2O} \cdot I_{OH^-}} \quad (6.16)$$

$$k_2 = \frac{\exp\left(\frac{-a}{\lambda_0^{film} \cdot \sin \theta}\right) - \exp\left(\frac{-b}{\lambda_0^{film} \cdot \sin \theta}\right)}{\exp\left(\frac{-b}{\lambda_0^{film} \cdot \sin \theta}\right) - \exp\left(\frac{-(a+x)}{\lambda_0^{film} \cdot \sin \theta}\right)} = \frac{c_{ox} \cdot I_{OH^-}}{c_{OH^-} \cdot I_{ox}} \quad (6.17)$$

From these ratios, thicknesses for each layer are obtained from:

$$b = -\lambda_0^{film} \cdot \sin \theta \cdot \ln \left( \frac{1 + k_2 \cdot \exp\left(\frac{-x}{\lambda_0^{film} \cdot \sin \theta}\right)}{1 + k_2 + k_1 k_2 \cdot \left(1 - \exp\left(\frac{-x}{\lambda_0^{film} \cdot \sin \theta}\right)\right)} \right) \quad (6.18)$$

$$a = -\lambda_0^{film} \cdot \sin \theta \cdot \ln \left( \frac{1 + k_1 \cdot \exp\left(\frac{-b}{\lambda_0^{film} \cdot \sin \theta}\right)}{1 + k_1} \right) \quad (6.19)$$

And finally the values  $x$  and  $a$  can be used to find the film thickness, defined as hydroxide and oxide, from:

$$d = x + a \quad (6.20)$$

For these calculations, it was assumed that the attenuation length in all three layers is the same [24]. The main uncertainty in the layer division originates from the curve fit, i.e. the ratios between the water, hydroxide and oxide contributions.

Following this iterative procedure, it is possible to determine the thickness of the layers (water, hydroxide and oxide) and the corresponding composition of the alloying elements in the oxide film. The calculated film thicknesses listed in **Table 6.III** are in good agreement with previously obtained results [22,23,32]. In all cases the water film is very thin (less than one monomolecular layer) and therefore was not further considered here. Thus, the passive film was considered to be formed by the hydroxide

layer and oxide layer only. The ratio between hydroxide and oxide film thickness is about 1:1 for passive potentials and 2:1 for the transpassive potential. The thickness obtained at transpassive potentials is much larger than in the passive domain. This is consistent with previous works [22,32]. The scan rate has not noticeable effect while films formed at 37°C are slightly thicker than the ones formed at room temperature.

**Table 6.III.** Film thicknesses calculated by the convolution of the XPS peaks of the different alloying elements at different applied potentials and scan rates of the CoCrMo alloy in PBS at room temperature and 37°C.

THICKNESS							
FIST STEP	SECOND STEP	T (K)	SCAN RATE (mV s <sup>-1</sup> )	OXIDE (nm)	HYDROXIDE (nm)	WATER (nm)	PASSIVE FILM* (nm)
OCP	-0.05V	RT	10	0.9	0.7	0.1	1.6
				1	0.6	0.0	1.6
OCP	-0.05V	37°C	10	0.9	0.7	0.2	1.6
				0.9	0.7	0.1	1.6
-0.05V	0.35V	RT	10	1.2	1.1	0.0	2.3
				1.2	1.1	0.1	2.3
-0.05V	0.35V	37°C	10	1.3	1.2	0.1	2.5
				1.1	1.2	0.1	2.4
-0.05V	0.35V	37°C	100	2.4	1.4	1.0	2.4
				2.3	0.8	1.5	2.3
-0.05V	0.55V	RT	10	4.8	3.1	0.0	7.8
				7.2	2.3	0.1	9.5
-0.05V	0.55V	37°C	10	5.0	2.8	0.2	7.8
				11.8	2.9	0.2	14.6

\*Oxide + Hydroxide

The atomic concentration ratios of the elements Co, Cr and Mo in their oxidized state in the passive film, determined by deconvolution of the XPS spectra, are plotted in **Figure 6.27**. Temperature and scan rate have no significant effect on the composition of the passive film. In the passive domain the passive film mainly contains Cr<sup>+3</sup> ions and its cobalt content decreases with increasing potential. In the transpassive domain Co constitutes more than 50 % of the cations and a significant fraction of Cr ions are

oxidized to the valence VI. The present XPS analysis are in good quantitative and qualitative agreement with literature results obtained on bulk CoCrMo alloys [22,23,32,33].

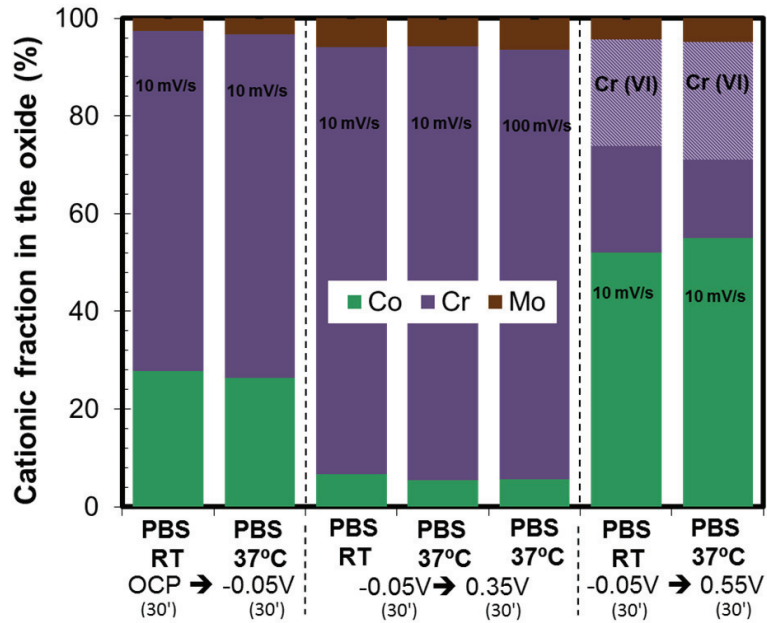
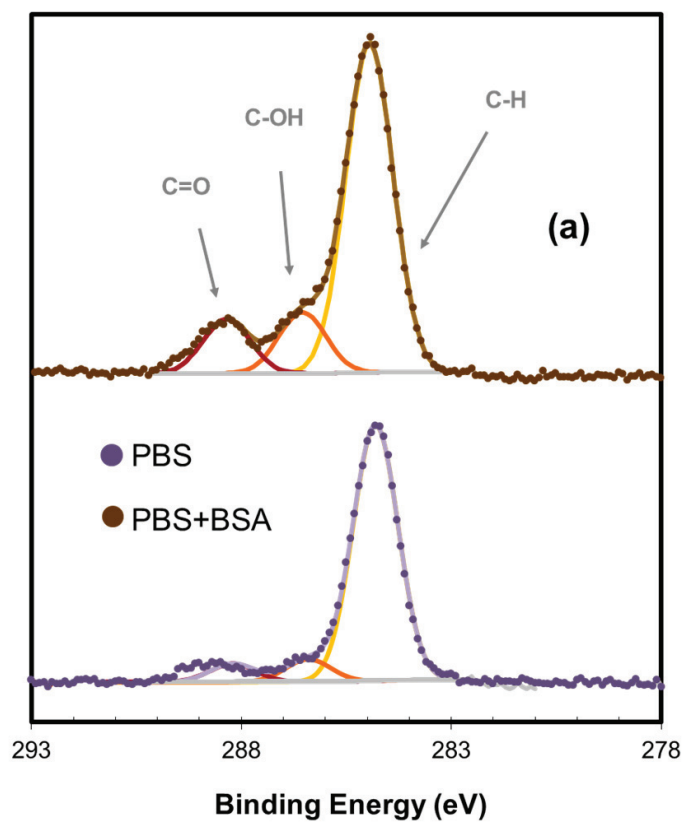
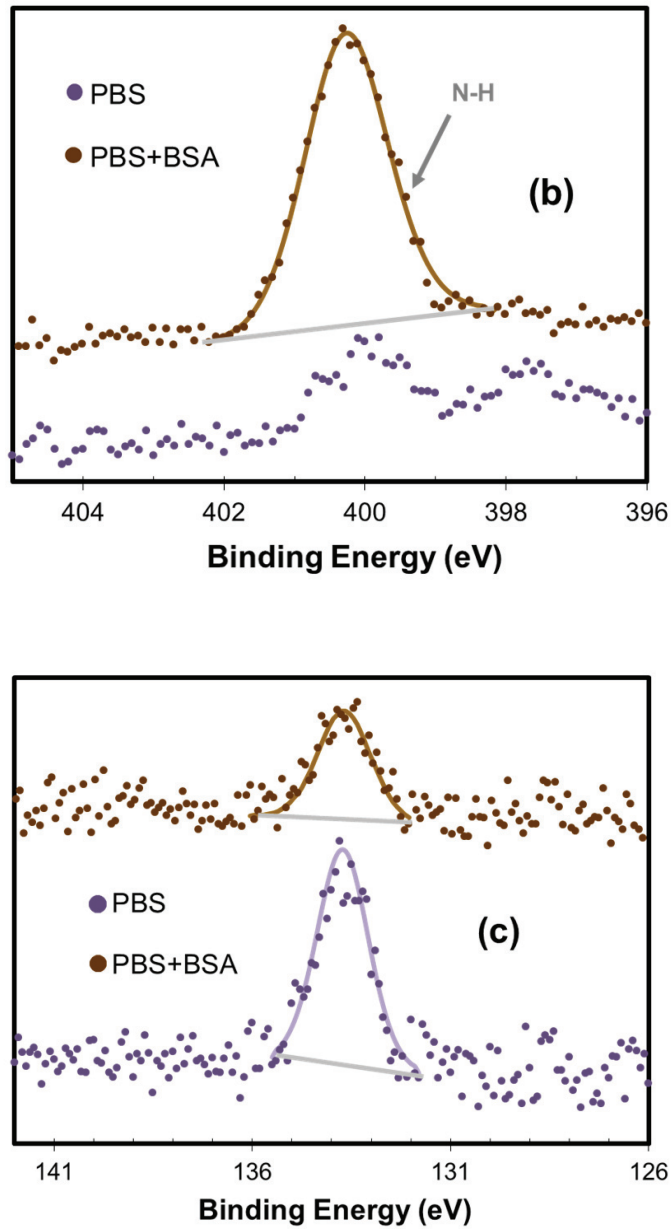


Figure 6.27. Cationic fraction in the oxide film as measured by XPS at different applied potentials and scan rates of the CoCrMo alloy in PBS at room temperature and 37°C.

The Carbon, Nitrogen and Phosphorous peaks of the XPS spectra obtained in the samples passivated in presence of BSA differ from the obtained in the PBS solution. The intensity of all the peaks that contribute to C1s peak becomes higher in the tests carried out in presence of BSA. The adsorbed protein on the CoCrMo surface shows C-H, C-OH and C=O carbon bonds which are detected by the XPS measurements while in the samples tested without presence of BSA, carbon contribution is only due to the presence of contamination. On the other hand, the nitrogen is a fingerprint of the protein (amino groups) and it is only detected in the presence of BSA. The latter can be specifically used to determine the thickness of the adsorbed layer whereas the protein was considering that it is adsorbed as a monolayer. Finally, the intensity of the P peak

decreases in the samples tested in presence of BSA (in approximately 25 %) which indicates that adsorption of BSA displaces the amount of adsorbed phosphates. As already explained in previous chapters, this behaviour could be related to the competitive effect of adsorption between both species (phosphates and BSA) [23].





**Figure 6.28.** XPS spectra and the corresponding fitted peaks measured on the CoCrMo alloy samples after the potential step test from -0.05 to 0.35 V at  $10 \text{ mV s}^{-1}$  in PBS and PBS+BSA at 37°C: (a) carbon, (b) nitrogen and (c) phosphate.

## 6.4. Discussion

### 6.4.1. FILM GROWTH IN THE PASSIVE DOMAIN

The current density peak obtained at the beginning of the anodic polarization (**Figure (6.17)-(6.20)(a)**) indicates high metal dissolution, exceeding the oxygen incorporation into the growing film, i.e. only a fraction of the cations formed at the metal/film interface contributes to film growth while the rest becomes dissolved in the solution. This behaviour was also observed working with stainless steel [4,34]. According to the results shown in **Figures (6.17)-(6.20)** (potential step tests) the balance in the film/electrolyte interface,  $mass_{EQCM}$ , is characterized by the dissolution of the cations through the passive film into the electrolyte. These results are in good agreement with the mass variation obtained in the passive domain of the polarization curves (**Figure 6.15**). In those tests a decrease in mass was observed during passivation; however, the mass that goes to the film growth,  $mass_{FILM}$ , is expected to increase with time.

The *passive film growth* can be correlated with the mass changes taking place at the electrode surface which are determined by the concurrent phenomena of passive film growth and passive dissolution. A procedure for the quantitative appraisal of these results has been developed previously [3,8,9] and has been applied in the present study.

**Figure 6.29** shows the mass balance of the ions implicated in the oxide film formation of the CoCrMo alloy. According to this representation all mass change going into the oxide film, through the interface metal/film (interface denoted as I) and film/electrolyte (interface II) are considered positive. Therefore, the incorporation of cations and anions into the passive film corresponds to a positive mass change. The negative mass change is due to ions moving from the oxide film to the electrolyte.

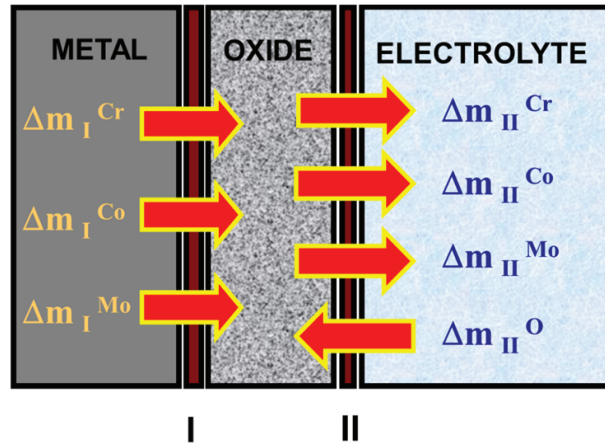


**Figure 6.29.** Mass flow convection of the metals that contributes to the oxide film formation. The sign is positive for the flows that favour the film formation through the interfaces I and II.

Three assumptions were made to interpret the EQCM data (i) all elements are oxidized corresponding to their relative bulk concentration at the metal-film interface, (ii) the cations remaining in the film have the same oxidation number as when they are first oxidized and (iii) only  $O^{2-}$  and  $OH^-$  anions were considered.

Thus, the **film thickness change** has been calculated using the following procedure which is adapted for the CoCrMo alloy according to previous works [8]:

The mass change for each cation ( $\Delta m_i^I$ ) of the alloying elements through the metal/oxide interface (I) is determined by Faraday's law (**equation (6.21)**):

$$\Delta m_i^I = \frac{q_i M r_i}{n_i F} \quad (6.21)$$

where  $q_i$  is the charge density,  $M r_i$  is the molar mass of the element  $i$ ,  $F$  is the Faraday's constant,  $n_i$  is the valency, and  $c_i$  is the bulk atomic concentration of the element  $i$ . If the oxidation at the metal/interface is assumed to be proportional to the bulk alloy content, one finds the elemental charge from:

$$q_i = q_{tot} \frac{n_i c_i}{\sum_{j=cation} n_j c_j} \quad (6.22)$$

The total faradic mass oxidized at the metal/oxide interface (I) is then expressed as:

$$\sum_{i=cation} \Delta m_i^I = \frac{q_{tot}}{F} \sum_{i=cation} \left( \frac{n_i c_i}{\sum_{j=cation} n_j c_j} \right) \left( \frac{M_i}{n_i} \right) \quad (6.23)$$

If the expression is readjusted, the total faradic mass oxidized can be rewritten:

$$\sum_{i=cation} \Delta m_i^I = \left( \frac{q_{tot}}{F} \right) \left( \frac{\sum c_i M r_i}{\sum c_j n_j} \right) \quad (6.24)$$

Where  $n_i$  is the valency of each element  $i$ . Finally, the mass change in the oxide for element  $i$  is:

$$\Delta m_{tot}^{film} = \Delta m_i^I + \Delta m_i^{II} \quad (6.25)$$

The entire film mass change is given by the sum of all the cation and oxygen which are incorporated in the film through the interface (I) and (II):

$$\Delta m_{tot}^{film} = \sum_{i=cation} (\Delta m_i^I + \Delta m_i^{II}) + \Delta m_O^{II} \quad (6.26)$$

where  $\Delta m_O^{II}$  represents the incorporation of oxygen in the film. The EQCM measures the mass change at the film/solution interface, which is calculated as:

$$\Delta m^{EQCM} = \Delta m_O^{II} + \sum_{i=cation} \Delta m_i^{II} \quad (6.27)$$

where  $\Delta m^{EQCM}$  is the mass change at the film/solution interface (II). The latter parameter includes the contribution of the cations (Co, Cr and Mo) and the oxygen (needed for oxide formation) from the electrolyte (**Figure 6.29**).

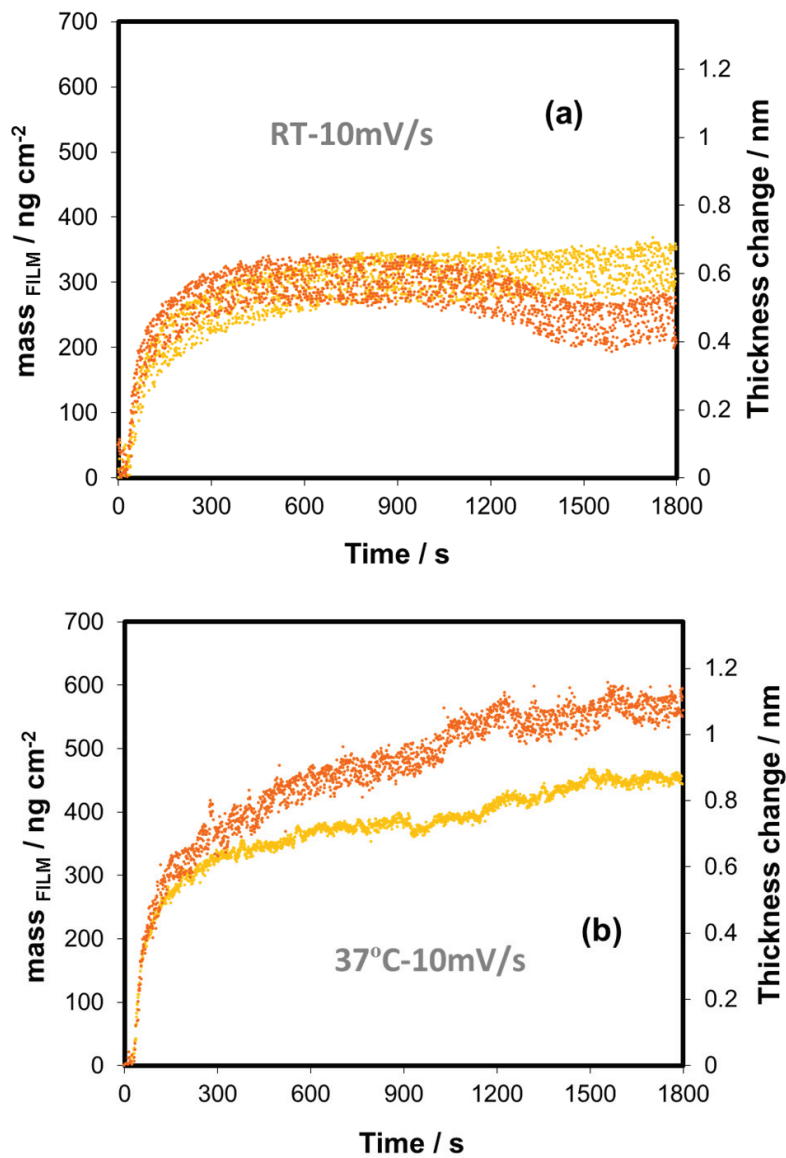
Thus, combining the **equation (6.24)** and **(6.25)**, one obtains:

$$\Delta m_{tot}^{film} = \sum_{i=cation} \Delta m_i^I + \Delta m^{EQCM} \quad (6.28)$$

which in combination with the **equations (6.21)** and **(6.22)** gives an estimate of the film mass change.



The mass variation of the oxide film ( $mass_{FILM}$ ) extracted from **equation (6.28)** has been represented in **Figure 6.30**. The change of the *thickness* of the passive film can be calculated by dividing the film mass change by the average film density  $\rho$  ( $g\ cm^{-3}$ ). The evolution of the film thickness with time is also illustrated in **Figure 6.30**.



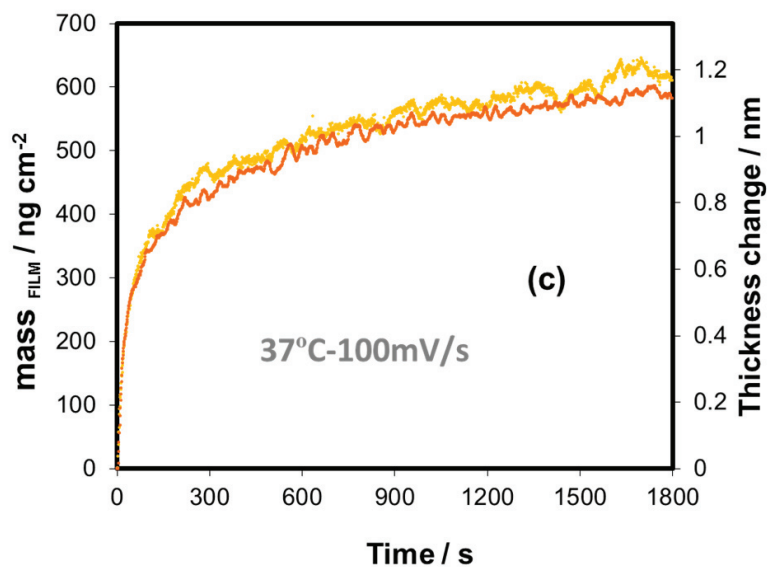


**Figure 6.30.** Total mass change ( $mass_{\text{FILM}}$ ) and thickness change (calculated by dividing the former parameter by the film density) of the film during passivation CoCrMo in PBS from -0.05 to 0.35 V **(a)** at  $10 \text{ mV s}^{-1}$  at room temperature, **(b)** at  $10 \text{ mV s}^{-1}$  at  $37^\circ\text{C}$  and **(c)** at  $100 \text{ mV s}^{-1}$  at  $37^\circ\text{C}$ . Results from two independent tests are shown in each Figure.

During passivation at 0.35 V the film grows initially (first 100 seconds) very fast. Afterwards the growth rate decreases progressively. Finally the film thickness reaches a plateau value after 600 s at room temperature or 1500 s at  $37^\circ\text{C}$ . The scan rate does not significantly affect the growth kinetics. The increase in film thickness due to passivation at 0.35 V was extracted from **Figure 6.30** for each experiment and listed in **Table 6.IV** together with the corresponding XPS values. The latter was determined by subtracting the total thickness (oxide+hydroxide) of the film formed at -0.05 V to the thickness of the passive films formed at 0.35 V (**Table 6.III**). Taking into account the uncertainties associated with EQCM measurements and XPS quantification (errors in peak fitting and calculation of electron means free path) the results of **Table 6.IV** show a good correlation between the two techniques. Both EQCM and XPS indicate that the passive film growth at room temperature is slightly lower than the one forming at  $37^\circ\text{C}$ .

**Table 6.IV.** Film thickness change obtained in the second potential step determined by EQCM and XPS (obtained subtracting to the total thickness the obtained after the first potentiostatic step) of the CoCrMo alloy at different scan rates and temperatures.

THICKNESS CHANGE					
FIRST STEP	SECOND STEP	T	SCAN RATE (mV s <sup>-1</sup> )	EQCM (nm)	XPS (nm)
-0.05 V	0.35 V	RT	10	0.6	0.7
				0.5	0.7
-0.05 V	0.35 V	37°C	10	0.9	0.9
				1.0	0.8
-0.05 V	0.35 V	37°C	100	1.2	0.8
				1.1	0.8
-0.05 V	0.55 V	RT	10	14.7	6.2
				16.5	7.9
-0.05 V	0.55 V	37°C	10	25.9	6.2
				23.9	13.0

These results (**Figure (6.17)-(6.20)** and **Figure 6.30**) clearly indicate that the potentiostatic passivation process is characterized by a continuous loss of mass through the film/electrolyte interface accompanied by film growth.

#### 6.4.2. FILM GROWTH IN THE TRANSPASSIVE DOMAIN

The same film growth quantification procedure described in the previous section was applied to the potentiostatic test carried out at the transpassive potential of 0.55 V. The obtained film growth kinetics are shown in **Figure 6.31** at room temperature and 37°C. At both temperatures the film thickness linearly increases with time. The average growth rate is  $0.49 \pm 0.05$  and  $0.77 \pm 0.06$  nm min<sup>-1</sup> at room temperature and 37°C respectively, i.e. being faster at higher temperature. **Figure 6.21** shows that the current density reaches a constant value after polarization despite the continuous growth of the oxide film. Thus the oxidation kinetics is apparently not influenced by the growth of the oxide film. Such situation typically arises when surface films are *cracked* or *porous*.

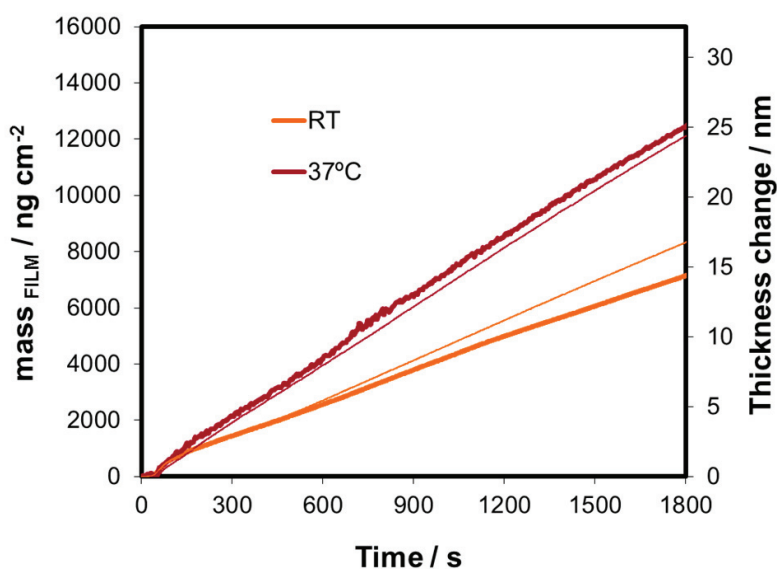


**Figure 6.31.** Total mass change ( $mass_{FILM}$ ) and thickness change of the film during transpassive polarization of CoCrMo in PBS from -0.05 to 0.55V at  $10 \text{ mV s}^{-1}$  at room temperature and 37°C.

The thickness change as measured by EQCM is very reproducible and corresponds to average values of 15 and 25 nm for room temperature and 37°C respectively (**Table 6.IV**). Interestingly XPS yields much lower values and significant scattering particularly at 37°C. These differences between the two techniques may be due to several reasons. First XPS being an ex-situ technique, film thinning can occur during

sample rinsing with water after polarization. The thinning is not necessarily uniform which could result in variations of film thickness measured by XPS depending on location of the analysed area on the sample surface. Furthermore, thick films attenuate the XPS metallic signal down to very low, intensities difficult to quantify. This uncertainty may affect the outcome and scattering of XPS quantification. The present results show that EQCM, thanks to its in-situ character, can constitute an extremely valid alternative to XPS for studying film thicknesses.

#### 6.4.3. TRANSPASSIVE OXIDATION AND DISSOLUTION OF THE CoCrMo ALLOY

In the measured EQCM polarization curves (Figure 6.15) the potential (transpassive oxidation potential) at which the current start to increase after the passive potential does not match the potential at which mass loss starts increasing (transpassive dissolution potential). In order to illustrate this, the derivative of the mass with respect to time during the polarization curve was calculated and plotted together with the current in Figure 6.32.

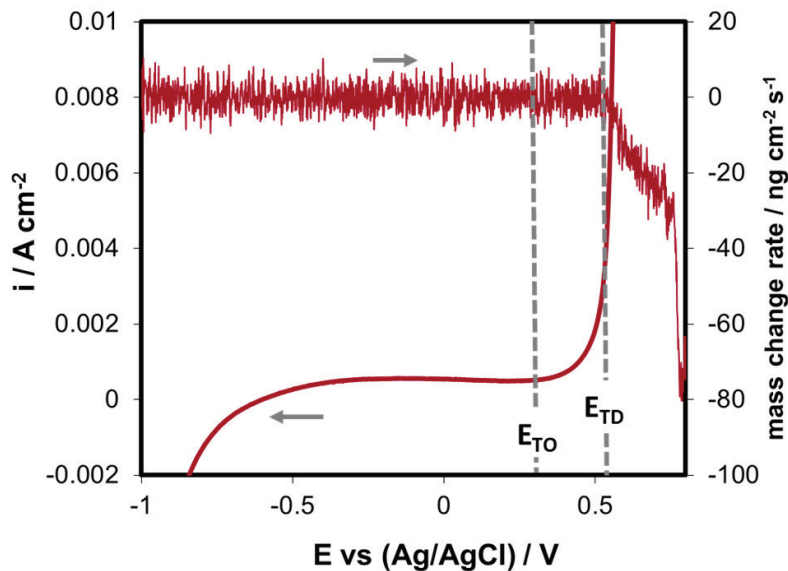


Figure 6.32. Current density and derivative of the mass with respect to time during the polarization curve of the CoCrMo alloy at  $1 \text{ mV s}^{-1}$  and  $37^\circ\text{C}$  in PBS.

This figure shows that up to the potential of 0.52 V the dissolution rate is negligible. Above this potential the dissolution rate abruptly increases. Thus the potential 0.52 V can be defined as the *transpassive dissolution potential* ( $E_{TD}$ ). Up to this potential the passive state is maintained. However, the *transpassive oxidation potential* ( $E_{TO}$ ) corresponding to the oxidation of  $Cr^{+3}$  to  $Cr^{+6}$  occurs at a lower potential (0.28 V) as indicated by the current curve. This indicates that  $Cr^{+6}$  ions can form in the passive film of CoCrMo alloy without affecting passive dissolution. Similar results were found by Schmuki et al. [35] when investigating transpassivity of  $Cr_2O_3$  films using in-situ X-Ray Near-Edge Spectroscopy combined with electrochemical techniques. They detected the presence of  $Cr^{+6}$  at passive potentials and concluded that  $Cr^{+6}$  is incorporated in the  $Cr_2O_3$  prior to transpassive dissolution. The factors responsible for triggering the transpassive dissolution are not clear at present. According to Schmuki et al. [35] formation of chromate ions occurs within the film by reaction of  $Cr^{+6}$  ions with inwards diffusing oxygen anions. Transpassive dissolution starts only when a critical concentration of chromate ions is reached at the oxide surface. Based on this hypothesis one could conclude that sufficient chromate ions formed on the CoCrMo passive film only above  $E_{TD}$  (0.52 V). However, this ignores possible influences by Co and Mo ions which cationic fraction increases significantly close to the transpassive potential of CoCrMo alloys [22,32].

#### 6.4.4. INFLUENCE OF TEMPERATURE ON MASS AND THICKNESS CHANGE

The results in **Figure 6.15** show that temperature affects the passive dissolution (potentials below  $E_{TD}$ ) but neither oxidation of  $Cr^{+3}$  to  $Cr^{+6}$  nor transpassive dissolution (for potentials larger than  $E_{TD}$ ). This is in good agreement with previous results showing an increase in corrosion rate of CoCrMo alloys with increasing temperature (Chapter 5).

On the other hand, the increase in temperature also enhances the oxide film thickness (0.3-0.4 and 0.12-0.1 nm with EQCM and XPS respectively) in the potentiostatic tests carried out at 0.35 V, **Table 6.IV**. This indicates that despite their larger thickness passive films formed at 37°C are less protective than the ones form at lower

**CHAPTER 6.** Study of the passivation and adsorption kinetics by EQCM and XPS

temperature. These results demonstrate the need of controlling temperature for the study of the electrochemical processes occurring on biomedical alloys such as the CoCrMo alloy in biological systems. EQCM results obtained at room temperatures may underestimate the kinetics of the film growth and passive dissolution.

#### 6.4.5. ADSORPTION KINETICS

The mass variation of the oxide film ( $mass_{FILM}$ ) in the potential step experiments at 0.35 V in PBS and PBS+BSA are shown in **Figure 6.33**. An increase of the mass variation was observed in all cases, reaching higher values of  $mass_{FILM}$  in PBS+BSA at the end of the potential step test ( $635.5 \pm 29 \text{ ng cm}^{-2}$ ).

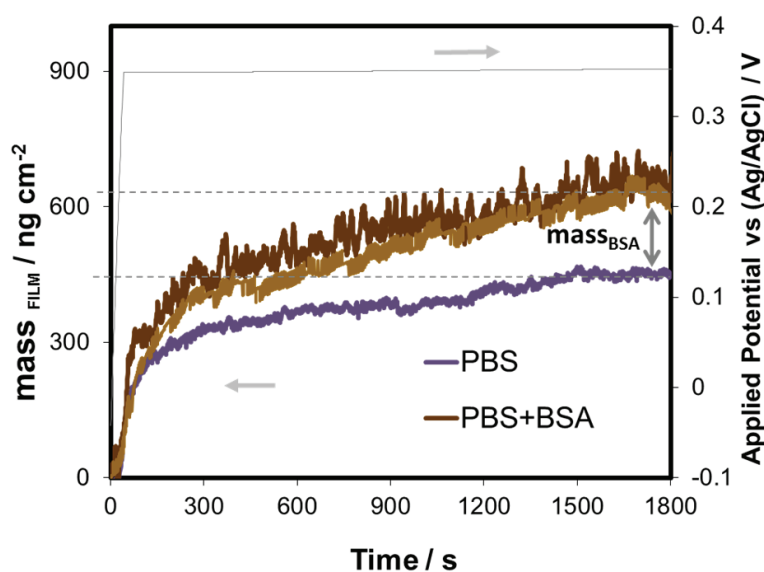


**Figure 6.33.** Total mass change ( $mass_{FILM}$ ) of the film during passivation CoCrMo in PBS and PBS+BSA from -0.05 to 0.35 V at  $10 \text{ mV s}^{-1}$  and  $37^\circ\text{C}$ . The variation of mass due to BSA adsorption ( $mass_{BSA}$ ) has been indicated by an arrow.

Initially, the passive film grows at the same rate in both simulated body fluids (below 60 sec) with a value of  $5.2 \text{ ng cm}^{-2} \text{ s}^{-1}$ , which corresponds to the slope of the variation of  $mass_{FILM}$  vs time. Between 60 and 300 seconds the  $mass_{FILM}$  variation in PBS and PBS+BSA is  $0.63$  and  $0.78 \pm 0.03 \text{ ng cm}^{-2} \text{ s}^{-1}$  respectively. Thus, the adsorption of protein increases the mass variation on the CoCrMo alloy during the potential step test. These results indicate that the oxide film formation is faster than the adsorption of the BSA. Finally, a quasi-steady state value in the variation of  $mass_{FILM}$  vs time was attained after 300 seconds with values of  $0.09 \pm 0.02$  in PBS and  $0.18 \pm 0.01 \text{ ng cm}^{-2} \text{ s}^{-1}$  in PBS+BSA.



**CHAPTER 6.** Study of the passivation and adsorption kinetics by EQCM and XPS

The final difference between the  $mass_{FILM}$  in PBS and PBS+BSA (final  $mass_{BSA}=185 \text{ ng cm}^{-2}$ ) can be attributed to the protein adsorption. Thus, the amount of adsorbed protein can be determined using this difference and taking into account the physical properties of the BSA where the standard dimension of one adsorbed molecule onto a metallic surface corresponds to  $15 \times 3.8 \text{ nm}$  (at the same pH and temperature conditions). The number of BSA molecules corresponding to those  $185 \text{ ng cm}^{-2}$  is  $3.887 \cdot 10^{11}$  molecules while the total molecules of BSA accepted for the conductive surface of the electrode ( $23.13 \text{ mm}^2$ ) theoretically corresponds to  $4.058 \cdot 10^{11}$  molecules. Therefore, protein takes up 96 % of the entire surface (coverage) under the studied experimental conditions.

The calculation of the film thickness by XPS was carried out using the procedure described in the **section 6.3.3**. The XPS data, summarized in the **Table 6.V**, indicates that the passive film is not modified by the adsorption of protein since the same values of thickness were obtained in PBS and PBS+BSA. Therefore, the formation of the oxide film in terms of thickness and composition is independent of the presence of protein. These results are in good agreement with previous works where the adsorption of the BSA did not affect the thickness of the oxide film in CoCrMo bulk alloys [23].

**Table 6.V.** Film thicknesses calculated by the convolution of the XPS peaks of the different alloying elements at different applied potentials and scan rates of the CoCrMo alloy in PBS+BSA at 37°C.

THICKNESS							
FIST STEP	SECOND STEP	T	SCAN RATE (mV s <sup>-1</sup> )	OXIDE (nm)	HYDROXIDE (nm)	WATER (nm)	PASSIVE FILM* (nm)
-0.05V	0.35V	37°C	10	1.2	1.5	0.1	2.7
				1.4	1.2	0.1	2.5
				1.4	1.4	0.1	2.6

\*Oxide + Hydroxide

#### 6.4.6. MODEL OF BSA-PHOSPHATES ADSORPTION LAYER ON THE CoCrMo INTERFACE

A model that reproduces the distribution of the different species present in the simulated body fluids was carried out in this section in order to understand their implication in the corrosion behaviour of the CoCrMo biomedical alloy.

The step potential tests at 0.35 V in presence of BSA (**Figure 6.20**) show that the adsorption of the protein enhances the passive dissolution of the alloy (higher mass loss). This statement was supported by the potentiostatic tests carried out under the same applied potential conditions in the Chapter 4 where a decrease of the  $R_p$  values was obtained in the BSA-containing solution.

The thickness of the adsorbed BSA was quantified in order to determine its conformation. For this, the nitrogen signal was taken since this element comes only from the BSA (**Figure 6.28**) [13]. X-Ray induced photoelectron intensity for nitrogen in the protein (integrating properly the **equation (3.51)**, Chapter 3) can be obtained by the expression:

$$I_N^{BSA} = \alpha_{sp} \cdot I_{RX} \cdot D^{BSA} \cdot \lambda_N^{BSA} \cdot \sigma_N \cdot T(E) \cdot \sin \theta \cdot \left( 1 - \exp\left(\frac{-d^{BSA}}{\lambda_N^{BSA} \cdot \sin \theta}\right) \right) \quad (6.30)$$

The thickness of the BSA layer was determined from the  $I_N^{BSA}/I_i^{film}$  ratio. Some assumptions were considered in order to estimate the thickness of the BSA adsorbed layer: no attenuation of the signal intensities as consequence of the BSA adsorption was taking into account and only film composed by  $Cr_2O_3$  was considered (since this exceeds more than 90% of the total composition). The values of the different parameters are:  $D^{BSA} = 0.01599 \text{ mole cm}^{-3}$  and  $\lambda_N^{BSA} = 3.2 \text{ nm}$  [13,29,30]

The thickness of the adsorbed layer was 3.6, 3.1 and 3.0 nm for the three independent experimental tests. This value corresponds well with the BSA thickness of one molecule orientation (3.8 nm) which suggests that the alloy was covered by a continuous monolayer of BSA oriented parallel to the surface. This statement is in good agreement with the coverage (96 %) obtained from the EQCM results in the **section 6.4.5**.

In order to confirm this result, the following equation was introduced into the expression  $I_N^{BSA}/I_i^{film}$  :

$$d^{BSA} = \frac{\Delta m}{\rho_{BSA}} \quad (6.31)$$

Where  $\Delta m=185 \text{ ng cm}^{-2}$  and  $\rho_{BSA}$  corresponds to the density of the BSA in aqueous solution which for the studied conditions is approximately  $1.36 \text{ g cm}^{-3}$  [14]. The coverage ( $\theta$ ) was also included in the expression  $I_N^{BSA}/I_i^{film}$  following the same procedure as Ithurbide et al. [14] and the results also indicated that the protein takes up the entire surface with a less thickness of a one monolayer.

On the other hand, when comparing the intensity of the P peak in the sample tested in PBS and PBS+BSA (Figure 6.28), a weaker P signal was observed in PBS+BSA (approximately 25 %). This observation clearly indicates that a competitive adsorption between phosphate ions and BSA takes place on the CoCrMo surface.

Figure 6.34 shows the scheme of the surface model in PBS+BSA electrolyte in which the protein adsorption takes up the entire surface reaching a protein coverage of nearby 100 %.

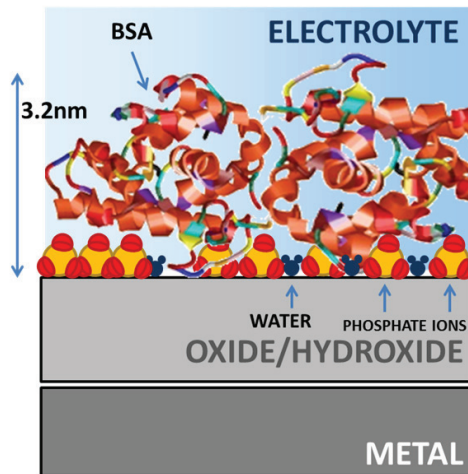


Figure 6.34. Adsorption layer model of the species present in the simulated body fluid after the passivation of the CoCrMo biomedical alloy in PBS+BSA from -0.05 to 0.35 V at  $10 \text{ mV s}^{-1}$  and  $37^\circ\text{C}$ . A continuous adsorption layer was obtained by the BSA.

The same procedure was carried out in the first potential step (from OCP to -0.05 V) in order to analyze the influence of the applied potential on the proposed model. The mass variation in the oxide film at -0.05 V in PBS and PBS+BSA was  $69 \text{ ng cm}^{-2}$  ( $\text{mass}_{\text{BSA}}$ ), which is equivalent to  $1.500 \cdot 10^{11}$  BSA molecules adsorbed on the CoCrMo surface. Therefore, the coverage of the protein at -0.05 V is 36 % which implies a reduction in the coverage of 60 % respect to the coverage at 0.35 V. These results indicate that the coverage depends on the applied passive potential, thus increasing when the potential increases.

XPS was also used to obtain the coverage under passive conditions at -0.05 V. At this potential the ratio between the intensity peaks of nitrogen and the oxide film was  $I_N^{BSA}/I_i^{film} = 0.139$ . Thus, the coverage was determined including the **equation (6.32)** within the expression  $I_N^{BSA}/I_i^{film}$  according to the procedure described by Iturbide et al. [14].

$$d^{BSA} = \frac{\Delta m}{\theta \cdot \rho_{BSA}} \quad (6.32)$$

Following this method, protein takes up 40 % of the entire surface (coverage) reaching a protein thickness of 1.45 nm (less than one monolayer). These results are consistent with the EQCM values taking into account the uncertainties associated with XPS technique. Rinsing and sample treatment after electrochemical tests can influence substantially the accuracy measurement of the nitrogen intensity peak.

A scheme of the adsorption layer on the CoCrMo alloy surface at -0.05 V is shown in **Figure 6.35**. In this, the coverage attained by the BSA adsorption is considerably lower than the obtained at higher applied passive potentials where the entire surface was covered. Furthermore, the model proposed in **Figure 6.35** is consistent with the EIS data obtained at the same potential (-0.05 V) in the Chapter 4. In this, a coverage of approximately 30 % was obtained using  $R_p$  values ( $643$  and  $894 \text{ k}\Omega \text{ cm}^{-2}$  in PBS and PBS+BSA respectively) and the **equation (5.1)** (Chapter 5).

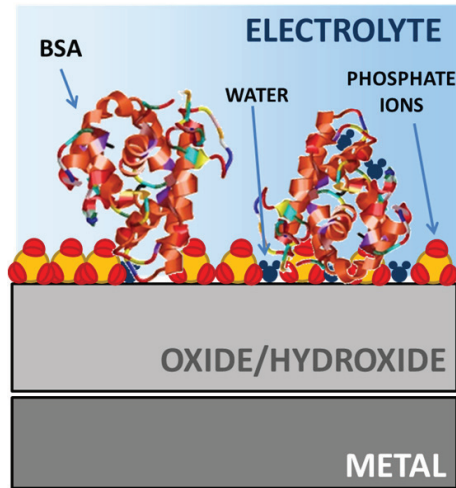


**Figure 6.35.** Adsorption layer model of the species present in the simulated body fluid after the passivation of the CoCrMo biomedical alloy in PBS+BSA at -0.05 V. A discontinuous adsorption layer was obtained for the BSA under those conditions.

## 6.5. Conclusions

Combined EQCM and XPS experiments have been used for analysing the electrochemical behaviour of a PVD-CoCrMo biomedical alloy in phosphate buffer solution at 37°C. The simultaneous measurements of the electrode mass change in the nanogram range, of the current and charge permitted, using the passive film composition determined by XPS, the evaluation of the passive film growth and passive dissolution kinetics. The following conclusions are drawn:

1. The electrochemical behaviour of the PVD-CoCrMo alloy corresponds well with the one observed for the CoCrMo bulk alloy.
2. Mass loss was observed in the whole investigated potential range. In the passive region, mass loss was considerably lower than in the transpassive region. Increasing temperature promotes passive and transpassive dissolution.
3. In the potentiostatic tests at 0.35 V (passive potential) the passive film initially grows at a fast rate of over 0.25 nm min<sup>-1</sup> (room temperature and 10 mV s<sup>-1</sup>), 0.33 nm min<sup>-1</sup> (37°C and 10 mV s<sup>-1</sup>) and 0.57 nm min<sup>-1</sup> (37°C and 100 mV s<sup>-1</sup>) while after 300 s the growth rate decreases one order of magnitude. Neither scan rate nor temperature has a significant influence on passive film growth. The mass loss rate (dissolution) decreases exponentially with time.
4. At the transpassive potential of 0.55 V the film grows from the beginning at a constant rate of 0.49 nm min<sup>-1</sup> at room temperature and 0.77 nm min<sup>-1</sup> at 37°C. The observed constant mass loss rate indicates that the passive film at the transpassive potential is cracked or porous.
5. The onset of the transpassive dissolution takes place at potentials above the transpassive potential as commonly defined by the increase in the current density on polarization curves. The latter corresponds well to the oxidation of Cr(III) oxide. This indicates that oxidation of Cr<sup>+3</sup> to Cr<sup>+6</sup> is not sufficient to trigger the transpassive dissolution of CoCrMo.
6. Mass variation of the oxide film is independent of the presence of BSA with a value of 5.2 ng cm<sup>-2</sup> s<sup>-1</sup> at the beginning of the potentiostatic test (below 60 s) at an applied passive potential. However, the adsorption of BSA increases the mass variation of the oxide film above 60 s reaching a steady-state value after

**CHAPTER 6.** Study of the passivation and adsorption kinetics by EQCM and XPS

300 s. The oxide film formation is faster than the adsorption of the BSA. XPS data shows that the passive film properties (chemical composition and thickness) are not modified by the BSA adsorption.

7. The mass difference of  $185 \text{ ng cm}^{-2}$  is attributed to the adsorption of the BSA which supposes a protein coverage of 96 % on the entire electrode surface at high passive potentials (0.35 V). Nevertheless, the protein coverage decreased considerably when the potential decrease (-0.05 V) reaching values lower than 40 %. Therefore, the protein coverage depends on the applied potential, thus increasing when the potential increases.

## 6.6. References

- [1] C.-O. A. Olsson, D. Landolt, *Electrochimica Acta* 48 (2003) 3999-4011.
- [2] M. G. Verge, C.-O. A. Olsson, D. Landolt, *Corrosion Science* 46 (2004) 2583-2600.
- [3] C.-O. A. Olsson, M. G. Verge, D. Landolt, *Journal of the Electrochemical Society* 151 (2004) B652-B660.
- [4] P. Schmutz, D. Landolt, *Electrochimica Acta* 45 (1999) 899-911.
- [5] P. Schmutz, D. Landolt, *Corrosion Science* 41 (1999) 2143-2163.
- [6] D. Hamm, K. Ogle, C.-O. A. Olsson, S. Weber, D. Landolt, *Corrosion Science* 44 (2002) 1443-1456.
- [7] C.-O. A. Olsson, D. Landolt, *Electrochimica Acta* 48 (2003) 1093-1104.
- [8] C.-O. A. Olsson, D. Landolt, *Journal of the Electrochemical Society* 148 (2001) B438-B449.
- [9] C.-O. A. Olsson, D. Hamm, D. Landolt, *Journal of the Electrochemical Society* 147 (2000) 2563-2571.
- [10] V. Payet, S. Brunner, A. Galtayries, I. Frateur, P. Marcus, *Surface and Interface Analysis* 40 (2008) 215-219.
- [11] M. Herranen, J.-O. Carlsson, *Corrosion Science* 43 (2001) 365-379.
- [12] F. Höök, J. Vörös, M. Rodahl, R. Kurrat, P. Böni, J. J. Ramsden, M. Textor, N. D. Spencer, P. Tengvall, J. Gold, B. Kasemo, *Colloids and Surfaces B: Biointerfaces* 24 (2002) 155-170.
- [13] I. Frateur, J. Lecoer, S. Zanna, C. O. A. Olsson, D. Landolt, P. Marcus, *Electrochimica Acta* 52 (2007) 7660-7669.
- [14] A. Ithurbide, I. Frateur, A. Galtayries, P. Marcus, *Electrochimica Acta* 53 (2007) 1336-1345.
- [15] S. Virtanen, I. Milosev, E. Gomez-Barrena, R. Trebse, J. Salo, Y. T. Konttinen, *Acta Biomaterialia* 4 (2008) 468-476.
- [16] V. Payet, T. Dini, S. Brunner, A. Galtayries, I. Frateur, P. Marcus, *Surface and Interface Analysis* (2010).
- [17] A. Igual Muñoz and S. Mischler, Inter-laboratory study on electrochemical methods for the characterisation of CoCrMo biomedical alloys in simulated



**CHAPTER 6.** Study of the passivation and adsorption kinetics by EQCM and XPS

body fluids, European Federation of Corrosion by Maney Publishing on behalf of The Institute of Materials, Minerals & Mining, 2011.

- [18] F. Galliano, C.-O. A. Olsson, D. Landolt, *Journal of the Electrochemical Society* 150 (2003) B504-B511.
- [19] S. Bruckenstein, M. Shay, *Electrochimica Acta* 30 (1985) 1295-1300.
- [20] P. Kern, D. Landolt, *Journal of the Electrochemical Society* 147 (2000) 318-325.
- [21] J. J. Kelly, K. M. A. Rahman, C. J. Durning, A. C. West, *Journal of the Electrochemical Society* 145 (1998) 492-497.
- [22] A. W. E. Hodgson, S. Kurz, S. Virtanen, V. Fervel, C.-O. A. Olsson, S. Mischler, *Electrochimica Acta* 49 (2004) 2167-2178.
- [23] A. Igual Muñoz, S. Mischler, *Journal of the Electrochemical Society* 154 (2007) C562-C570.
- [24] C.-O. A. Olsson, D. Landolt, *Corrosion Science* 46 (2004) 213-224.
- [25] B. Brox, I. Olefjord. *Proceedings of Stainless Steel 1984*, 134. 1985.
- [26] L. Wegrelius, I. Olefjord. *Proceedings of 12th International Corrosion Congress (NACE) 5B*, 3887. 1993.
- [27] A. Savitzky, M. J. E. Golay, *Analytical Chemistry* 36 (1964) 1627-1639.
- [28] A. Ouerd, C. Alemany-Dumont, B. Normand, S. Szunerits, *Electrochimica Acta* 53 (2008) 4461-4469.
- [29] S. Tanuma, C. J. Powell, R. Penn, *Surface and Interface Analysis* 21 (1994) 165-176.
- [30] S. Tanuma, C. J. Powell, R. Penn, *Surface and Interface Analysis* 35 (2003) 268-275.
- [31] I. Olefjord, B.-O. Elfström, *Corrosion* 38 (1982) 46-52.
- [32] I. Milosev, H.-H. Strehblow, *Electrochimica Acta* 48 (2003) 2767-2774.
- [33] A. Kocijan, I. Milosev, B. Pihlar, *Journal of Materials Science-Materials in Medicine* 15 (2004) 643-650.
- [34] D. Hamm, C.-O. A. Olsson, D. Landolt, *Corrosion Science* 44 (2002) 1009-1025.
- [35] P. Schmutz, S. Virtanen, A. J. Davenport, C. M. Vitus, *Journal of the Electrochemical Society* 143 (1996) 3997-4005.



## CHAPTER 7: CONCLUSIONS

---

The corrosion mechanisms of a high-carbon CoCrMo biomedical alloy for surgical implants in physiological conditions were analysed by electrochemical techniques (Open-Circuit measurements, potentiodynamic polarization curves, potentiostatic tests, Electrochemical Impedance Spectroscopy and Electrochemical Quartz Crystal Microbalance) and surface analysis (X-Ray Photoelectron Spectroscopy).

The results obtained in this Thesis have been presented in three main chapters analysing several electrochemical aspects of the CoCrMo degradation mechanisms. The main contributions to the Thesis have been included at the end of each chapter and the final and general conclusions are summarized here.

These final conclusions are divided into four groups: the first group is related to the suitability of different electrochemical and surface analysis techniques for the characterization of biomedical alloys; the other set of conclusions is related to the three degradation phenomena occurring in the CoCrMo alloy (i.e. passive dissolution, transpassive dissolution and adsorption).

**1. Electrochemical techniques** have demonstrated to be useful and sensitive tools for characterizing the corrosion behaviour of the CoCrMo biomedical alloy in physiological conditions.

**1.1.** Potentiodynamic and potentiostatic tests allow the identification of the general electrochemical behaviour of the CoCrMo alloy in simulated body fluids. Four main potential domains were observed in the polarization curves: the cathodic domain where the current is determined by the reduction of water and partially of dissolved oxygen, the cathodic-anodic transition at the corrosion potential, the passive plateau and the transpassive domain in which current increase is due to transpassive dissolution of metallic oxides and water oxidation.

**1.2.** Electrochemical Impedance Spectroscopy (EIS) was used to characterize the electrolyte/biomaterial interface. The surface processes were successfully modelled by the Equivalent Electrical Circuit approach, which consist of two serial *RC* subcircuits: one for the inner passive oxide layer and one for the outer adsorbed layer. The selected model was found to be consistent with the *DC* electrochemical results and it was appropriately modified depending on the electrode potential and surface chemistry.

**1.3.** Kinetics of passive film growth on the CoCrMo biomedical alloys was studied by Electrochemical Quartz Crystal Microbalance at room temperature and 37°C. Good correlation between the results from Electrochemical Quartz Crystal Microbalance and X-Ray Photoelectron Spectroscopy was obtained related to the oxide film growth in PVD-CoCrMo alloy under simulated physiological conditions. The PVD-CoCrMo alloy was used in EQCM measurements and its electrochemical behaviour corresponded well with the CoCrMo bulk alloy.

2. The main corrosion mechanism of the CoCrMo alloy in physiological systems is the **passive dissolution**. The electrochemical reactions occurring at the interface of the CoCrMo alloy oxide film/electrolyte strongly depend on the potential electrode and electrolyte (chemical composition and temperature).

2.1. The passive film consists of a hydroxide and an oxide layer with a hydroxide and oxide film thickness ratio of about 1:1. This passive film is mainly composed of  $\text{Cr}^{+3}$  ions and Co is dissolved into the solution. In addition, the Co content decreases with the increasing potential within the passive domain.

2.2. The resistance of the passive film was influenced by the presence of the inorganic compounds:  $\text{H}_2\text{PO}_4^-$  favours the formation of passive film which improves the resistance of the CoCrMo alloy to passive dissolution. When the concentration of the  $\text{H}_2\text{PO}_4^-$  increases (when pH decreases), the polarization resistance of the alloy also increases.

2.3. Oxygen effect on CoCrMo passivity depends on the pH of the PBS solution but reduces the passive dissolution resistance of the alloy in all conditions studied.

2.4. Passivity was accompanied by a mass loss in the investigated passive potential range (-0.05 to 0.35 V). The mass loss rate (dissolution) exponentially decreases with time. Increasing temperature promotes this passive dissolution, thus generating higher mass loss.

2.5. At an applied passive potential 0.35 V, the passive film initially grows at the fast rate of  $0.25 \text{ nm min}^{-1}$  (room temperature and  $10 \text{ mV s}^{-1}$ ),  $0.33 \text{ nm min}^{-1}$  ( $37^\circ\text{C}$  and  $10 \text{ mV s}^{-1}$ ) and  $0.57 \text{ nm min}^{-1}$  ( $37^\circ\text{C}$  and  $100 \text{ mV s}^{-1}$ ) while after 300 s the growth rate decreases one order of magnitude. Neither scan rate nor temperature has a significant influence on passive film growth.

3. At higher anodic potentials, the *transpassive dissolution* is the main corrosion mechanism since no evidence of localized or pitting corrosion was detected on the CoCrMo alloy. Thus, under moderately strong oxidizing conditions transpassive dissolution is relevant, because it induces the release of the toxic and carcinogenic Cr<sup>+6</sup> species.

3.1. In the transpassive domain Co constitutes more than 50 % of the cations and a significant fraction of Cr ions are oxidized to valence VI. The film thickness obtained at applied transpassive potential is much larger than in the passive domain. In addition, the ration between hydroxide and oxide thickness varies to 2:1 regarding the passive domain.

3.2. In the transpassive region, mass loss was considerably higher than in the passive region, where the increase of temperature also promotes transpassive dissolution.

3.3. At the transpassive potential of 0.55 V the film grows from the beginning at a constant rate of 0.49 nm min<sup>-1</sup> at room temperature and 0.77 nm min<sup>-1</sup> at 37°C. The observed constant mass loss rate indicates that the passive film on the PVD-CoCrMo alloy deposit at the transpassive potential is cracked or porous.

3.4. The onset of the transpassive dissolution takes place at potentials above the transpassive potential as commonly defined by the increase in the current density on polarization curves. The latter corresponds well to the oxidation of Cr<sup>+3</sup> oxide. This indicates that the oxidation of Cr<sup>+3</sup> to Cr<sup>+6</sup> is insufficient to trigger the transpassive dissolution of CoCrMo.

4. The **adsorption** process of the Bovine Serum Albumin on the CoCrMo biomedical alloy was studied, allowing to draw following conclusions:

4.1. A charge-transfer resistance value, which represents a direct measure of a corrosion rate, proved to be very sensitive to the amount of adsorbed protein (surface concentration). This indicates that the protein adsorption (*i*) was accompanied by the transfer of the charge, via chemisorption, and (*ii*) influenced the mechanism and kinetics of the corrosion reaction. This also became apparent by the decrease in the corrosion activation energy, caused by protein adsorption. BSA shows a very high affinity towards adsorption at a CoCrMo surface via chemisorption.

4.2. The adsorption process was modelled using the Langmuir adsorption isotherm. The corresponding thermodynamic data was calculated to obtain the Gibbs free energy, enthalpy and entropy of adsorption. The positive value of enthalpy indicates that energetic excess is involved in the breaking of intramolecular interactions relative to those involved in the formation of protein-metal bonds. However, since the adsorption process was found to be entropically governed, structural unfolding of the protein likely occurs at the electrode surface.

4.3. The influence of BSA adsorption on the electrochemical behaviour of the CoCrMo alloy depends on the electrode potential:

- BSA acts as cathodic inhibitor impeding the access of the oxidant to the metallic surfaces and accelerating the anodic reaction. This effect on the cathodic domain depends on the pH. At pH 3 no influence of BSA in the cathodic domain was observed in deoxygenated solutions. This implies that BSA acts over the oxygen reduction reaction in acidic media. On the contrary, a noticeable influence of BSA addition was observed at pH 7.4 (mainly in aerated solution). In this case, a strong effect of oxygen was detected in the potentiodynamic curves due to the mass transport

limitation in the oxygen content solution. Finally, at pH 10, the influence of BSA was similar to that in neutral solutions. Thus, in neutral-alkaline solutions BSA suppresses mass transport limitation produced by the excess of oxygen in the electrolyte.

- At low applied passive potentials BSA increases the corrosion resistance (blocking the surface), while at high passive potentials the opposite effect is obtained (increase of the passive dissolution). In both cases, BSA competes with the different phosphates species for this adsorption thus enhancing or reducing the passive dissolution of the alloy depending on the solution pH. The adsorption of phosphates individually acts reducing the corrosion rate of the alloy. BSA effect is detrimental when substituting  $\text{H}_2\text{PO}_4^-$  sites (pH 3) but it increases the CoCrMo resistance when substituting  $\text{HPO}_4^{2-}$  sites (pH 7.4 and pH 10).

**4.4.** At OCP the BSA adsorption kinetics depends on the immersion time. BSA adsorption kinetics was influenced by surface passivation when passivation time was less than 1 hour. At higher passivation times, no apparent modification in the kinetic mechanisms of adsorption was observed. Furthermore the amount of adsorbed BSA decreased with the passivation time on the CoCrMo surface.

**4.5.** Mass variation of the oxide film is independent of the presence of BSA with a value of  $5.2 \text{ ng cm}^{-2} \text{ s}^{-1}$  at the beginning of the tests (below 60 s) at an applied passive potential. However, the adsorption of BSA increases the mass variation of the oxide film above 60 s reaching a steady-state value after 300 s. Therefore, the oxide film formation is faster than the adsorption of the BSA. XPS data shows that the passive film properties (composition and thickness) are not modified by the adsorption of BSA.



4.6. Difference in mass increase in the film of  $185 \text{ ng cm}^{-2}$  in PBS+BSA with regard to the PBS at 0.35 V is attributed to the adsorption of the BSA. This means a protein coverage of 96 % on the entire electrode surface. However, this protein coverage decreases considerably at lower potentials (-0.05 V) reaching values below 40 %. Therefore, the protein coverage depends on the applied potential, thus increasing when the potential increases.



## APPENDIX. List of symbols and abbreviations

---

### List of symbols:

$A$	Active area ( $\text{cm}^2$ )
$A_{Ar}$	Pre-exponential factor
$A_S$	Passivation kinetics constant
$a_a$	Anodic Tafel constant (V)
$a_c$	Cathodic Tafel constant (V)
$B$	Diffusion parameter
$B_{ADS}$	Affinity of the adsorbate molecules ( $\text{cm}^3 \text{mol}^{-1}$ )
$b_a$	Anodic Tafel constant (V)
$b_c$	Cathodic Tafel constant (V)
$C$	Capacitance ( $\text{F cm}^{-2}$ )
$C_f$	Sensitivity factor ( $\text{Hz cm}^2 \text{g}^{-1}$ )
$C_{dl}$	Double layer capacitance ( $\text{F cm}^{-2}$ )
$C_i$	Concentration of the specie $i$ ( $\text{mol m}^{-3}$ )
$c_i$	Concentration of the element $i$ (fraction or %)
$C_{in}$	Capacitance of the inner layer ( $\text{F cm}^{-2}$ )
$C_{out}$	Capacitance of the outer layer ( $\text{F cm}^{-2}$ )
$c_s$	Protein concentration ( $\text{mol cm}^{-3}$ )
$D$	Diffusion coefficient ( $\text{m}^2 \text{s}^{-1}$ )
$D^i$	Bulk concentration of the element in the matrix $i$ ( $\text{mol cm}^{-3}$ )
$d$	Film thickness (m)
$d_q$	Quartz thickness (m)

$d_f$	Film thickness (m)
$E_a$	Activation energy ( $\text{J mol}^{-1}$ )
$E_b$	Binding energy of the electron
$E_{br}$	Breakdown potential (V)
$E_{corr}$	Corrosion potential (V)
$E_k$	Kinetic energy of the photoelectrons emitted by the sample (eV)
$E_{pass}$	Passivation potential (V)
$E_{rev}$	Equilibrium potential for a single electrode (V)
$E_{st}$	Steady State Potential (V)
$E_{TD}$	Transpassive dissolution potential (V)
$E_{TO}$	Transpassive oxidation potential (V)
$F$	Faraday constant ( $96485 \text{ C mol}^{-1}$ )
$\Delta f$	Frequency change (Hz)
$\Delta f_m$	Frequency due to mass loading (Hz)
$\Delta f_v$	Frequency due to viscous loading (Hz)
$f$	Frequency (Hz)
$f_0$	Quartz frequency (Hz)
$f_q$	Resonance frequency of the unloaded crystal (Hz)
$\Delta G_{ADS}$	Gibbs free energy of adsorption ( $\text{J mol}^{-1}$ )
$g$	Common spectrometer constant
$\Delta H_{ADS}$	Enthalpy of adsorption ( $\text{J mol}^{-1}$ )
$I_{RX}$	Intensity of the incident radiation
$i$	Current density ( $\text{A cm}^{-2}$ )
$i_a$	Anodic current density ( $\text{A cm}^{-2}$ )
$i_c$	Cathodic current density ( $\text{A cm}^{-2}$ )
$i_{corr}$	Corrosion current density ( $\text{A cm}^{-2}$ )

**APPENDIX.** List of symbols and abbreviations

$i_f$	Final current density ( $A\text{ cm}^{-2}$ )
$i_{lim}$	Limiting current density ( $A\text{ cm}^{-2}$ )
$i_p$	Passive current density, potentiodynamic curves ( $A\text{ cm}^{-2}$ )
$i_{pass}$	Passivation current density ( $A\text{ cm}^{-2}$ )
$i_{pp}$	Passive current density, potentiostatic test ( $A\text{ cm}^{-2}$ )
$j$	Complex or imaginary number
$K$	Adsorption coefficient
$K_1$	Constant ( $m^4\text{ s}^{-1}\text{ g}^{-1}$ )
$K_2$	Constant ( $2.75 \cdot 10^{-11}\text{ m}^2\text{ N}^{-1}$ )
$K_v$	Proportional constant between frequency and resistance ( $\text{Hz}\ \Omega^{-1}$ )
$k_{ads}$	Rate constant for adsorption
$k_{des}$	Rate constant for desorption
$L$	Inductance ( $\text{H cm}^2$ )
$M$	Mass unrelated to the quartz crystal mass (ng)
$m$	Mass ( $\text{ng cm}^{-2}$ )
$m_{EQCM}$	Mass measured by the EQCM ( $\text{ng cm}^{-2}$ )
$M_f$	Mass of the film (ng)
$m_f$	Mass of the film per surface units respectively ( $\text{ng cm}^{-2}$ )
$m_{FILM}$	Mass variation of the oxide film ( $\text{ng cm}^{-2}$ )
$M_q$	Mass of the quartz crystal (ng)
$m_q$	Mass of the quartz per surface units respectively ( $\text{ng cm}^{-2}$ )
$M_r$	Atomic mass ( $\text{g mol}^{-1}$ )
$\Delta m$	Mass change (g)
$N$	Armonic resonance number ( $N=1$ )
$n$	CPE exponent
$n_i$	Charge number or valence of dissolution of the metal $i$

$n_s$	Passivation rate parameter
$\Delta p$	Difference of pressure between the quartz sides ( $\text{g m}^{-2}$ )
$q$	Electrical charge ( $\text{C cm}^{-2}$ )
$R$	Gas constant ( $8.314 \text{ J mol}^{-1} \text{ K}^{-1}$ )
$R_{ct}$	Charge transfer resistance ( $\Omega \text{ cm}^2$ )
$R_s$	Solution resistance ( $\Omega \text{ cm}^2$ )
$R_{in}$	Resistance of the inner layer ( $\Omega \text{ cm}^2$ )
$R_{out}$	Resistance of the outer layer ( $\Omega \text{ cm}^2$ )
$R_p$	Polarization resistance ( $\Omega \text{ cm}^2$ )
$\Delta R_{cryst}$	Crystal resistance ( $\Omega$ )
$\Delta S_{ADS}$	Entropy of adsorption ( $\text{J mol}^{-1} \text{ K}^{-1}$ )
$T(E)$	Transmission function
$T$	Temperature (K)
$t$	Time (s)
$Y_0$	Admittance
$Z$	Impedance ( $\Omega \text{ cm}^2$ )
$Z_{Re}$	Real part of the Impedance ( $\Omega \text{ cm}^2$ )
$Z_{Im}$	Imaginary part of the impedance ( $\Omega \text{ cm}^2$ )
$z$	Depth (m)
$\alpha$	Proportional factor
$\alpha$	Charge transfer coefficient (0-1)
$\alpha_{sp}$	Spectrometer constant
$\beta_a$	Anodic Tafel coefficient (V)
$\beta_c$	Cathodic Tafel coefficient (V)
$\delta$	Thickness of the diffusion layer (m)
$\varepsilon$	Relative dielectric constant

**APPENDIX.** List of symbols and abbreviations

$\varepsilon_0$	Permittivity of the vacuum ( $8.85 \cdot 10^{-14} \text{ F cm}^{-1}$ )
$\phi$	Escape angle of the detected electrons with respect to the normal to the sample surface
$\phi_{w,det}$	Work function of the detector
$\Gamma$	Amount of protein adsorbed ( $\text{mol cm}^{-2}$ )
$\Gamma_{max}$	Maximum amount of protein adsorbed ( $\text{mol cm}^{-2}$ )
$\Delta\gamma$	Change in surface tension ( $\text{N m}^{-1}$ )
$\eta$	Overpotential (V)
$\eta_l$	Absolute viscosity of the liquid ( $\text{N s m}^{-2}$ )
$\varphi$	Phase (degrees)
$\Lambda$	Escape depth (m)
$\lambda$	Potential sweep rate ( $\text{V s}^{-1}$ )
$\lambda_i$	Inelastic mean free path of the photoelectrons emitted by the X core level in the matrix M (m)
$\lambda_q$	Length wave in shear mode ( $\mu\text{m}$ )
$\mu_q$	Elastic shear modulus of the quartz ( $\text{N cm}^{-2}$ )
$v_q$	Transverse wave propagation speed ( $\text{m s}^{-1}$ )
$\theta$	Protein coverage
$\theta_{max}$	Maximum level of protein coverage
$\rho$	Density ( $\text{kg m}^{-3}$ )
$\rho_q$	Quartz density ( $\text{kg cm}^{-3}$ )
$\rho_l$	Density of the liquid ( $\text{kg cm}^{-3}$ )
$\sigma$	Cross section for generation of photoelectrons
$\tau_v^*$	Dimensionless time for characterize the transition from non-steady-state to steady-state conditions.
$\omega$	Radial frequency ( $\text{rad s}^{-1}$ )

## Abbreviations:

<i>BS</i>	Bovine Serum
<i>BSA</i>	Bovine Serum Albumin
<i>CPE</i>	Constant Phase Element
<i>EEC</i>	Equivalent Electrical Circuit
<i>EQCM</i>	Electrochemical Quartz Crystal Microbalance
<i>FRA</i>	Frequency Response Analyzer
<i>HIP</i>	Hot Isostatic Pressing
<i>IHP</i>	Inner Helmholtz Layer
<i>IMFP</i>	Inelastic Mean Free Path
<i>OCP</i>	Open Circuit Potential
<i>OHP</i>	Outer Helmholtz Layer
<i>PBS</i>	Phosphate Buffer Saline
<i>PC</i>	Porous coating
<i>RSF</i>	Relative Sensitivity Factors
<i>SA</i>	Solution Annealing
<i>XPS</i>	X-Ray Photoelectron Spectroscopy



## RESUMEN

---

La aleación biomédica CoCrMo se emplea en la elaboración de prótesis de sustituciones articulares totales o parciales de cadera y rodilla debido a su biocompatibilidad y a sus buenas propiedades mecánicas entre las que destacan su elevada resistencia a la corrosión y al desgaste. La superficie del biomaterial CoCrMo reacciona de manera espontánea con el medio que la rodea formando una capa pasiva de óxidos metálicos que auto-protege a la aleación del medio y condiciona su comportamiento frente a la corrosión. Hay que tener en cuenta que el medio en el que trabajan estas prótesis es uno de los más agresivos que se conocen lo que agrava el proceso de corrosión. Dicho proceso contribuye a la liberación de iones metálicos dentro del cuerpo humano acelerando el deterioro de dichas prótesis y problemas clínicos en los pacientes.

En este contexto, la presente Tesis Doctoral pretende estudiar los mecanismos de biocorrosión que determinan la degradación de la aleación CoCrMo en condiciones fisiológicas.

Para ello, en primer lugar se ha realizado la caracterización electroquímica del biomaterial en diferentes condiciones físico-químicas de relevancia biológica (composición química del fluido simulado, pH, contenido en oxígeno y potencial aplicado) las cuales influyen notablemente en las reacciones electroquímicas que tienen lugar en la interfase biomaterial/medio. Posteriormente, se ha estudiado cómo influye la adsorción de albúmina (proteína modelo y mayoritaria en el cuerpo humano) en el comportamiento electroquímico de la aleación en función de la concentración de proteína y la temperatura del medio. Este estudio se ha llevado a cabo desde el punto de vista termodinámico y se ha demostrado que el proceso de adsorción de la proteína sobre la superficie de la aleación CoCrMo ocurre de manera espontánea por quimisorción modelándose correctamente mediante la Isoterma de Langmuir. Finalmente, se han estudiado las cinéticas de pasivación y de adsorción de proteína mediante la puesta a punto de una microbalanza electroquímica de cristal de cuarzo sobre la aleación CoCrMo a 37°C y el posterior análisis de superficies ex-situ. La utilización complementaria de ambas técnicas

ha permitido cuantificar la cantidad de cationes metálicos liberados por el material al medio fisiológico así como las propiedades de la capa pasiva formada (composición química y espesor).

Con todo ello se ha visto que la disolución pasiva del CoCrMo depende críticamente del potencial electroquímico y de las características del medio (temperatura y composición química).

Los resultados obtenidos en la presente Tesis Doctoral suponen el primer paso necesario para el análisis del comportamiento de la aleación biomédica CoCrMo en condiciones reales no sólo de corrosión sino también de desgaste (fenómeno de tribocorrosión).

## RESUM

---

L'aliatge biomèdic CoCrMo s'utilitza en l'elaboració de pròtesis de substitucions articulars totals o parcials de maluc i genoll gràcies a la seua biocompatibilitat i les seues bones propietats mecàniques entre les quals destaquen la seua elevada resistència a la corrosió i al desgast. La superfície del biomaterial CoCrMo reacciona espontàniament amb l'entorn que l'envolta formant una capa passiva d'òxids metàl·lics que auto-protegeix a l'aliatge del medi i condiona el seu comportament contra la corrosió. S'ha de tenir en compte que l'entorn on treballen aquestes pròtesis és un dels més agressius coneguts fet que agreuja el procés de corrosió. Aquest procés contribueix a l'alliberament d'ions metàl·lics dins del cos humà i accelera el deteriorament de les pròtesis fet que genera problemes clínics als pacients.

En aquest context, la present Tesi Doctoral pretén estudiar els mecanismes de biocorrosió que determinen la degradació de l'aliatge CoCrMo en condicions fisiològiques.

Per tant, en primer lloc s'ha realitzat la caracterització electroquímica del biomaterial en les diferents condicions fisico-químiques de rellevància biològica (composició química del fluït simulat, pH, contingut d'oxigen i potencial aplicat) les quals influeixen notablement en les reaccions electroquímiques que es duen a terme en la interfície biomaterial/medi. Posteriorment, s'ha estudiat com influeix l'adsorció d'albumina (proteïna model i majoritària en el cos humà) sobre el comportament electroquímico de l'aliatge en funció de la concentració de proteïna i la temperatura del medi. Aquest estudi s'ha realitzat des d'un punt de vista termodinàmic i s'ha demostrat que el procés d'adsorció de la proteïna a la superfície de l'aliatge CoCrMo es produeix espontàniament per quimisorció modelant-se correctament a través de la Isoterma de Langmuir. Finalment, s'ha estudiat la cinètica de passivació i d'adsorció de la proteïna mitjançant una microbalança electroquímica de cristall de quars sobre un aliatge de CoCrMo a 37°C junt amb l'anàlisi de superfícies ex-situ. La utilització complementària de les dues tècniques ha permès quantificar la

quantitat d'ions metàl·lics alliberats del material al medi fisiològic així com les propietats de la capa passiva formada (composició química i espessor).

Amb tot això s'ha observat que la dissolució passiva del CoCrMo depèn fonamentalment del potencial electroquímic i les característiques del medi (temperatura i composició química).

Els resultats obtinguts en la present Tesi Doctoral suposen el primer pas necessari per a l'anàlisi del comportament de l'aliatge biomèdic CoCrMo en condicions reals no només de corrosió sinó també de desgast (fenomen de tribocorrosió).

## ABSTRACT

---

CoCrMo biomedical alloys are used in the design of total or partial hip and knee joints due to their biocompatibility and their good mechanical properties such as high corrosion and wear resistance. The biomaterial surface spontaneously reacts with the environment forming a passive film of metallic oxides which protects the alloy from the medium and determines its corrosion behaviour. The physiological media are one of the most aggressive electrolytes which enhance the corrosion process. This process contributes to metallic ions release into the human body and accelerates the degradation of these prostheses generating clinical problems in the patients.

In this panorama, the present Doctoral Thesis aims to study the biocorrosion mechanisms of the CoCrMo alloy degradation under physiological conditions.

For this, the electrochemical characterization of the biomaterial under different physico-chemical conditions with biological relevance has been carried out (chemical composition of the simulated body fluid, pH, oxygen content and applied potential) which noticeably influences the electrochemical reactions occurring at the biomaterial/media interface. Subsequently, the influence of the albumin adsorption (model and main protein in the human body) on the electrochemical behaviour of the alloy depending on the protein concentration and temperature of the medium has been studied. This adsorption study has been carried out from the thermodynamic point of view and it was observed that the protein adsorption process onto the CoCrMo alloy surface occurs spontaneously by chemisorption and can be modelled by the Langmuir Isotherm. Finally, the passivation and the protein adsorption kinetics have been studied by an electrochemical quartz crystal microbalance applied used on a CoCrMo alloy at 37°C and by ex-situ surface analysis. The complementary use of both techniques allows quantifying the amount of metallic cations released from the material to the physiological medium as well as the properties of the passive film (chemical composition and thickness).

With all these results, it has been observed that the CoCrMo passive dissolution critically depends on the electrochemical potential and the electrolyte properties (temperature and chemical composition).

The results obtained in the present Doctoral Thesis are the first step to analyse the behaviour of the CoCrMo biomedical alloy under more realistic conditions involving corrosion and wear phenomena (tribocorrosion phenomena).

